MODULATION AND DETECTION IN WIRELESS OPTICAL CHANNELS

MODULATION AND DETECTION IN WIRELESS OPTICAL CHANNELS USING TEMPORAL AND SPATIAL DEGREES OF FREEDOM

BY

MOHAMED DARWISH A. MOHAMED,

B.Sc., M.Sc.

A Thesis

Submitted to the School of Graduate Studies

in Partial Fulfilment of the Requirements

for the Degree

Doctor of Philosophy

McMaster University

Doctor of Philosophy (2010)	McMaster University
(Electrical & Computer Engineering)	Hamilton, Ontario, Canada

TITLE:	Modulation and Detection in Wireless Optical Channels using Temporal and Spatial Degrees of Freedom
AUTHOR:	Mohamed Darwish A. Mohamed B.Sc. (Electronics and Communications Engineering), M.Sc. (Engineering Mathematics), Cairo University, Cairo, Egypt.
SUPERVISOR:	Steve Hranilovic, Associate Professor
NUMBER OF PAGES:	xxxiv, 218

To my parents

Abstract

Most wireless optical modems are able to modulate and detect only the intensity of the optical carrier. As a result, conventional techniques, designed for radio frequency communications, are seldom efficient. This thesis designs new efficient modulation and detection techniques for wireless optical communication systems that take into consideration the characteristics and constraints of wireless optical channels.

Many degrees of freedom are available at the transmitter and the receiver in both temporal and spatial domains. The main theme of this thesis is to use such degrees of freedom to achieve higher power/spectral efficiencies and simpler transceivers. A new modulation technique, *optical impulse modulation* (OIM), is proposed for indoor diffuse wireless infrared channels. Present-day laser diodes have higher pulse rates than the channel bandwidth. OIM utilizes such extra temporal degrees of freedom to satisfy the channel amplitude constraints, while the transmit data are confined to the lowpass region that represents the channel passband. Another modulation technique, *halftoned spatial discrete multitone* (HSDMT) modulation, is proposed for indoor multi-input/multi-output (MIMO) point-to-point wireless optical links. Current spatial light modulators (SLMs) have higher spatial bandwidth than can be supported by the spatially lowpass MIMO channel. Such bandwidth provides extra spatial degrees of freedom that are employed by HSDMT modulation to decrease the transmitter

complexity by considering binary-level SLMs. Finally, a novel detection technique is proposed which employs the receiver spatial degrees of freedom to mitigate the effects of atmospheric turbulence in outdoor free-space optical communications. By using digital micromirror devices, the receiver optically computes linear projections of the turbulence-degraded focal-plane signal distribution onto an orthogonal basis. These projections are used to select the portions of the focal-plane which contain significant energy for symbol detection. Performance improvements are quantified via simulations for all the proposed techniques.

Acknowledgements

My first and foremost praise and gratitude is to God, the Most Merciful, the Most Compassionate. Without His help and guidance, this work would not be possible.

I would like to express my deep gratitude to my parents who have been taking good care of me and my education. I would like to express my greatest appreciation to their endless love, effort and sacrifice throughout my life.

I would like to express my sincere gratitude to my Ph.D. supervisor, Dr. Steve Hranilovic, for his consistent encouragement, support and insightful discussions. He has been a supervisor and an elder brother to me throughout the entire period of my Ph.D. I would also like to extend my thanks to my research supervisory committee members, Dr. Timothy Davidson and Dr. Kon Max Wong, for their valuable discussions, comments and suggestions. I would like to thank my comprehensive exam committee members, Dr. Timothy Field, Dr. Timothy Davidson, Dr. James Reilly, and Dr. Sorina Dumitrescu, for their encouraging remarks. I would like to thank all my lab colleagues, especially Awad Dabbo for his effort in the experimental work done in this thesis. In addition, I want to thank Cheryl Gies, Cosmin Coroiu, and all the administrative and technical staff at the Department of Electrical and Computer Engineering at McMaster University.

I owe a huge debt of gratitude to my university professors, teaching assistants, and school teachers for their contribution towards building my academic background. I would also like to thank my siblings who were always there when I needed their support and encouragement. Many thanks to my wife and my little son, Zeyad, who arrived to this world few weeks before finishing this thesis.

Acronyms

Note: The page numbers in brackets indicate where the acronyms are first defined.

2D	Two-Dimensional (p. 9)
AU	Astronomical Unit (p. 20)
BER	Bit Error-Rate (p. 19)
CCD	Charge Coupled Device (p. 9)
CMOS	Complementary Metal Oxide Semiconductor (p. 9)
dBo	Optical Decibel (p. 29)
DFE	Decision Feedback Equalization (p. 56)
DFT	Discrete Fourier Transform (p. 95)
DLP	Digital Light Processing (p. 123)
DMD	Digital Micromirror Device (p. 98)
DMT	Discrete Multitone (p. 95)
DTFT	Discrete-time Fourier transform (p. 187)
FOV	Field-Of-View (p. 34)
fps	Frames per second (p. 125)
FSO	Free-Space Optical (p. 2)
Gbps	Gigabits per second (p. 8)
GEOLite	Geosynchronous Lightweight Technology Experiment (p. 18)

GOLD	Ground/Orbiter Lasercomm Demonstration (p. 18)
GOPEX	Galileo Optical Experiment (p. 20)
HAP	High Altitude Platform (p. 19)
HSDMT	Halftoned Spatial Discrete Multitone (p. 29 and 98)
IEEE	Institute of Electrical and Electronics Engineers (p. 12)
IM/DD	Intensity Modulation with Direct Detection (p. 4)
IrDA	Infrared Data Association (p. 8)
IrFM	Infrared Financial Messaging (p. 8)
ISI	Inter-Symbol Interference (p. 57)
JPL	Jet Propulsion Laboratory (p. 19)
kbpf	kilobits per frame (p. 128)
kfps	kiloframes per second (p. 9)
LD	Laser Diodes (p. 2)
LED	Light-Emitting Diodes (p. 2)
Mbps	Megabits per second (p. 7)
Mfps	Megaframes per second (p. 10)
MIMO	Multiple-input/multiple-output (p. 9)
MLCD	Mars Laser Communications Demonstration (p. 21)
MLSD	Maximum Likelihood Sequence Detection (p. 56)
NASA	National Aeronautics and Space Administration (p. 20)
OIM	Optical Impulse Modulation (p. 27 and 51)
OOK	On-Off Keying (p. 28)
OTF	Optical Transfer Function (p. 33)
PAM	Pulse-Amplitude Modulation (p. 28)

PPM	Pulse-Position Modulation (p. 28)
PSD	Power Spectral Density (p. 42)
PSF	Point Spread Function (p. 23 and 33)
Rect-OOK	Rectangular on-off keying (p. 55)
Rect-PAM	Rectangular pulse-amplitude modulation (p. 55)
Rect-PPM	Rectangular pulse-position modulation (p. 55)
RF	Radio Frequency (p. 2)
SDMT	Spatial Discrete Multitone (p. 29 and 95)
SER	Symbol Error-Rate (p. 24)
SLM	Spatial Light Modulator (p. 9)
SNR	Signal-to-Noise Ratio (p. 4)
SILEX	Semi-Conductor Inter-Satellite Link EXperiment (p. 18)
Sinc-PAM	Sinc pulse-amplitude modulation (p. 57)
SLM	Spatial Light Modulator (p. 9)
Tbps	Terabits per second (p. 17)
TV	Television (p. 2)
WMF	Whitened Matched Filter (p. 66)
VCSELs	Vertical-Cavity Surface-Emitting Lasers (p. 98)
VLC	Visible Light Communications (p. 13)

Notations

Note: The page numbers in brackets indicate where the notations are first defined.

$\star$	Complex conjugate (p. 54)
$*$	Continuous-time convolution (p. 41)
$\otimes$	Discrete-time convolution (p. 54)
$\circledast$	Two dimentional linear convolution (p. 45)
$\mathcal{A}_d$	Photodetector area (p. 32)
$\mathcal{A}_r$	Receiver aperture area (p. 33)
$\mathcal{A}_t$	Transmitter aperture area (p. 47)
$\{a_k\}$	Discrete symbol sequence (p. 52)
$bg(t)$	OIM receive filter (p. 60)
D	Receiver aperture diameter (p. 48)
$\mathcal{D}$	Root-mean-square channel delay spread (p.42)
D_T	Transmitter aperture diameter (p. 32)
$\mathbb{E}$	Expectation operator (p. 54)
e_{ph}	Photon energy (p. 36)
$\mathcal{F}$	Discrete Fourier transform (p. 97)
$\mathcal{F}^{-1}$	Inverse discrete Fourier transform (p. 96)
f_ℓ	Focal length (p. 34)

H_0	Channel DC-gain (p. 42)
$H(f)$	Continuous-time Fourier transform of the impulse response, $h(t)$ (p. 43)
$h(t)$	Optical channel impulse response (p. 41)
$\hbar$	Differential entropy (p. 85)
$\bar{\hbar}$	Differential entropy rate (p. 85)
I	Intensity (p. 4)
$I_{\text{Lambertian}}$	Lambertian intensity pattern (p. 39)
I_r	Irradiance (p. 4)
$I_n^{(j)}$	Photon count of the n^{th} detector at the end of the j^{th} PPM chip (p. 138)
$I_{\mathcal{G}}^{(j)}$	Decision statistic at the end of the j^{th} PPM chip (p. 140)
$\tilde{I}_+^{(i)}$	Output Poisson counts of the photodetector D_+ (p. 147)
$\tilde{I}_-^{(i)}$	Output Poisson counts of the photodetector D_- (p. 147)
$I^{(0,t)}$	Number of electrons released during the time interval $(0, t)$ (p. 35)
$I(a; \hat{a})$	Mutual information between a and $\hat{a}$ (p. 85)
$\Im\{\cdot\}$	Imaginary-part operator (p. 70)
K_b	Background noise energy per array element per PPM chip (p. 139)
$K^{(j)}$	Total signal energy incident on the entire array during the j^{th} PPM chip (p. 139)
$K_n^{(j)}$	Signal energy incident on the n^{th} array element during the j^{th} PPM chip (p. 139)
K^{ON}	Total signal energy per PPM chip duration, when the chip is on (p. 139)
$\tilde{K}_b$	Background noise energy received by the n^{th} micromirror during a DMD switching period (p. 145)
$\tilde{K}$	Total energy received by the entire DMD array during

	a DMD switching period (p. 145)
$\tilde{K}_n^{(i)}$	Signal energy received by the n^{th} micromirror during the i^{th} DMD switching period (p. 145)
L	Number of PAM levels, or number of PPM chips (p. 53 and 55)
M	Length of the channel impulse response tails (p. 76)
N	Number of array elements (p. 138)
$N_0/2$	Noise double-sided power spectral density (p. 42)
$N(f)$	Spectral radiance function (p. 37)
$P(u,v)$	Pupil function (p. 33)
$P_f(f_u, f_v)$	Continuous Fourier transform of the pupil function, $P(u,v)$ (p. 33)
$\mathbb{P}$	Probability of an event (p. 85)
$\mathcal{P}$	Optical average power limit imposed by eye-safety constraints (p. 44)
$\mathcal{P}_b$	Background noise power (p. 37)
$\mathcal{P}_t$	Transmitted optical average power (p. 44)
$\mathcal{P}_t^{\text{OOK}}$	Transmitted optical average power required by a Rect-OOK system, transmitting at a given bit-rate, to achieve a given BER over a flat channel with a given noise power (p. 74)
$\mathscr{P}(f)$	Fourier transform of $p(t)$ (p. 61)
$p(t)$	Transmitter pulse shape (p. 52)
$Q(x)$	$\int_x^\infty \exp(-u^2/2)/\sqrt{2\pi}\, du$ (p. 178)
$Q^{-1}(x)$	Inverse of $Q(x)$ (p. 181)
q_k	Equivalent discrete-time impulse response (p. 53)
R	Photodetector responsivity (p. 41)
r_0	Atmospheric coherence width, also known as Fried's parameter (p. 48)

$r(t)$	Unit-energy receive filter (p. 52)
$r_d(t)$	Power incident over the detector surface (p. 36)
$r_n(t)$	Received power incident on the n^{th} array element at time t (p. 137)
$\Re\{\cdot\}$	Real-part operator (p. 70)
S	Set of indices, $\{1, 2, \cdots, N\}$, of array elements (p. 140)
$\mathsf{S}_{\mathcal{G}}$	Set of indices of high SNR array elements (p. 140)
$\mathsf{S}_{\mathcal{B}}$	Set of indices of low SNR array elements (p. 140)
S_{+}	Index set of the micromirrors that reflect their optical powers toward the photodetector D_{+} (p. 146)
S_{-}	Index set of the micromirrors that reflect their optical powers toward the photodetector D_{-} (p. 146)
T	Symbol duration (p. 52)
T_b	Bit duration (p. 74)
T_c	PPM chip duration (p. 138)
T_{coh}	Atmospheric coherence time (p. 48)
T_D	DMD switching period (p. 143)
$U(t)$	Unit step function (p. 43)
$\mathbf{x}^{(j)}$	Collection of signal energies incident on the array elements during the j^{th} PPM chip (p. 139)
$\tilde{\mathbf{x}}^{(i)}$	Collection of signal energies incident on the DMD micromirrors during the i^{th} DMD switching period (p. 146)
$\hat{\mathbf{x}}^{(i)}$	An estimate of $\tilde{\mathbf{x}}^{(i)}$ (p. 149)
$y(t)$	Photodetector output current (p. 4 and 35)
$y_e(t)$	Current response function due to a single released electron (p. 35)

$\tilde{Z}(k_1, k_2)$ Effective channel noise (p. 103)

α Receiver filter excess bandwidth, $0 \leq \alpha \leq 1$ (p. 68)

γ Gain in average optical power of a PAM system (p. 56)

δ_k Kronecker delta function (p. 55)

$\delta(t)$ Dirac delta function (p. 59)

$\delta_\varepsilon(t)$ OIM transmit filter (p. 64)

ε Pulse duty cycle (p. 64)

η_q Quantum efficiency (p. 36)

Θ_t Kolmogorov phase screen (p. 49)

κ Normalization factor such that $bg(t)$ is unit-energy (p. 60)

λ Wavelength (p. 32)

$\lambda_b(t)$ Background noise power incident on the n^{th} array element at time t (p. 137)

$\lambda_n(t)$ Signal power incident on the n^{th} array element at time t (p. 137)

μ Mean of $I^{(0,t)}$ (p. 36)

μ_a Mean of the sequence $\{a_k\}$ (p. 53)

$\mu_n^{(j)}$ Mean of $I_n^{(j)}$ (p. 138)

$\mu_{\mathcal{G}}^{(j)}$ Mean of $I_{\mathcal{G}}^{(j)}$ (p. 141)

$\mu_+^{(i)}$ Mean of $\tilde{I}_+^{(i)}$ (p. 147)

$\mu_-^{(i)}$ Mean of $\tilde{I}_-^{(i)}$ (p. 147)

ρ Optical signal-to-noise ratio (p. 108)

ϱ Mean delay (p. 42)

σ_z^2 Channel noise variance (p. 54)

$\Phi_{\mathsf{PAM}}(f)$ Power spectral density of a PAM signal (p. 61)

$\Phi_{\mathsf{Rect}}(f)$ Power spectral density of a Rect-PAM signal (p. 62)

$\Phi_{\mathsf{Sinc}}(f)$	Power spectral density of a Sinc-PAM signal (p. 62)
$\Phi_{\mathsf{OIM}}(f)$	Power spectral density of an ideal OIM-PAM signal (p. 62)
$\Phi_{\varepsilon}(f)$	Power spectral density of an OIM-PAM signal (p. 65)
$\Phi_q(k_1, k_2)$	Power spectral density of the quantizer error, q (p. 102)
$\Phi_{\tilde{q}}(k_1, k_2)$	Power spectral density of the quantization noise, $\tilde{q}$ (p. 102)
$\Phi_{\tilde{z}}(k_1, k_2)$	Power spectral density of the effective channel noise, $\tilde{z}$ (p. 103)
Ω_{fv}	Field-of-view (p. 34)

Contents

	iii
Abstract	**v**
Acknowledgements	**vii**
Acronyms	**ix**
Notations	**xiii**
List of Tables	**xxv**
List of Figures	**xxxiv**
1 Introduction	**1**
1.1 Intensity Modulation with Direct Detection	3
1.2 Indoor Wireless Optical Communications	6
1.2.1 Point-to-Point Links	6
1.2.2 Diffuse Links	12
1.2.3 Advantages and Disadvantages	14
1.3 Outdoor Wireless Optical Communications	16

1.3.1 Free-space optical communication links 16
1.3.2 Complications and Challenges 21
1.3.3 Single-Detector Receivers 22
1.3.4 Array Receivers 24
1.4 Thesis Contributions 27

2 Channel Models 31

2.1 Wireless Optical Communication Systems 31
2.1.1 Transmitter 31
2.1.2 Receiver 32
2.1.3 Noise 34
2.2 Indoor Wireless Optical Diffuse Channels 38
2.3 Indoor Point-to-Point Wireless Optical MIMO Channels 44
2.4 Outdoor Free-Space Optical Channels 47
2.5 Conclusions 49

3 Optical Impulse Modulation 51

3.1 Introduction 51
3.2 Optical Intensity Pulse Amplitude Modulation 52
3.3 Optical Impulse Modulation 57
3.3.1 OIM Definition 59
3.3.2 Practical OIM Implementation 64
3.4 OIM Receiver Design 66
3.4.1 Whitened Matched Filter Receiver 66
3.4.2 Double-Jump Receiver 68

3.5 Numerical Results 73

3.5.1 Average Optical Power Requirements 74

3.5.2 Peak Optical Power and Eye-Safety 83

3.5.3 Information Rate 84

3.6 Conclusions 90

4 Halftoned Spatial Discrete Multitone Modulation 93

4.1 Introduction 93

4.2 Spatial Discrete Multitone Modulation 95

4.3 Binary-Level 2D Optical Channels 98

4.3.1 Digital Image Halftoning 100

4.3.2 Halftoned Spatial Discrete Multitone Modulation 102

4.3.3 Linearized Analytical Model 103

4.3.4 Halftoning Design 105

4.4 Example: Pixelated Wireless Optical Channel 108

4.4.1 Simulation Setup 108

4.4.2 Halftoning Design 111

4.4.3 Discussion 120

4.5 Experimental Prototype Pixelated Wireless Optical Channel 123

4.5.1 Experimental Setup 123

4.5.2 Halftoning Design 127

4.5.3 Discussion 128

4.6 Conclusions 133

5 **Diversity Reception for FSO Communications using Linear Projections** **135**

5.1 Introduction 135

5.2 Array Receiver 137

5.2.1 Receiver Model 137

5.2.2 PSF Estimation 139

5.2.3 Selection Combining 140

5.3 DMD Receiver 142

5.3.1 Digital Micromirror Devices 142

5.3.2 Selection Combining using a DMD 143

5.3.3 PSF Estimation using a DMD 145

5.4 3-chip DMD Optical Receiver Architecture 149

5.5 2-chip DMD Optical Receiver Architecture 156

5.6 Simulation results 158

5.6.1 Simulating a Time-Evolved PSF 158

5.6.2 Measurement Matrices 160

5.6.3 Symbol Error Rates 161

5.6.4 Beam Splitter Reflection Coefficient 167

5.7 Conclusions 170

6 **Conclusions and Future Work** **171**

6.1 Conclusions 171

6.2 Future Work 174

A **Bit Error-Rate of L-PAM over Dispersive ISI Channels** **177**

A.1 Performance at Zero Delay Spread 180

B Bit Error-Rate of L-PPM over Dispersive ISI Channels 183

B.1 Performance at Zero Delay Spread 186

C Development of (5.22) 187

List of Tables

1.1 Examples of commercial terrestrial FSO links. 18

1.2 The main theme of this thesis is to use the extra degrees of freedom available at the transmitter/receiver to improve link performance. . . 28

3.1 Optical power gain (dBo) over Rect-OOK at normalized delay spread $\mathcal{D}/T_b = 0.2$. For OIM, $\varepsilon = 0.2$ is used. 79

4.1 Measured parameters of a pixelated wireless optical channel in [57,58]. The measured ρ is a worst case, calculated at the highest noise variance measured in [57,58]. 110

4.2 Raster scanning procedure. The feedback filter, $j(n_1, n_2)$, is assumed to be causal and have support on $n_1 \in \{0, 1, \cdots, M_1 - 1\}$ and $n_2 \in \{0, 1, \cdots, M_2 - 1\}$. 117

List of Figures

1.1 Intensity Modulation/Direct Detection (IM/DD) channels 5

1.2 Indoor wireless optical link topologies. (a) Point-to-point link, (b) point-to-point MIMO link, and (c) diffuse link. 7

1.3 An example 2D barcode encoding the quotation, "Wireless communications is indeed one of the most active and fast growing sectors of the telecommunication industry. It has notably evolved since Guglielmo Marconi transmitted Morse-coded signals with his radio apparatus in the late 1800s." The barcode was generated online at http://www.terryburton.co.uk/barcodewriter/generator/, where the barcode type was chosen to be *QR-Code*, and the website default generation parameters were used. 11

1.4 Free-space optical (FSO) links. Different atmospheric effects degrade the link performance in case of terrestrial and space-to-earth links. . . 17

1.5 Conventional single-detector receiver. 23

1.6 A power plot of an example turbulence-degraded PSF for $D/r_0 = 11.92$, where D is the receiver aperture diameter and r_0 is the atmospheric coherence width. The outline of a circular photodetector is indicated. While a large detector diameter is required to collect a majority of the PSF energy, a small one is required to reject a majority of background noise. 24

1.7 Multiple-detector array receiver. 26

2.1 Conventional wireless optical transmitter. 32

2.2 Conventional wireless optical receiver. 33

2.3 Receiver field-of-view. 35

2.4 The Lambertian reflection pattern for $\mathcal{P}_{\rm elem} = 1$ and mode number $n = 3$. The $x - y$ plane represents the surface of the differential reflecting element. 40

2.5 Wireless optical diffuse link. The Lambertian reflection pattern is shown for ceiling and wall differential reflecting elements, and a mode number $n = 1$. The receiver detects multiple diffusively reflected versions of the transmitted signal. 41

2.6 Wireless optical MIMO link. 45

3.1 Block diagram of an optical intensity PAM communication system. . 52

3.2 Block diagram of an optical intensity PAM communication system. . 60

3.3 Block diagram of an OIM communication system. 61

3.4 The PSDs for Rect-PAM, Sinc-PAM and OIM, along with sample time-domain waveforms. The vertical arrows represent Dirac impulses. The pulses amplitudes, in time domain, are selected randomly and independently since, in general, the sequence $\{a_k\}$ need not be constrained to a finite set of PAM levels. 63

3.5 The double-jump pulse. 72

3.6 Normalized optical power, $10\log(\mathcal{P}_t/\mathcal{P}_t^{\mathrm{OOK}})$, required by Rect-OOK and OIM-OOK with double-jump receiver to achieve BER=10^{-6}. . . 75

3.7 Normalized optical power, $10\log(\mathcal{P}_t/\mathcal{P}_t^{\mathrm{OOK}})$, required by Rect-PAM and OIM-PAM to achieve BER=10^{-6} at $L = 4$. For OIM, a double-jump receiver is used with $\alpha = 1$ and $\varepsilon = 0.2$. 77

3.8 Normalized optical power, $10\log(\mathcal{P}_t/\mathcal{P}_t^{\mathrm{OOK}})$, required by Rect-OOK and OIM-OOK using WMF and DFE to achieve BER=10^{-6}. 79

3.9 Normalized optical power, $10\log(\mathcal{P}_t/\mathcal{P}_t^{\mathrm{OOK}})$, required by Rect-PPM and OIM-PPM to achieve BER=10^{-6}. 81

3.10 Normalized optical power, $10\log(\mathcal{P}_t/\mathcal{P}_t^{\mathrm{OOK}})$, required by precursor equalized Rect-PPM and OIM-PPM to achieve BER=10^{-6}. 82

3.11 Information rate versus the sequence length, $\mathcal{N}$, for OIM-OOK with double-jump receiver ($\alpha = 1$) at a normalized delay spread of 0.2. Results are presented for $\mathcal{P}_t H_0 \sqrt{T_b}/\sigma_z = -5, -4, \cdots, +5$ dBo. 88

3.12 Information rate versus optical SNR for Rect-OOK with WMF receiver, and OIM-OOK with double-jump receiver ($\alpha = 1$). Results are presented at normalized delay spreads of 10^{-2} and 0.2. 89

3.13 Information rate versus normalized channel delay spread at optical SNR of $\mathcal{P}_t H_0 \sqrt{T_b}/\sigma_z = 3$ dBo 90
4.1 SDMT transmitter block diagram. 96
4.2 SDMT receiver block diagram. 96
4.3 An example SDMT symbol, $X(k_1, k_2)$, of 256×256 pixels with a cyclic extension of width 8 pixels. For clarification, white border lines separate the SDMT symbol from its cyclic extension. 97
4.4 A Gaussian OTF, $H(k_1, k_2) = \exp\left(-\frac{k_1^2}{2w_{h_1}^2} - \frac{k_2^2}{2w_{h_2}^2}\right)$, where w_{h_1} and w_{h_2} are measures of the OTF widths. The in-band and out-of-band regions are indicated. 99
4.5 HSDMT transmitter block diagram. 101
4.6 Linearized HSDMT transmitter block diagram. 104
4.7 The Gaussian OTF of (4.17) for $N = 256$ and $N = 512$. Values of w_{h_1} and w_{h_2} are as in Table 4.1. 111
4.8 The upper bound (4.11) on σ_x^2. 112
4.9 Cross-sections of the noise power shaping function, $|1 - J(k_1, k_2)|^2$, for $k_1 = k_2$ and a variety of feedback filter parameters a. 113
4.10 The noise power shaping function, $|1 - J(k_1, k_2)|^2$, for $N = 256$ and $N = 512$. The error diffusion filter parameter is taken as $a = 0.9$. . . 114
4.11 *Optical power-limited system.* The noise bowl, $N_1 N_2 \sigma_q^2 |1 - J(k_1, k_2)|^2 + N_1 N_2 / |\rho H(k_1, k_2)|^2$, and the water pouring power allocation are shown for $N_1 = N_2 = 512$. The error diffusion filter parameter is taken as $a = 0.9$, w_{h_1} and w_{h_2} as given in Table 4.1, and ρ as given by (4.18). An example transmit image is shown in Fig. 4.13. 115

4.12 *Quantization noise-limited system.* The noise bowl, $N_1N_2\sigma_q^2|1-J(k_1,k_2)|^2 + N_1N_2/|\rho H(k_1,k_2)|^2$, and the water pouring power allocation are shown for $N_1 = N_2 = 256$. The error diffusion filter parameter is taken as $a = 0.9$, w_{h_1} and w_{h_2} as given in Table 4.1, and ρ as given by (4.18). An example transmit image is shown in Fig. 4.14. 116

4.13 *Optical power-limited system.* (a) Continuous-tone image. (b) Corresponding halftoned image. (c) Spectrum of continuous-tone image. (d) Spectrum of halftoned image. $N = 512$, $a = 0.9$, $\sigma_x^2 = 0.1$, w_{h_1} and w_{h_2} as given in Table 4.1, and ρ as given by (4.18). 118

4.14 *Quantization noise-limited system.* (a) Continuous-tone image. (b) Corresponding halftoned image. (c) Spectrum of continuous-tone image. (d) Spectrum of halftoned image. $N = 256$, $a = 0.9$, $\sigma_x^2 = 0.1$, w_{h_1} and w_{h_2} as given in Table 4.1, and ρ as given by (4.18). 119

4.15 Iterations used in simulations to evaluate $\Phi_{\tilde{q}}(k_1,k_2)$ and the power allocation. 120

4.16 Capacity of the pixelated channel versus $N = N_1 = N_2$ with $\sigma_x^2 = 0.1$. Results of the linearized analytical model in Sec. 4.3.4 are compared to those from simulations, and to those of a continuous SDMT transmitter without non-negativity constraint. The capacity estimate ($\triangle$) and code rate ($\bigtriangledown$) achieved in [58] using 256-level transmitter are also shown at $N = 154$. 122

4.17 MIMO link prototype setup 124

4.18 Measured noise variance, σ_z^2, of the experimental prototype link versus frame rate for different values of N. 126

4.19 *Optical power-limited system.* (a) Continuous-tone image. (b) Corresponding halftoned image. (c) Spectrum of continuous-tone image. (d) Spectrum of halftoned image. For 7.142 kfps, $N = 256$, $\sigma_x^2 = 0.2$, $w_{h_1} = 49.57$, $w_{h_2} = 48.29$, and $\rho = 2.13$. The images are based on experimental measurements. 129

4.20 *Quantization noise-limited system.* (a) Continuous-tone image. (b) Corresponding halftoned image. (c) Spectrum of continuous-tone image. (d) Spectrum of halftoned image. For 400 fps, $N = 256$, $\sigma_x^2 = 0.2$, $w_{h_1} = 49.57$, $w_{h_2} = 48.29$, and $\rho = 20.83$. The images are based on experimental measurements. 130

4.21 Capacity of the pixelated channel, in kbpf, versus frame rate with $\sigma_x^2 = 0.2$. The linearized analytical model in Sec. 4.3.4 is compared to a continuous SDMT transmitter without non-negativity constraint. The presented results are based on the measured channel parameters. 131

4.22 Capacity of the pixelated channel, in Mbps, versus frame rate with $\sigma_x^2 = 0.2$. The linearized analytical model in Sec. 4.3.4 is compared to a continuous SDMT transmitter without non-negativity constraint. The presented results are based on the measured channel parameters. 132

5.1 An illustration of how the DMD array is used to pixelate the PSF, and to perform the selection combining detection. For drawing simplicity, the number of micromirrors is taken as $N = 4$. In this diagram, $\mathsf{S} = \{1, 2, 3, 4\}$, $\mathsf{S}_{\mathcal{B}} = \{1\}$, and $\mathsf{S}_{\mathcal{G}} = \{2, 3, 4\}$. 144

5.2 An illustration of how the DMD array is used to estimate the PSF through linear measurements. For drawing simplicity, the number of micromirrors is taken as $N = 4$. In this diagram, $\mathsf{S} = \{1, 2, 3, 4\}$, $\mathsf{S}_- = \{1, 2\}$, and $\mathsf{S}_+ = \{3, 4\}$. That is, $\mathbf{a}_{m(i)} = [-1, -1, +1, +1]^{\mathrm{T}}$. . . . 148

5.3 3-chip DMD optical receiver [162]. 151

5.4 An illustrative example of the 3-chip DMD optical receiver. For drawing simplicity, the number of micromirrors is taken as $N = 4$. In this example, $\mathsf{S} = \{1, 2, 3, 4\}$, $\mathsf{S}_{\mathcal{B}} = \mathsf{S}_{\mathcal{B}^+} \cup \mathsf{S}_{\mathcal{B}^-} = \{1\}$, $\mathsf{S}_{\mathcal{G}} = \mathsf{S}_{\mathcal{G}^+} \cup \mathsf{S}_{\mathcal{G}^-} = \{2, 3, 4\}$, $\mathsf{S}_+ = \mathsf{S}_{\mathcal{B}^+} \cup \mathsf{S}_{\mathcal{G}^+} = \{3, 4\}$, and $\mathsf{S}_- = \mathsf{S}_{\mathcal{B}^-} \cup \mathsf{S}_{\mathcal{G}^-} = \{1, 2\}$. Notice that this configuration gives the same values of $\mathsf{S}_{\mathcal{B}}$ and $\mathsf{S}_{\mathcal{G}}$ as in Fig. 5.1, and the same values of S_- and S_+ as in Fig. 5.2. Imaging lenses are omitted for diagram clarity. 152

5.5 A timing diagram showing that each DMD period, $[iT_D, (i+1)T_D)$, is divided to ζ PPM chips such that $[iT_D, (i+1)T_D) = \bigcup_{j=i\zeta}^{(i+1)\zeta-1} [jT_c, (j+1)T_c)$. The counts $\tilde{I}_{\mathcal{B}+}^{(i)}$ and $\tilde{I}_{\mathcal{G}+}^{(i)}$ are shown, while $\tilde{I}_{\mathcal{B}-}^{(i)}$ and $\tilde{I}_{\mathcal{G}-}^{(i)}$ are eliminated for diagram clarity. The counts $I_{\mathcal{G}+}^{(j)}$, where $i\zeta \leq j < (i+1)\zeta$, are used for detecting the ζ chips, while their sum $\tilde{I}_{\mathcal{G}+}^{(i)}$ is used to compute the i^{th} PSF measurement, y_i. 154

5.6 2-chip DMD optical receiver. A beam splitter is used to split the incident energy $K^{(j)}$ to two components $K_{est}^{(j)}$ and $K_{det}^{(j)}$ for PSF estimation and PPM chip detection respectively. 157

5.7 The instantaneous turbulence-degraded PSF for $D/r_0 = 11.92$. (a) An energy plot of the PSF. (b) The integration of the PSF over the surface of a 16×16 array receiver. 159

5.8 A simplified version of the 3-chip DMD optical receiver of Fig. 5.3 when employing a full identity measurement matrix. The simplified DMD receiver uses two DMDs and two high-speed detectors. 162
5.9 SER upper bound for 2-PPM system using the 3-chip DMD receiver at $K_b = 1.0$, $D/r_0 = 11.92$ and $\zeta = 1000$. The optimal number of detection elements used is shown for each K^{ON}. 164
5.10 SER upper bound for 2-PPM system using the 3-chip DMD receiver at $K_b = 0.1$, $D/r_0 = 11.92$ and $\zeta = 1000$. The optimal number of detection elements used is shown for each K^{ON}. 165
5.11 SER upper bound for 2-PPM at $K_b = 1.0$, $D/r_0 = 11.92$ and $\zeta = \eta = 1000$. A 3-chip full Hadamard DMD receiver is compared to a 2-chip full Hadamard DMD receiver at different values of $\mathcal{R}$. 168
5.12 SER upper bound for 2-PPM at $K_b = 0.1$, $D/r_0 = 11.92$ and $\zeta = \eta = 1000$. A 3-chip full Hadamard DMD receiver is compared to a 2-chip full Hadamard DMD receiver at different values of $\mathcal{R}$. 169
A.1 Conditional probability densities associated with two neighbouring constellation points. 179

Chapter 1

Introduction

Wireless communication is indeed one of the most active and fast growing sectors of the telecommunication industry. It has notably evolved since Guglielmo Marconi transmitted Morse-coded signals with his radio apparatus in the late 1800s [1]. Wired local area networks are currently being replaced by wireless networks in many homes, schools and businesses. The developments in wireless communication systems and networks are motivated by the rapidly growing demand for new wireless capacity, and are being driven primarily by advances in hardware and antenna technologies which enable widespread deployment [2].

While increasing the capacity of wired communication systems can be fulfilled with the addition of new infrastructure, increasing the capacity of wireless systems is fulfilled mainly with the addition of more bandwidth and/or transmitter power. Unfortunately, radio bandwidth is a limited resource because of the extremely overcrowded radio spectrum. Transmitter power is also limited in order to minimize interference between different devices, and due to the fact that portable devices require the use of limited battery power.

In this thesis, the term *radio spectrum*, or *radio frequency* (RF), refers to the spectral regions from 3 Hz to 300 GHz, while the term *optical spectrum* refers to the spectral regions from 30 THz to 750 THz, which include both infrared and visible light.* Since the radio spectrum is a scarce resource that is shared by many users, regional and global regulatory bodies put restrictions on its use. That is, to build RF wireless links, spectrum licensing fees are paid to regulatory bodies and emitted signals must be confined within strict spectral regions. Moreover, these regulations vary from country to country, which makes standardization difficult for wireless RF modems. As a result, a new trend in wireless communication systems exploits the use of the optical spectral bands, which are unlicensed worldwide, and have many THz of bandwidth [3–10].

Wireless optical transmitters are constructed from light-emitting diodes (LEDs) or laser diodes (LDs), while optical receivers are constructed from photodetectors. These devices are characterized by low power consumption, light weight, small size, low price, and high speed. These characteristics make wireless optical modems particularly appealing in portable applications. In fact, indoor applications employing the optical spectrum for wireless communications go back to the 1950s. For example, the first wireless television (TV) remote control, called Flash-Matic, was developed by the Zenith Radio Corporation in 1955 [11]. Nowadays, the majority of TV sets, video recorders, DVD players, laptops, and air-conditioners include infrared remote controls.

Optical spectral bands also find application in outdoor free-space optical (FSO) communication links, which are point-to-point links that transmit information through

*Throughout the thesis, wireless optical channels are assumed to utilize infrared light unless explicitly stated that visible light is utilized.

free-space by modulating the intensity of an optical carrier [12–19]. FSO links provide high bandwidth connectivity for terrestrial, inter-satellite and deep-space communication applications. They are attractive alternatives to RF links for long-range communication due to the fact that the shorter wavelength allows for the use of highly collimated optical beams, which reduces the transmitted power required to maintain a given link performance. Small volume, light weight, and the absence of government regulations on the use of the optical bandwidth are other attractive features of FSO communication systems.

The first FSO link was developed by Alexander Graham Bell in 1880 when he invented the *photophone*, a wireless telephone that transmits voice signals by modulating the sun light reflected from a mirror. The voice signal is projected toward the mirror such that the voice vibrations cause similar vibrations in the mirror, and consequently, cause similar fluctuations in the reflected light intensity. The reflected light propagates to the receiver where the intensity fluctuations are converted back to sound. With this system design, Bell was able to transmit an audible signal over a distance of 213 m [9, Sec. 1.1]. Although Bell's photophone did not work when sun light is obscured by clouds or fog, it is considered the oldest successful FSO prototype link [20].

1.1 Intensity Modulation with Direct Detection

An optical field is said to be *spatially coherent* if the phases of the field at different points in space are varying with time in a perfectly correlated way, while it is said to be *spatially incoherent* if the phases are varying in uncorrelated fashions [21, Sec. 6.1]. Accordingly, optical detection can be divided into two basic types, coherent and incoherent detection. For incoherent detection, also referred to as direct detection, no use is made of the spatial coherence of the optical field, and the detector responds only to the power of the received field [22, Chapter 5]. Whereas, coherent detection requires the mixing of a spatially coherent received field with another well-aligned spatially coherent field that is locally generated at the receiver [22, Chapter 6].

While coherent detection offers large gains in the signal-to-noise ratio (SNR) for wireless optical communication [23–25], direct detection is currently the detection type chosen for commercial use due to its low cost [26, Sec. 8.8]. Currently available optical modems utilize inexpensive optoelectronic components which are incapable of modulating the phase or frequency of the THz optical signal. Moreover, for terrestrial and space-to-earth FSO links, the spatial coherence of the transmitted optical beam is broken due to atmospheric effects. This makes it more difficult to employ coherent detection schemes for such links, even if expensive transceivers that are capable of generating and detecting coherent fields are used [27–29]. Therefore, direct detection is the detection scheme considered in this thesis for both short-range indoor and long-range outdoor wireless optical communication links.

The most common practical modulation technique used for both indoor and outdoor wireless optical links is intensity modulation with direct detection (IM/DD) [6]. As shown in Fig. 1.1, the transmitted information signal is an electrical current, $i(t)$. The instantaneous *intensity*, $I(t)$, of the optical emitter is defined as the emitted power per unit solid angle, in Watts per steradian. Intensity modulation is done at the transmitter, where $I(t)$ is directly proportional to $i(t)$. At the receiver, direct detection is done via a photodetector which produces an output current, $y(t)$, proportional to the received instantaneous optical *irradiance*, $I_r(t)$, defined as the power

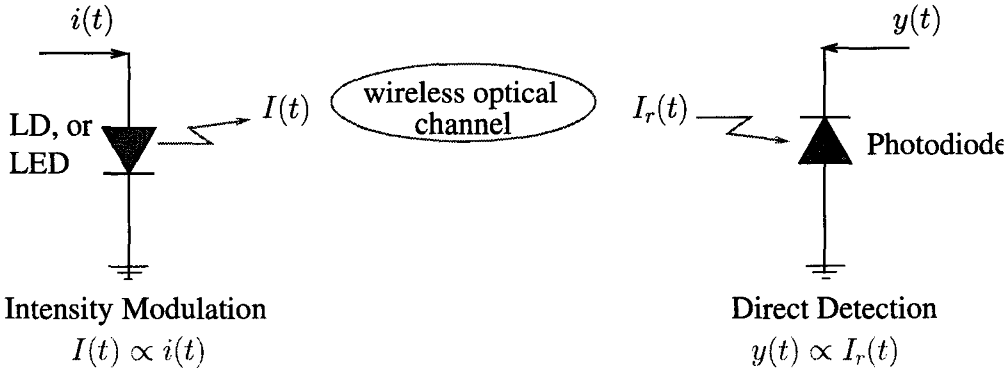

Figure 1.1: Intensity Modulation/Direct Detection (IM/DD) channels

per unit area incident over the detector surface. The exact dependence of $I_r(t)$ on $I(t)$ is a function of the specific wireless optical channel model and channel propagation characteristics. Communication performance is also dependent on noise signals that interfere with the data-bearing signal at the receiver. For example, ambient noise from incandescent and fluorescent lighting degrades the performance of indoor links, while sky background radiation degrades the performance of outdoor links. Optical wireless channel models and noise are studied in more detail in Chapter 2.

Since the signal being modulated and detected is a power signal, the average transmitted optical power is given by the average signal amplitude rather than the average square amplitude as is the case with conventional RF channels. Two constraints are imposed on the transmitted signal amplitude: (i) it must be non-negative, and (ii) its average value is bounded above by a limit defined by eye and skin-safety standards [6], [9, Sec. 2.1]. As a result of these constraints, conventional modulation and detection schemes designed for RF channels cannot be applied directly to optical channels, and new optical signalling schemes are required. This thesis treats the design of such modulation and detection schemes.

1.2 Indoor Wireless Optical Communications

The enormous growth in the number and functionality of portable devices and information terminals in indoor environments requires a corresponding advance in communication system design. Indoor applications require low power consumption, low cost, light weight, small size, and high speed modems. These requirements have motivated ongoing studies into indoor wireless optical communications [3, 4, 6–10]. While the capacity of traditional RF wireless systems is limited due to the scarcity and cost of bandwidth, optical signals are unlicensed worldwide, are confined by opaque boundaries, are immune to RF interference, and have many THz of bandwidth.

In indoor wireless communications, the transmitted signal may suffer multiple reflections off walls and different room objects between the transmitter and receiver. Many of these reflections propagate to the receiver along multiple paths. This kind of propagation is referred to as *multipath propagation*. Multipath propagation leads to time dispersion of the transmitted pulse due to different time delays along different propagation paths. This kind of pulse dispersion is known as *multipath dispersion*. Effects of multipath propagation on indoor optical wireless links depend on the link topology since such links exist in different topologies characterized by different degrees of directionality and mobility as shown in Fig. 1.2.

1.2.1 Point-to-Point Links

The simplest link topology is the *point-to-point link* shown in Fig. 1.2(a). This link topology assumes the existence of a line-of-sight from transmitter to receiver. It uses narrow-angle directional transmitters and receivers. Therefore, the received power is maximized and the majority of ambient light noise is rejected. Since the transmitter

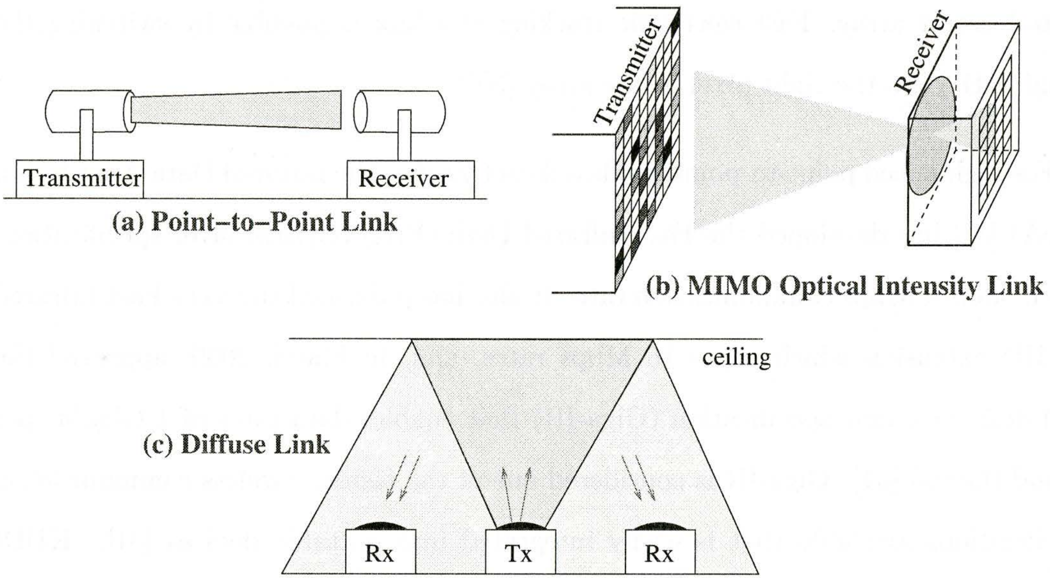

Figure 1.2: Indoor wireless optical link topologies. (a) Point-to-point link, (b) point-to-point MIMO link, and (c) diffuse link.

points precisely to the receiver, multipath dispersion is minimized. On the other hand, the link is sensitive to blocking and misalignment errors, and does not permit high degrees of user mobility.

Non-interfering indoor point-to-point links have been used in [4], where data rates of 50 Megabits per second (Mbps) per link can be accommodated for up to 100 links in a large room. This has been accomplished by using a ceiling-mounted multiple-spot base station to transmit a number of directive narrow beams to receivers placed in different room locations. Large aggregate data rates can be achieved at the expense of increased system complexity [4]. Fast electronic tracking have been used in [30] to align the transmitter and receiver. Rates of 155 Mbps have been shown over a distance of nearly 2 m. The transmitter is made of an LD array combined with multiple-beam forming optics, while the receiver is made of a wideangle lens and a photodetector array. Fast electronic tracking of a link is possible by switching the signal path onto the right pixel in the array [30].

For high-speed point-to-point wireless data transfer, the Infrared Data Association (IrDA) [31] has developed the Fast Infrared Data (FIR) physical layer specification, which offers 4 Mbps communication rate. It also has published the Very Fast Infrared (VFIR) extension which offers 16 Mbps rates, and, in March 2009, approved the final draft of a new specification (Giga-IR) that enables data rates of 1 Gigabit per second (Gbps) [31]. Giga-IR is considered one of the fastest wireless communication specifications available that is easily integrated into portable devices [31]. KDDI Corporation demonstrated the Giga-IR at its booth in Expo Comm Wireless Japan in 2008 and 2009, and is considering implementing Giga-IR as a new feature in cellular phones [32].

IrDA compatible links have been used for short-range point-to-point communications in remote control units, printers, scientific calculators, laptops and cellular phones. An application of such links is the IrDA Infrared Financial Messaging (IrFM) system [31,33]. This system is a future digital payment system that is capable of integrating different payment systems such as credit cards, debit cards, loyalty cards and automated teller machine cards. It provides a quick and secure way for consumers to use their personal devices, such as cellular phones, to pay for services and merchandise. This is done by transmitting financial data, such as credit card numbers, to a payment terminal by using short-range infrared beams. The advantage of using wireless optical links is the low cost and light weight of optical transceivers, and the inherent security of using highly directive beams [33]. Another interesting application is the Talking Signs communication systems [34] that provide remote directional human voice messages that help vision impaired and print-handicapped individuals to travel safely. The system sends short audio signals by directional infrared beams from fixed transmitters to hand-held receivers carried by the impaired persons. The receiver decodes the signal and delivers the voice message through its speaker or headset [34].

Multiple-input/multiple-output (MIMO) techniques are signalling techniques where multiple antennas are used at both the transmitter and receiver to improve the link performance. As shown in Fig. 1.2(b), such techniques can be applied to point-to-point links by using a spatial light modulator (SLM) transmitter consisting of an array of optical emitters and an imager receiver consisting of an array of photodetectors. In this case, information is conveyed through the channel by transmitting a series of time-varying two-dimensional (2D) optical intensity images from transmitter to receiver. The 2D MIMO channel model is discussed in Sec. 2.3. Such 2D optical intensity channels have been used in a variety of applications such as holographic data storage [35–37], page-oriented optical recording [38, 39], 2D barcodes [40, 41], and MIMO wireless optical communications [6, 42–44]. Spatial diversity techniques have also been applied to indoor wireless optical communications by using multiple line-of-sights and diffusing spots [5].

The receiver samples the spatial distribution of the optical intensity wavefront incident on its surface at discrete time intervals. Examples of imaging-type receivers are arrays of photodetectors, charge coupled device (CCD) cameras, and complementary metal oxide semiconductor (CMOS) imagers. Several such arrays have been constructed for free-space and indoor wireless optical communications [45,46], as well as for high-speed imaging applications with rates near 10 kiloframes per second (kfps) for arrays of over 10^5 pixels [47, 48]. Higher frame rates have been designed for ultra high-speed imaging applications at the expense of a limited number of captured frames. For example, a 32×32 pixel imager that can take 8 frames at a rate of a billion frames per second has been designed in [49]. A 312×260 imager that can take 100 frames at a Megaframes per second (Mfps) has been developed in [50], and a 12×12 imager that can take 32 frames at 4 Mfps has been fabricated in [51].

An example application of wireless optical MIMO channels is the 2D barcode reader used by cellular phones. The 2D barcode may be displayed on a computer screen, a piece of paper, or a street billboard. The barcode can be imaged by the cellular phone high-resolution camera, and using a pre-installed barcode reader, the phone retrieves the data stored in the barcode. Barcodes storing web addresses may appear in supermarkets, newspapers and magazines. For example, 2D barcodes are printed in pages of the Metro newspaper [52]. The codes can be imaged by cellular phones to be taken directly to the newspaper website for more information [52, 53]. An example 2D barcode is shown in Fig. 1.3.

Another example is wireless optical backplanes, which are interconnect systems for parallel data exchanges between electronic boards. In conventional electrical backplanes, a major bottleneck to high-speed communication between boards is the limited communication bandwidth due to signal propagation delay, power consumption, and capacitive effects. Strictly aligned wireless optical backplanes are better alternatives for solving these problems [44,54]. For example, wireless optical backplanes have been used to implement intra-craft data buses in [55].

Figure 1.3: An example 2D barcode encoding the quotation, "Wireless communications is indeed one of the most active and fast growing sectors of the telecommunication industry. It has notably evolved since Guglielmo Marconi transmitted Morse-coded signals with his radio apparatus in the late 1800s." The barcode was generated online at http://www.terryburton.co.uk/barcodewriter/generator/, where the barcode type was chosen to be *QR-Code*, and the website default generation parameters were used.

A major practical problem of many of these applications is the requirement of strict spatial alignment between the transmitter and receiver in order to avoid inter-channel interference [35, 36, 56]. Such a system is termed "pixel matched", i.e. each receive pixel images a single transmit pixel. A signalling technique that does not require such strict spatial alignment has been introduced in [57, 58] for 2D wireless optical MIMO channels. The technique provides high spectral efficiency, which is the data rate that can be transmitted per unit bandwidth, by modelling inter-channel interference and exploiting it at the transmitter and receiver.

1.2.2 Diffuse Links

Another link topology for indoor wireless optical links is the *diffuse link* shown in Fig. 1.2(c). Unlike point-to-point links, diffuse links use wide-angle transmitters and receivers, and do not assume the existence of a line-of-sight [3, 6, 59, 60]. For this link topology, the received signal is composed of reflections of the transmitted signal by the room ceiling, walls and other pieces of furniture, and therefore a line-of-sight is not necessary. Since they were introduced in 1979 [3], diffuse links have received much attention due to the fact that they offer high degrees of mobility, robustness and immunity to shadowing. However, this comes at the expense of high signal power loss due to wide-angle transmitters, high noise due to wide-angle receivers, and low bandwidth due to multipath dispersion. The diffuse channel can be modelled as a dispersive baseband channel [61]. Various techniques have been used to evaluate its impulse response [61–72], and many equalization and coding techniques have been considered to mitigate the dispersive nature of the channel [6, 61, 73–76]. The diffuse channel model is discussed in more detail in Sec. 2.2.

The IrDA has developed the Advanced Infrared (AIr) physical layer specification for diffuse infrared channels, which offers 4 Mbps communication rate [31, 77, 78]. In addition, the Institute of Electrical and Electronics Engineers (IEEE) defines a specification for the physical layer of the diffuse infrared channel as a part of its IEEE 802.11 standard for wireless local area networks. This infrared physical layer was designed to support two data rates (1 and 2 Mbps), and includes provisions for a smooth migration to higher data rates [79]. Diffuse infrared experimental links have been demonstrated in [80] at 25 Mbps, and in [81, 82] at 50 Mbps.

While the above mentioned standards and demonstrations consider the infrared optical spectrum, the visible optical spectrum can also be used for communication over diffuse channels. Visible LEDs are used for illumination purposes as they have long life expectancy and high power efficiency. The visible light emitted can be modulated to convey information over the diffuse channel, while providing illumination for a room [8]. In this case, the SNR is about 30 dB higher than that for a link utilizing the infrared light [83]. This is because infrared links suffer from high noise due to illumination devices, while visible links do not.

The visible light communications (VLC) consortium [84] was founded in 2003 to research and standardize VLC systems in Japan. The VLC system standard, JEITA CP-1221, was issued in 2007 by the Japan Electronics and Information Technology Industries Association [85]. In Europe, the OMEGA project [86] is funded by the European Commission [87] to set a standard for ultra-broadband home area networks that enables 1 Gbps speeds via heterogeneous communication technologies, such as RF, optical wireless, and power line communications. The project aims to combine optical wireless communications techniques to provide a range of communication channels. For example, infrared can be used to provide high rate point-to-point communications, while VLC can be used to provide diffuse broadcast coverage at lower rates [88]. The project consortium consists of 20 partners, with a total cost of about €19 million, and a European Commission fund of €12.4 million [89]. In the USA, the National Science Foundation [90] granted $18.5 million to Boston University [91], Rensselaer Polytechnic Institute [92] and the University of New Mexico [93] to develop VLC technology. This fund is used by the Smart Lighting Engineering Research Center [94] to create VLC systems. Such well-funded projects indicate a strong interest in indoor wireless optical communications for a wide host of applications.

1.2.3 Advantages and Disadvantages

Indoor wireless optical links offer many advantages over indoor wireless RF links. However, they also have some disadvantages. In this section, a comparison between optical and RF indoor wireless links is presented.

The propagation environment surrounding the transmitter and the receiver includes many time-varying objects that act as signal reflectors. Therefore, the received signal is the sum of time-varying multiple reflections that may add constructively or destructively in the receiver plane. This results in time-varying random nulls and peaks in the received spatial power distribution, which are separated on the order of the wavelength. As a result, the signal power detected by the receiver suffers from random time-varying fluctuations, a phenomenon known as *multipath fading*. For wireless RF links, such fluctuations may be very large due to the fact that the dimensions of the receiving antenna are comparable to the RF wavelength. Whereas, for wireless optical links, the detector surface area is very large compared to the short optical wavelength. This leads to inherent spatial diversity that mitigates multipath fading, and hence, greatly simplifies optical modem design [6].

Since radio signals are not confined to a room, they are susceptible to eavesdropping by any nearby antenna. On the other hand, optical signals are confined to a room by opaque boundaries, and therefore optical wireless channels are inherently secure. This security feature is very important for applications that include highly confidential or financial information. For example, the IrDA has standardized a financial application, IrFM, that provides high levels of security [31, 33]. Moreover, the same optical spectral band can be reused without interference with other optical channels in neighboring rooms, and without interference with coexisting RF systems.

This increases the aggregate capacity of wireless optical networks and simplifies their design since transmissions in neighboring rooms need no coordination [6,9].

However, if wireless communication between different rooms is required, then optical links are not advantageous as they require the installation of access points that are connected by means of a wired backbone [6]. Optical links also suffer intense ambient noise from sun and artificial light sources. While the transmit optical power can be increased to mitigate the effect of ambient noise, it is limited by skin and eye safety constraints [95,96]. Therefore IM/DD optical links usually operate in low SNR regimes [6].

In fact, RF and optical links are complementary technologies, and it is up to the designer to choose the technology that is best suited to the application requirements. Optical links are preferred for short-range applications where the bit rate per link and the aggregate bit rate need to be maximized. They are also preferred when the cost needs to be minimized, when international compatibility is required or, when receiver signal-processing complexity needs to be minimized. On the other hand, RF links are preferred for long-range applications when user mobility needs to be maximized or when transmission through walls is required [6].

It is also possible to use both RF and optical links simultaneously in order to maximize the net throughput. An example of this approach is to augment low bandwidth RF coverage with a high bandwidth localized optical link in locations where people congregate, such as lobbies of buildings [97]. Since optical wireless links are capable of confining optical power within relatively smaller areas than RF channels, it is possible to use optical hotspots that offer localized high bandwidth connectivity. Hotspots can be made by optical transmitters that are mounted on the ceiling. This is especially useful in environments with higher download capacity than the upload one, as is the case with regular Internet traffic. Since the optical hotspot requires a line-of-sight between transmitter and receiver, it is subject to blocking. In the case of such blocking, the system performs a handover to the RF link depending on the blocking duration. That is, the optical link increases the efficiency of the communication system by augmenting the capacity of the RF coverage when needed. Since the fourth generation of wireless communication systems will be based on multiple access techniques, it is expected that wireless optical communication will contribute considerably to future communication systems [83, 98].

1.3 Outdoor Wireless Optical Communications

1.3.1 Free-space optical communication links

Free-space optical (FSO) communication links are point-to-point links that transmit data by modulating the intensity of an optical beam propagating through free-space from the transmitter to the receiver as shown in Fig. 1.4. These links are similar to indoor point-to-point links of Sec. 1.2.1, but they operate over much longer ranges and are affected by different outdoor effects. FSO links provide high-speed terrestrial, inter-satellite and space-to-earth communication links. For terrestrial and space-to-earth links, the performance is degraded by different atmospheric effects as mentioned in Sec. 1.3.2.

For terrestrial applications, FSO links provide efficient solutions to the last-mile problem as they offer rates of about 1−2.5 Gbps over distances in the range of 1−5 km [99]. Using wavelength-division multiplexing, FSO links have been shown to

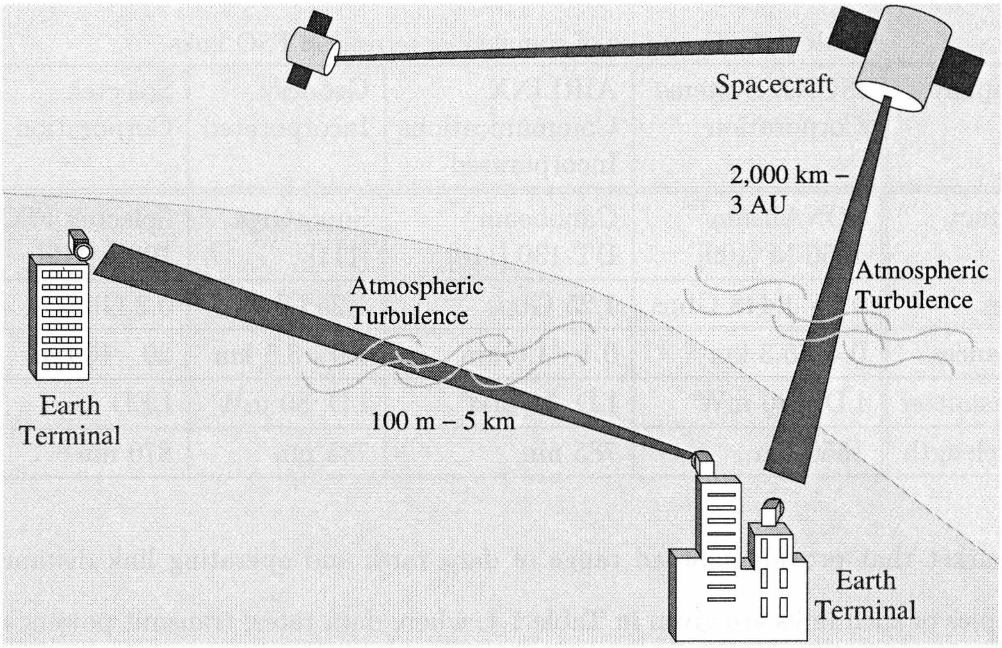

Figure 1.4: Free-space optical (FSO) links. Different atmospheric effects degrade the link performance in case of terrestrial and space-to-earth links.

provide higher rates of about 80 Gbps over 3.4 km distance [100], and much higher rates in the order of Terabits per second (Tbps) at distances in the order of a couple hundred meters [101]. FSO communications provide secure high-speed links, because the optical beam is difficult to find or intercept, which is particularly important for military applications [102–106]. FSO links are notably useful to distribute broadband services in communities with little infrastructure. The light weight, low cost, and rapid deployment features make FSO links a good choice for humanitarian assistance in disasters [107]. For example, Qwest Communications, among other U.S. carriers, used FSO links to put customers back online in the aftermath of the Sept. 11, 2001 tragedy [108]. Having recognized these attractive features, the FSO industry is growing rapidly, and various commercial terrestrial FSO links are available in

Table 1.1: Examples of commercial terrestrial FSO links.

Company	fSONA Systems Corporation	AIRLINX Communications Incorporated	Geodesy Incorporated	Solectek Corporation
Product	SONAbeam$^{\text{TM}}$ 1250-M [109]	Canobeam DT-130 [110]	SuperGiga [111]	Solectek FSO-100E [112]
Rates	0.1 - 1.448 Gbps	1.25 Gbps	1.25 Gbps	0.2 Gbps
Distances	0.4 - 5.3 km	0.1 - 1.0 km	1.0 - 3.5 km	20 - 100 m
Transmitter	LD, 640 mW	LD, 11 mW	LD, 80 mW	LED
Wavelength	1550 nm	785 nm	785 nm	870 nm

the market that provide a broad range of data rates and operating link distances. Examples of such links are given in Table 1.1, where data rates, transmit powers and operating link distances are contrasted [109–112].

Short-range FSO links can also employ visible light to convey information. For example, the visible light emitted from LED traffic signals can be used to broadcast voice messages to distant receivers. For drivers, the message can announce the time until the next signal change, and for pedestrians or people with visual impairments, the voice message can tell location or directional information [8, 113, 114].

FSO technology has the potential to revolutionize space communications due to its efficient low-divergence beams. Example demonstrations of near-earth FSO communication links include, (i) the geosynchronous lightweight technology experiment (GEOLite) [19, Sec. 7.1], (ii) the ground/orbiter lasercomm demonstration (GOLD) between the Japanese engineering test satellite (ETS-VI) and an optical ground station at the Table Mountain Facility in California, USA [115, 116], and (iii) the semiconductor inter-satellite link experiment (SILEX) between a low-earth orbit satellite (SPOT-IV) and a geostationary spacecraft (Artemis), where a 50 Mbps link was demonstrated [19, Sec. 1.13], [117,118]. A downlink from Artemis to a ground station showed an average bit error-rate (BER) of 10^{-6} over a geostationary distance of about 36,000 km and a transmission rate of 2 Mbps, while an uplink to Artemis showed an average BER of 10^{-3} at a 49 Mbps rate [119]. The goals of such demonstrations are to demonstrate spatial acquisition and tracking of optical beams with spacecrafts, and to gather atmospheric transmission statistics from actual space-to-earth links.

The Jet Propulsion Laboratory (JPL) [120] optical communications telescope laboratory has propagated 30-μrad beams to low-earth orbit satellites as part of an active satellite tracking experiment [121]. Horizontal ground-to-ground FSO links have been demonstrated as precursors to space-to-earth links. Such links enable the comparison between theory and observations of atmospheric effects. For example, horizontal FSO links have been demonstrated at an altitude of 2 km and a range of 46.8 km, where bit error-rates as low as 10^{-5} were reported at a 400 Mbps transmission rate [122–124]. Another horizontal link has been demonstrated over a range of 32 km, where bit error-rates as low as 10^{-9} were reported at 2.5 Gbps transmission rate under low atmospheric turbulence conditions (defined in Sec. 1.3.2), and average visibility [104].

FSO links also find application in high altitude platforms (HAPs), which are airships that float at an altitude of about 20 km, and provide broadband communication services to stationary and mobile users on the ground. For example, FSO technology has been considered by the CAPANINA consortium [125] to establish HAP interplatform links. Such links are used above cloud height, and therefore, they do not suffer outages due to rain and clouds [126].

Successful studies and demonstrations for near-earth FSO communications have resulted in a serious interest to employ FSO communication technology for deep-space applications [17–19]. There is a continuously increasing demand for higher data rates for communication between deep-space terminals and earth. Deep-space missions employ high resolution sensors and imagers that require very high-rate links to send measurement data to earth. The National Aeronautics and Space Administration (NASA) [127] anticipates a significant increase in the near future demand for deep-space to earth communications over distances from 0.1 to 40 astronomical units (AU)† and data rate requirements range from a few megabits to a few gigabits per second [128]. FSO links are attractive alternatives to RF links for such long-range communication. With smaller transmit and receive apertures, FSO links can potentially deliver signal power more efficiently than RF links since the shorter wavelength allows for the use of highly collimated optical beams. This feature is extremely important since the main problem with deep-space communication is the extreme link distance. FSO communications promise lighter and smaller spacecrafts, and are capable of providing orders-of-magnitude more data return from deep-space missions than that provided by conventional RF communications [129, 130], [19, Sec. 1.1].

The Galileo optical experiment (GOPEX) demonstrated an optical uplink to a deep-space spacecraft, Galileo, from two earth terminals at the Table Mountain Facility in California, and Starfire Optical Range in New Mexico, USA. The demonstration link distance ranged from 1 to 6 million km. The GOPEX objectives were to demonstrate optical beam transmission at deep-space distances, to verify beam pointing strategies, and to validate the models developed to predict the link performance. Not all the transmitted frames were successfully detected due to unfavorable weather

†One AU is equal to 149.6 million kilometers conditions, restrictions on transmissions by regulatory agencies, temporary signal-to-noise anomalies on the downlink, and unexpected pointing bias error [131]. Another demonstration is the Mars laser communications demonstration (MLCD) that was initiated to demonstrate optical communications from Mars to earth at data rates from 1 to 80 Mbps and distances from 0.67 to 2.4 AU [19, Sec. 7.1], [128, 132]. The project was part of the Mars Telesat orbiter, which, before its cancellation, was scheduled to launch a spacecraft to Mars in 2009. Insights gained from these projects may be applied to any deep-space FSO system [132].

1.3.2 Complications and Challenges

FSO communications exhibit a number of complications that impose challenges on FSO link design.

Atmospheric attenuation, due to fog, clouds and other atmospheric particles, causes a decrease in the effective FSO link distance. The intensity of the optical beam is attenuated, or even vanishes, due to absorption, scattering, and reflection by various atmospheric particles [19, Sec. 3.2]. Another form of attenuation is *free-space loss*, which is the attenuation caused by the optical beam divergence due to free-space propagation.

For the proper operation of FSO links, it is necessary to accurately direct the transmitted beam toward the receiver. That is, FSO links are highly dependent on the pointing performance. Pointing errors in terrestrial FSO links arise due to mechanical misalignment, building sway, or other mechanical vibrations present in the transceivers. In space-to-earth and inter-satellite links, the relative motion between the transmitter and receiver exacerbates pointing errors. Therefore, it is necessary to have accurate pointing and tracking systems to avoid severe performance degradation [133].

The main source of background noise that affects FSO links is sky background radiation due to scattered solar photons. This noise is characterized by the *sky radiance*, defined as the power radiated per unit source area into a unit solid angle, where the sky is regarded as an extended uniform background source. For space links, the optical receiver may also collect undesired background photons from point sources such as illuminated planets or stars [19, Sec. 3.2].

Inhomogeneities in atmospheric temperature, pressure, water vapour content, and wind velocity lead to random variations of the medium refractive index along the transmission path. These random variations are known as *atmospheric turbulence*, which tends to vary on time-scales of 10–100 msec [134]. That is, its variation time is much longer than the pulses transmitted over the channel, which are typically on the order of nanoseconds. Atmospheric turbulence causes phase fluctuations in the received field, particularly for FSO links longer than 1 km in distance. These fluctuations result in random variations of the detected intensity at the receiver, a phenomenon known as *optical scintillation*. Twinkling of stars when viewed from the earth surface is an example of optical scintillation. In fact, stars would not twinkle if viewed from the outer space, i.e., in absence of the turbulent atmosphere [135–138].

1.3.3 Single-Detector Receivers

The lens of a conventional receiver focuses the collected optical field onto a single photodetector in the focal-plane as shown in Fig. 1.5. The photodetector produces an electrical signal that is proportional to the intensity of the field incident on its

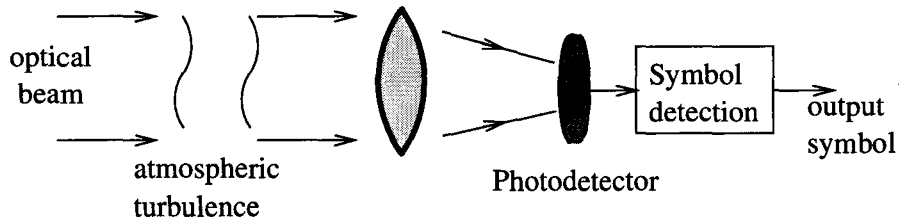

Figure 1.5: Conventional single-detector receiver.

surface, and is used to detect the output symbol. The *point spread function* (PSF) is defined as the intensity distribution in the focal-plane when a spatial intensity impulse is transmitted. Ideally, the PSF is a very narrow spatial pulse whose shape and size depend on the diffraction of the received field by the receiver aperture as described in Sec. 2.1.2. This narrow pulse coincides with the photodetector, and hence, in the absence of atmospheric turbulence, a small photodetector is capable of detecting all of the power incident on the receiver aperture.

In practical links, the received optical wavefront is distorted by atmospheric turbulence. The phase of the received field tends to become uncorrelated over distances greater than the atmospheric coherence width, defined in Sec. 2.4, which is on the order of a few centimeters [139, Sec. 12.4], [124]. This leads to random fluctuations of the intensity distribution in the focal-plane, where the collected intensity is distributed over a much larger spot. That is, the dimensions of the receiver PSF increase, as shown in the example turbulence-degraded PSF of Fig. 1.6, and its location in the focal-plane is subject to random excursions.

A conventional FSO receiver uses a single photodetector as shown in Fig. 1.5. However, a large photodetector area[‡] is required in order to collect a majority of the PSF power. This degrades the receiver performance due to the fact that a great deal

[‡]As implied by (2.3), a large photodetector area is equivalent to a large field-of-view.

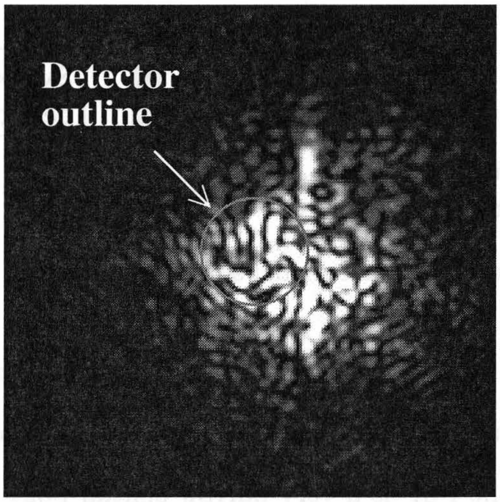

Figure 1.6: A power plot of an example turbulence-degraded PSF for $D/r_0 = 11.92$, where D is the receiver aperture diameter and r_0 is the atmospheric coherence width. The outline of a circular photodetector is indicated. While a large detector diameter is required to collect a majority of the PSF energy, a small one is required to reject a majority of background noise.

of background noise is also collected. In other words, while a large detector area is required to collect a majority of the PSF energy, a small one is required to reject a majority of background noise. This tradeoff can be mitigated by using array receivers as described in Sec. 1.3.4.

1.3.4 Array Receivers

Spatial diversity reception is the use of a multiple-element receiver to mitigate the PSF degradation due to atmospheric turbulence [140–152]. In [140,141], it was shown that spatial diversity, by using an array of smaller receiver apertures, considerably decreases the symbol error-rate (SER) when compared to a single large aperture receiver. This is due to the fact that multiple receiver apertures are separated in space such that they see independent signal fades, and therefore, their measurements can be combined to improve symbol detection.

Adaptive optics compensation systems have been used in [142–146] to correct the phase of the optical beam after it propagates through a turbulent atmosphere. The phase of the received laser beam is measured using a wavefront sensor, and is compensated using a spatial phase modulator. A deformable mirror is an example of such phase modulators, where the mirror shape is changed by using mechanical actuators and a real-time control system. The main disadvantage of using adaptive optics systems is the increased receiver complexity and cost.

An adaptive multiple-detector array receiver is presented in [134, 147, 148] which reduces the background noise by assigning higher confidence levels to detector elements that contain significant signal energy and suppressing those that do not. That is, the receiver pictures the incident intensity image, as shown in Fig. 1.7, and uses this picture to estimate the PSF. Preliminary experimental verification of the optical array receiver was reported in [149, 150] by the JPL as part of a research and technology development effort. Two telescopes were used for these experiments, where each telescope was equipped with a high-sensitivity 16-element photon-counting detector array. However, the processing algorithms, available at the time of the experiments, did not allow for the proper combining of the individual detector outputs to account for the effect of noise or atmospheric turbulence, and therefore, only the summed output of the entire focal-plane detector array was used. Data collected in the field were processed off-line to validate the Poisson channel model and to demonstrate optical array reception in the photon-counting regime.

A key limitation of all of the above approaches is the increased complexity and necessity for many high-speed photodiodes and preamplifiers. The increased complexity

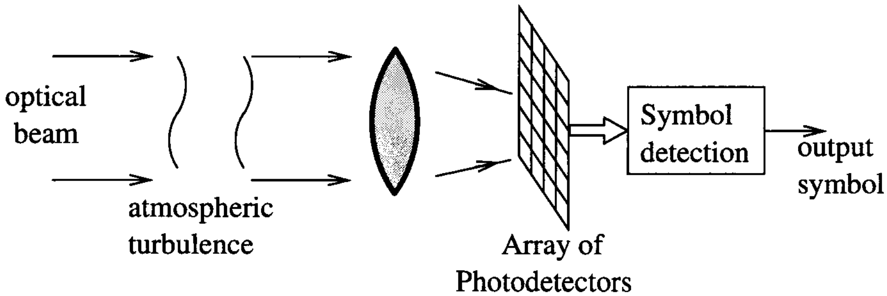

Figure 1.7: Multiple-detector array receiver.

of the multiple-detector array receiver stems from the fact that its frame rate is equal to the very high transmitted pulse rate. This array receiver can be regarded as a very high-speed digital camera such that, each pulse duration, an intensity image is captured and used to detect the transmitted pulse. These intensity images, captured successively in time, are also stored and used to estimate the PSF. A key point is that the PSF varies at a much slower rate than the pulse transmission rate. The transmitted pulse is on the order of nanoseconds, while the PSF variations follow the atmospheric turbulence which tends to vary on time-scales of 10−100 msec as mentioned in Sec. 1.3.2. Therefore, there is no need to capture an entire image every pulse duration for the purpose of PSF estimation.

This fact is particularly important since FSO communication links employ the infrared wavelength range between 800-1550 nm. While building high-speed imager arrays is expensive in general, building them in the infrared wavelength range is even more costly. This is due to the fact that the quantum efficiency of silicon is low in the infrared range, which leads to low bandwidth-efficiency product [153]. Moreover, for multiple-detector array imagers, very low noise photodetectors are required to maximize the gain of combining the array outputs, and to achieve background noise-limited reception. In this case, more expensive compound semiconductors are needed to implement such photon-counting detectors [154]. That is, it is quite expensive to build multiple-detector array imagers which are (i) high-speed, (ii) operating in the photon-counting mode, and (iii) operating in the infrared spectral region.

1.4 Thesis Contributions

This thesis provides contributions to both indoor and outdoor wireless optical communications. Many degrees of freedom are available at the transmitter in temporal and spatial frequency domains, and at the receiver in the spatial intensity domain. The main theme of this thesis is to use such degrees of freedom to improve the wireless optical link performance. While the majority of previous work considers conventional modulation and detection schemes that were originally designed for RF communication, this thesis designs new modulation and detection schemes which are capable of matching the transmitted signal to the optical channel and its amplitude constraints. Consequently, these new schemes achieve higher power and spectral efficiencies, and simpler transmitters and receivers. An outline of the contributions of individual chapters is given in Table 1.2.

Chapter 3 treats the modulation design problem for indoor diffuse wireless optical links. Current lasers and LEDs have far higher pulse rates than can be supported by the lowpass indoor diffuse channel. High-frequency emissions are attenuated by the channel and are not detected by the receiver. Such emissions provide extra degrees of freedom in the temporal frequency domain that are available at the transmitter. A new modulation scheme, *optical impulse modulation* (OIM), is proposed that employs these degrees of freedom to improve the link power efficiency, to improve its immunity to multipath dispersion, and to decrease receiver complexity. Data are confined to the

Table 1.2: The main theme of this thesis is to use the extra degrees of freedom available at the transmitter/receiver to improve link performance.

Chapter	Channel considered	Location of extra degrees of freedom	Domain of extra degrees of freedom	Contributions and publications arising
3	Indoor diffuse link	Transmitter	Temporal frequency domain	• Improved power efficiency and immunity to multipath dispersion • Decreased receiver complexity [155–157]
4	Indoor MIMO link	Transmitter	Spatial frequency domain	• Improved link spectral efficiency • Decreased transmitter complexity [158–160]
5	Outdoor FSO link	Receiver	Spatial intensity domain	• Mitigate atmospheric turbulence effects • Decreased receiver complexity [160–163]

lowpass region while the highpass region, which is attenuated by the channel, is used to satisfy the channel amplitude constraints. A mathematical framework for OIM is presented, and a simple sub-optimal channel-independent receiver filter is designed. OIM is shown to be a general scheme to transmit non-negative discrete sequences over a dispersive optical intensity channel. It can be used with all pulse-amplitude modulation (PAM) schemes such as on-off keying (OOK) and pulse-position modulation (PPM), which are defined in Sec. 3.2. Using a well-known exponential model for indoor diffuse optical channels, at a normalized delay spread of 0.2, the gain in average optical power of OIM with a simple lowpass receiver is shown to be 4.9 optical decibels (dBo) which exceeds the gain of rectangular OOK with a complex decision feedback equalizer. From an information theory point of view, at the same normalized delay spread of 0.2, the information rate of OIM with a lowpass receiver is shown to be 11.5% higher than that of rectangular OOK with a more complex whitened matched filter receiver. Similar gains are reported in Chapter 3 in case of PPM [155–157].

Chapter 4 treats the modulation design problem for indoor MIMO wireless optical links. Current SLMs have higher spatial bandwidth than can be supported by the spatially lowpass MIMO channel. The high spatial frequency emissions are attenuated by the channel and are not detected by the receiver. Such emissions provide extra degrees of freedom in the spatial frequency domain that are available at the transmitter. A new modulation scheme, *halftoned spatial discrete multitone* (HSDMT) modulation, is proposed that employs these degrees of freedom to improve the link spectral efficiency and to decrease the transmitter complexity by considering binary-level SLMs. A binary-level transmit image is produced by exploiting the excess high spatial frequency regions to shape quantization noise away from the data-bearing low spatial frequency regions. Our approach combines *spatial discrete multitone* (SDMT) modulation, developed for spatially frequency selective channels, with halftoning to produce binary-level transmit images. Neither strict spatial alignment between transmitter and receiver nor independence among the spatial channels is required. A general mathematical framework is presented in Chapter 4 in which such systems can be analyzed and designed. In a pixelated wireless optical channel application, halftoning achieves 99.8% of the capacity of an equivalent unconstrained continuous amplitude channel using 1 megapixel arrays [158–160].

Chapter 5 treats the spatial diversity reception problem for outdoor long-range FSO links. The receiver extra degrees of freedom in the spatial intensity domain are used to mitigate the atmospheric turbulence effects and to decrease receiver complexity. Using digital micromirror devices, the receiver optically computes linear projections of the turbulence-degraded PSF onto an orthogonal binary basis. By using such projections, an estimate of the PSF is computed and updated adaptively to follow the time variations of the PSF. The estimate is used to perform selection combining, i.e., to select the portions of the focal-plane which contain significant energy for symbol detection. The proposed receiver is less complex, requires fewer high-speed components, has lower preamplifier noise and can operate at higher rates than a comparable multiple-detector array receiver. SER is simulated on a photon-counting channel and performance improvements near 3.0 dBo over a conventional single-detector receiver are obtained at SER $= 10^{-2}$. The proposed receiver is best suited to long range terrestrial, or space-to-earth FSO links, where atmospheric turbulence effects are considerable [160–163].

Chapter 2

Channel Models

2.1 Wireless Optical Communication Systems

Wireless optical communication systems share a number of common components and characteristics. This section overviews these common aspects, while the following sections present details of three specific wireless optical channels.

2.1.1 Transmitter

A block diagram of a conventional transmitter used by wireless optical communication systems is shown in Fig. 2.1. In general, the emitted intensity, in Watts per steradian, is a function of direction. The transmitter optical beam angle, Ω_a, is the solid angle in steradians, measured from the transmitter antenna, into which the maximum intensity must be concentrated in order to have the same total transmitted power. In other words, the total transmitted power is equal to the product of Ω_a and the maximum intensity. The beam angle can be well described by its planar angular beamwidth,

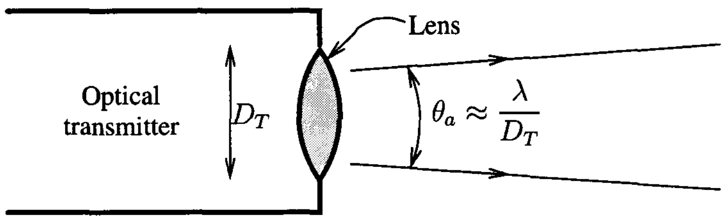

Figure 2.1: Conventional wireless optical transmitter.

θ_a, where

$$\Omega_a = 2\pi\left(1 - \cos\left(\frac{\theta_a}{2}\right)\right) \approx \frac{\pi}{4}\theta_a^2,$$

for small θ_a [19, Sec. 3.4]. For a circular lens antenna of diameter D_T,

$$\theta_a \approx \frac{\lambda}{D_T},$$

which indicates that highly directional beams are possible at the very short optical wavelength, λ, with a practical transmitter diameter, D_T [22, Sec. 1.2]. On the other hand, to have a comparable beam width at RF wavelengths, very large transmitter dimensions are required. This fact makes the optical wavelength very attractive for long-range wireless communications since the narrow collimated optical beams deliver signal power more efficiently than their RF counterparts.

2.1.2 Receiver

A block diagram of a conventional direct detection wireless optical receiver is shown in Fig. 2.2. The receiver front-end lens focuses the collected optical field onto a photodetector, which outputs a current proportional to the optical power focused on its surface. The focusing lens acts as a concentrator that allows a smaller size photodetector than that of the lens. That is, $\mathcal{A}_d \ll \mathcal{A}_r$, where $\mathcal{A}_d$ is the photodetector

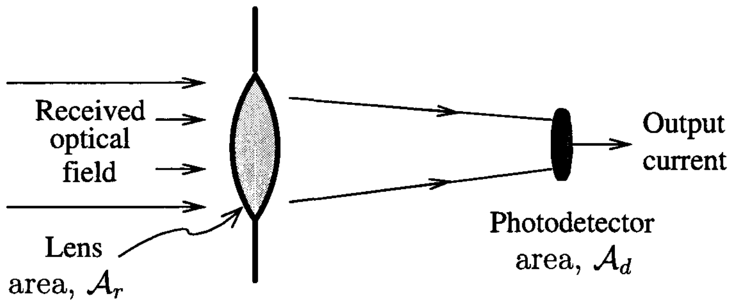

Figure 2.2: Conventional wireless optical receiver.

area and $\mathcal{A}_r$ is the receiver aperture area. The field emitted by a distant point source, and collected by the receiver lens aperture, is ideally focused onto a single point in the focal-plane. However, due to effects of field diffraction by the finite lens aperture, the collected field is focused onto the focal-plane according to a certain pattern, termed, *diffraction pattern*, which depends on the receiver aperture shape and dimensions. The corresponding normalized focal-plane power pattern is called the *point spread function* (PSF) [22, Sec. 1.6]. The Fourier transform of the PSF is called the *optical transfer function* (OTF).

The PSF is dependent on the finite extent of the lens aperture. This extent can be represented by defining a pupil function

$$P(u,v) = \begin{cases} 1 & : \text{ inside the lens aperture} \\ 0 & : \text{ otherwise,} \end{cases} \tag{2.1}$$

where (u,v) are continuous spatial coordinates. The PSF is given by

$$h_t(u,v) = \frac{\left|P_f\left(\frac{u}{\lambda f_\ell}, \frac{v}{\lambda f_\ell}\right)\right|^2}{\iint \left|P_f\left(\frac{u}{\lambda f_\ell}, \frac{v}{\lambda f_\ell}\right)\right|^2 dudv} = \frac{\left|P_f\left(\frac{u}{\lambda f_\ell}, \frac{v}{\lambda f_\ell}\right)\right|^2}{(\lambda f_\ell)^2 \mathcal{E}_P} \tag{2.2}$$

where f_ℓ is the focal length, $\mathcal{E}_P = \iint |P_f(f_u, f_v)|^2 \, df_u df_v$, and $P_f(f_u, f_v)$ is the continuous Fourier transform of $P(u, v)$ [21, Chapter 6], [29]. In the absence of atmospheric turbulence, as is the case with indoor links, $h_t(u, v)$ is constant with time. However, the subscript t is retained to represent the time-varying nature of the PSF in the general case when turbulence effects are considered [29, 147], as is the case with outdoor links. Notice that in the ideal case of an infinite-extent lens aperture, the PSF is a Dirac impulse. Qualitatively, due to the Fourier transform relationship, the PSF extent gets wider as the lens aperture extent gets narrower.

The receiver *field-of-view* (FOV) is the solid angle, measured from the receiver antenna, within which all point sources must occur in order to project their PSFs onto the photodetector. As shown in the geometrical clarification of Fig. 2.3, the FOV is the solid angle subtended by the photodetector area at the lens center,

$$\Omega_{\mathrm{fv}} \approx \frac{\mathcal{A}_d}{f_\ell^2}, \tag{2.3}$$

where Ω_{fv} is much smaller than unity. The area of the PSF is approximately equal to $f_\ell^2 \left(\frac{\lambda^2}{\mathcal{A}_r} \right)$, in both cases of a rectangular or circular apertures [22, Sec. 1.6]. All close by point sources, which lie within the FOV and whose PSFs superimpose, are indistinguishable. That is, the PSF extent defines the inherent spatial resolution of an optical imaging system [22, Sec. 1.6].

2.1.3 Noise

An inherent source of noise is the probabilistic nature of the photodetection process. The photodetector photosensitive material releases free electrons in response to the light incident over its surface. The released electrons compose the detector output

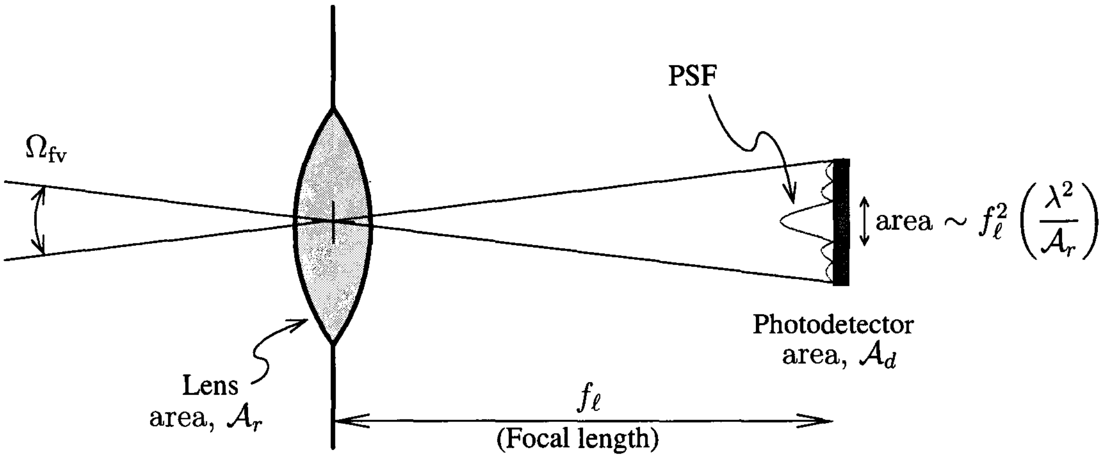

Figure 2.3: Receiver field-of-view.

current process. This process is a random process since each photon absorbed by the photodetector releases an output electron with probability equal to the *quantum efficiency* of the photosensitive material. If the m^{th} released electron produces a current response function $y_e(t)$ shifted at the release time, $t_m \in (0, t)$, then the photodetector output current process can be written as

$$y(t) = \sum_{m=1}^{I^{(0,t)}} y_e(t - t_m),$$

where $I^{(0,t)}$ is the number of electrons released during the time interval $(0, t)$, which is a random counting process termed a *shot noise* process, and the functions $\{y_e(t-t_m)\}$ are called the shot noise component functions. The counting process at time t is often modelled using a Poisson random variable, denoted by

$$I^{(0,t)} \sim \text{Poisson}[\mu(t)],$$

where $\mu(t)$ is the mean of $I^{(0,t)}$. In this case, the process is termed, *Poisson shot noise* process [22, Sec. 4.1]. If η_q is the quantum efficiency and e_{ph} is the photon energy, then

$$\mu(t) = \frac{\eta_q}{e_{ph}} \int_0^t r_d(\tau)\, d\tau,$$

where $r_d(t)$ is the instantaneous power incident over the detector surface [22, Sec. 2.2].

While the output process, $I^{(0,t)}$, is referred to as a shot noise process, it should be clear that it also conveys useful information through its mean, μ, which is proportional to the energy incident on the detector surface during the integration time. From a communication system perspective, the deviation of $I^{(0,t)}$ away from its mean is the actual noise that degrades the detection performance. Notice also that this noise is signal-dependent since the variance of a Poisson process is equal to its mean.

An additional noise source that degrades the link performance is the circuit thermal noise following the photodetection process. However, the effect of thermal noise can be reduced by using expensive photodetectors, such as avalanche photodiodes, that offer *photomultiplication* [154]. The photomultiplication process is a detector internal amplification process that amplifies the current response function, $y_e(t)$, of each released electron, so that the detector output power is much larger than that of the additive thermal noise [22, Sections 1.8 and 7.8]. In this case, thermal noise can be ignored, the system is termed *shot noise-limited*, and the receiver photodetector is said to be operating in a *photon-counting* mode.

For indoor wireless optical links, ambient background radiation from incandescent and fluorescent lighting contains considerable infrared emissions. The spectral energy distribution of a tungsten lamp is the most unfavorable for an infrared receiver [4]. Traditionally, fluorescent lamps emit 120 Hz infrared emissions with harmonics up to 50 kHz during turn-on time [4]. However, recent high-efficiency electronic ballasts drive fluorescent lamps at frequencies of tens to hundreds of kilohertz, which makes fluorescent lamps a considerable noise source for indoor infrared links [6]. Moreover, indoor infrared links may be affected by sunlight, especially near windows [4].

The shot noise induced by such background radiation is usually of high intensity. Since a Poisson distribution with a high mean can be well approximated as a Gaussian distribution [164], the intense shot noise due to ambient illumination can be well approximated as Gaussian signal-independent additive noise [6]. Indoor links also suffer from the receiver thermal circuit noise, which is also Gaussian and signal-independent [6]. Therefore, it is assumed that the noise affecting indoor wireless optical links is Gaussian and signal-independent. In this case, the signal-dependent shot noise component is negligible compared to the intense background and circuit noises. The high mean of the background radiation is assumed known and compensated for at the receiver, and hence the noise can be modelled as zero-mean noise.

For outdoor FSO links, the main source of noise is the sky background radiation. The sky is modelled as an extended uniform background source that is characterized by its *spectral radiance function*, $N(f)$, defined as the power radiated into a unit solid angle, per cycle bandwidth, per unit source area [22, Sec. 1.7]. In this case, the received background noise power is given by

$$\begin{aligned} \mathcal{P}_b &= N(f)\, B\, (\mathcal{A}_r/l^2)\, (l^2\Omega_{\text{fv}}) \\ &= N(f)\, B\, \mathcal{A}_r\, \Omega_{\text{fv}}, \end{aligned}$$

where B is the receiver bandwidth which is assumed much smaller than the frequency, f, of the optical field, l is the distance between the receiver and the background source, $(\mathcal{A}_r/l^2)$ is the solid angle, and $(l^2\Omega_{\text{fv}})$ is the source area within the receiver FOV [22, Sec. 1.7]. Therefore, the received background noise power is proportional to both the receiver aperture area, $\mathcal{A}_r$, and the receiver FOV, Ω_{fv}.

Sky background radiation induces shot noise at the FSO receiver. Circuit noise may also exist as is the case with indoor receivers. The dominant source of noise may vary from one FSO link to another. If the background radiation power, or circuit noise power, is much higher than the signal power, then the signal-dependent shot noise can be ignored, and the background and circuit noises can be well modelled as signal-independent Gaussian noise [136]. Whereas, if the background radiation power is on the order of signal power, then both signal-dependent and signal-independent shot noise components have to be considered. Moreover, if photomultiplication is used at the receiver, then the circuit noise can be ignored and photon-counting reception is achieved. An example of shot noise-limited links is the high rate deep space FSO link, where the received power is very low, on the order of tens of photons, due to the very long link distance and the short transmit pulses, and the background radiation is low due to the narrow FOV [129, 132, 134].

2.2 Indoor Wireless Optical Diffuse Channels

Indoor wireless optical diffuse links depend on the reflection of optical power from surfaces in the room and do not necessarily require an uninterrupted line-of-sight between the transmitter and receiver [3, 6, 59, 60]. While optical waves may experience mirror-type, or specular, reflection off shiny surfaces, their reflection off different room surfaces is dominated by diffuse-type reflection. This is because optical wavelengths are on the order of the dimensions of the surface roughness of different room objects, which generates reflections in many different angles [70]. According to the diffusive reflection model, the direction of the optical power reflected from a differential surface element is independent of the angle of incidence. In fact, the *optical intensity*, in Watts per steradian, reflected from many typical materials is well approximated by a Lambertian radiation pattern, which is given by

$$I_{\text{Lambertian}}(\theta, \phi) = \mathcal{P}_{\text{elem}} \frac{n+1}{2\pi} \cos^n(\theta),$$

where $I_{\text{Lambertian}}(\theta, \phi)$ is the optical intensity in W/sr reflected at a polar angle $\theta \in \left[0, \frac{\pi}{2}\right]$ and an azimuthal angle $\phi \in [0, 2\pi)$, with respect to the normal to the reflecting element as shown in Fig. 2.4, $\mathcal{P}_{\text{elem}}$ is the total power, in Watts, reflected by the surface element, and n is the *mode number* of the Lambertian pattern [3, 9, 61]. Notice that $I_{\text{Lambertian}}(\theta, \phi)$ is independent of ϕ due to symmetry in the azimuthal coordinate as shown in Fig. 2.4.

As depicted in Fig. 2.5, the optical intensity transmitted is diffusively reflected by the ceiling, walls and different room objects. The reflected radiations cover the room, and therefore, diffuse links are insensitive to pointing errors, immune to shadowing and permit receiver mobility. These properties are particularly appealing in portable devices. As mentioned in Sec. 1.2, diffuse links do not suffer from multipath fading due to the large surface area of the photodetector in relation to the wavelength of light. The received optical field shows spatial intensity variations due to multipath propagation so that multipath fading is experienced if the detector diameter is less than an optical wavelength. However, typical detector diameters are on the order of thousands of wavelengths. That is, the received optical field is integrated over an area that is on the order of millions of square wavelengths, which leads to spatial

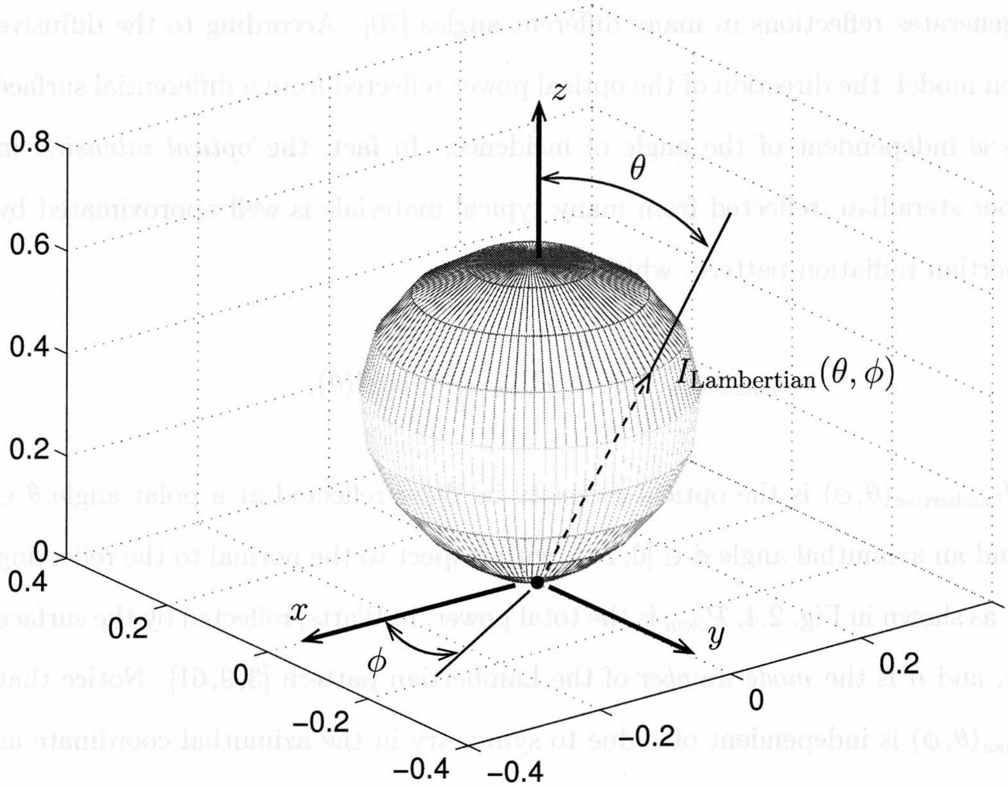

Figure 2.4: The Lambertian reflection pattern for $\mathcal{P}_{\text{elem}} = 1$ and mode number $n = 3$. The $x - y$ plane represents the surface of the differential reflecting element.

diversity that eliminates multipath fading [6]. This also leads to unaltered channel characteristics if the detector moves by a distance on the order of a wavelength [6].

On the other hand, indoor wireless optical diffuse links suffer from low SNR and low bandwidth. The low SNR is due to the high optical power loss resulting from the use of wide-angle transmitters and the high ambient noise collected by wide-angle receivers. The low bandwidth is due to multipath dispersion which is the dispersion of the transmit pulse due to the fact that the receiver detects multiple diffusively reflected versions of the transmit pulse as shown in Fig. 2.5 and discussed in Sec. 1.2.

For IM/DD channels, the instantaneous intensity $I(t)$, in Watts per steradian, of

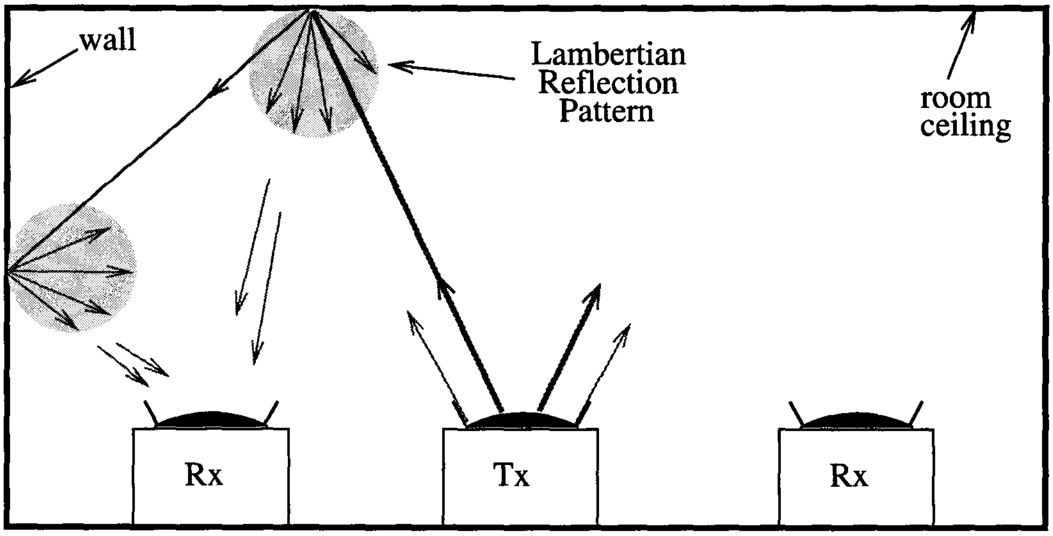

Figure 2.5: Wireless optical diffuse link. The Lambertian reflection pattern is shown for ceiling and wall differential reflecting elements, and a mode number $n = 1$. The receiver detects multiple diffusively reflected versions of the transmitted signal.

the optical emitter is directly proportional to the information signal as mentioned in Sec. 1.1. The instantaneous emitted optical power $x(t)$, in Watts, is given by the integral of $I(t)$ over the transmitter solid angle. Direct detection is done via a photodetector receiver which produces an output current $y(t)$, in Amperes, proportional to the integral of the received irradiance, in Watts per unit area, over the detector surface. The indoor IM/DD optical communication system can be modelled as a baseband linear system

$$y(t) = Rx(t) * h(t) + z(t), \tag{2.4}$$

where R is the photodetector *responsivity* in Amperes per Watt, $h(t)$ is the optical channel impulse response, $*$ is continuous-time convolution, and $z(t)$ is the channel noise [3,6,9,59]. The channel model (2.4) can be rewritten as

$$y(t) = x(t) * h(t) + z(t), \tag{2.5}$$

by assuming, without loss of generality, that the photodetector responsivity is unity. As discussed in Sec. 2.1.3, $z(t)$ is a high intensity shot noise process which is well modelled as zero-mean, Gaussian, and independent of $x(t)$. Moreover, $z(t)$ is assumed white with double-sided power spectral density (PSD) $N_0/2$ [6].

The channel multipath dispersion is modelled by a lowpass impulse response, $h(t)$, whose DC-gain,

$$H_0 = \int_{-\infty}^{\infty} h(t)\, dt, \tag{2.6}$$

ranges from 10^{-7} to 10^{-5} [6,64]. The temporal dispersion is quantified by the root-mean-square (rms) delay spread of $h(t)$,

$$\mathcal{D} = \sqrt{\frac{\int_{-\infty}^{\infty} (t-\varrho)^2\, h^2(t)\, dt}{\int_{-\infty}^{\infty} h^2(t)\, dt}}, \tag{2.7}$$

which ranges from 2 to 10 nanoseconds [6,64], where

$$\varrho = \frac{\int_{-\infty}^{\infty} t\, h^2(t)\, dt}{\int_{-\infty}^{\infty} h^2(t)\, dt}$$

is the mean delay [6,64]. Experimental measurements [62–65], ray-tracing simulations [61,66], Monte Carlo-based ray-tracing simulations [67–69], photon-tracing simulations [70], and functional modelling [71, 72] have been used to estimate $h(t)$. Both $h(t)$ and $\mathcal{D}$ are dependent on the specific room dimensions, objects within the room and on the positions of the transmitter and receiver. For a given transmitter, receiver and room configuration, $h(t)$ and $\mathcal{D}$ are considered fixed [6].

Two functional models for $h(t)$ have been developed in [71], namely, the exponential-decay model and the ceiling-bounce model. The exponential-decay model,

$$h(t) = \frac{H_0}{2\mathcal{D}} \exp\left(\frac{-t}{2\mathcal{D}}\right) U(t) \longleftrightarrow H(f) = \frac{H_0}{1 + j4\pi\mathcal{D}f}, \tag{2.8}$$

is used in this thesis to contrast the performance of different modulation schemes over diffuse channels, where $U(t)$ is the unit step function, and $H(f)$ is the continuous-time Fourier transform of $h(t)$. Similar results can be obtained by using the ceiling-bounce, however, the exponential model (2.8) is used in this thesis due to its convenient analytical form. The 3-dB cutoff frequency, $f_{3\mathrm{dB}}$, is the frequency for which $20\log_{10}|H_0/H(f_{3\mathrm{dB}})| = 3$ dB, which is given by

$$f_{3\mathrm{dB}} = \frac{1}{4\pi\mathcal{D}},$$

for the exponential model (2.8). Using this model, if $\mathcal{D}$ ranges from 2 to 10 nanoseconds [6, 64], then the 3-dB channel bandwidth approximately ranges from 10 to 40 MHz.

Due to the fact that the transmitted signal, $x(t)$, is a power signal, it must satisfy the constraints

$$x(t) \geq 0, \tag{2.9}$$

$$\mathcal{P}_t = \lim_{u \to \infty} \frac{1}{2u} \int_{-u}^{u} x(t)\, dt \leq \mathcal{P} \tag{2.10}$$

where $\mathcal{P}_t$ is the transmitted average optical power, and $\mathcal{P}$ is the average optical power limit imposed by eye-safety constraints. The non-negativity constraint (2.9) arises due to the modulation and detection of solely the intensity of the carrier. Constraint (2.10) indicates that the average optical power is given by the average signal amplitude, rather than the squared signal amplitude as is the case with conventional RF channels. These channel constraints prohibit the direct application of most traditional signalling schemes, and power and bandwidth efficient modulation schemes must be designed with (2.9) and (2.10) in mind.

2.3 Indoor Point-to-Point Wireless Optical MIMO Channels

Indoor wireless optical MIMO intensity channels are short-range point-to-point channels, as shown in Fig. 2.6. As mentioned in Sec. 1.2.1, the transmitter is an SLM consisting of a 2D array of pixels, while the receiver consists of a 2D array of photodiode pixels. Information is conveyed through the channel by sending time-varying optical intensity images.

It is assumed that imaging optics are employed, and that the optical axes of the transmitter and the receiver are aligned so that the receive intensity image $y(u, v)$ is an orthographic projection of the transmit intensity image $x(u, v)$. According to scalar diffraction theory, the impact of the imaging system can be well modelled as a lowpass linear space-invariant system filter that is characterized by the system PSF [21, Chapter 6]. The effect of the non-zero extent of the transmit and receive

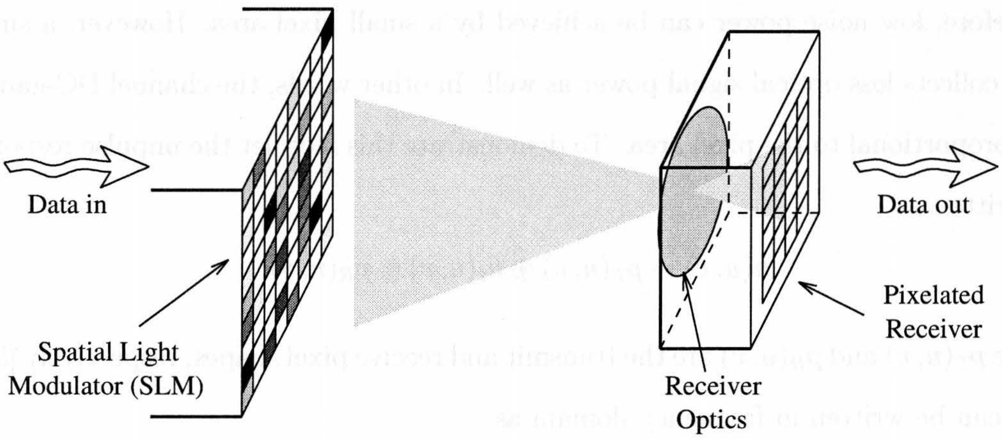

Figure 2.6: Wireless optical MIMO link.

pixels can be modelled as spatial lowpass filters as well [57, 58]. The channel model can be written as

$$y(u, v) = x(u, v) \circledast h(u, v) + z(u, v), \tag{2.11}$$

where $z(u, v)$ is the channel noise, which is assumed white in spatial frequency, $\circledast$ is 2D linear convolution, and $h(u, v)$ is the optical impulse response that models the combined lowpass filtering effect due to the PSF, (2.2), and the transmit and receive pixels [57, 58]. It is also assumed that the imaging system magnification is unity. Systems with non-unity magnification have been considered in [165, 166]. The channel model in (2.11) is a generalization of a previous model used in holographic data storage [37] and 2D optical recording [38], where the channel was modelled as a finite-extent 2D linear filter that represents the optical blur, or the 2D inter-symbol interference. The same model has been used in wireless optical communication applications [57, 58], and can also be regarded as a 2D generalization of the model (2.5) used for indoor wireless optical diffuse channels.

The noise power per receive pixel is proportional to the receive pixel area [167, 168].

Therefore, low noise power can be achieved by a small pixel area. However, a small pixel collects less optical signal power as well. In other words, the channel DC-gain is also proportional to the pixel area. To demonstrate this fact, let the impulse response be written as

$$h(u,v) = p_T(u,v) \circledast h_t(u,v) \circledast p_R(u,v),$$

where $p_T(u,v)$ and $p_R(u,v)$ are the transmit and receive pixel shapes, respectively [58]. This can be written in frequency domain as

$$H(f_u, f_v) = P_T(f_u, f_v)\, H_t(f_u, f_v)\, P_R(f_u, f_v),$$

where $H(f_u, f_v)$ is the system frequency response, $P_T(f_u, f_v)$ and $P_R(f_u, f_v)$ are the Fourier transforms of the pixel shapes, and $H_t(f_u, f_v)$ is the OTF. Therefore, the channel DC-gain is given by

$$H(0,0) = P_T(0,0)\, H_t(0,0)\, P_R(0,0),$$

which is proportional to the receive pixel area, since $P_R(0,0) = \iint p_R(u,v)\; dudv$. That is, both the channel noise power and DC-gain are proportional to the receive pixel area. This fact is used to calculate the optical SNR in the simulations presented in Sec. 4.4.1. While the receive pixel size affects the DC-gain, its effect on the system bandwidth is negligible since the pixel size is very small when compared to the PSF, $h_t(u,v)$. That is, the bandwidth of $h(u,v)$ is dominated by that of $h_t(u,v)$. With a slight abuse of notation, the system impulse response, $h(u,v)$, is referred to as the PSF in Chapter 4, and its Fourier transform is referred to as the OTF.

Since the transmitted image, $x(u, v)$, is an optical power signal, two channel amplitude constraints are imposed on it: a non-negativity constraint,

$$x(u, v) \geq 0, \tag{2.12}$$

and an average power constraint,

$$\mathcal{P}_t = \frac{1}{\mathcal{A}_t} \iint x(u, v)\, dudv \leq \mathcal{P}, \tag{2.13}$$

where $\mathcal{A}_t$ is the transmitter aperture area, and the integration is performed over the transmitter aperture. It is assumed that each transmit frame has the same average optical power, and therefore the transmit signal satisfies (2.10) as well.

2.4 Outdoor Free-Space Optical Channels

As shown in Fig. 1.4, FSO communication links are point-to-point links that transmit data by modulating the intensity of an optical beam propagating through free-space from the transmitter to receiver. The channel model can be written as

$$y(t, u, v) = x(t)\, h_0\, h_t(u, v) + z(t, u, v), \tag{2.14}$$

where $z(t, u, v)$ is the background noise, $h_t(u, v)$ is given by (2.2), and h_0 is a scaling factor that accounts for the transmit power and optical path loss.

As mentioned in Sec. 1.3.2, atmospheric turbulence breaks the spatial coherence of a propagating optical beam. The phase of the optical field, at two points in the plane transverse to propagation direction, tends to be uncorrelated if the two points are separated by a distance on the order of the *atmospheric coherence width*, r_0, which is also known as *Fried's parameter* [139, Sec. 12.4], [19, Sec. 3.4]. As the strength of atmospheric turbulence gets higher, r_0 gets shorter. At sea level, r_0 is roughly 2−30 cm at visible and infrared wavelengths [139, Sec. 14.1]. An expression for r_0 in terms of the propagation path length and other atmospheric parameters is given by [139, Sec. 14.3, Eq. (25)], which shows that r_0 decreases with path length.

Ideally, the PSF diameter is approximately proportional to the ratio, λ/D, where D is the receiver aperture diameter. In this case, the imaging system is termed *diffraction-limited* as shown in Fig. 2.3 [19, Sec. 3.4]. However, due to turbulence effects, the PSF diameter is proportional to the ratio, λ/r_0, which is usually referred to as *atmospheric seeing*, expressed in units of radians. That is, the PSF diameter increases by the ratio, D/r_0, which is a measure of the atmospheric turbulence strength. In this case, the performance is limited by turbulence effects and the system is termed *turbulence-limited* [19, Sec. 3.4]. Atmospheric turbulence causes alternate patches of constructive and destructive interference in the focal-plane, and causes random fluctuations in the beam angle of arrival. This results in the random distribution of the received focal-plane energy, and in random PSF excursions in the focal-plane, which are referred to as *beam wander* [19, Sec. 3.4].

As a result, there exists a relative displacement between the PSF position and the receiving photodetector. A small photodetector placed in the focal-plane will suffer from random fluctuations in the detected irradiance, which are referred to as *optical scintillation* as mentioned in Sec. 1.3.2. The received optical irradiance tends to be uncorrelated over time periods on the order of the *atmospheric coherence time*, T_{coh}, which is about 10−100 msec [134, 136]. Notice that T_{coh} is much longer than typical transmit pulse widths that are on the order of nanoseconds.

The PSF degradation due to atmospheric turbulence is simulated by replacing the constant pupil function of equation (2.1) by a random Kolmogorov phase screen,

$$P(u,v) = \begin{cases} \exp(j\Theta_t(u,v)) & : \text{ inside the lens aperture} \\ 0 & : \text{ otherwise,} \end{cases} \tag{2.15}$$

where $\Theta_t(u,v)$ is a Kolmogorov phase screen at time t [28, 29, 147]. Substituting by (2.15) in (2.2), a realization of the turbulence degraded PSF can be obtained. Numerical simulation of Kolmogorov phase screens and a time-varying PSF is discussed in Sec. 5.6.1.

2.5 Conclusions

In this chapter, the indoor and outdoor channel models used in this thesis are presented. Due to the unique features and constraints of wireless optical channels, conventional RF modulation and detection schemes are seldom efficient. In the following three chapters, new modulation and detection schemes are proposed for use over the wireless optical channel models presented.

Chapter 3

Optical Impulse Modulation

3.1 Introduction

This chapter treats the modulation design problem for indoor wireless optical diffuse channels. A new modulation scheme, *optical impulse modulation* (OIM), is designed that provides higher information rates and significant power gains over conventional modulation schemes. Moreover, the proposed scheme utilizes a simple lowpass receiver. That is, OIM offers significant performance improvements while decreasing receiver complexity over equalized rectangular PAM [155–157].

The channel model of indoor wireless optical diffuse channels has been presented in Sec. 2.2. The channel temporal dispersion is modelled by the channel impulse response, $h(t)$, in (2.5), and is quantified by the channel delay spread defined in (2.7). Conventional modulation schemes designed for RF channels cannot be applied directly to optical diffuse channels due to their amplitude constraints, (2.9) and (2.10), and new schemes are required to design efficient communication systems.

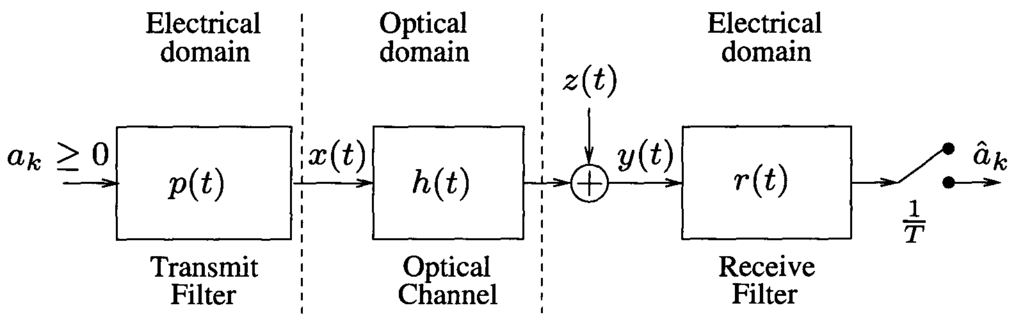

Figure 3.1: Block diagram of an optical intensity PAM communication system.

3.2 Optical Intensity Pulse Amplitude Modulation

A classical optical communication system is optical intensity PAM, shown in Fig. 3.1. A discrete symbol sequence $\{a_k\}$ is transmitted across the channel at a rate $1/T$ by forming the transmitted signal $x(t)$ as

$$x(t) = \sum_k a_k p(t - kT), \tag{3.1}$$

where $p(t)$ is the transmitter pulse shape, and T is the symbol duration. The output of the receive filter $r(t)$ is sampled at the same rate so that an estimate $\hat{a}_k$ of a_k is obtained. The channel noise, $z(t)$, is zero-mean, white, Gaussian and signal-independent with double-sided PSD of $N_0/2$ as mentioned in Sec. 2.2.

The non-negativity constraint (2.9) can be written in terms of the symbol sequence $\{a_k\}$ and the transmitter pulse shape as

$$a_k \geq 0 \tag{3.2}$$

$$p(t) \geq 0 \quad \forall t. \tag{3.3}$$

In general, the sequence $\{a_k\}$ only needs to satisfy (3.2) and does not need to be constrained to a finite set of PAM levels. However, in practical digital communication systems, it is constrained to a finite number of levels. In this case, the system is denoted by L-PAM, where L is the number of levels. Combining (2.10) and (3.1), the transmitted average optical power is expressed as

$$\mathcal{P}_t = \mu_a \bar{p}, \tag{3.4}$$

where μ_a is the mean of $\{a_k\}$, and $\bar{p}$ is defined by

$$\bar{p} = \frac{1}{T} \int_{-\infty}^{\infty} p(t)\, dt.$$

That is, $\mathcal{P}_t$ is factored to two terms: the first is dependent on the transmitted discrete sequence and the second is dependent on the pulse shape. Without loss of generality, in the remainder of the chapter, we assume that $p(t)$ is normalized so that $\int p(t)\, dt = 1$ and

$$\mathcal{P}_t = \frac{\mu_a}{T}. \tag{3.5}$$

A discrete-time model for the PAM system can be developed by setting

$$q(t) = p(t) \ * \ h(t) \ * \ r(t). \tag{3.6}$$

The equivalent discrete-time impulse response of the system is

$$q_k = q(t_0 + kT), \tag{3.7}$$

where t_0 is the sampling phase at the receiver. The sample with the highest amplitude is called the *cursor* sample. The preceding samples are called the precursor samples, while the following samples are called the postcursor samples. The sampling phase, t_0, is chosen to maximize the cursor sample, q_0. The estimate $\hat{a}_k$ is given by

$$\hat{a}_k = q_k \otimes a_k + z_k, \tag{3.8}$$

where $\otimes$ is discrete-time convolution, and

$$z_k = z(t) * r(t)|_{t=t_0+kT}$$

is zero-mean Gaussian noise.

The autocorrelation of z_k is calculated as

$$\begin{aligned} \mathbb{E}[z_k z_m^\star] &= \iint \mathbb{E}[z(\tau_1)z^\star(\tau_2)]\, r(t_0 + kT - \tau_1) r^\star(t_0 + mT - \tau_2)\, d\tau_1 d\tau_2, \\ &= \frac{N_0}{2} \int r(\tau) r^\star(\tau - (k-m)T)\, d\tau, \end{aligned} \tag{3.9}$$

where $\mathbb{E}$ is the expectation operator, and $\star$ denotes the complex conjugate. Therefore, the noise variance is given by

$$\sigma_z^2 = \frac{N_0}{2} \int |r(\tau)|^2\, d\tau,$$

which reduces to

$$\sigma_z^2 = \frac{N_0}{2}$$

when $r(t)$ is a unit-energy pulse. Without loss of generality, the receive filter, $r(t)$, is restricted to be unit-energy throughout this chapter so that the noise variance at the sampler output is $N_0/2$. If the right-hand side of (3.9) vanishes for all $k \neq m$, then $r(t)$ is called a *square-root Nyquist pulse*, and z_k is white noise with autocorrelation function $\sigma_z^2\,\delta_k$, where δ_k is the Kronecker delta.

Rectangular pulse-amplitude modulation (Rect-PAM) is defined as a PAM system where both $p(t)$ and $r(t)$ are rectangular pulses of width T, i.e.,

$$\text{Rect-PAM} \quad : \quad p(t) = \frac{1}{T}\,\mathrm{rect}\left(\frac{t}{T}\right), \tag{3.10a}$$

$$r(t) = \frac{1}{\sqrt{T}}\,\mathrm{rect}\left(\frac{t}{T}\right), \tag{3.10b}$$

where

$$\mathrm{rect}(x) = \begin{cases} 1 & : \quad |x| < 1/2 \\ 0 & : \quad \text{otherwise.} \end{cases}$$

Rectangular on-off keying (Rect-OOK) is a special case of Rect-PAM when a_k is uniformly distributed over $\{0, 2\mu_a\}$. Rectangular pulse-position modulation (Rect-PPM) is coded Rect-OOK in which each symbol is divided into L sub-intervals, termed *chips*, such that one of the L chips is on, and $L-1$ chips are off. A total of $\log_2(L)$ bits per symbol are used to select the location of the on chip. A PPM system that uses L chips per symbol is denoted by L-PPM. The detection of PAM signals requires the knowledge of detection thresholds that are channel dependent as mentioned in Appendix A. On the other hand, the detection of PPM signals requires no knowledge of such thresholds since the detected symbol is that corresponding to the chip of highest amplitude. The detection of PAM and PPM signals over dispersive channels is discussed in Appendices A and B, along with the corresponding error probabilities.

The relationship between the optical output power of an LD (or LED) and its electrical input current is ideally linear. However, because these devices are sensitive to temperature, this relationship is partially nonlinear [169, Sec. 6.2]. Such nonlinearity makes it difficult to accurately convert the electrical transmit pulse, $p(t)$, from the electrical to the optical domain. Rect-OOK and Rect-PPM are conventional scenarios used in previous studies [6,61,64,73], where the linearity of the optoelectronic transmitter is not a sensitive issue as the transmitter is only turned on/off during transmission.

PPM increases the peak-to-average ratio of the modulated optical signal. That is, it increases the electrical energy for a given average, which enhances the SNR at a cost of additional bandwidth. For wide bandwidth channels, PPM outperforms PAM while the performance of PPM degrades quickly as the channel becomes more dispersive [73]. Thus, there exists a fundamental tradeoff in the modulation design for optical wireless channels between power efficiency and immunity to channel dispersion [9]. To reduce the degradation of PPM performance at higher delay spreads, maximum likelihood sequence detection (MLSD) and decision feedback equalization (DFE) have been employed at a cost of higher complexity receivers [73–76].

In order to compare different PAM systems, we define the gain in average optical power of the PAM system as

$$\gamma = \frac{\mathcal{P}_{\mathsf{Rect}}}{\mathcal{P}_t}, \tag{3.11}$$

where $\mathcal{P}_t$ and $\mathcal{P}_{\mathsf{Rect}}$ are the average optical powers of the system under consideration and Rect-PAM system, respectively. Both systems are operating at the same BER and bit-rate, and are transmitting the same sequence $\{a_k\}$ over the same optical channel $h(t)$. The optical power gain, in optical decibels, is given by $10\log(\gamma)$ dBo. Since the emitted optical power is proportional to the laser diode driving current, therefore the electrical power gain, in electrical decibels, is given by $20\log(\gamma)$ dB. That is, an optical power gain of 1 dBo is equivalent to an electrical power gain of 2 dB.

Despite the fact that many bandlimited pulses outperform rectangular pulses over inter-symbol interference (ISI) channels, many such pulses cannot be used over optical intensity channels due to the fact that they do not satisfy the non-negativity constraint (3.3), such as sinc pulses, root-raised-cosine pulses, and many others [26,170]. However, for the sake of comparison, define a Sinc-PAM system as

$$\begin{aligned} \text{Sinc-PAM} \quad : \quad p(t) &= \frac{1}{T}\,\mathrm{sinc}\left(\frac{t}{T}\right), \\ r(t) &= \frac{1}{\sqrt{T}}\,\mathrm{sinc}\left(\frac{t}{T}\right), \end{aligned}$$

where

$$\mathrm{sinc}(x) = \frac{\sin(\pi x)}{\pi x}.$$

In the following section, OIM is proposed to enable the use of arbitrary pulse shapes over optical intensity channels, and thus approaches the ISI immunity of bandlimited pulse shapes, such as Sinc-PAM, while satisfying (2.9) and (2.10).

3.3 Optical Impulse Modulation

The fact that the optical spectrum is unregulated and the availability of very fast laser diodes provide the potential for high pulse rates [9, Sec. 2.2.1]. These rates are not supported by the lowpass diffuse optical channel which typically has a 3-dB bandwidth of tens of MHz [6, 61]. Previous techniques reduced symbol rates or employed complicated equalizers in order to avoid severe multipath penalties [74, 82]. An insight of this work is that the extra degrees of freedom available at the transmitter due to high-speed modulators can be exploited to mitigate the channel amplitude constraints. One way of doing this is by using a set of reserved high-frequency carriers in a multiple-subcarrier modulated wireless optical system [171, 172]. In this section, OIM is presented as an alternative approach of achieving the same goal for optical intensity PAM and PPM systems [155–157].

PPM has a qualitatively higher power efficiency than PAM that results from transmitting narrower pulses which concentrates the optical power in smaller time slots. However, this is the same reason why PPM has a lower immunity to channel dispersion. The idea behind OIM is to achieve a compromise between the dispersion immunity of PAM and the power efficiency of PPM. This is done by transmitting narrow pulses which approximate Dirac impulses on the limit. That is, the transmitted sequence of symbols is essentially a modulated impulse train, and hence OIM is power efficient since the impulses concentrate the power in very narrow time intervals. Despite the fact that the transmitted impulse train is wideband, its spectrum is periodic and the transmitted data can be recovered by knowledge of only the lowpass region of the transmitted spectrum, and hence OIM is also immune to channel dispersion.

3.3.1 OIM Definition

Optical impulse modulation is optical intensity PAM in which the transmit pulse shape approximates an impulse. To conceptualize OIM, consider a PAM system with pulse shape $p(t) = b(t)$ and receive filter $r(t) = g(t)$ as shown in Fig. 3.2. As in Sec. 3.2, assume that $g(t)$ is unit-energy and $\int b(t)\,dt = 1$ so that $\mathcal{P}_t = \mu_a/T$. The equivalent system impulse response can be factored as follows

$$\begin{aligned} q_{\mathsf{PAM}}(t) &= \underbrace{b(t)}_{p(t)} * h(t) * \underbrace{g(t)}_{r(t)} \\ &= \delta(t) * b(t) * h(t) * g(t), \end{aligned}$$

where $\delta(t)$ is the Dirac delta function. From the commutativity of the convolution operator, the filter $b(t)$ can be moved from the transmitter side to the receiver side without affecting the combined channel impulse response to give

$$q_{\mathsf{PAM}}(t) = \underbrace{\delta(t)}_{p(t)} * h(t) * \underbrace{b(t) * g(t)}_{r(t)}.$$

That is, $b(t)$ is pushed beyond the non-negative optical intensity channel into the receiver. As a result, the non-negativity constraint (3.3) on $b(t)$ is relaxed, while the non-negativity constraint (3.2) on the transmitted sequence $\{a_k\}$ remains. Notice also that $\mathcal{P}_t$ is unaffected by moving $b(t)$ since $\int \delta(t)\,dt = 1$.

Although the signal path is unaffected by moving $b(t)$, the noise at the output of the receiver is changed. In order to have the same noise variance at the output of the

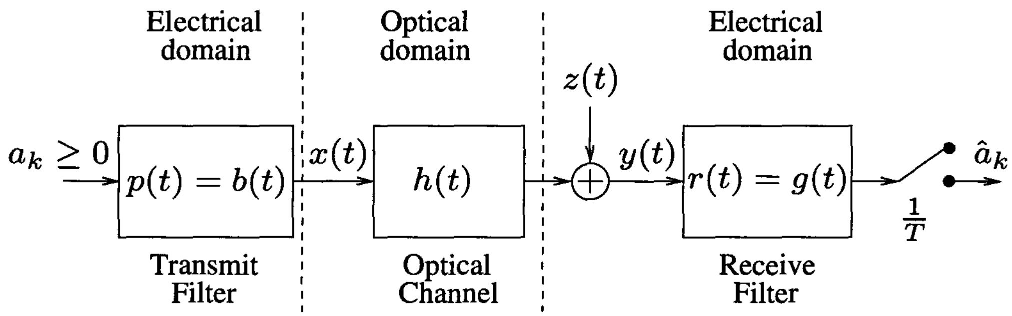

Figure 3.2: Block diagram of an optical intensity PAM communication system.

sampler as in Fig. 3.2, define

$$bg(t) = \kappa\, b(t) * g(t)$$

as the combined receive filter due to $b(t)$ and $g(t)$, and κ is a normalization factor such that $bg(t)$ is unit-energy. The equivalent OIM system is presented in Fig. 3.3, and the equivalent system impulse response can be written as

$$q_{\mathsf{OIM}}(t) = \underbrace{\delta(t)}_{p(t)} * h(t) * \underbrace{bg(t)}_{r(t)}.$$

Notice, that the noise variance at the output is the same in both Figs. 3.2 and 3.3, and that the only difference between $q_{\mathsf{PAM}}(t)$ and $q_{\mathsf{OIM}}(t)$ is the scaling factor κ. Therefore, if $\kappa > 1$, then OIM exhibits an optical power gain of $10\log(\kappa)$ over the corresponding optical PAM system. That is, OIM not only relaxes the non-negativity constraint on $b(t)$, but is also capable of achieving an average power gain. Notice, however, that the parameter κ is used only in this section to show how OIM is conceptually developed, while in practical designs, as in Sec. 3.4.2, the filter $bg(t)$ is jointly designed without factoring it to $b(t) * g(t)$.

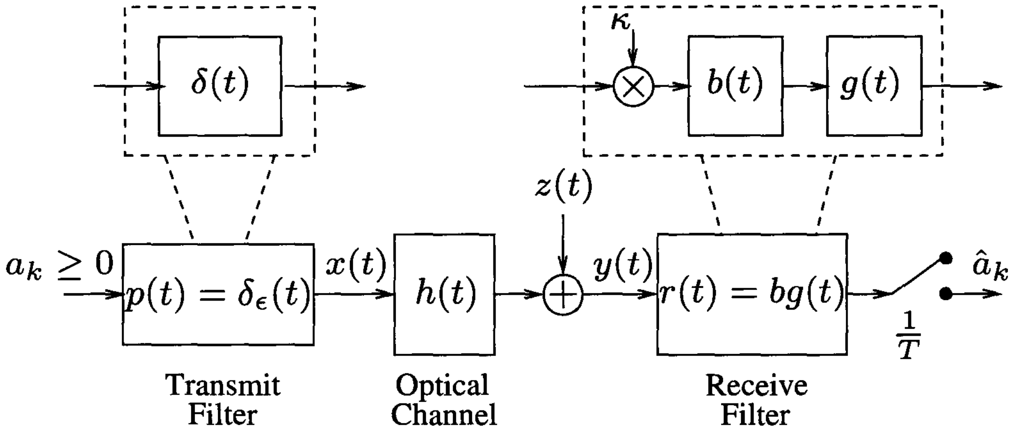

Figure 3.3: Block diagram of an OIM communication system.

The OIM transmitted signal is given by substituting $\delta(t)$ for $p(t)$ in (3.1) to get

$$x(t) = \sum_k a_k\, \delta(t - kT),$$

which is equivalent to transmitting an impulse train sampled version of a lowpass bandlimited PAM signal. Thus, the combination $h(t) * bg(t)$ can be viewed as an interpolating filter for the transmitted samples. Notice that, in this case, the OIM receiver design is independent of the transmitter, and is equivalent to picking the interpolating filter that gives the highest optical power gain.

The PSD of the transmitted signal in (3.1) is given by

$$\Phi_{\mathsf{PAM}}(f) = |\mathscr{P}(f)|^2 \left[\frac{\sigma_a^2}{T} + \frac{\mu_a^2}{T^2} \sum_{m=-\infty}^{\infty} \delta\left(f - \frac{m}{T}\right)\right] \tag{3.13}$$

where $\mathscr{P}(f)$ is the Fourier transform of $p(t)$, σ_a^2 is the variance of $\{a_k\}$, and the $\{a_k\}$ are assumed to be independent and identically distributed [170, Sec. 4.4]. Substituting $\frac{1}{T}\text{rect}(\frac{t}{T})$, $\frac{1}{T}\text{sinc}(\frac{t}{T})$ and $\delta(t)$ for $p(t)$, the PSDs for Rect-PAM, Sinc-PAM and OIM, respectively, can be obtained,

$$\Phi_{\mathsf{Rect}}(f) = \frac{\sigma_a^2}{T}\mathrm{sinc}^2(Tf) + \frac{\mu_a^2}{T^2}\delta(f), \tag{3.14a}$$

$$\Phi_{\mathsf{Sinc}}(f) = \frac{\sigma_a^2}{T}\mathrm{rect}(Tf) + \frac{\mu_a^2}{T^2}\delta(f), \tag{3.14b}$$

$$\Phi_{\mathsf{OIM}}(f) = \frac{\sigma_a^2}{T} + \frac{\mu_a^2}{T^2}\sum_{m=-\infty}^{\infty}\delta\left(f - \frac{m}{T}\right). \tag{3.14c}$$

These PSDs are plotted in Fig. 3.4, along with sample time-domain waveforms. In light of (3.4), the transmitted average optical power is the same for all three schemes due to the same value of $\bar{p}$.

Comparing the PSDs of Rect-PAM and Sinc-PAM in Figs. 3.4(a) and 3.4(c), Sinc-PAM shows better ISI immunity due to its bandlimited spectrum. However, Sinc-PAM cannot be applied to optical IM/DD channels due to the fact that its pulse shape does not satisfy the constraint (3.3), and consequently its time-domain signal does not satisfy the channel non-negativity constraint (2.9) as shown in Fig. 3.4(d). The PSD of OIM, shown in Fig. 3.4(e), is a $1/T$ frequency repetition of the bandlimited PSD of Sinc-PAM. This is evident by comparing (3.14b) and (3.14c), or by comparing Figs. 3.4(c) and 3.4(e). That is, OIM uses the high-frequency spectral regions supported by the high-speed transmitter to satisfy the channel non-negativity constraint, while at the same time the transmitted data are confined to the low-frequency spectral regions supported by the lowpass channel. Therefore, OIM is as immune to ISI as Sinc-PAM, and at the same time satisfies the channel non-negativity constraint. It should also be noted that the OIM signal in Fig. 3.4(f) is an impulse train sampling of the Rect-PAM signal in Fig. 3.4(b) or the Sinc-PAM signal in Fig. 3.4(d). Therefore, the OIM PSD in Fig. 3.4(e) is a $1/T$ frequency repetition of the Rect-PAM PSD in

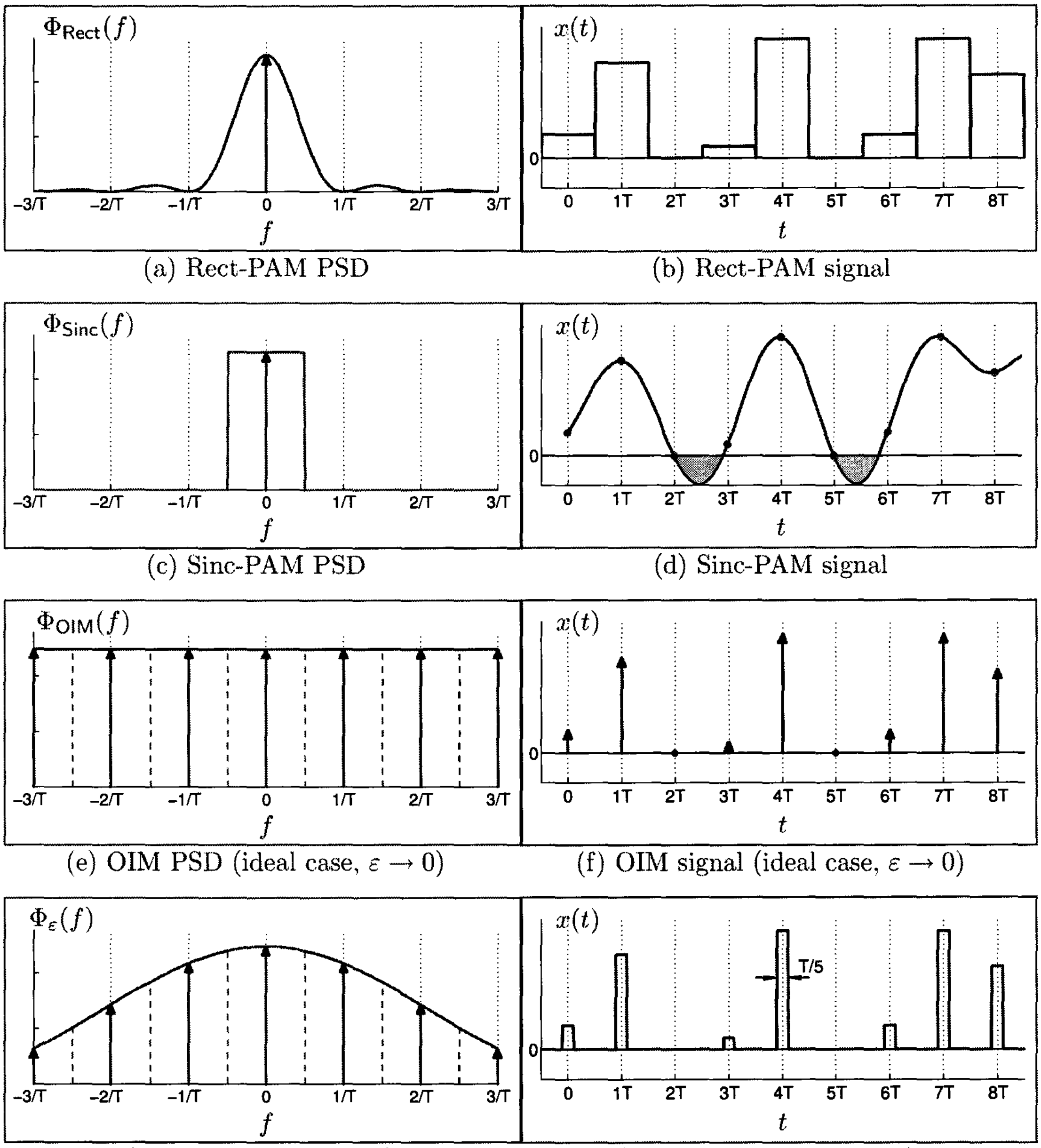

(a) Rect-PAM PSD

(b) Rect-PAM signal

(c) Sinc-PAM PSD

(d) Sinc-PAM signal

(e) OIM PSD (ideal case, $\varepsilon \rightarrow 0$)

(f) OIM signal (ideal case, $\varepsilon \rightarrow 0$)

(g) OIM PSD for $\varepsilon = 1/5$

(h) OIM signal for $\varepsilon = 1/5$

Figure 3.4: The PSDs for Rect-PAM, Sinc-PAM and OIM, along with sample time-domain waveforms. The vertical arrows represent Dirac impulses. The pulses amplitudes, in time domain, are selected randomly and independently since, in general, the sequence $\{a_k\}$ need not be constrained to a finite set of PAM levels.

Fig. 3.4(a) or the Sinc-PAM PSD in Fig. 3.4(c).

Generating an arbitrary optical pulse $b(t)$, in case of the conventional PAM system of Fig. 3.2, is difficult due to the nonlinearity of the optoelectronic transmitter (i.e., LD or LED). On the other hand, implementing an arbitrary filter $bg(t)$ in case of the OIM system of Fig. 3.3 is done in the electrical domain at the receiver, and hence is not affected by the transmitter nonlinearity. Therefore, OIM simplifies the optical pulse generation process in addition to the relaxation of the non-negativity constraint (3.3) on $b(t)$ and the possibility of achieving an optical power gain in case $\kappa > 1$ as mentioned before. Moreover, the PSD of OIM includes discrete frequency components at the symbol rate, $1/T$, and its harmonics. This is indicated by the Dirac impulse train given by the second term of (3.14c) and shown in Fig. 3.4(e). Such discrete frequency components can be used at the receiver for symbol timing recovery.

3.3.2 Practical OIM Implementation

Practically, it is impossible to use a Dirac impulse as the transmit filter. Therefore, this impulse can be approximated by any narrow pulse $\delta_\varepsilon(t)$. For example, it can be approximated by a rectangular pulse of the form

$$\delta_\varepsilon(t) = \frac{1}{\varepsilon T} \operatorname{rect}\left(\frac{t}{\varepsilon T}\right), \tag{3.15}$$

as shown in Fig. 3.3, where $\varepsilon \in (0, 1]$ is the pulse duty cycle. Notice that a rectangular shape for $\delta_\varepsilon(t)$ is not required. In fact, the specific pulse shape is immaterial as long as it is non-negative, i.e. satisfies the channel constraints, and is wideband. This gives greater flexibility in the implementation of the transmit filter, and hence the system performance is no longer sensitive to the transmitter nonlinearity. The degradation of the performance due to this approximation is mild and is quantified in Sec. 3.5.

The PSD of the practical OIM implementation is obtained from (3.13) by replacing $\mathscr{P}(f)$ by $\Delta_\varepsilon(f)$,

$$\Phi_\varepsilon(f) = |\Delta_\varepsilon(f)|^2 \left[\frac{\sigma_a^2}{T} + \frac{\mu_a^2}{T^2}\sum_m \delta\left(f - \frac{m}{T}\right)\right], \tag{3.16}$$

where $\Delta_\varepsilon(f)$ is the Fourier transform of $\delta_\varepsilon(t)$. That is, the ideal spectrum of (3.14c) is shaped by $|\Delta_\varepsilon(f)|^2$. The PSD and a sample time-domain waveform are shown in Figs. 3.4(g) and 3.4(h) for $\varepsilon = 0.2$ and $\delta_\varepsilon(t)$ as in (3.15), i.e., $|\Delta_\varepsilon(f)|^2 = \text{sinc}^2(\varepsilon T f)$. The time-domain waveform is similar to that of Rect-PAM, except that the pulse width is reduced by the ratio $\varepsilon = 0.2$. As ε decreases, $|\Delta_\varepsilon(f)|^2$ becomes flatter and the distortion in the lowpass data bearing spectrum is small allowing for recovery using a simple lowpass filter.

OIM is suitable for optical wireless communications because there exists a huge amount of unregulated bandwidth. Higher frequency bands, that are used to satisfy the channel amplitude constraint, do not affect the transmitted average optical power. OIM is relatively immune to multipath since data are confined to the lowpass region of the optical spectrum. Moreover, linearity of the optical transmitter is not a severe constraint. Conceptually, OIM is analogous to ultra-wide band communications in RF systems, however, significant differences exist in the channel models employed, power constraints, and non-negativity amplitude constraints [173].

OIM can also be regarded as a return-to-zero PAM scheme with low duty cycle. However, the OIM receiver designed in Sec. 3.4 is fundamentally different than conventional receivers used with return-to-zero PAM systems. In this sense, OIM can be described as a novel detection rather than modulation scheme.

3.4 OIM Receiver Design

OIM refers to the transmission of data by modulating the amplitudes of a train of optical impulses. In this section, the problem of detecting these amplitudes is considered. As in Sec. 3.2, the receive filter, $bg(t)$, is normalized to have unit energy in order to have the same noise power at the sampler output as previous techniques. The optimal receiver depends on $h(t)$ and is presented in Sec.3.4.1. The complexity of this receiver is high and depends on the channel impulse response. As a result, a different receiver is required whenever the channel delay spread changes. To overcome these difficulties, a novel simple receiver is designed in Sec. 3.4.2. This suboptimal receiver is independent of $h(t)$ and is shown in Sec. 3.5 to approach the performance of the optimal receiver at high channel delay spreads.

3.4.1 Whitened Matched Filter Receiver

The optimal front-end receive filter is one that is matched to the received pulse, i.e. $bg(t) = \kappa\, \delta_\varepsilon(-t) * h(-t)$. That is, $h(t)$ must be known at the receiver. The matched filter is followed by a digital precursor equalizer to whiten the noise. The cascade of the two filters is termed a whitened matched filter (WMF). Moreover, a DFE can also be applied to remove postcursor ISI [26].

For high delay spreads, $h(t)$ is much wider in time than $\delta_\varepsilon(t)$, and the front-end filter is nearly matched to the channel impulse response, $h(t)$. Matched filtering is practical in this case as the received pulse is lowpass.

For low delay spreads, both pulses $h(t)$ and $\delta_\varepsilon(t)$ are narrow, and so is the received pulse. In this case, matched filtering is quite difficult to implement in practice due to the wide bandwidth and sensitivity to timing errors.

Notice also that for each channel delay spread, different WMFs and DFEs are required because $bg(t)$ is a function of $h(t)$. Due to these difficulties, a simple receiver filter, which is independent of channel delay spread, is designed in Sec. 3.4.2.

Power Gain at Zero Delay Spread

At zero delay spread, $h(t) = H_0\delta(t)$. In this case, the front-end filter is matched to $\delta_\varepsilon(t)$. That is, the unit-energy receive filter is given by $bg(t) = \frac{1}{\sqrt{\varepsilon T}}\text{rect}\left(\frac{t}{\varepsilon T}\right)$. In this case, the equivalent discrete-time impulse response (3.7) reduces to $q_k = \frac{H_0}{\sqrt{\varepsilon T}}\,\delta_k$, which is obtained by substituting in (3.6). Therefore, the OIM system reduces to

$$\hat{a}_k = \frac{H_0}{\sqrt{\varepsilon T}} \cdot a_k + z_k,$$

at zero delay spread. Similarly, the Rect-PAM system reduces to

$$\hat{a}_k = \frac{H_0}{\sqrt{T}} \cdot a_k + z_k,$$

at zero delay spread. Therefore, OIM achieves an average optical power gain of

$$\gamma = \frac{1}{\sqrt{\varepsilon}} \tag{3.17}$$

using the definition in (3.11). This gain increases unboundedly as ε decreases, however, achieving this gain is impractical for small values of ε due to the wide bandwidth and timing accuracy required.

3.4.2 Double-Jump Receiver

The WMF is complex and requires channel knowledge at the receiver. Moreover, at low delay spreads and small values of ε, the received pulse is wideband, and hence matched filtering is impractical. In this section, a simpler receiver that requires no channel information is designed.

As given by equation (3.16) and shown in Fig. 3.4(g), the OIM spectrum is wideband. For high channel delay spreads, the received spectrum is a lowpass filtered version of the OIM spectrum, and consequently using a wideband receiver is not necessary. For low channel delay spreads, the received spectrum is wideband, but it is practically difficult to match the receiver front-end filter to this wideband spectrum. Moreover, the useful information is confined to the lowpass region of the OIM spectrum as shown in Fig. 3.4(g). Therefore, in this section, we restrict our attention to lowpass receiver filters that are independent of the channel impulse response. Specifically, the OIM receive filter $bg(t)$ is chosen to be a bandlimited unit-energy filter with excess bandwidth α, i.e. the support set of the filter frequency response is $|f| \leq (1+\alpha)/2T$, where $0 \leq \alpha \leq 1$.

For the purpose of design, the spectrum of the received pulse, $\Delta_\varepsilon(f)H(f)$, is assumed to be flat within the range $|f| \leq (1+\alpha)/2T$, where $H(f)$ is the Fourier transform of $h(t)$ as defined in Sec. 2.2. That is, $\Delta_\varepsilon(f)H(f) = H_0$ for $|f| \leq (1+\alpha)/2T$, where H_0 is the channel DC-gain defined in (2.6), and $\Delta_\varepsilon(0) = \int \delta_\varepsilon(t)\,dt = 1$. This is a reasonable assumption as $H(f)$ is typically lowpass and $\Delta_\varepsilon(f)$ is a wideband pulse. The impact of non-flat frequency response in the lowpass region is quantified in the simulation results presented in Sec. 3.5. Additionally, in order to eliminate ISI, the filter $bg(t)$ is chosen to satisfy the Nyquist criterion. As a result, the equivalent discrete-time impulse response q_k is zero for $k \neq 0$, and the discrete-time system model (3.8) reduces to

$$\hat{a}_k = H_0 \cdot bg(0) \cdot a_k + z_k, \tag{3.18}$$

where $bg(0)$ is the filter cursor. Therefore, a sensible design procedure is to find the bandlimited unit-energy Nyquist receive filter that maximizes the cursor $bg(0)$. Notice that the OIM receiver $bg(t)$ is designed independently of the non-negativity constraint and can be changed from one unit-energy Nyquist pulse to another without the need to feedback any information to the transmitter.

Consider a general bandlimited Nyquist pulse with excess bandwidth α written in the frequency domain as [174, 175]

$$BG(f) = \begin{cases} \beta T\left[1 - \mathcal{Q}\left(\frac{1+\alpha}{2T} + f\right)\right], & -\frac{1+\alpha}{2T} \leq f < -\frac{1}{2T} \\ \beta T\, \mathcal{Q}^{\star}\left(-f - \frac{1-\alpha}{2T}\right), & -\frac{1}{2T} \leq f \leq -\frac{1-\alpha}{2T} \\ \beta T, & -\frac{1-\alpha}{2T} < f < \frac{1-\alpha}{2T} \\ \beta T\, \mathcal{Q}\left(f - \frac{1-\alpha}{2T}\right), & \frac{1-\alpha}{2T} \leq f \leq \frac{1}{2T} \\ \beta T\left[1 - \mathcal{Q}^{\star}\left(\frac{1+\alpha}{2T} - f\right)\right], & \frac{1}{2T} < f \leq \frac{1+\alpha}{2T} \\ 0, & \text{otherwise,} \end{cases}$$

where $\mathcal{Q}(f)$ is a function satisfying $\mathcal{Q}(0) = 1$ with support on $[0, \frac{\alpha}{2T}]$, and β is the filter cursor given by

$$bg(0) = \int_{-\infty}^{\infty} BG(f)\, df = \beta.$$

Notice that $BG(-f) = BG^{\star}(f)$, thus $bg(t)$ is real. The energy of $bg(t)$ is given by

$$\begin{aligned}\mathcal{E}_{bg} &= \int_{-\infty}^{\infty} |BG(f)|^2 \, df \\ &= \beta^2 T + 4\beta^2 T^2 \int_0^{\alpha/(2T)} \Big(|\mathcal{Q}(f)|^2 - \Re\{\mathcal{Q}(f)\} \Big) \, df,\end{aligned}$$

where $\Re\{\cdot\}$ is the real-part operator. Therefore, the optimal filter can be found by solving the optimization problem

$$\begin{aligned}&\max_{\mathcal{Q}} \quad \beta \\ &s.t. \quad \mathcal{E}_{bg} = 1.\end{aligned}$$

Solving the constraint for $1/\beta^2$, we get

$$\frac{1}{\beta^2} = T + 4T^2 \int_0^{\alpha/(2T)} \Big(|\mathcal{Q}(f)|^2 - \Re\{\mathcal{Q}(f)\} \Big) \, df, \tag{3.19}$$

and therefore the optimization problem reduces to

$$\min_{\mathcal{Q}} \int_0^{\alpha/(2T)} \Big(|\mathcal{Q}(f)|^2 - \Re\{\mathcal{Q}(f)\} \Big) \, df.$$

Since $|\mathcal{Q}(f)|^2 = \Re\{\mathcal{Q}(f)\}^2 + \Im\{\mathcal{Q}(f)\}^2$ where $\Im\{\cdot\}$ is the imaginary-part operator, and both the real and imaginary parts of $\mathcal{Q}(f)$ are optimized independently, then $\Im\{\mathcal{Q}(f)\} = 0$, and the optimization problem reduces to

$$\min_{\mathcal{Q}} \int_0^{\alpha/(2T)} \Big(\mathcal{Q}(f)^2 - \mathcal{Q}(f) \Big) \, df,$$

where $\mathcal{Q}(f)$ is a real function. Define the integral

$$\mathcal{I}(\mathcal{Q}) = \int_0^{\alpha/(2T)} \Psi(\mathcal{Q}(f))\, df,$$

where $\Psi(\mathcal{Q}) = \mathcal{Q}^2 - \mathcal{Q}$. Therefore the optimization problem is given by

$$\min_{\mathcal{Q}} \quad \mathcal{I}(\mathcal{Q}).$$

Notice that the requirement that $\mathcal{Q}(0) = 1$ is immaterial in evaluating the integral $\mathcal{I}(\mathcal{Q})$.

The problem is solved by calculus of variations where $\mathcal{Q}(f)$ is written as $\mathcal{Q}(f) = \tilde{\mathcal{Q}}(f) + \epsilon\,\eta(f)$, where $\tilde{\mathcal{Q}}(f)$ is the optimal solution and $\eta(f)$ is an arbitrary trajectory [176]. Therefore,

$$\mathcal{I}(\tilde{\mathcal{Q}} + \epsilon\,\eta) = \int_0^{\alpha/(2T)} \Psi(\tilde{\mathcal{Q}}(f) + \epsilon\,\eta(f))\, df.$$

If $\tilde{\mathcal{Q}}$ minimizes $\mathcal{I}(\mathcal{Q})$, then $\mathcal{I}(\tilde{\mathcal{Q}}+\epsilon\,\eta)$ must have a minimum at $\epsilon = 0$ for all trajectories $\eta(f)$. That is

$$V_{\mathcal{I}} = \left.\frac{d\mathcal{I}}{d\epsilon}\right|_{\epsilon=0} = 0,$$

where $V_{\mathcal{I}}$ is the first variation of the integral $\mathcal{I}$ along $\tilde{\mathcal{Q}}(f)$ [176]. Therefore,

$$\begin{aligned} V_{\mathcal{I}} &= \left.\int_0^{\alpha/(2T)} \frac{d\Psi}{d\mathcal{Q}}\frac{d\mathcal{Q}}{d\epsilon}\, df\right|_{\epsilon=0} \\ &= \int_0^{\alpha/(2T)} (2\tilde{\mathcal{Q}}(f) - 1)\,\eta(f)\, df \end{aligned}$$

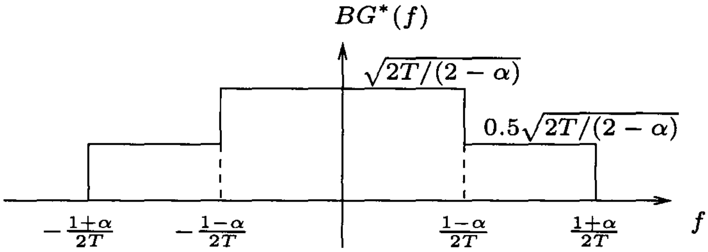

Figure 3.5: The double-jump pulse.

For $V_{\mathcal{I}}$ to vanish for all $\eta(f)$, we must have $(2\tilde{\mathcal{Q}}(f) - 1) = 0$ which yields

$$\tilde{\mathcal{Q}}(f) = \frac{1}{2}, \quad f \in \left(0, \frac{\alpha}{2T}\right].$$

Substituting by $\tilde{\mathcal{Q}}(f)$ into (3.19) yields the optimal filter cursor:

$$\tilde{bg}(0) = \beta = \frac{1}{\sqrt{T}}\sqrt{\frac{2}{2-\alpha}}. \tag{3.20}$$

As a result, the optimal receive filter is given by

$$\tilde{BG}(f) = \begin{cases} \sqrt{2T/(2-\alpha)} & 0 \quad \leq |f| < \frac{1-\alpha}{2T} \\ \frac{1}{2}\sqrt{2T/(2-\alpha)} & \frac{1-\alpha}{2T} \leq |f| \leq \frac{1+\alpha}{2T} \\ 0 & \text{otherwise,} \end{cases} \tag{3.21}$$

which is the unit-energy double-jump pulse shown in Fig. 3.5. In fact, the double-jump pulse was developed independently by Franks in 1968 when he showed that, in addition to satisfying the Nyquist criterion, it introduces minimal interference for small carrier phase errors at the receiver [177].

Power Gain at Zero Delay Spread

At zero delay spread, the channel impulse response is $h(t) = H_0\delta(t)$. Substituting this $h(t)$ and (3.10) into (3.6), the Rect-PAM equivalent discrete-time impulse response (3.7) reduces to $q_k = \frac{H_0}{\sqrt{T}}\,\delta_k$. Therefore, the Rect-PAM system reduces to

$$\hat{a}_k = \frac{H_0}{\sqrt{T}} \cdot a_k + z_k, \tag{3.22}$$

at zero delay spread. Whereas, the OIM system, with double-jump receiver and $\varepsilon \to 0$, reduces to

$$\hat{a}_k = \frac{H_0}{\sqrt{T}}\sqrt{\frac{2}{2-\alpha}} \cdot a_k + z_k,$$

by substituting from (3.20) in (3.18). Consequently, for a flat channel, the gain in average optical power, defined in (3.11), of OIM over Rect-PAM is given by

$$\gamma = \sqrt{\frac{2}{2-\alpha}} \tag{3.23}$$

Notice that this gain is increasing in α and reaches a maximum of 1.5 dBo at $\alpha = 1$. Moreover, this gain is shown to increase at higher delay spreads in Sec. 3.5, which is justified by the high ISI immunity of OIM when compared to Rect-PAM.

3.5 Numerical Results

In this section, the exponential functional model (2.8) is used to simulate the impulse response of indoor diffuse wireless optical channels. This functional form will be used to predict the power requirements and the information rates of such multipath communication systems in Sections 3.5.1 and 3.5.3. The equivalent impulse response,

$q(t)$, is computed by convolving the exponential functional model with the transmit and receive filters. The receiver sampling phase is computed by solving the problem, $t_0 = \arg\max_t q(t)$, numerically, and $q(t)$ is sampled to obtained the equivalent discrete-time impulse response $q_k = q(t_0 + kT)$.

3.5.1 Average Optical Power Requirements

The BER calculation for L-PAM systems over dispersive ISI channels is presented in Appendix A. In order to compare the average optical power requirements for different PAM systems, the BER is fixed at 10^{-6}, and the value of $\mathcal{P}_t$ that is required to maintain this BER is calculated by solving (A.4) for $\mathcal{P}_t$. This is done by putting BER $= 10^{-6}$ in (A.4), and calculating the corresponding value of $\mathcal{P}_t$ by numerical optimization. As is conventional, $\mathcal{P}_t$ is normalized to the power, $\mathcal{P}_t^{\mathrm{OOK}}$, required by a Rect-OOK system, transmitting at the same bit-rate, to achieve the same BER over a flat channel with the same noise power [71, 73, 74]. As given by (A.5), $\mathcal{P}_t^{\mathrm{OOK}}$ is proportional to $\frac{\sigma_z}{H_0\sqrt{T_b}}$, where T_b is the bit duration. Therefore this normalization eliminates the dependence of the normalized power, $\mathcal{P}_t/\mathcal{P}_t^{\mathrm{OOK}}$, on the channel noise, channel DC-gain and bit-rate. In practice, however, the transmit power level is first defined according to eye and skin safety standards, as mentioned in Sec. 2.2, and the transmission bit-rate is then defined in terms of the transmit power level, the channel noise, the channel DC-gain and the required BER.

Fig. 3.6 presents a plot of the normalized optical power required to achieve BER of 10^{-6} versus the normalized channel delay spread, $\mathcal{D}/T_b$, for Rect-OOK and OIM-OOK with double-jump receiver. The results presented in the figure are for $\alpha = 0$ and $\alpha = 1$. Notice that for these values of α, the filter $bg(t)$ is a root-Nyquist filter

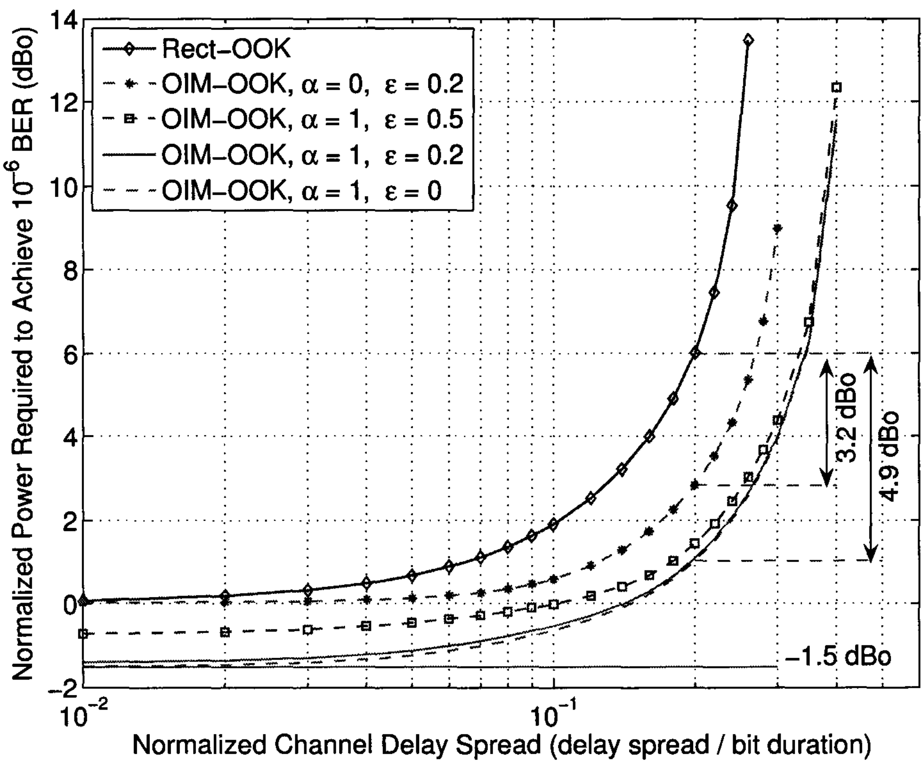

Figure 3.6: Normalized optical power, $10\log(\mathcal{P}_t/\mathcal{P}_t^{\text{OOK}})$, required by Rect-OOK and OIM-OOK with double-jump receiver to achieve BER=10^{-6}.

and hence the noise, z_k, at the sampler output is white. For other values of α, the noise is colored, and a whitening filter is required to improve the detection.

The effect of non-zero values of ε is quantified in Fig. 3.6 for OIM-OOK by taking $\varepsilon = 0, 0.2, 0.5$, where the curve at $\varepsilon = 0$ is simulated by using an impulse $\delta(t)$ instead of $\delta_\varepsilon(t)$. The optical power required at $\varepsilon = 0.2$ nearly coincides with that at $\varepsilon = 0$ over a wide range of delay spreads. Thus, a duty cycle of $\varepsilon = 0.2$ achieves nearly all of the gain and there is no need to use narrower pulses. For a typical indoor diffuse channel, the bandwidth is 10 to 40 MHz as mentioned in Sec. 2.2. Therefore, using $\varepsilon = 0.2$ implies a pulse rate from 50 to 200 MHz, which is far below the rates available in present day laser diodes.

The gain in optical power of OIM with double-jump receiver, given by (3.23), is evident in Fig. 3.6 as the delay spread approaches zero. Notice that the gain is higher at larger delay spreads. For instance, in Fig. 3.6 with $\alpha = 1$, the gain is approximately 1.5 dBo at zero delay spread as suggested by (3.23), and increases gradually as the channel delay spread increases. This is attributed to the fact that the useful information is confined to the lowpass region of the OIM spectrum as shown in Fig. 3.4(g), while the spectrum of Rect-PAM is wideband. Therefore, OIM shows better immunity to channel multipath dispersion. For example, at a normalized channel delay spread of 0.2, the gain of OIM-OOK over Rect-OOK is 3.2 dBo at $\alpha = 0$, and 4.9 dBo at $\alpha = 1$. It is clear that the gain at $\alpha = 1$ is higher than that at $\alpha = 0$. This can be attributed to the higher initial gain at zero delay spread, given by (3.23).

To produce the results in Fig. 3.6, the equivalent discrete-time impulse response (3.7) is computed numerically. Although q_k is defined for all integer values of k, it is truncated to a finite number of samples, $M + 1$, which constitutes the cursor sample, q_0, in addition to M samples that represent the channel impulse response tails as discussed in Appendix A. The samples that are ignored are those whose amplitudes are less than 0.5% of q_0 at the highest values of ε and $\mathcal{D}/T_b$ considered in the figure. At lower values of ε and $\mathcal{D}/T_b$, the ignored samples are less than this percentage since the impulse response decays faster.

Similar results are presented in Fig. 3.7 for 4-PAM. Since the summation in (A.4) is done over L^M different sequences, the complexity of computing the BER of L-PAM is proportional to L^M. Therefore, it is difficult to compute the BER in (A.4) for $L = 4$

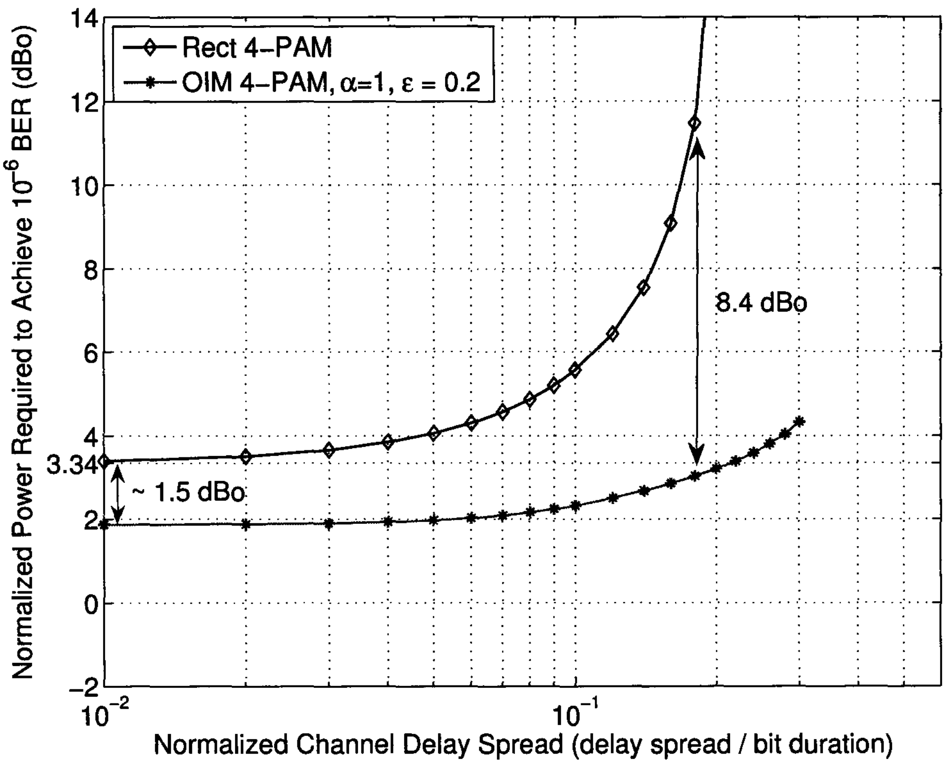

Figure 3.7: Normalized optical power, $10\log(\mathcal{P}_t/\mathcal{P}_t^{\mathrm{OOK}})$, required by Rect-PAM and OIM-PAM to achieve BER=10^{-6} at $L = 4$. For OIM, a double-jump receiver is used with $\alpha = 1$ and $\varepsilon = 0.2$.

at high delay spreads where high M is required. In Fig. 3.7, the power requirements are simulated up to $\mathcal{D}/T_b = 0.3$, where samples whose amplitudes are less than 0.5% of q_0 are ignored as mentioned before.

At zero delay spread, the normalized optical power of 4-PAM is 3.34 dBo, which is the value obtained from (A.6) at $L = 4$ and BER $= 10^{-6}$. This value and the initial ~1.5 dBo gain of OIM with double-jump receiver are evident in Fig. 3.7 as the delay spread approaches zero. The OIM gain increases as the delay spread increases. For instance, the gain is approximately 8.4 dBo at $\mathcal{D}/T_b = 0.18$, which is attributed to the fact that OIM has high immunity to channel multipath dispersion as mentioned before. Despite this high gain, it should be noticed that the performance, at $\mathcal{D}/T_b = 0.18$, of OIM-OOK in Fig. 3.6 is better than that of OIM 4-PAM in Fig. 3.7.

Fig. 3.8 presents a comparison of Rect-OOK and OIM-OOK when a WMF is employed as well as the case when a DFE is employed. At high delay spreads, the use of a WMF and DFE greatly improves the performance of both Rect-OOK and OIM-OOK. Notice that the performance of OIM-OOK with WMF and DFE remains better than a comparable Rect-OOK, however, the incremental gain in using the equalizer is less for OIM-OOK versus Rect-OOK. Notice also that the performance of equalized OIM-OOK is relatively insensitive to the choice of ε so long as it is chosen small enough, i.e., $\varepsilon \leq 0.2$.

As the channel delay spread tends to zero, the gain in optical power of OIM-OOK over Rect-OOK with matched receive filters is given by (3.17). The fact that the gain increases unboundedly as ε decreases is evident in Fig. 3.8. As mentioned earlier, despite this high gain at low delay spread, matched filtering to a narrow transmitted pulse is difficult to implement in practice. Thus, the use of a WMF for OIM-OOK is practical only at moderate to high delay spreads. In the case of a wide bandwidth channel, the OIM-OOK receiver can switch its front-end filter to the double-jump filter (3.21), without the need to feedback any information to the transmitter.

The gain in optical power over Rect-OOK is listed in Table 3.1 for different OOK schemes at a normalized channel delay spread of 0.2. The gain of OIM-OOK with double-jump receiver is slightly greater than that of Rect-OOK with WMF and DFE receiver.

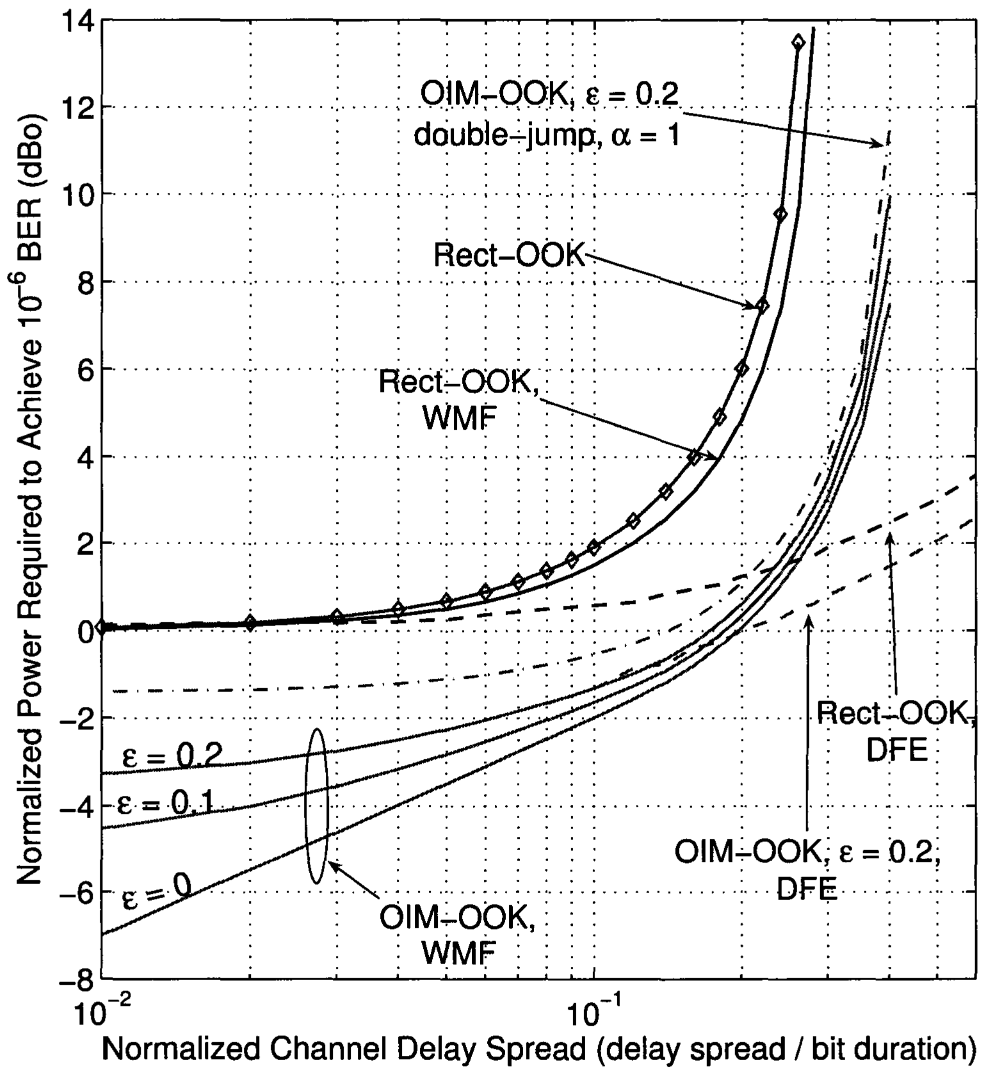

Figure 3.8: Normalized optical power, $10\log(\mathcal{P}_t/\mathcal{P}_t^{\mathrm{OOK}})$, required by Rect-OOK and OIM-OOK using WMF and DFE to achieve BER=10^{-6}.

Table 3.1: Optical power gain (dBo) over Rect-OOK at normalized delay spread $\mathcal{D}/T_b = 0.2$. For OIM, $\varepsilon = 0.2$ is used.

Rect-OOK			OIM-OOK		
—	WMF	DFE	double-jump ($\alpha = 1$)	WMF	DFE
0	1.14	4.76	4.92	5.4	5.99

That is, OIM with a single, simple lowpass receive filter provides better performance than the more complex receiver Rect-OOK with WMF and DFE. Notice that in addition to the lower complexity, a single double-jump receive filter is used for OIM for all delay spreads, while different WMFs and DFEs are required for each channel delay spread in the case of Rect-OOK.

In the case of PPM, inter- and intra-symbol interference exists between neighboring received PPM symbols and within the same symbol, respectively. The BER calculation for L-PPM systems over dispersive ISI channels is presented in Appendix B. OIM can be applied to PPM in the same way it was applied to PAM. The normalized optical power is plotted in Fig. 3.9 for Rect-PPM and OIM-PPM with double-jump receiver, and in Fig. 3.10 for WMF equalized PPM. At zero delay spread, the normalized powers for Rect-PPM at L = 4, 8 and 16 are -2.89, -5.15 and -7.17 dBo, respectively, which are the values obtained from (B.6) at BER = 10^{-6}. These values are evident in Fig. 3.9 as the delay spread approaches zero.

Similar optical power gains, to those achieved with PAM systems, are achieved by OIM-PPM in both the unequalized and WMF scenarios. This indicates that OIM is a general technique that can boost the performance of all PAM-based modulation schemes. For instance, as shown in Fig. 3.9 and suggested by (3.23), the average optical power gain of OIM-PPM with double-jump receiver ($\alpha = 1$) over Rect-PPM for the same L is about 1.5 dBo at zero delay spread. A DFE can also be applied to PPM at the chip-rate or the symbol-rate. The performance of these DFE systems is not examined in this chapter due to the increased difficulty of its numerical simulation, and the fact that it is not key to the current discussion. The interested reader may refer to [74], where the performance of these DFE systems is examined on measured

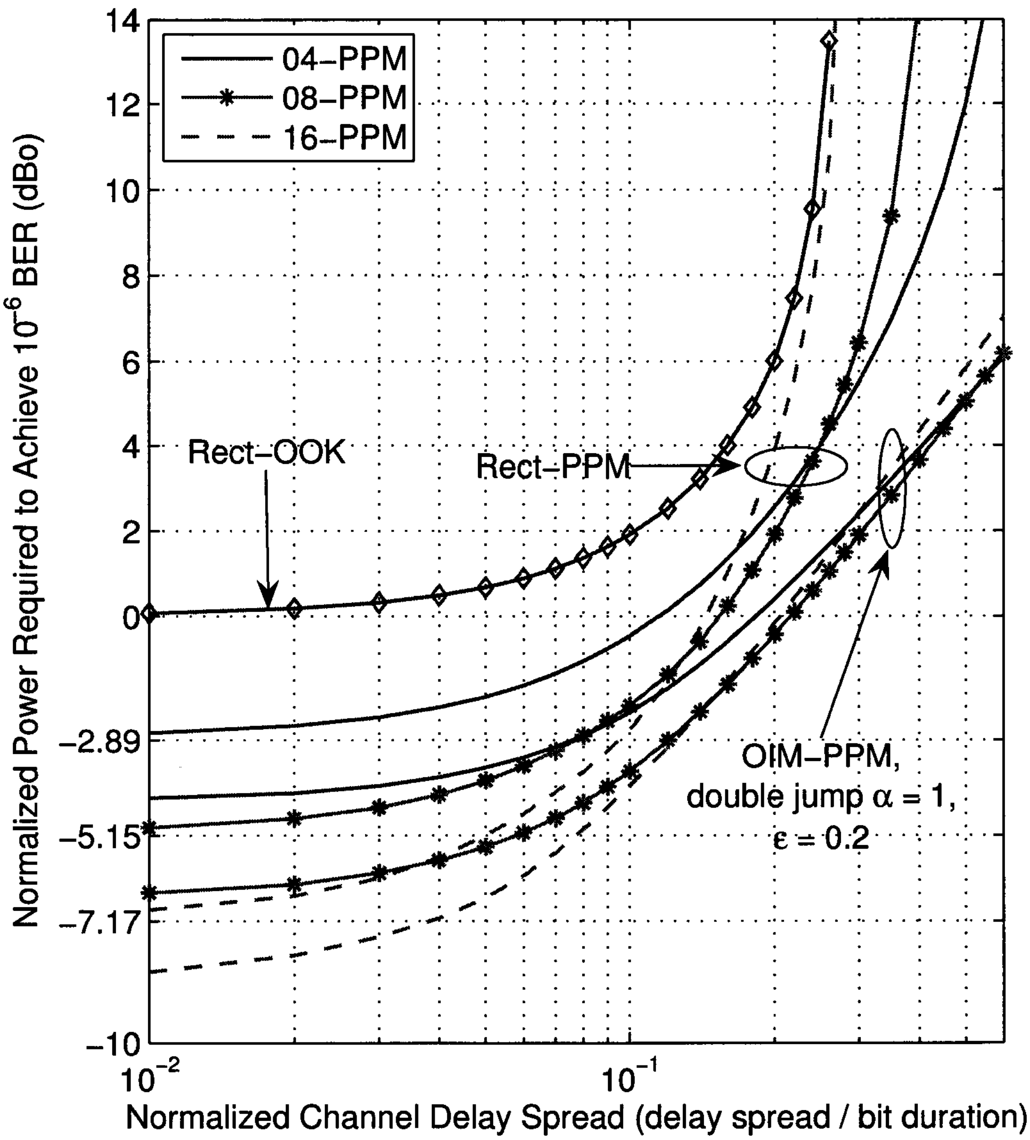

Figure 3.9: Normalized optical power, $10\log(\mathcal{P}_t/\mathcal{P}_t^{\mathrm{OOK}})$, required by Rect-PPM and OIM-PPM to achieve BER$=10^{-6}$.

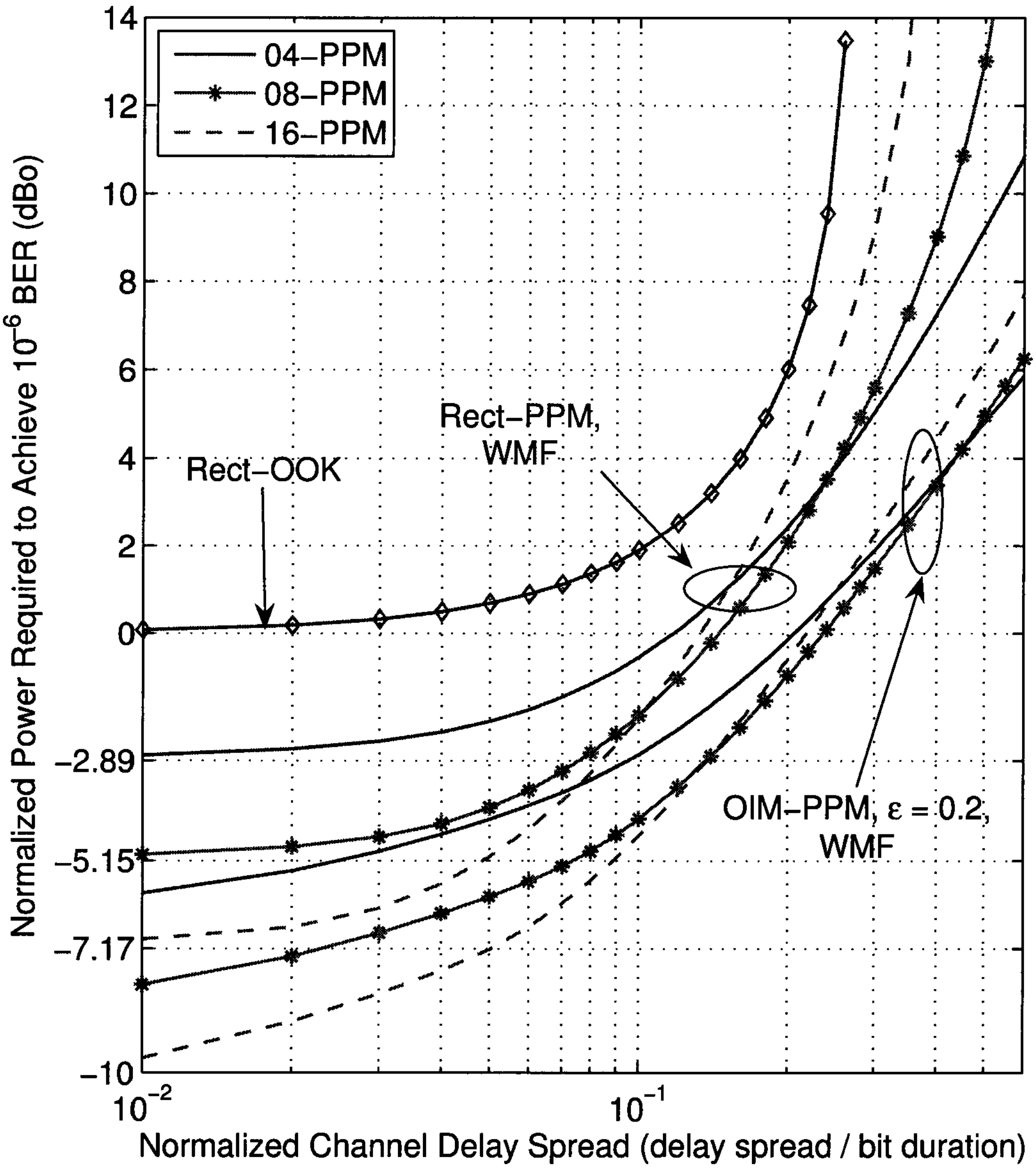

Figure 3.10: Normalized optical power, $10\log(\mathcal{P}_t/\mathcal{P}_t^{\mathrm{OOK}})$, required by precursor equalized Rect-PPM and OIM-PPM to achieve BER=10^{-6}.

indoor channels.

3.5.2 Peak Optical Power and Eye-Safety

Even though OIM reduces the average power required to achieve a certain BER compared to Rect-PAM, an increase in the peak optical power is evident from (3.15) as ε gets smaller. In this section, the increase in peak power is shown to be mild for practical values of ε, and to be compliant with international eye-safety standards [95].

For the same BER, OIM achieves an average power gain, γ, over Rect-PAM. As a result, the increase in peak optical power of OIM over Rect-PAM is $1/(\gamma\,\varepsilon)$ for the same BER. Consider the case when $\varepsilon = 0.2$. The gain at $\mathcal{D} = 0$ can be obtained using (3.23) in case of a double-jump receiver. Although (3.23) is strictly valid only for $\varepsilon \to 0$, it was shown in Fig. 3.6 that $\varepsilon = 0.2$ is close to this ideal case of $\varepsilon \to 0$. Therefore, for $\varepsilon = 0.2$, the increase in peak power is about $5/\sqrt{2} \approx 3.5$ for a double-jump receiver with $\alpha = 1$. Moreover, γ increases with the channel delay spread due to the fact that the transmitted information is confined to the lowpass region of the OIM spectrum. Hence, the increase in peak power of OIM at zero delay spread is a conservative estimate for those at higher delay spreads.

Constraints on the maximum peak optical power as well as the maximum average optical power are defined to guarantee eye-safety. For pulse amplitude modulated optical radiations, the average power constraint dominates the peak power constraint for modulation frequencies over 55 kHz [95]. Detailed calculations of both constraints for some consumer electronic products are given in [96]. For example, for a commercial IrDA link, the allowed peak-to-average power ratio is about 17 [96]. In this specific instance an increase of about 3.5 in the peak optical power due to OIM can be easily tolerated although experimental verification is required in all cases to ensure compliance with eye-safety standards.

3.5.3 Information Rate

While the performance of uncoded PAM systems is considered in Sec. 3.5.1, the performance of PAM systems from a more fundamental perspective is studied in this section. An information theoretic performance measure of a communication system is its information rate, defined as the maximum rate at which reliable communication is possible given a certain input distribution and arbitrarily high coding and decoding complexities. Information rates are very important in comparing different communication systems since they provide fundamental limits on the achievable communication rates. Calculating the information rates of binary signalling over ISI channels has been considered in [178–180]. Information rates of wireless optical diffuse channels have been investigated for Rect-PAM and Rect-PPM modulation schemes in [181, 182] for a uniform binary input distribution. In this section, the information rates of optical Rect-OOK and OIM-OOK are calculated and contrasted.

Referring to the discrete channel model (3.8), if the input sequence $\{a_k\}$ takes binary values, i.e. $a_k \in \{0, 2\mu_a\}$, then the channel can be modelled as a finite state machine with 2^M states, followed by additive Gaussian noise. This allows for a trellis diagram representation, where each vertical column of nodes corresponds to the 2^M distinct states at a given time instant k, and each branch represents a transition from the current state to the next state. That is, the trellis shows how the channel state evolves with time such that there exists a unique path through the trellis for every possible state sequence.

Assuming that the input sequence $\{a_k\}$ is chosen independently and uniformly distributed over $\{0, 2\mu_a\}$, the information rate over the binary-input channel is given by the mutual information

$$I(a; \hat{a}) = \bar{\hbar}(\hat{a}) - \bar{\hbar}(\hat{a}|a) = \bar{\hbar}(\hat{a}) - \bar{\hbar}(z),$$

where $\bar{\hbar}(a)$, $\bar{\hbar}(\hat{a})$ and $\bar{\hbar}(z)$ are the differential entropy rates of the channel input process, output process and noise process, respectively, and $\bar{\hbar}(\hat{a}|a)$ is the conditional differential entropy rate [183, Chapter 11]. In case of independent and identically distributed Gaussian channel noise with noise power σ_z^2, then $\bar{\hbar}(z) = \frac{1}{2}\log(2\pi e \sigma_z^2)$, and computing the mutual information reduces to computing the entropy rate $\bar{\hbar}(\hat{a})$ defined as

$$\bar{\hbar}(\hat{a}) = \lim_{\mathcal{N} \to \infty} \frac{\hbar(\hat{\mathbf{a}}_{\mathcal{N}})}{\mathcal{N}},$$

where $\hbar(\hat{\mathbf{a}}_{\mathcal{N}})$ is the differential entropy of a sequence of $\mathcal{N}$ realizations,

$$\hat{\mathbf{a}}_{\mathcal{N}} = (\hat{a}_1, \hat{a}_2, \cdots, \hat{a}_{\mathcal{N}}),$$

of the stochastic process, $\hat{a}$.

According to the Shannon-McMillan-Breiman theorem, for a stationary ergodic finite-state hidden-Markov process $\hat{a}$,

$$-\frac{1}{\mathcal{N}} \log(\mathbb{P}(\hat{\mathbf{a}}_{\mathcal{N}})) \longrightarrow \bar{\hbar}(\hat{a}) \qquad (3.24)$$

with probability one as $\mathcal{N} \to \infty$, where $\mathbb{P}(\hat{\mathbf{a}}_{\mathcal{N}})$ is the probability of the sequence $\hat{\mathbf{a}}_{\mathcal{N}}$ [183, Sec. 15.7], [178, 184]. As a result, $\bar{\hbar}(\hat{a})$ can be estimated by computing the probability $\mathbb{P}(\hat{\mathbf{a}}_{\mathcal{N}})$ for a sufficiently long sequence. This probability can be computed by the forward recursion of the BCJR (forward/backward) algorithm [185] which operates on the channel trellis [178–180].

For this computation, a random input sequence of length $\mathcal{N}$ is generated, and the corresponding channel output sequence $\hat{\mathbf{a}}_{\mathcal{N}}$ is simulated via (3.8). For the k^{th} trellis section, a trellis state m, where $0 \leq m \leq 2^M - 1$, is assigned a state metric

$$s_k(m) = \mathbb{P}(m, \hat{\mathbf{a}}_k), \tag{3.25}$$

where $\mathbb{P}(m, \hat{\mathbf{a}}_k)$ is the joint probability of being in state m and having $\hat{\mathbf{a}}_k = (\hat{a}_1, \hat{a}_2, \cdots, \hat{a}_k)$ as the channel output up to time k. Similarly, a trellis branch, connecting state m' to state m, is assigned a branch metric

$$b_k(m', m) = \mathbb{P}(m|m')\,\mathbb{P}(\hat{a}_k|m', m),$$

where $\mathbb{P}(m|m')$ is the state transition probability from state m' to state m, and $\mathbb{P}(\hat{a}_k|m', m)$ is the probability that the channel output is $\hat{a}_k$ given the state transition (m', m). In order to find $s_{\mathcal{N}}(m)$, the channel trellis is processed iteratively according to the recursive relation

$$s_k(m) = \sum_{m'} s_{k-1}(m')\, b_k(m', m), \tag{3.26}$$

and by using the initial conditions $s_0(0) = 1$ and $s_0(m) = 0$ for $m \neq 0$. Finally,

$$\mathbb{P}(\hat{\mathbf{a}}_{\mathcal{N}}) = \sum_{m} s_{\mathcal{N}}(m),$$

by virtue of (3.25). Numerically, the state metrics computed by (3.26) tend to zero very quickly for large $\mathcal{N}$. As a result, the recursive relation (3.26) is modified to

$$s_k(m) = \sum_{m'} A_k \, s_{k-1}(m') \, \mathscr{b}_k(m', m),$$

where A_k is a scaling factor such that $\sum_m s_k(m) = 1$. In this case, $\sum_{k=1}^{\mathcal{N}} \log(A_k) = -\log(\mathbb{P}(\hat{\mathbf{a}}_{\mathcal{N}}))$ and hence,

$$\frac{1}{\mathcal{N}} \sum_{k=1}^{\mathcal{N}} \log(A_k) \longrightarrow h(\hat{a}) \tag{3.27}$$

by using (3.24) [178, 180].

The information rates obtained by using the left-hand side of (3.27) as an estimate for $h(\hat{a})$ are plotted versus the sequence length, $\mathcal{N}$, in Fig. 3.11. The information rates presented are for OIM-OOK with double-jump receiver ($\alpha = 1$), at a normalized delay spread of 0.2 and different values of $\mathcal{P}_t H_0 \sqrt{T_b}/\sigma_z$. The standard deviation of the information rate simulated over the range $10^4 < \mathcal{N} \leq 10^5$ is normalized to the information rate simulated at $\mathcal{N} = 10^5$. This normalized standard deviation ranges from about 0.02 at $\mathcal{P}_t H_0 \sqrt{T_b}/\sigma_z = -5$ dBo to about 0.001 at +5 dBo. That is, the rates almost converge to a constant value for $\mathcal{N} > 10^4$ as shown in Fig. 3.11. Therefore, a sequence length of $\mathcal{N} = 10^5$ is used to compute the information rates presented in this section.

Fig. 3.12 compares the information rates of Rect-OOK with WMF receiver, and OIM-OOK with double-jump receiver ($\alpha = 1$) over the indoor diffuse optical channel. The information rates of OIM at $\mathcal{D}/T_b = 0.2$ are equivalent to the values in Fig. 3.11 at $\mathcal{N} = 10^5$. At both high and low delay spreads, the information rate of OIM-OOK with the simple channel-independent double-jump receiver is higher than that

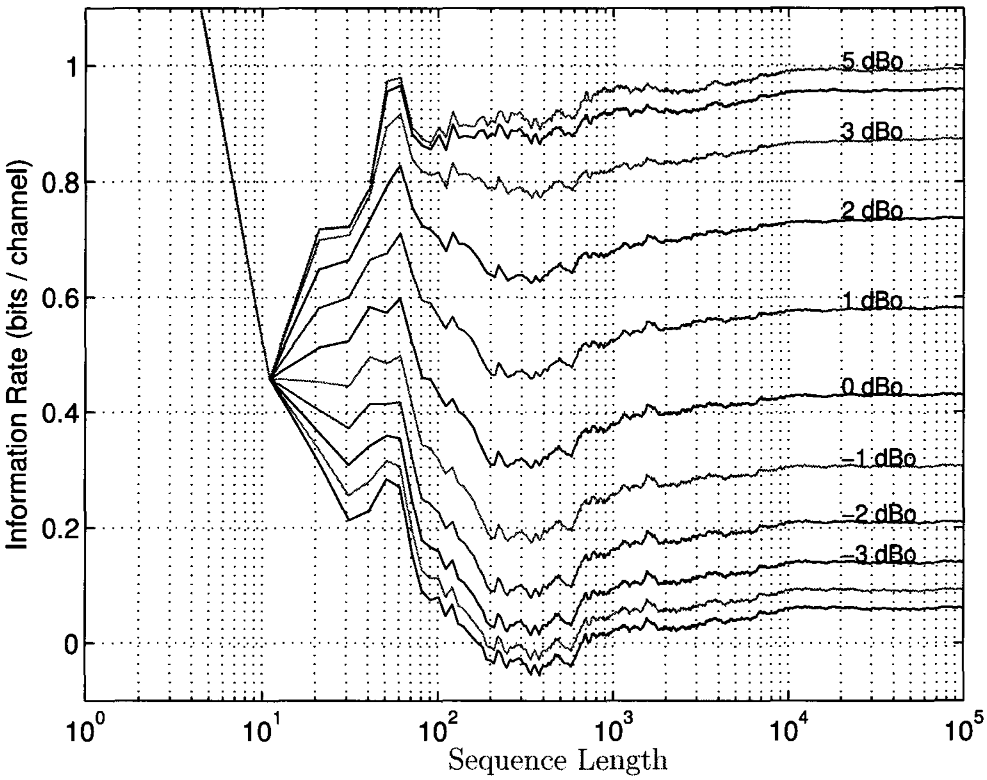

Figure 3.11: Information rate versus the sequence length, $\mathcal{N}$, for OIM-OOK with double-jump receiver ($\alpha = 1$) at a normalized delay spread of 0.2. Results are presented for $\mathcal{P}_t H_0 \sqrt{T_b}/\sigma_z = -5, -4, \cdots, +5$ dBo.

of Rect-OOK with the complex WMF receiver. This shows that, in the case of equally likely binary inputs, OIM-OOK is fundamentally better than Rect-OOK while being significantly less complex. Notice that, at a normalized delay spread of 10^{-2}, the gain in optical SNR of OIM-OOK with double-jump receiver over Rect-OOK is about 1.5 dBo as shown in Fig. 3.12. This gain corresponds to the 1.5 dBo optical power gain in Fig. 3.6 and equation (3.23) at low delay spread.

Fig. 3.13 compares the information rates versus normalized channel delay spread at $\mathcal{P}_t H_0 \sqrt{T_b}/\sigma_z = 3$ dBo. At $\mathcal{D}/T_b = 0.2$, the information rate of OIM-OOK with double-jump receiver is 14.5% higher than that of Rect-OOK, while its rate when

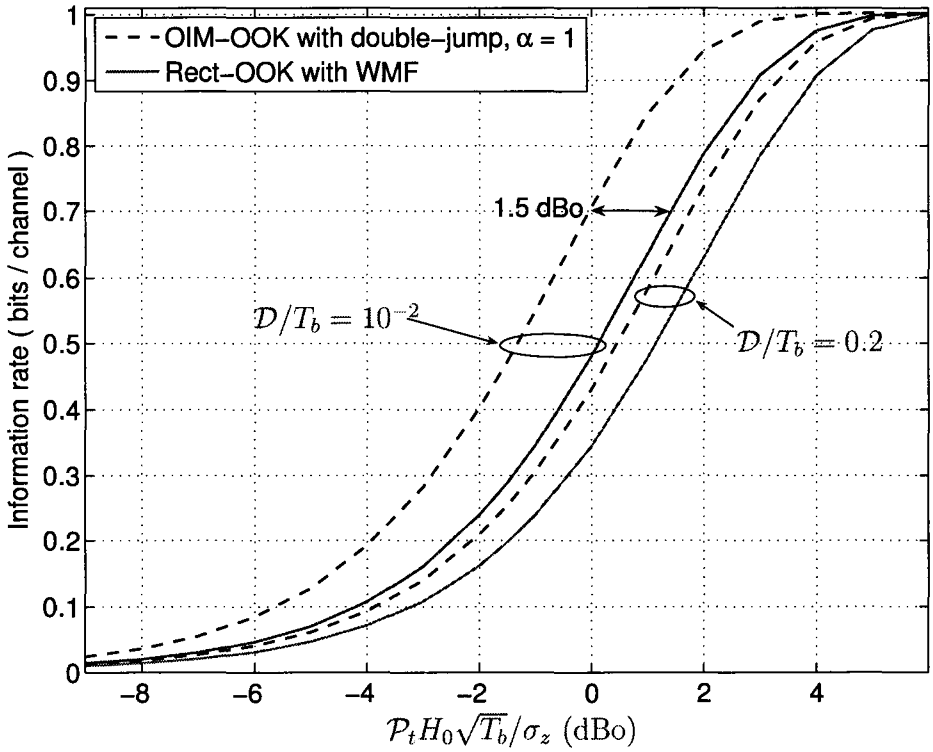

Figure 3.12: Information rate versus optical SNR for Rect-OOK with WMF receiver, and OIM-OOK with double-jump receiver ($\alpha = 1$). Results are presented at normalized delay spreads of 10^{-2} and 0.2.

using a WMF receiver is 17.9% higher than that of Rect-OOK with WMF receiver. At the same delay spread, the rate of OIM-OOK with double-jump receiver is 11.5% higher than that of Rect-OOK with WMF receiver, at a much reduced complexity cost. Thus, in all cases OIM provides a significant gain in information rate over rectangular modulation while simultaneously reducing the complexity of the receiver. At a low delay spread of 10^{-2}, the rate of OIM-OOK with WMF receiver is much higher than with the double-jump receiver. However, as mentioned earlier, matched filtering to a narrow transmitted pulse is difficult to implement in practice.

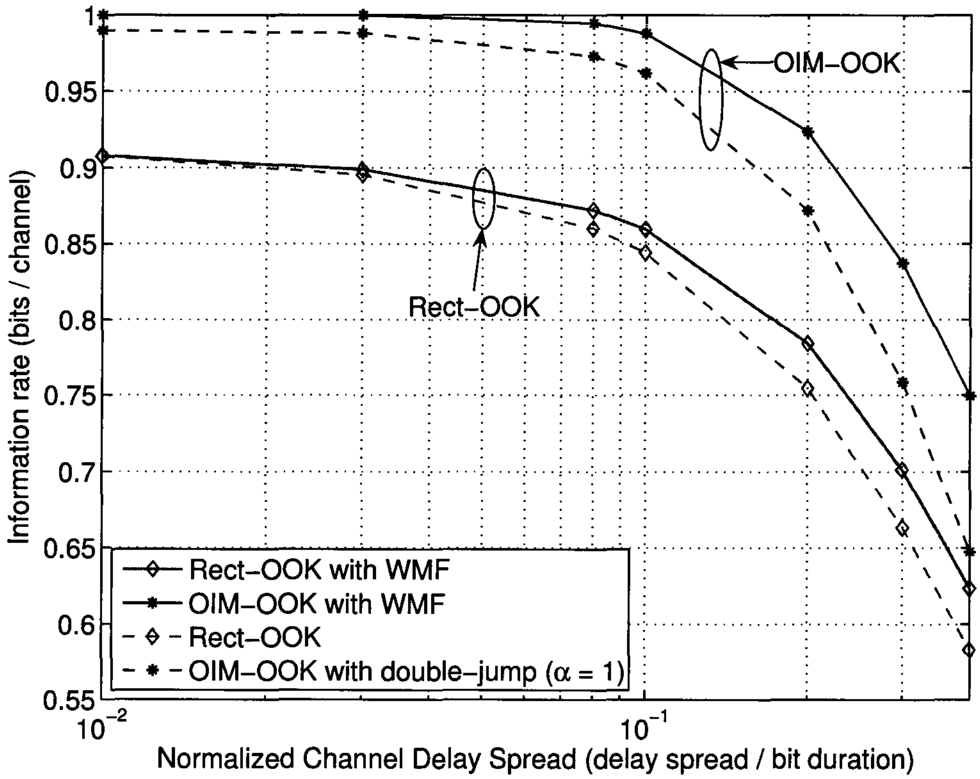

Figure 3.13: Information rate versus normalized channel delay spread at optical SNR of $\mathcal{P}_t H_0 \sqrt{T_b}/\sigma_z = 3$ dBo

3.6 Conclusions

This chapter defines OIM which provides good optical power efficiencies for temporally dispersive optical wireless channels, at a low implementation complexity. A key insight of OIM is that it confines the useful information to the lowpass region of the spectrum. The higher frequency regions, which are attenuated by the channel, carry no independent information and are only used to satisfy the channel amplitude constraints. As a result, the detector operates on the lowpass region of the spectrum and can be implemented with a simple lowpass filter whose design requires no knowledge of the channel impulse response. OIM provides high optical power gain over Rect-PAM and Rect-PPM over a wide range of channel delay spreads. Moreover, it has been shown that the information rate of OIM is higher than that of Rect-OOK over a wide range of delay spreads.

The next chapter treats the modulation design problem for spatially dispersive optical wireless channels, which are 2D generalizations of the temporally dispersive optical wireless channels considered in this chapter.

Chapter 4

Halftoned Spatial Discrete Multitone Modulation

4.1 Introduction

This chapter treats the modulation design problem for indoor point-to-point wireless optical MIMO channels. While indoor wireless optical diffuse channels, treated in Chapter 3, use wide-angle transceivers and do not assume the existence of a line-of-sight between the transmitter and receiver, indoor point-to-point wireless optical MIMO channels use imaging-type transceivers and assume the existence of such a line-of-sight. Comparing the channel models (2.5) and (2.11) of the diffuse and MIMO channels, it is evident that both channels share the same general dispersive model, however, the dispersion occurs in different domains. For diffuse channels, the dispersion is in the temporal domain, whereas it is in the spatial domain for MIMO channels. While temporal degrees of freedom have been used in Chapter 3 for modulation design over indoor wireless optical diffuse channels, spatial degrees of freedom are used in this chapter for modulation design over indoor point-to-point wireless optical MIMO channels.

Indoor wireless optical MIMO links employ the spatial dimensions to improve the performance of point-to-point links [9, Chapter 7]. As mentioned in Sec. 1.2.1, they have been used in different applications, such as holographic data storage [35–37], page-oriented optical recording [38, 39], 2D barcodes [40, 41], and MIMO wireless optical communications [6, 42–44]. An example of an indoor point-to-point wireless optical MIMO link is shown in Fig. 2.6. Information is conveyed through the channel by transmitting a time-varying 2D optical intensity image. As in (2.11), the channel is modelled as a linear space-invariant system, characterized by the PSF, which is the spatial optical intensity impulse response of the system. The transmitter is an SLM consisting of a 2D array of pixels, while the receiver consists of a 2D array of photodetector pixels. The constraints (2.12) and (2.13) imply that the transmitted signal should be non-negative, and the average transmitted power is given by the average image amplitude rather than the average square amplitude as in conventional electrical channels. As a result of these amplitude constraints, the direct application of conventional RF signalling theory is seldom efficient.

As mentioned in Sec. 1.2.1, in “pixel matched” channels, each receive pixel images a single transmit pixel and requires strict spatial alignment between transmitter and receiver in order to avoid inter-channel interference. To avoid this practically difficult condition, a recent signalling technique has been introduced in [57, 58] which does not require such strict alignment. However, the transmitter array is assumed to be able to generate multiple (e.g., 256) intensity levels, and the non-negativity constraint of the generated image is not considered explicitly, rather, amplitudes are clipped to ensure that the constraints are met.

In this chapter, the earlier work in [57,58] is extended by considering transmitter arrays in which each pixel is able to output a *binary-level* intensity, i.e., on or off. Such transmitters are far simpler to construct than those previously assumed and can be operated at very high frame rates. The non-negativity constraint is treated explicitly through the design of modified halftoning algorithms that produce binary-level transmit images. First order noise shaping filters are used to shape the quantization noise away from the data bearing spatial spectral regions. Thus, excess degrees of freedom in spatial frequency domain are exploited to provide binary-level output images which satisfy all amplitude constraints while maintaining the relaxation on strict spatial alignment [158–160]. The results presented in this chapter can be extended by considering multi-level quantization and/or higher order noise shaping filters as in [166,186].

4.2 Spatial Discrete Multitone Modulation

Discrete multitone (DMT) is a modulation scheme developed for frequency selective channels [187], [170, Sec. 12.2.2]. Spatial discrete multitone (SDMT) modulation is a generalization of DMT to 2D spatial frequency [57,58], [9, Sec. 7.5]. An appealing advantage is that SDMT is insensitive to the receiver sampling phase, and hence, strict alignment between the transmitter and receiver is not necessary.

Let the transmit SDMT symbol, $x(n_1, n_2)$, be an image of $N_1 \times N_2$ pixels, and let $X(k_1, k_2)$ be the discrete Fourier transform (DFT) of $x(n_1, n_2)$. The complex data to be transmitted are loaded into frequency bins such that Hermitian symmetry, $X(k_1, k_2) = X^{\star}(N_1 - k_1, N_2 - k_2)$, is satisfied in order to guarantee real transmit

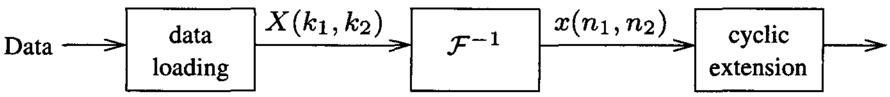

Figure 4.1: SDMT transmitter block diagram.

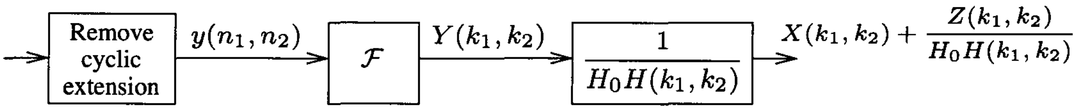

Figure 4.2: SDMT receiver block diagram.

images. As shown in Fig. 4.1, the transmit SDMT symbol is given by the inverse DFT of $X(k_1, k_2)$,

$$x(n_1, n_2) = \mathcal{F}^{-1}\{X(k_1, k_2)\},$$

where the inverse DFT is denoted by $\mathcal{F}^{-1}$. The receive image is equal to the linear convolution of the transmit image and the channel PSF. By appending a cyclic extension [58, 187] around the transmit SDMT symbol, whose size is at least half the channel memory, the periodicity assumption of the DFT is satisfied. In this case, the channel model (2.11) can be simplified in discrete spatial frequency domain (k_1, k_2) as

$$Y(k_1, k_2) = H_0\, X(k_1, k_2)\, H(k_1, k_2) + Z(k_1, k_2) \tag{4.1}$$

where H_0 is the channel DC-gain, $Y(k_1, k_2)$ and $Z(k_1, k_2)$ are the DFTs of the receive symbol and channel additive Gaussian noise respectively, and $H(k_1, k_2)$ is the OTF which is normalized to have unity DC-gain. Upon reception, the cyclic extension is removed by cropping the received image to the SDMT symbol as shown in Fig. 4.2. Since the transmit and receive images are defined over rectangular spatial regions, both the 2D DFT and the 2D inverse DFT are separable, which allows for their efficient implementation.

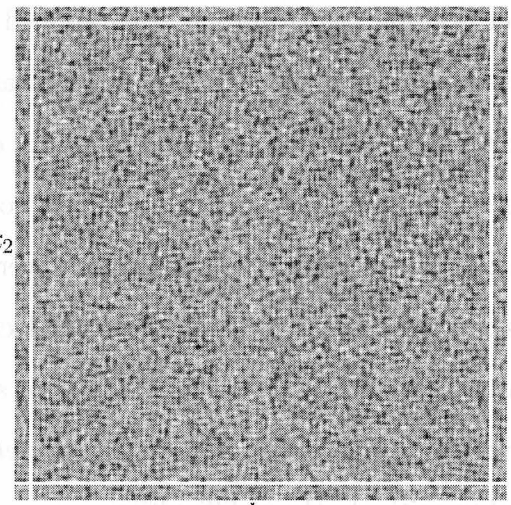

Figure 4.3: An example SDMT symbol, $X(k_1, k_2)$, of 256×256 pixels with a cyclic extension of width 8 pixels. For clarification, white border lines separate the SDMT symbol from its cyclic extension.

An example transmit image is shown in Fig. 4.3, which is composed of an SDMT symbol surrounded by its cyclic extension. After the cyclic extension removal at the receiver, the DFT, denoted by $\mathcal{F}$, is computed as shown in Fig. 4.2. For such SDMT systems, channel equalization is a complex multiplication by $\frac{1}{H_0\, H(k_1,k_2)}$ per spatial frequency bin [58, 187]. That is,

$$\frac{Y(k_1,k_2)}{H_0\, H(k_1,k_2)} = X(k_1,k_2) + \frac{Z(k_1,k_2)}{H_0\, H(k_1,k_2)}.$$

Therefore, the indoor point-to-point wireless optical MIMO channel can be considered as a number of parallel Gaussian channels in spatial frequency domain, and the aggregate capacity, in the absence of amplitude constraints, is maximized by a water pouring algorithm over the spatial frequency channels [183, Chapter 10], [58].

In [57, 58], the water pouring algorithm has been applied in absence of the non-negativity amplitude constraint, and the signal amplitude has been clipped in order to satisfy the constraint. However, due to the constraints of the spatial intensity domain, pouring power to the spatial frequency domain is not straight forward, and does not necessarily maximize the capacity [57, 58]. Moreover, the complexity of the technique in [57, 58] is increased since it requires an SLM capable of outputting a continuous range of intensities with a high dynamic range, as is noted in electrical DMT systems. In the next section, *halftoned spatial discrete multitone* (HSDMT) modulation, is proposed to mitigate these difficulties.

4.3 Binary-Level 2D Optical Channels

In an effort to reduce the complexity of the transmitter, SLMs with binary-level output are considered. Binary-level signalling over the 2D optical wireless channel simplifies not only the SLM design but also ensures that the channel non-negativity constraint can be easily met since dark/bright pixels are only transmitted over the channel.

Two popular examples of such binary-level SLMs include digital micro-mirror devices (DMD) and arrays of vertical-cavity surface-emitting lasers (VCSELs). Commercial DMDs can operate at switching speeds of 40 kHz with array sizes of 1024×768 mirrors [188, DLP® Discovery™ 1100], while faster DMDs whose switching period is about 8-16 µsec are used to eliminate motion blur in high-definition television [188, DLP® HDTV]. A 540-element array with 1080 VCSELs has been produced for optical interconnect in which each pixel can be modulated in excess of 200 Mbps [189]. An integrated solid-state array of transceivers has been designed to operate at 155

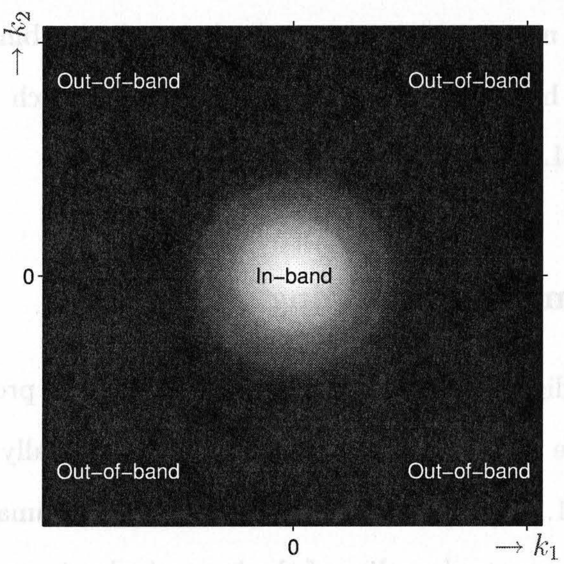

Figure 4.4: A Gaussian OTF, $H(k_1, k_2) = \exp\left(-\frac{k_1^2}{2w_{h_1}^2} - \frac{k_2^2}{2w_{h_2}^2}\right)$, where w_{h_1} and w_{h_2} are measures of the OTF widths. The in-band and out-of-band regions are indicated.

Mbps per pixel, where arrays of resonant cavity LEDs are bonded to arrays of CMOS driver circuits [190].

The high frame rates permit many channel uses per second, while the large number of pixels gives many spatial degrees of freedom. Since the OTF of the channel is typically spatially lowpass, it is not possible to transmit data in high spatial frequency modes as these modes are effectively filtered by the channel. That is, these modes are excess degrees of freedom that are available at the transmitter, but not supported by the channel. The high-frequency modes are termed the *out-of-band* region, while the low-frequency modes which carry independent data are termed the *in-band* region. These spatial frequency regions are indicated in Fig. 4.4 for a Gaussian OTF.

In this section, a method that utilizes these out-of-band spatial modes is proposed to satisfy the channel non-negativity constraint by producing binary-level output images while achieving high communication rates that approach the rates of unconstrained continuous SLM transmitter.

4.3.1 Digital Image Halftoning

In image processing, digital image halftoning is defined as the process of converting a continuous-tone image to a binary-level one which is perceptually close to the original continuous image [191, 192]. The difference between the two images is termed *quantization noise*. The perceptual quality of the image is dominated by the low spatial frequency region since the human visual system is more sensitive to this region of the spectrum. Therefore, the PSD of the quantization noise is shaped to the high spatial frequency region where the human visual system is not sensitive.

Error diffusion halftoning is the most popular halftoning algorithm first proposed empirically by Floyd and Steinberg in 1975 [193]. Later, Anastassiou defined a rigorous unifying framework linking $\Delta\Sigma$ modulation and error diffusion halftoning [194]. He showed that the error diffusion algorithm is an extension of $\Delta\Sigma$ modulation to two dimensions and that both algorithms are oversampled analog-to-digital converters that rely on the spectral shaping of quantization noise. The error diffusion system used in this work is surrounded by a dashed box in Fig. 4.5. The error diffusion feedback filter $j(n_1, n_2)$ was chosen empirically by Floyd, however, others have presented more rigorous designs based on classical filter theory [195]. An all-optical implementation of the error diffusion algorithm has been described in [196], where all pixel quantizations are computed in parallel.

In 2D optical intensity communication channels, considered here, the perceptual

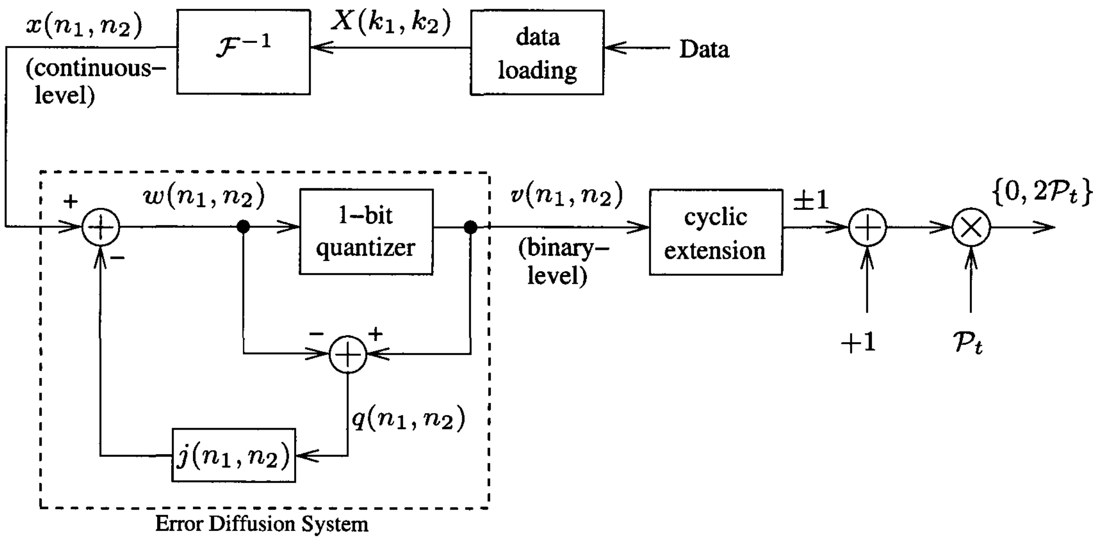

Figure 4.5: HSDMT transmitter block diagram.

quality of the transmitted images is not of concern. Instead, the goal is to design a series of binary-level images which maximize the rate at which reliable communication can take place over the channel. Since the channel OTF is analogous to the lowpass human visual system, data are loaded into spatial frequency bins where the channel attenuation is low. Halftoning is then used to produce a binary-level transmit image in which the quantization noise is shaped to the out-of-band frequency bins that are heavily attenuated by the channel OTF. This high frequency quantization noise will be filtered out by the channel and the received image will be a continuous-tone image which carries the transmitted data along with some residual quantization noise.

In Fig. 4.5, let q be the *quantizer error*, and $\tilde{q} = v - x$ be the closed loop *quantization noise*, where x and v are the input continuous-tone image and the output halftoned image respectively. Therefore,

$$\tilde{Q}(k_1,k_2) = Q(k_1,k_2)\left[1 - J(k_1,k_2)\right], \tag{4.2}$$

where $Q(k_1, k_2)$ and $\tilde{Q}(k_1, k_2)$ are the DFTs of $q(n_1, n_2)$ and $\tilde{q}(n_1, n_2)$, respectively, and $J(k_1, k_2)$ is the DFT of the feedback filter. The PSD of the quantization noise, $\tilde{q}$, is given by

$$\Phi_{\tilde{q}}(k_1, k_2) = \Phi_q(k_1, k_2)\, |1 - J(k_1, k_2)|^2, \tag{4.3}$$

where $\Phi_q(k_1, k_2)$ is the PSD of the quantizer error, q. That is, the power of the quantizer error is shaped by the noise power shaping function $|1 - J(k_1, k_2)|^2$. In order to shape the quantizer error power to the out-of-band region, the error diffusion feedback filter $J(k_1, k_2)$ is chosen to be a unity DC-gain filter such that the noise power shaping function $|1 - J(k_1, k_2)|^2$ will have a null at DC.

4.3.2 Halftoned Spatial Discrete Multitone Modulation

The binary-level SDMT communication system based on halftoning is shown in Fig. 4.5. The SDMT transmit symbol, $x(n_1, n_2)$, is formed as described in Sec. 4.2 and is the input of the error diffusion system. A cyclic extension is added to the halftoned image and the frame is biased by a constant bias of $+1$ to satisfy the non-negativity constraint. Finally the entire frame is multiplied by $\mathcal{P}_t$ to scale the output levels to $\{0, 2\mathcal{P}_t\}$. Since the input continuous SDMT symbol, $x(n_1, n_2)$, is assumed to be zero mean, the output halftoned binary image, $v(n_1, n_2)$, is also zero mean, and hence the average transmit optical power is equal to $\mathcal{P}_t$. That is, the transmitted signal is $\mathcal{P}_t\,[x(n_1, n_2) + \tilde{q}(n_1, n_2) + 1]$.

The received image is calculated by replacing $X(k_1, k_2)$ in (4.1) by the DFT of the transmitted signal,

$$Y(k_1,k_2) = \mathcal{P}_t H_0 \left[X(k_1,k_2) + \tilde{Q}(k_1,k_2) + N_1 N_2 \delta(k_1,k_2)\right] H(k_1,k_2) + Z(k_1,k_2). \quad (4.4)$$

Channel equalization is done at the receiver by dividing (4.4) by $\mathcal{P}_t H_0 H(k_1,k_2)$, which yields

$$\frac{Y(k_1,k_2)}{\mathcal{P}_t H_0 H(k_1,k_2)} = \left[X(k_1,k_2) + N_1 N_2 \delta(k_1,k_2)\right] + \tilde{Q}(k_1,k_2) + \tilde{Z}(k_1,k_2)$$

where

$$\tilde{Z}(k_1,k_2) = \frac{Z(k_1,k_2)}{\mathcal{P}_t H_0 H(k_1,k_2)}$$

is the effective channel Gaussian noise. That is, the effective received SDMT symbol is equal to a DC-biased version of the transmit SDMT symbol contaminated by two noise components: $\tilde{Q}(k_1,k_2)$ and $\tilde{Z}(k_1,k_2)$ whose PSDs are $\Phi_{\tilde{q}}(k_1,k_2)$ and $\Phi_{\tilde{z}}(k_1,k_2)$ respectively.

4.3.3 Linearized Analytical Model

The analysis of this error diffusion system is not straightforward because the binary-level quantizer is a highly nonlinear element. A conventional simplifying assumption is to linearize the quantizer by assuming that the quantizer error, q, is signal-independent as shown in Fig. 4.6 [197, Sec. 2.3], [198, Chapter 14]. This assumption is more likely to be valid for small input electrical power, σ_x^2 [197, Sec. 2.3], [198, Chapter 14]. Moreover, since it is difficult to determine the distribution of the quantization

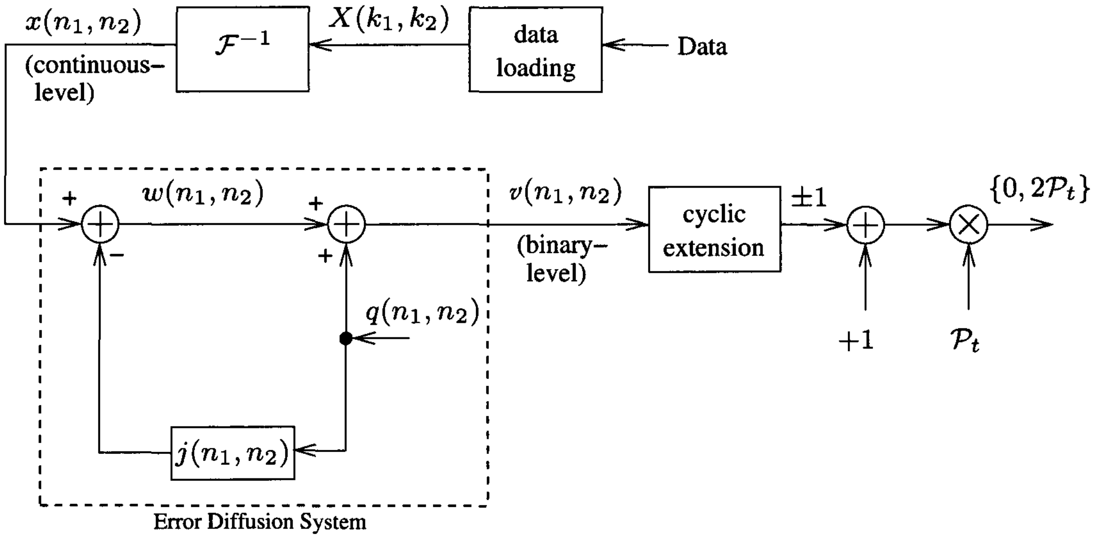

Figure 4.6: Linearized HSDMT transmitter block diagram.

noise, $\tilde{q}$, a simplifying assumption that it is Gaussian distributed is made in order to have tractable expressions. This assumption represents a worst case study since the worst additive noise, that minimizes the mutual information between the channel input and output, subject to average power constraints is a Gaussian distributed noise [199]. According to this assumption, $\Phi_{\tilde{q}}(k_1, k_2) + \Phi_{\tilde{z}}(k_1, k_2)$ defines the Gaussian noise "bowl" over which the total available electrical power is poured in order to maximize the aggregate channel capacity [183, Chapter 10], [58]. If $\Phi_{\tilde{q}}(k_1, k_2) \gg \Phi_{\tilde{z}}(k_1, k_2)$ in the in-band region, the quantization noise dominates and the system is termed *quantization noise-limited.* On the other hand, if $\Phi_{\tilde{q}}(k_1, k_2) \ll \Phi_{\tilde{z}}(k_1, k_2)$ in the in-band region, the channel noise dominates and the system is then termed *optical power-limited.* Examples of quantization noise- and optical power-limited systems are presented in Sec. 4.4.

Notice that the non-negativity constraint is no longer an issue while pouring power to the bowl $\Phi_{\tilde{q}}(k_1, k_2) + \Phi_{\tilde{z}}(k_1, k_2)$, as was the case in [57, 58], because the output image is a binary one. Let $\Phi_x(k_1, k_2)$ be the electrical power allocated to the complex frequency bin (k_1, k_2) such that the total frame electrical power is equal to $\frac{1}{N_1 N_2}\sum \Phi_x(k_1, k_2) = \sigma_x^2 N_1 N_2$ for some fixed input electrical power σ_x^2. Then, the aggregate system capacity C is given by

$$C \approx \frac{1}{2}\sum_{k_1=0}^{N_1-1}\sum_{k_2=0}^{N_2-1}\log\left(1+\frac{\Phi_x(k_1,k_2)}{\Phi_{\tilde{q}}(k_1,k_2)+\Phi_{\tilde{z}}(k_1,k_2)}\right) \tag{4.5}$$

where $\Phi_x(k_1, k_2)$ is calculated by the water pouring algorithm to maximize the capacity C [183, Chapter 10], and no power is poured to the DC-bin, i.e. $\Phi_x(0,0) = 0$, because a constant DC-level of $\mathcal{P}_t$ is added to each frame such that the transmit signal satisfies (2.10).

Notice that the expression in (4.5) for the capacity is only valid under the aforementioned simplifying assumptions of signal-independent quantizer error, q, and Gaussian quantization noise, $\tilde{q}$. In fact, the larger the electrical power of the quantizer input, the more likely the quantizer is to saturate, and the more likely the signal-independence assumption is to fail. In this case, the halftoning system is said to be unstable, where the system instability means that the quantization noise is much higher than that predicted by the linearized model [197, Chapter 4]. In Sec. 4.3.4, upper bounds that are necessary to ensure the consistency of the system model are deduced on the total input electrical power and feedback filter energy.

4.3.4 Halftoning Design

In Sec. 4.3.3, the quantizer is linearized by assuming that the quantizer error, q, is signal-independent as shown in Fig. 4.6. Moreover, it is conventional to assume that

q is white with variance σ_q^2 [197, Sec. 2.3], [198, Chapter 14]. In this case, (4.3) can be written as

$$\Phi_{\tilde{q}}(k_1, k_2) = N_1 N_2\, \sigma_q^2\, |1 - J(k_1, k_2)|^2, \tag{4.6}$$

where the PSD of q is $\Phi_q(k_1, k_2) = N_1 N_2\, \sigma_q^2$. The total quantization noise power, in all complex frequency bins, after noise shaping is given by:

$$\begin{aligned} \sum_{k_1,k_2} \Phi_{\tilde{q}} &= N_1 N_2 \sigma_q^2 \sum_{k_1,k_2} [1 - J(k_1, k_2)]^* [1 - J(k_1, k_2)] \\ &= (N_1 N_2)^2 \sigma_q^2 \left(1 + \mathcal{E}_j - 2j(0,0)\right), \end{aligned} \tag{4.7}$$

where

$$\mathcal{E}_j = \sum_{n_1,n_2} |j(n_1, n_2)|^2$$

is the feedback filter energy, and the fact that $\sum J(k_1, k_2) = N_1 N_2\, j(0,0)$ is used.

Therefore, the total quantization noise power increases with the filter energy $\mathcal{E}_j$. However, high values of $\mathcal{E}_j$ are not problematic as long as the noise is well shaped to the out-of-band region that is attenuated by the channel OTF. The key point is to maximize the channel capacity, defined in (4.5), and not to minimize the total quantization noise power.

Using the signal-independence and whiteness assumptions of q, the variance σ_w^2 of the input to the quantizer can be written as

$$\sigma_w^2 = \sigma_x^2 + \sigma_q^2\, \mathcal{E}_j, \tag{4.8}$$

where σ_x^2 is the average electrical power of the input SDMT signal as shown in Fig. 4.5.

The availability of some information about the statistical properties of the input

SDMT signal can further aid the estimation of the quantizer error power σ_q^2. The amplitude of DMT signals is known to closely approximate Gaussian distributed signal [200, Sec. 3.3]. Moreover, from (4.2) and the Gaussianity assumption of the $\tilde{q}$, the quantizer error q is also Gaussian. Consequently, the input w to the quantizer is Gaussian distributed as well, and the quantizer error power is given by

$$\begin{aligned}\sigma_q^2 &= \int_{-\infty}^{0} f_w(w)(-1-w)^2 dw + \int_{0}^{\infty} f_w(w)(1-w)^2 dw \\ &= 1 + \sigma_w^2 - 4\sigma_w/\sqrt{2\pi}, \end{aligned} \tag{4.9}$$

where $f_w(w)$ is a zero-mean Gaussian probability density function with variance σ_w^2. Solving (4.8) and (4.9) for σ_w,

$$\sigma_w = \frac{-\sqrt{2/\pi} + \sqrt{2/\pi + (1/\mathcal{E}_j - 1)(1 + \sigma_x^2/\mathcal{E}_j)}}{1/\mathcal{E}_j - 1}, \tag{4.10}$$

Therefore, σ_q^2 can be estimated from knowledge of σ_x^2 by using (4.9) and (4.10). For σ_w to be real, the discriminant under the square root in (4.10) must be non-negative, and hence, the following upper bound on σ_x^2 exists when $\mathcal{E}_j > 1$,

$$\sigma_x^2 \leq \mathcal{E}_j \left[\frac{2}{\pi(1 - 1/\mathcal{E}_j)} - 1 \right]. \tag{4.11}$$

Since $\sigma_x^2 \geq 0$, then so too is the right hand side of (4.11). Hence, the following upper bound exists on the feedback filter energy, $\mathcal{E}_j$,

$$\mathcal{E}_j \leq \frac{\pi}{\pi - 2} \approx 2.75. \tag{4.12}$$

That is, for the model to be consistent with the assumptions made, the feedback filter energy cannot exceed 2.75, and the input electrical power cannot exceed the bound in (4.11) when $\mathcal{E}_j > 1$. Results obtained by using this model are compared to those obtained by simulations in Sections 4.4 and 4.5

4.4 Example: Pixelated Wireless Optical Channel

The pixelated wireless optical channel (2.11) is introduced in [57, 58], where each transmitter element is assumed to be able to generate 256 intensity levels. Additionally, the non-negativity constraint of the generated image was not considered explicitly, rather, amplitudes are clipped to ensure non-negativity. In this section, HSDMT is applied to the channel measured in [57, 58], and the obtained channel capacity is compared to the results of [57, 58].

4.4.1 Simulation Setup

In Sec. 4.3, it has been assumed that the quantizer error is white and signal-independent with variance σ_q^2. It is also assumed in the simulations that the channel noise is white, Gaussian, and signal-independent with variance σ_z^2 per pixel. Therefore the PSD of the effective noise $\tilde{Z}$ is equal to

$$\Phi_{\tilde{z}}(k_1, k_2) = \frac{\sigma_z^2 N_1 N_2}{|\mathcal{P}_t H_0 H(k_1, k_2)|^2} = \frac{N_1 N_2}{|\rho H(k_1, k_2)|^2}, \tag{4.13}$$

where

$$\rho = \frac{\mathcal{P}_t H_0}{\sigma_z} \tag{4.14}$$

is the optical SNR. Substituting from (4.13) in (4.5), the capacity is given by

$$C \approx \frac{1}{2} \sum_{k_1=0}^{N_1-1} \sum_{k_2=0}^{N_2-1} \log\left(1 + \frac{\Phi_x(k_1,k_2)}{\Phi_{\tilde{q}}(k_1,k_2) + N_1 N_2/|\rho H(k_1,k_2)|^2}\right), \tag{4.15}$$

and by further substitution from (4.6), it is given by

$$C \approx \frac{1}{2} \sum_{k_1=0}^{N_1-1} \sum_{k_2=0}^{N_2-1} \log\left(1 + \frac{\Phi_x(k_1,k_2)}{N_1 N_2 \sigma_q^2 |1 - J(k_1,k_2)|^2 + N_1 N_2/|\rho H(k_1,k_2)|^2}\right). \tag{4.16}$$

As defined in Sec. 4.3.3, the system is quantization noise-limited if $\rho \gg 1/\sigma_q$, and is optical power-limited if $\rho \ll 1/\sigma_q$.

In the simulations presented in this section, it is assumed that spatial synchronization is achieved through scaling of the imaging optics such that the system magnification is unity and both the transmitter and receiver have the same number of pixels [58], [9, Sec. 7.5.2]. The presented results can be extended by considering links with non-unity magnification as in [165, 166]. The transmitted image is required to be in the FOV of the receiver, while strict alignment between the transmitter and receiver is not necessary. The simulations are done for a square frame $N_1 = N_2 = N$, and a unity DC-gain Gaussian OTF,

$$H(k_1,k_2) = \exp\left(-\frac{k_1^2}{2w_{h_1}^2} - \frac{k_2^2}{2w_{h_2}^2}\right), \tag{4.17}$$

where w_{h_1} and w_{h_2} are measures of the OTF widths, and k_1 and k_2 are integers in the range $\left\{-\lfloor \frac{N}{2} \rfloor, \lfloor \frac{N-1}{2} \rfloor\right\}$, where $\lfloor x \rfloor$ is the greatest integer that is less than or equal to x. In all simulations, the channel parameters are taken from a measured pixelated wireless optical channel [58], and the parameters are presented in Table 4.1.

Table 4.1: Measured parameters of a pixelated wireless optical channel in [57,58]. The measured ρ is a worst case, calculated at the highest noise variance measured in [57,58].

N	w_{h_1}	w_{h_2}	ρ
154	41.01	41.85	56.05

All the measurements presented in Table 4.1 were done for a single receiver array with $N = 154$ pixels. For a given imager size, the receiving pixel area is inversely proportional to the number of pixels, N^2. Since, as mentioned in Sec. 2.3, both the DC-gain, H_0, and the channel noise power, σ_z^2, are directly proportional to the pixel area, then both of them are inversely proportional to N^2. Therefore, in light of (4.14), ρ is inversely proportional to N, and the following appropriate scaling of ρ is used during simulations

$$\rho_N = \rho_{154} \times \frac{154}{N}, \tag{4.18}$$

where ρ_N is the value of ρ when the imager is $N \times N$ pixels, and ρ_{154} is the value of ρ when the imager is 154×154 pixels, given in Table 4.1. Notice that the effect of changing the pixel area on the bandwidth of the OTF is negligible due to the very small pixel size relative to the PSF size as mentioned in Sec. 2.3.

The Gaussian OTF in (4.17) is plotted in Fig. 4.7 for $N = 256$ and $N = 512$. Due to the assumption that the imager size is fixed, increasing N results in a corresponding increase in the number of out-of-band spatial frequency bins as shown in Fig. 4.7(b). These extra out-of-band degrees of freedom can be used to accommodate the quantization noise power as shown in the next section.

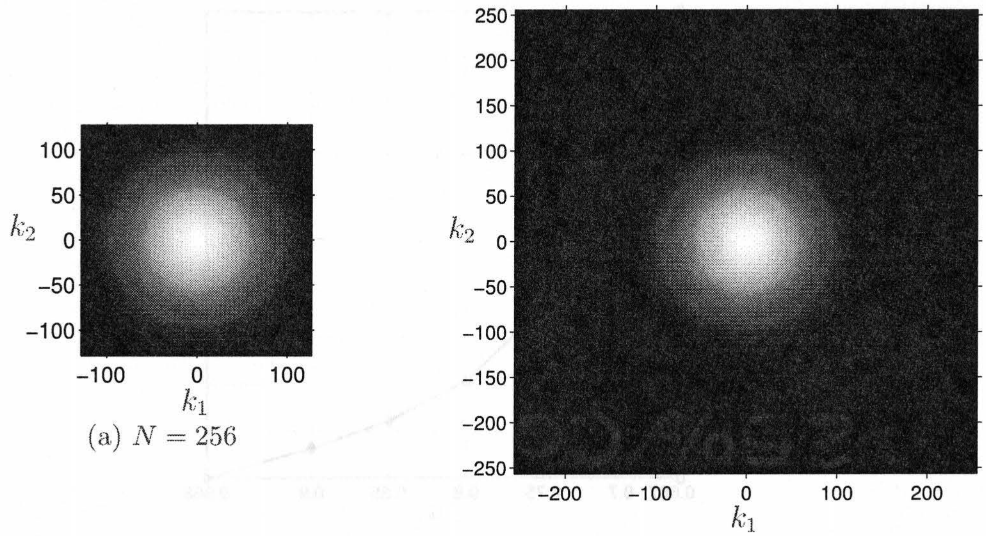

(a) $N = 256$

(b) $N = 512$

Figure 4.7: The Gaussian OTF of (4.17) for $N = 256$ and $N = 512$. Values of w_{h_1} and w_{h_2} are as in Table 4.1.

4.4.2 Halftoning Design

In this example, the following form for the error diffusion feedback filter is proposed

$$\begin{aligned} \jmath(0,0) &= 0, \\ \jmath(0,1) &= \jmath(1,0) = a, \\ \jmath(1,1) &= 1-2a. \end{aligned} \tag{4.19}$$

This filter is symmetric, causal, has unity DC-gain, and is among the simplest feedback filters that can be used for digital halftoning. The short length of the filter makes it faster and less complex to implement in real time. Another attractive feature is that a single parameter, a, indexes the entire family of filters. In this case,

$$\mathcal{E}_\jmath = \sum |\jmath(n_1,n_2)|^2 = 6a^2 - 4a + 1. \tag{4.20}$$

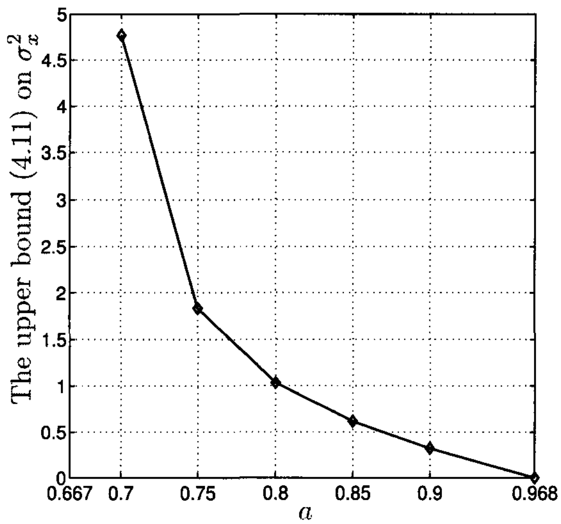

Figure 4.8: The upper bound (4.11) on σ_x^2.

Substituting from (4.20) in the bound (4.12), a is restricted to the interval

$$-0.3 < a < 0.968, \tag{4.21}$$

in order for the model to be consistent. For $a \in (-0.3, 0)$ or $(0.667, 0.968)$, then $\mathcal{E}_j > 1$, and the upper bound (4.11) on σ_x^2 is necessary. Notice also that $\mathcal{E}_j$ is increasing with $|a|$ on these two intervals. This upper bound is plotted in Fig. 4.8 for $a \in (0.667, 0.968)$, where it is shown that smaller values of σ_x^2 are required for higher values of a. This is attributed to the fact that higher values of σ_w^2 can saturate the binary-level quantizer, which consequently causes system instability as mentioned in Sec. 4.3.3. Since σ_w^2 is the sum of σ_x^2 and $\sigma_q^2 \mathcal{E}_j$, from (4.8), then a smaller σ_x^2 is required when $\mathcal{E}_j$ is high in order to prevent quantizer saturation. In the simulation results that follow, $\sigma_x^2 = 0.1$ is used which satisfies the upper bound (4.11) for all values of a considered.

A cross-section for $k_1 = k_2$ through the noise power shaping function $|1 - J(k_1, k_2)|^2$

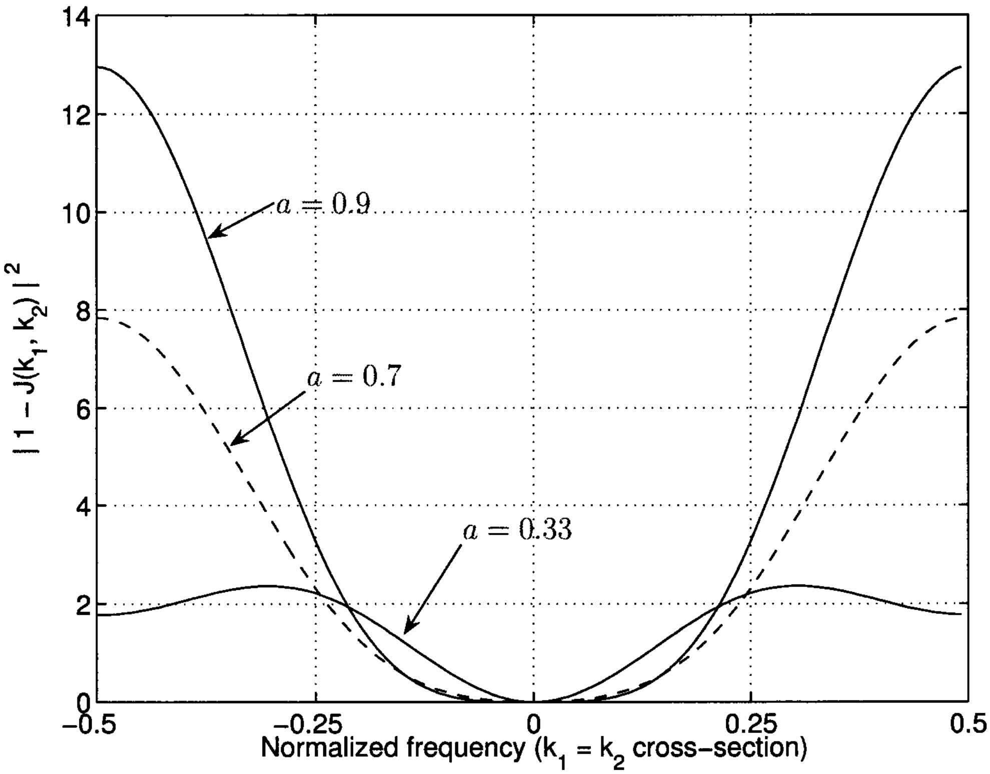

Figure 4.9: Cross-sections of the noise power shaping function, $|1 - J(k_1, k_2)|^2$, for $k_1 = k_2$ and a variety of feedback filter parameters a.

is plotted for different values of a in Fig. 4.9. It is straight forward to show that for $a = 1/3$, $\mathcal{E}_j$ is minimized. Consequently, $a = 1/3$ minimizes the total quantization noise power, in (4.7). However, $a = 1/3$ is not necessarily the best choice for J since the goal is to minimize the residual quantization noise in the spatial frequency bins which carry data, rather than minimizing the total quantization noise power. From the figure, it is evident that maximizing a is desirable, within (4.21), in order to widen the low quantization noise region around DC. The noise power shaping function, $|1 - J(k_1, k_2)|^2$, is plotted in Fig. 4.10 at $a = 0.9$.

The noise bowl, $N_1 N_2 \sigma_q^2 |1 - J(k_1, k_2)|^2 + N_1 N_2 / |\rho H(k_1, k_2)|^2$, is shown in Figs. 4.11

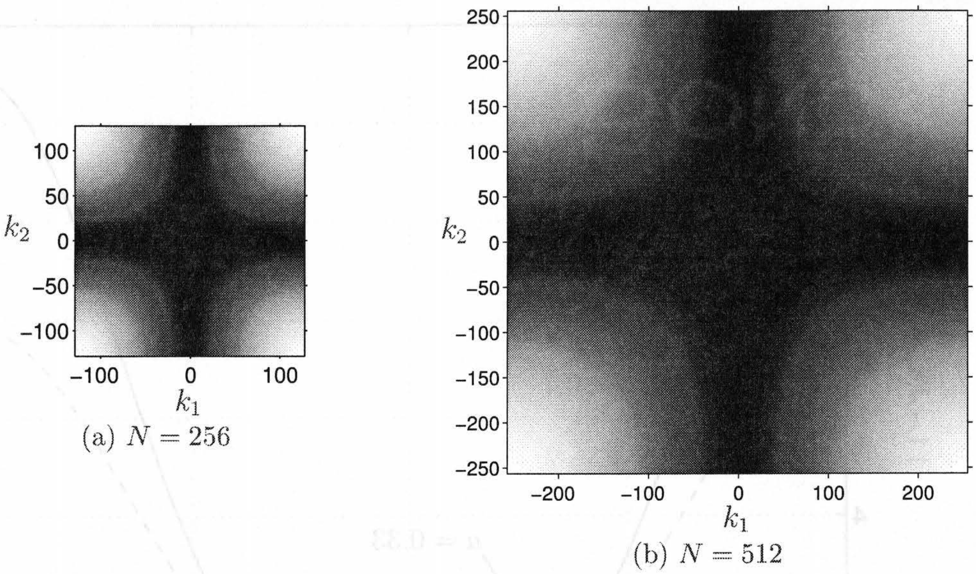

Figure 4.10: The noise power shaping function, $|1 - J(k_1, k_2)|^2$, for $N = 256$ and $N = 512$. The error diffusion filter parameter is taken as $a = 0.9$.

and 4.12 for $N = 512$ and $N = 256$, respectively. In general, the shape of the noise bowl depends on both the OTF and the noise shaping function. Comparing the bowls in Fig. 4.11(a) and Fig. 4.12(a), the shape of the noise bowl is dominated by the OTF at $N = 512$, and by the noise shaping function at $N = 256$. In order to maximize the capacity, power is poured over such noise bowls according to the water pouring algorithm [183, Sec. 10.4]. The capacity-maximizing power allocations are also shown in Figs. 4.11(b) and 4.12(b).

The error diffusion halftoning is performed by processing the input image, $x(n_1, n_2)$, in a raster scanning fashion as shown in Table 4.2. An example of a continuous-tone image is shown in Fig. 4.13 for $N = 512$, along with the corresponding halftoned image and their spectra. The complex data to be transmitted are loaded to the low frequency bins of the continuous-tone image as implied by the water pouring allocation of Fig. 4.11(b). By comparing the spectra in Figs. 4.13(c) and 4.13(d), it is

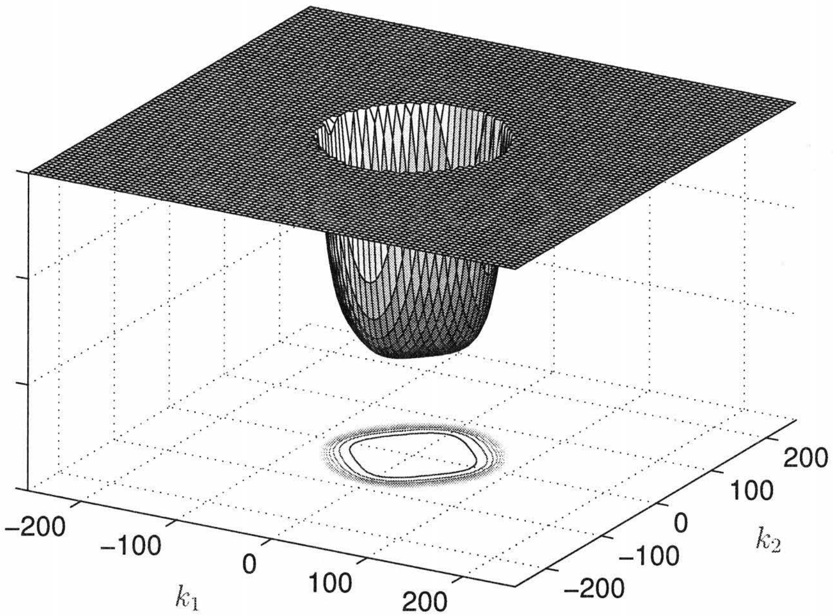

(a) Noise bowl

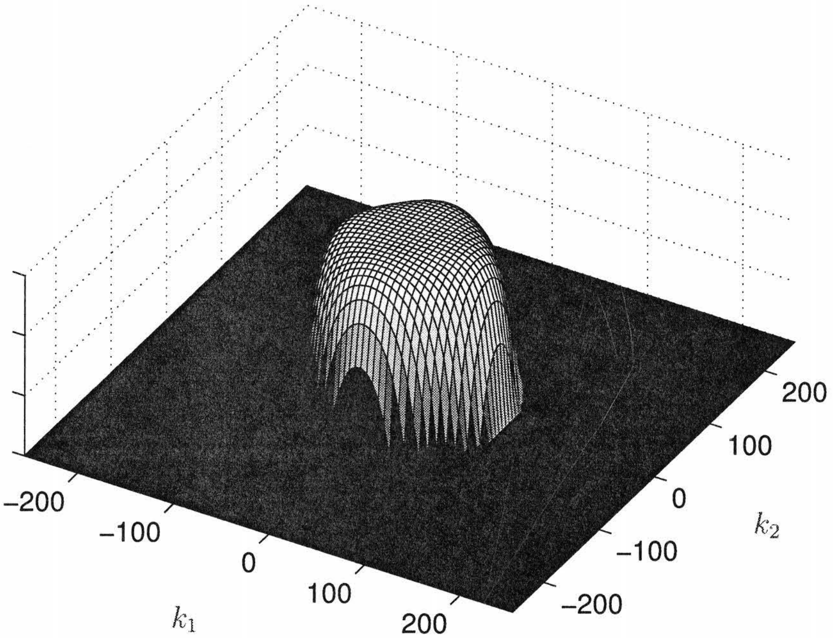

(b) Power allocation

Figure 4.11: *Optical power-limited system.* The noise bowl, $N_1N_2\sigma_q^2|1 - J(k_1, k_2)|^2 + N_1N_2/|\rho H(k_1, k_2)|^2$, and the water pouring power allocation are shown for $N_1 = N_2 = 512$. The error diffusion filter parameter is taken as $a = 0.9$, w_{h_1} and w_{h_2} as given in Table 4.1, and ρ as given by (4.18). An example transmit image is shown in Fig. 4.13.

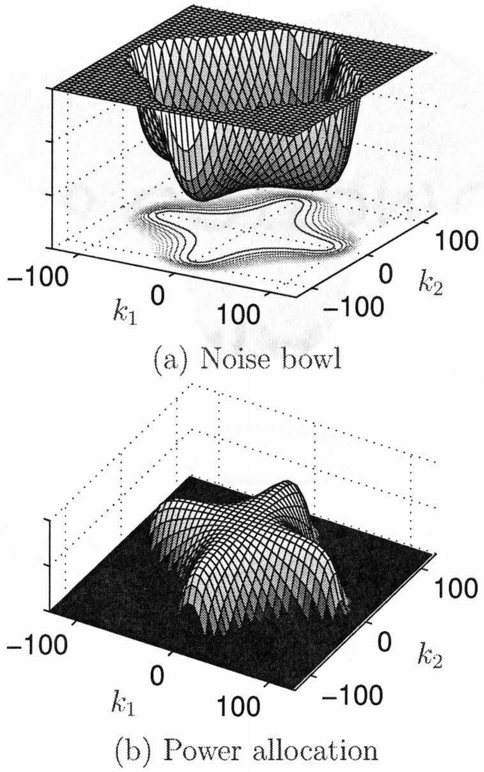

Figure 4.12: *Quantization noise-limited system.* The noise bowl, $N_1N_2\sigma_q^2|1 - J(k_1,k_2)|^2 + N_1N_2/|\rho H(k_1,k_2)|^2$, and the water pouring power allocation are shown for $N_1 = N_2 = 256$. The error diffusion filter parameter is taken as $a = 0.9$, w_{h_1} and w_{h_2} as given in Table 4.1, and ρ as given by (4.18). An example transmit image is shown in Fig. 4.14.

evident that the data can be recovered from the low frequency region of the halftoned binary-level image. A great majority of the quantization noise power is shaped to the out-of-band region, which is indicated by the four high power corners of the halftoned image spectrum. In this case, the system is optical power-limited as the effect of quantization noise is mild, and the shape of the in-band power allocation is dominated by the OTF.

A similar example is shown in Fig. 4.14 for $N = 256$. The complex data to be transmitted are loaded to the low frequency bins of the continuous-tone image as

Table 4.2: Raster scanning procedure. The feedback filter, $j(n_1, n_2)$, is assumed to be causal and have support on $n_1 \in \{0, 1, \cdots, M_1 - 1\}$ and $n_2 \in \{0, 1, \cdots, M_2 - 1\}$.

Input: $x(n_1, n_2)$ and $j(n_1, n_2)$
Output: $v(n_1, n_2)$
initialization: $\forall n_1, n_2,\ \ w(n_1, n_2) = x(n_1, n_2)$;
for $n_1 = 0$ **to** $N_1 - 1$ **do**
  for $n_2 = 0$ **to** $N_2 - 1$ **do**
    $v(n_1, n_2) = \begin{cases} +1 & : \text{ if } w(n_1, n_2) \geq 0 \\ -1 & : \text{ otherwise} \end{cases}$;
    $q(n_1, n_2) = v(n_1, n_2) - w(n_1, n_2)$;
    for $m_1 = 0$ **to** $M_1 - 1$ **do**
      for $m_2 = 0$ **to** $M_2 - 1$ **do**
        $w(n_1 + m_1, n_2 + m_2) = w(n_1 + m_1, n_2 + m_2) - q(n_1, n_2)\, j(m_1, m_2)$;
      end
    end
  end
end

implied by the water pouring allocation of Fig. 4.12(b). In this case, the system is quantization noise-limited due to the reduced number of out-of-band spatial modes to which quantization noise can be shaped, and the shape of the in-band power allocation is dominated by the quantization noise shaping function $|1 - J(k_1, k_2)|^2$. Qualitatively, data can not be fully recovered from the low frequency region of the spectrum of the halftoned image because of the in-band quantization noise. As will be shown in Sec. 4.4.3, the reduction in capacity resulting from reducing N from 512 to 256 is nearly 51.7%.

Notice that the capacity of the HSDMT system, or any finite-level SDMT system, is upper bounded by that of a continuous SDMT transmitter with the same σ_x^2 neglecting the non-negativity amplitude constraints. This upper bound is given by (4.15) with $\Phi_{\tilde{q}}(k_1, k_2) = 0$.

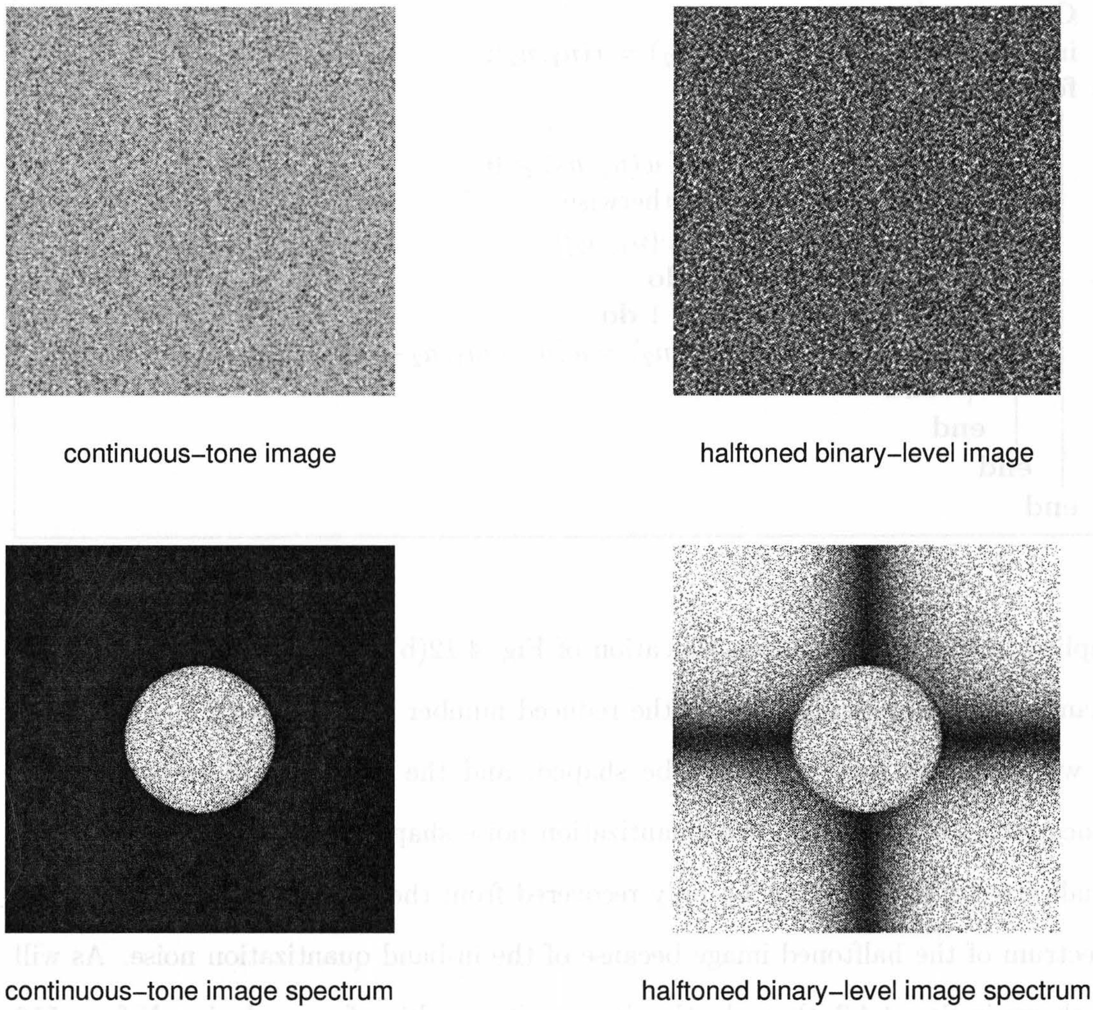

Figure 4.13: *Optical power-limited system.* (a) Continuous-tone image. (b) Corresponding halftoned image. (c) Spectrum of continuous-tone image. (d) Spectrum of halftoned image. $N = 512$, $a = 0.9$, $\sigma_x^2 = 0.1$, w_{h_1} and w_{h_2} as given in Table 4.1, and ρ as given by (4.18).

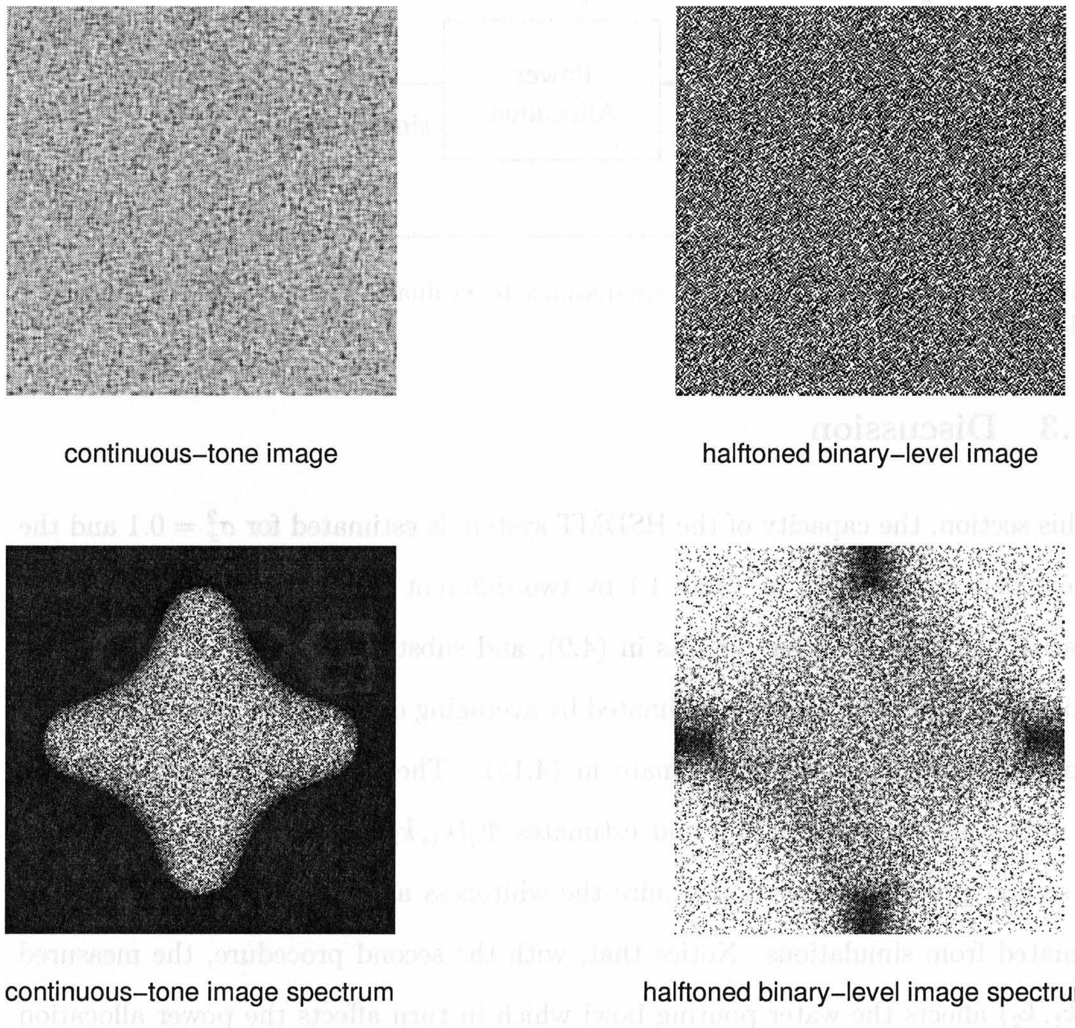

Figure 4.14: *Quantization noise-limited system.* (a) Continuous-tone image. (b) Corresponding halftoned image. (c) Spectrum of continuous-tone image. (d) Spectrum of halftoned image. $N = 256$, $a = 0.9$, $\sigma_x^2 = 0.1$, w_{h_1} and w_{h_2} as given in Table 4.1, and ρ as given by (4.18).

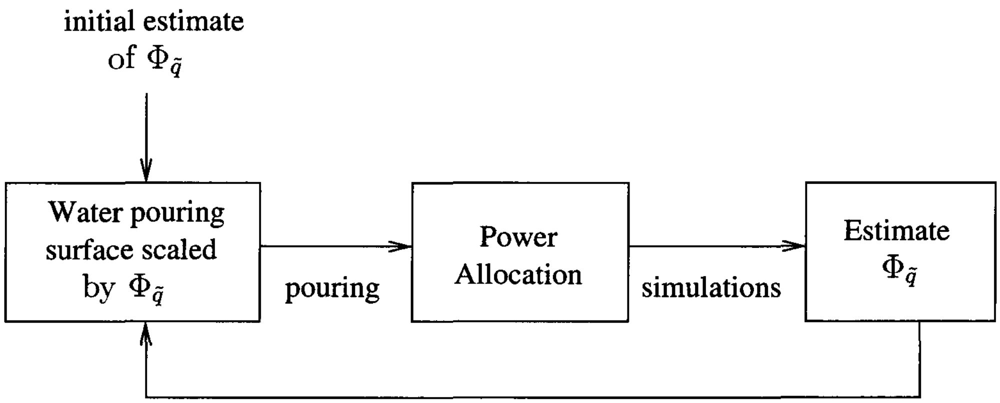

Figure 4.15: Iterations used in simulations to evaluate $\Phi_{\tilde{q}}(k_1, k_2)$ and the power allocation.

4.4.3 Discussion

In this section, the capacity of the HSDMT system is estimated for $\sigma_x^2 = 0.1$ and the system parameters given in Table 4.1 by two different procedures: (i) by using the linearized model to estimate σ_q^2, as in (4.9), and substituting in (4.16), and (ii) by simulations, where $\Phi_{\tilde{q}}(k_1, k_2)$ is estimated by averaging over 1000 randomly generated frames and substituting this estimate in (4.15). The first procedure is based on the whiteness assumption of q and estimates $\Phi_{\tilde{q}}(k_1, k_2)$ by using (4.6). Whereas, the second procedure does not require the whiteness assumption since $\Phi_{\tilde{q}}(k_1, k_2)$ is estimated from simulations. Notice that, with the second procedure, the measured $\Phi_{\tilde{q}}(k_1, k_2)$ affects the water pouring bowl which in turn affects the power allocation over the complex frequency bins which again impacts the quantization noise. As a result, the iterative scenario shown in Fig. 4.15 is used during simulations to allow $\Phi_{\tilde{q}}(k_1, k_2)$ to converge to the correct value for power allocation.

The results obtained from the linearized analytical model are compared to simulations in Fig. 4.16. It is evident that both model and simulations are in close agreement. Notice that the capacity increases with N due to the fact that the size of the out-of-band region increases with N^2, and hence the quantization noise can be shaped further from the data bearing region as in Figs. 4.13 and 4.14. However, the capacity saturates to a limiting value as N increases. This is due to the fact that, although the number of channels increases as N^2, the electrical SNR (proportional to ρ^2) decreases at the same rate as in (4.18). Additionally, larger values of a lead to high channel capacities. This is due to the fact seen in Fig. 4.9, that larger a allows for lower residual quantization noise in the band of interest. Notice however, as mentioned in Sec. 4.4.2 and shown in Fig 4.8, as a increases, σ_x^2 must decrease to ensure stability of the halftoning modulator.

Fig. 4.16 compares the capacity of the HSDMT system to an upper bound obtained by employing a continuous unconstrained SDMT transmitter with the same σ_x^2. The gap between the capacities of the binary-level transmission and the continuous-amplitude transmission diminishes as N increases. This gap approaches zero in the limit $N \to \infty$ as the in-band quantization noise also approaches zero on this limit. Thus, for a given OTF, increasing the number of excess spatial degrees of freedom allows a binary-level SDMT transmitter to approach the same capacity as the optical power-limited regime.

Fig. 4.16 also compares the capacity of the HSDMT system to that of the experimental 256-level SDMT system measured in [58] at $N = 154$. The coded rate achieved in [58] is also indicated at the same value of N. The binary-level system with $a = 0.9$ achieves 57.37% of the capacity of the 256-level system for $N = 154$. Thus, for small N, quantization noise-limited channels benefit greatly from multi-level output. The capacity of the continuous system is an upper bound for both the 256-level and the

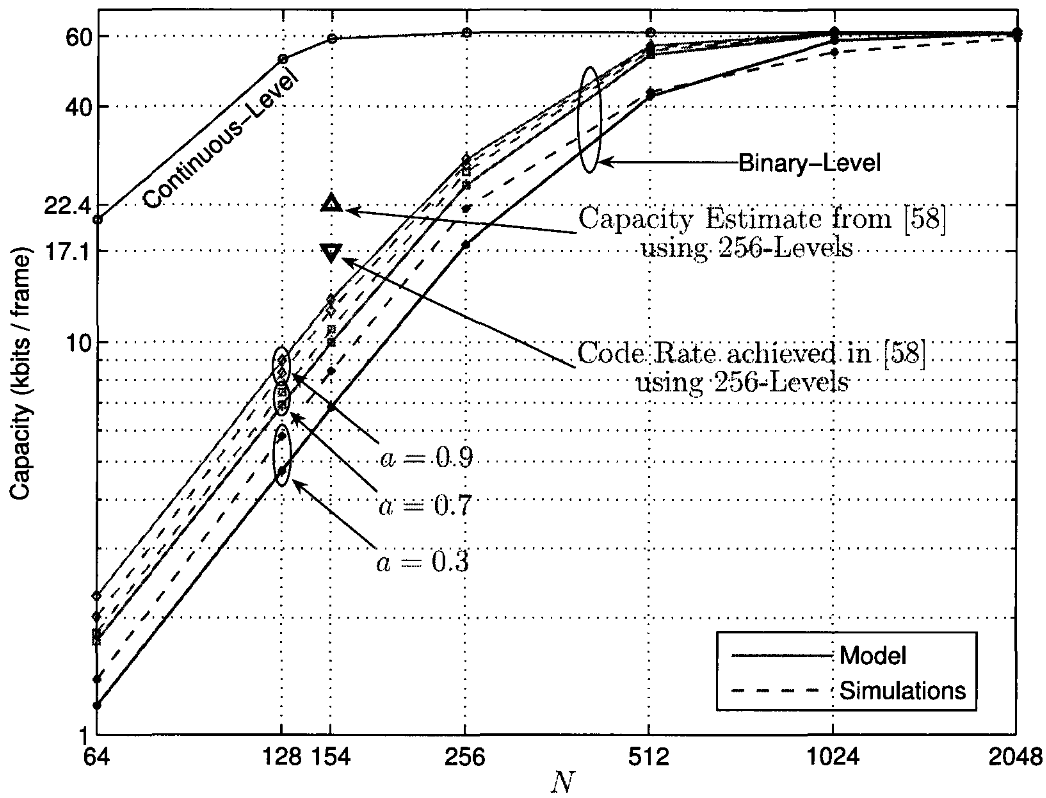

Figure 4.16: Capacity of the pixelated channel versus $N = N_1 = N_2$ with $\sigma_x^2 = 0.1$. Results of the linearized analytical model in Sec. 4.3.4 are compared to those from simulations, and to those of a continuous SDMT transmitter without non-negativity constraint. The capacity estimate ($\triangle$) and code rate ($\bigtriangledown$) achieved in [58] using 256-level transmitter are also shown at $N = 154$.

binary systems. At higher values of N, the capacity of the binary system approaches the continuous-amplitude upper bound. For instance, the binary system ($a = 0.9$) achieves approximately 92.6% of the upper bound at $N = 512$, and nearly 99.8% at $N = 1024$. This suggests that employing more than two quantization levels is not necessary as N gets large, because the system is optical power-limited in this case, and quantization noise is effectively shaped out-of-band.

4.5 Experimental Prototype Pixelated Wireless Optical Channel

In this section, an experimental prototype of a pixelated wireless optical channel is constructed to measure the salient channel parameters [159]. Unlike Sec. 4.4, where the imager size has been assumed constant and increasing the number of receiving pixels has been achieved by decreasing the pixel size, a more practical assumption of having a fixed pixel size is considered in this section. This allows for ρ to be independent of the array size, N, and for the capacity to increase proportional to the number of pixels, N^2, since the sizes of both the in-band and out-of-band regions increase with the same proportion. That is, if N is doubled, the number of complex frequency channels is multiplied by four, and so approximately is the capacity.

4.5.1 Experimental Setup

The transmitter is based on a commercial digital light processing (DLP) projector [201, LT30] which projects its image onto a flat wall. The circuitry of the projector has been replaced with a controller board for the DLP which allows freedom to transmit any sequence of stored images [188]. This configuration allows for frame rates of up to 10 kfps and a maximum resolution of 1024×768 pixels. The illumination source of the projector has been replaced with a metal halide machine vision illuminator that is coupled to the projector optics using a 1/2" fiber optic lightguide as shown in Fig. 4.17.

The receiver is a high speed mega-pixel CMOS digital camera [202, MC1310] which captures the image projected on the wall. The camera is connected to a frame

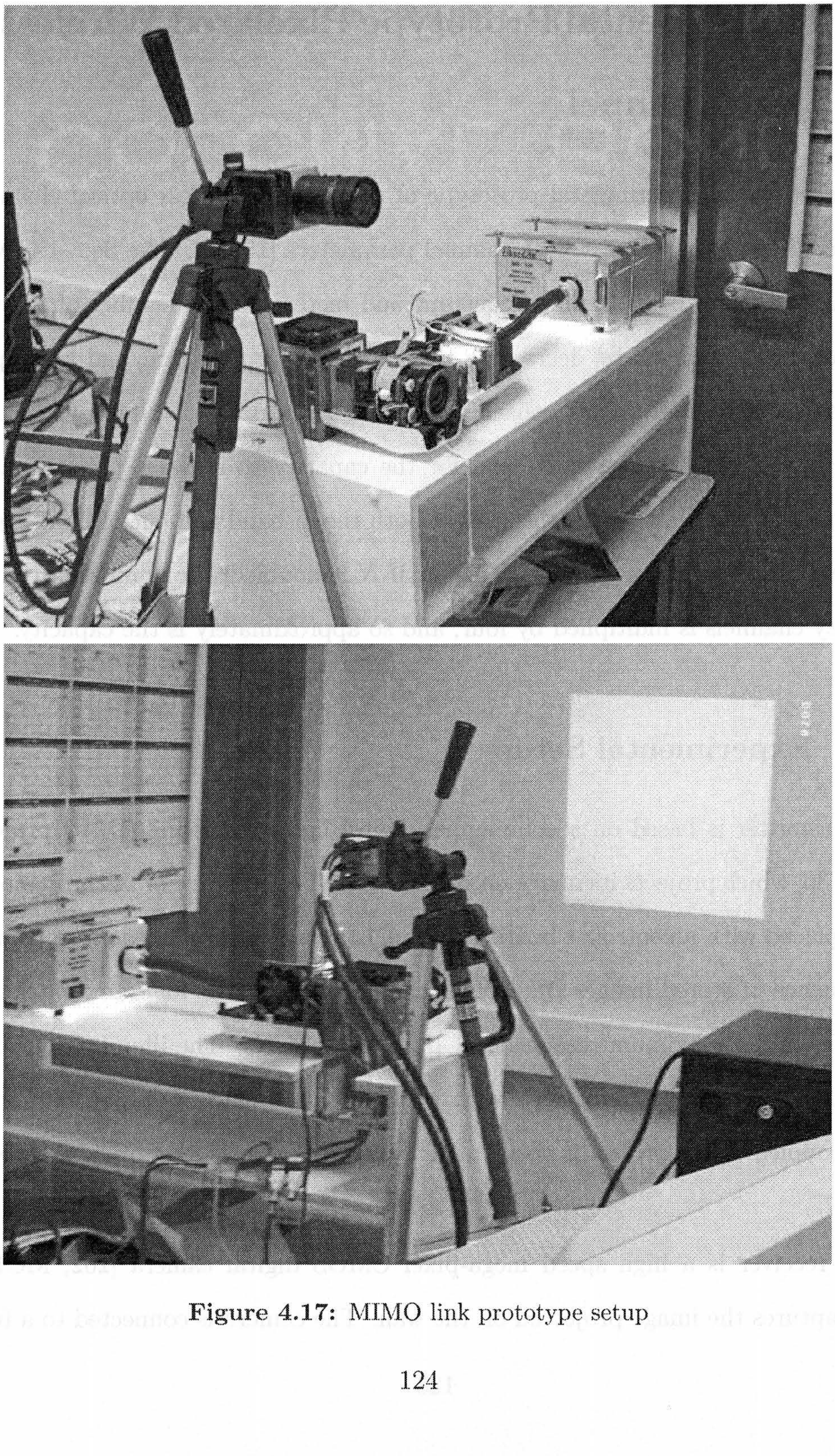

Figure 4.17: MIMO link prototype setup

grabber [203, Odyssey XCL] using the full camera link configuration which is capable of transferring data at a maximum rate of 660 Megabytes per second (MBps). Digital recording software [204, Streampix] is used to capture and store the received frames. Temporal synchronization is achieved by using a signal generator card [205, NI6601] that generates trigger pulses that drive both the transmitter and receiver. When a trigger pulse is received by the projector, an image is projected onto the wall. After a few microseconds delay, the camera starts integrating the spatial intensity image. The integration time of the camera is controlled by a programmable shutter, with exposure time less than the illumination period of the frame.

The separation distance between the camera, and the projected image was set to 1.1 m. The camera was positioned to ensure that its optical axis aligns with that of the image in order to minimize the projective distortion. The focal length of the projector was adjusted to get unity magnification (i.e. image size in pixels is the same at both transmitter and the receiver). To mitigate hardware limitations and generate consistent measurements, the operating frame rate was fixed to 100 frames per second (fps), and the programmable shutter was used to adjust the exposure time such that the effective frame rate is given by the inverse of the exposure time. As the exposure time changes, the sensor gain was manually adjusted such that the histogram of the received image occupies the full dynamic range (0 to 255) of the sensor. Therefore the optical SNR is given by $\rho = 127.5/\sigma_z$ for the experimental prototype link considered.

Channel noise measurements were performed by transmitting and receiving sequences of dark and illuminated frames. The channel noise consists of fixed pattern noise, due to variations over the sensor array, and signal-independent noise. For each frame rate, the fixed pattern noise is estimated by sending 1000 dark frames and

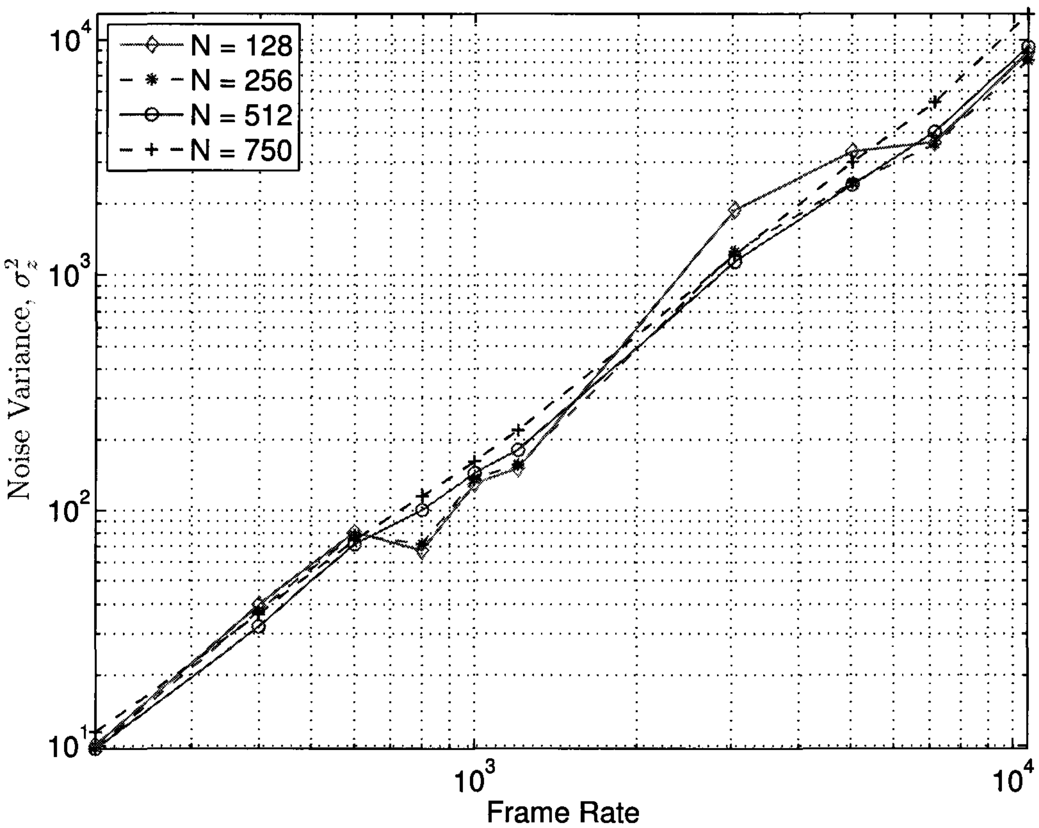

Figure 4.18: Measured noise variance, σ_z^2, of the experimental prototype link versus frame rate for different values of N.

averaging over the received frames. The signal-independent noise is estimated by averaging over 1000 dark frames and 1000 illuminated frames. By assuming that the noises of neighboring pixels are independent, the complex noise in the discrete frequency domain is white. The measured values of σ_z^2 are plotted versus frame rate in Fig. 4.18.

Since the OTF is the Fourier transform of the channel impulse response, it can be measured by computing the Fourier transform of the received image given that a spatial intensity impulse is transmitted. The transmit impulse can be approximated by turning a single transmit pixel on, while all other pixels are kept off. However, the received power in this case is very low to be accurately detected by the receiver array. Therefore, the channel OTF is measured by sending a narrow spatial pulse (2×2 pixels) at different positions in space (top left, top right, center, bottom left, and bottom right). For each pulse position, 1000 frames were captured and the average OTF was computed. Using least-squares fitting, the average OTF is fitted to a 2D Gaussian shape. The obtained widths are $w_{h_1} = 137.12$ and $w_{h_2} = 141.16$ for a 768×768 frame. Therefore, $w_{h_1} = 137.12 \times \frac{N}{768}$ and $w_{h_2} = 141.16 \times \frac{N}{768}$ are used in simulations. It is also possible to measure the OTF by performing a 2D frequency sweep. That is, by sending a sequence of all spatial harmonics, and measuring the corresponding frequency response. However, this approach is difficult in practice since the number of spatial harmonics is on the order of N^2.

4.5.2 Halftoning Design

As in Sec. 4.4.1, the receiver is $N \times N$ pixels, while the transmitter is $(N+\tilde{N}) \times (N+\tilde{N})$, where $\tilde{N}$ is the width of the cyclic extension. The feedback filter is taken as

$$\begin{aligned} \jmath(0,0) &= 0, \\ \jmath(0,1) &= \jmath(1,0) = 0.9, \\ \jmath(1,1) &= -0.8, \end{aligned}$$

and $\sigma_x^2 = 0.2$ is used, which satisfies the upper bound (4.11) that is necessary for the modulator stability. At this value of σ_x^2, the cross-correlation between the signal and the quantization noise,

$$\frac{\sum_{n_1}\sum_{n_2}\left(\tilde{q}(n_1,n_2)-\mu_{\tilde{q}}\right)\left(x(n_1,n_2)-\mu_x\right)}{\sqrt{\left(\sum_{n_1}\sum_{n_2}\left(\tilde{q}(n_1,n_2)-\mu_{\tilde{q}}\right)^2\right)\left(\sum_{n_1}\sum_{n_2}\left(x(n_1,n_2)-\mu_x\right)^2\right)}},$$

is about 2.5%, where $\mu_{\tilde{q}} = \frac{1}{N^2}\sum_{n_1}\sum_{n_2}\tilde{q}(n_1,n_2)$ and $\mu_x = \frac{1}{N^2}\sum_{n_1}\sum_{n_2}x(n_1,n_2)$. The higher σ_x^2, the higher the correlation, which violates the aforementioned assumption of signal-independent quantization noise.

An example of a continuous-tone image is shown in Fig. 4.19 for a frame rate of 7.142 kfps, along with the corresponding halftoned image and their spectra. Comparing the spectra in Figs. 4.19(c) and 4.19(d), it is clear that a great majority of the quantization noise power is shaped to the out-of-band region, and the system is optical power-limited. A similar example for a frame rate of 400 fps is shown in Fig. 4.20. The channel noise at this frame rate is far lower than that at the higher frame rate of Fig. 4.19, i.e. higher value of ρ. As a result, the system is quantization noise-limited.

4.5.3 Discussion

The capacity of the HSDMT system, or any finite-level SDMT system, is bounded above by that obtained by setting $\Phi_{\tilde{q}}(k_1,k_2) = 0$ in (4.15). The capacity of the HSDMT system, measured in kilobits per frame (kbpf) and Mbps, is compared to this upper bound in Figs. 4.21 and 4.22 respectively.

At a given frame size, the capacity per frame decreases with the frame rate in Fig. 4.21. This is because the channel noise variance, σ_z^2, increases with the frame

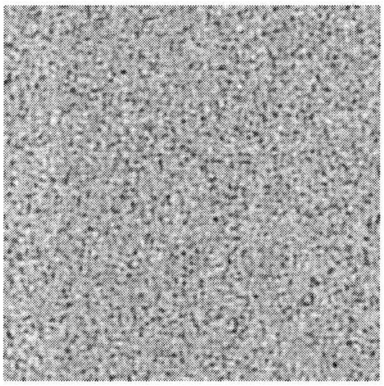

(a) continuous–tone image

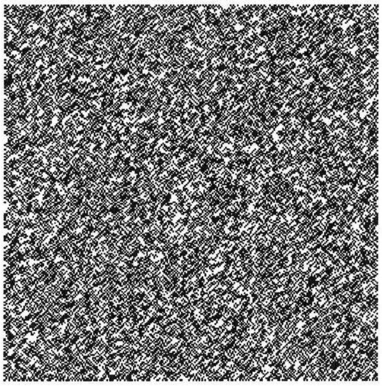

(b) halftoned binary–level image

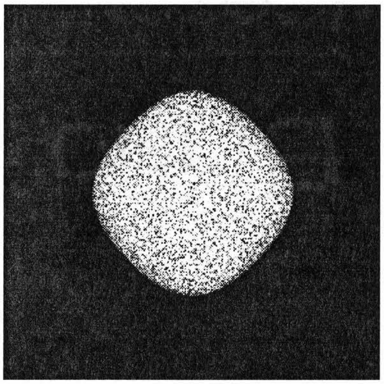

(c) continuous–tone image spectrum

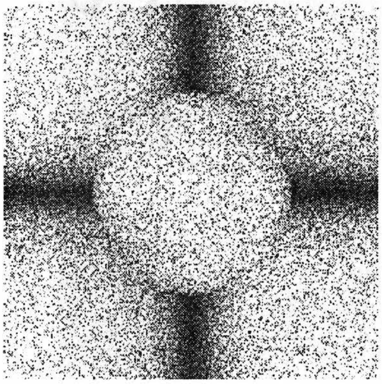

(d) halftoned binary–level image spectrum

Figure 4.19: *Optical power-limited system.* (a) Continuous-tone image. (b) Corresponding halftoned image. (c) Spectrum of continuous-tone image. (d) Spectrum of halftoned image. For 7.142 kfps, $N = 256$, $\sigma_x^2 = 0.2$, $w_{h_1} = 49.57$, $w_{h_2} = 48.29$, and $\rho = 2.13$. The images are based on experimental measurements.

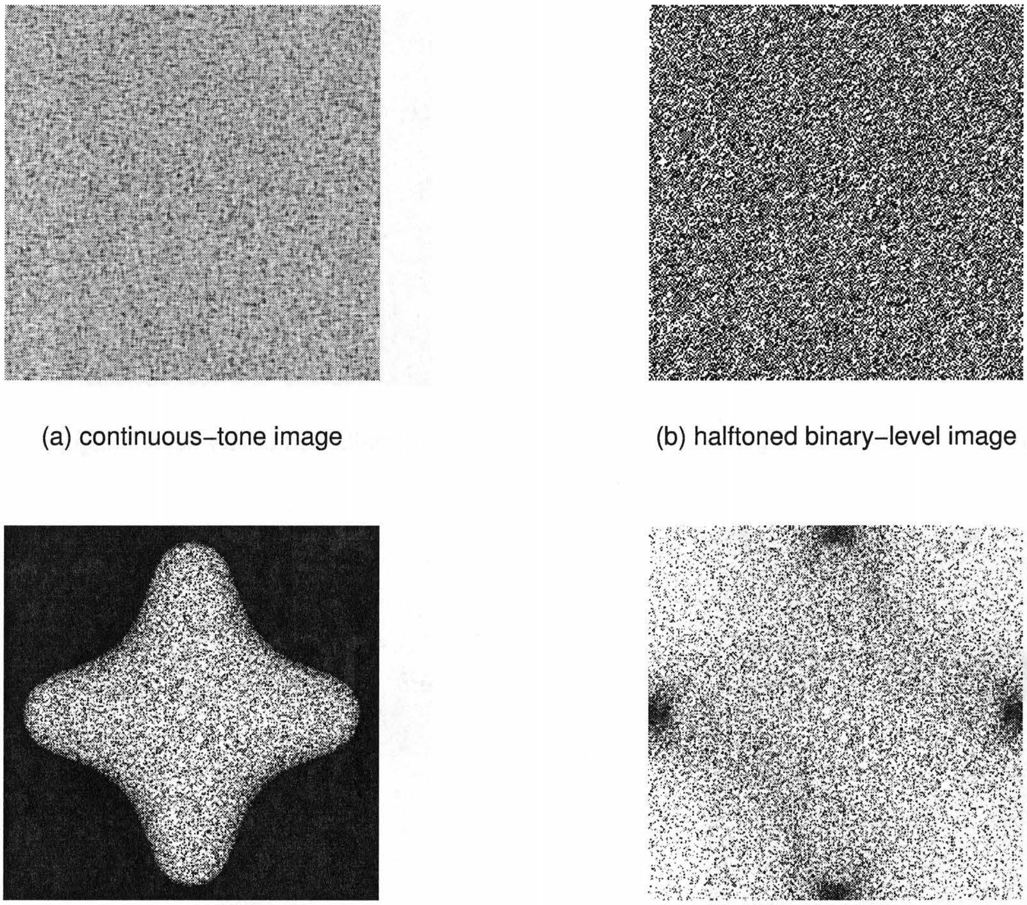

(a) continuous–tone image

(b) halftoned binary–level image

(c) continuous–tone image spectrum

(d) halftoned binary–level image spectrum

Figure 4.20: *Quantization noise-limited system.* (a) Continuous-tone image. (b) Corresponding halftoned image. (c) Spectrum of continuous-tone image. (d) Spectrum of halftoned image. For 400 fps, $N = 256$, $\sigma_x^2 = 0.2$, $w_{h_1} = 49.57$, $w_{h_2} = 48.29$, and $\rho = 20.83$. The images are based on experimental measurements.

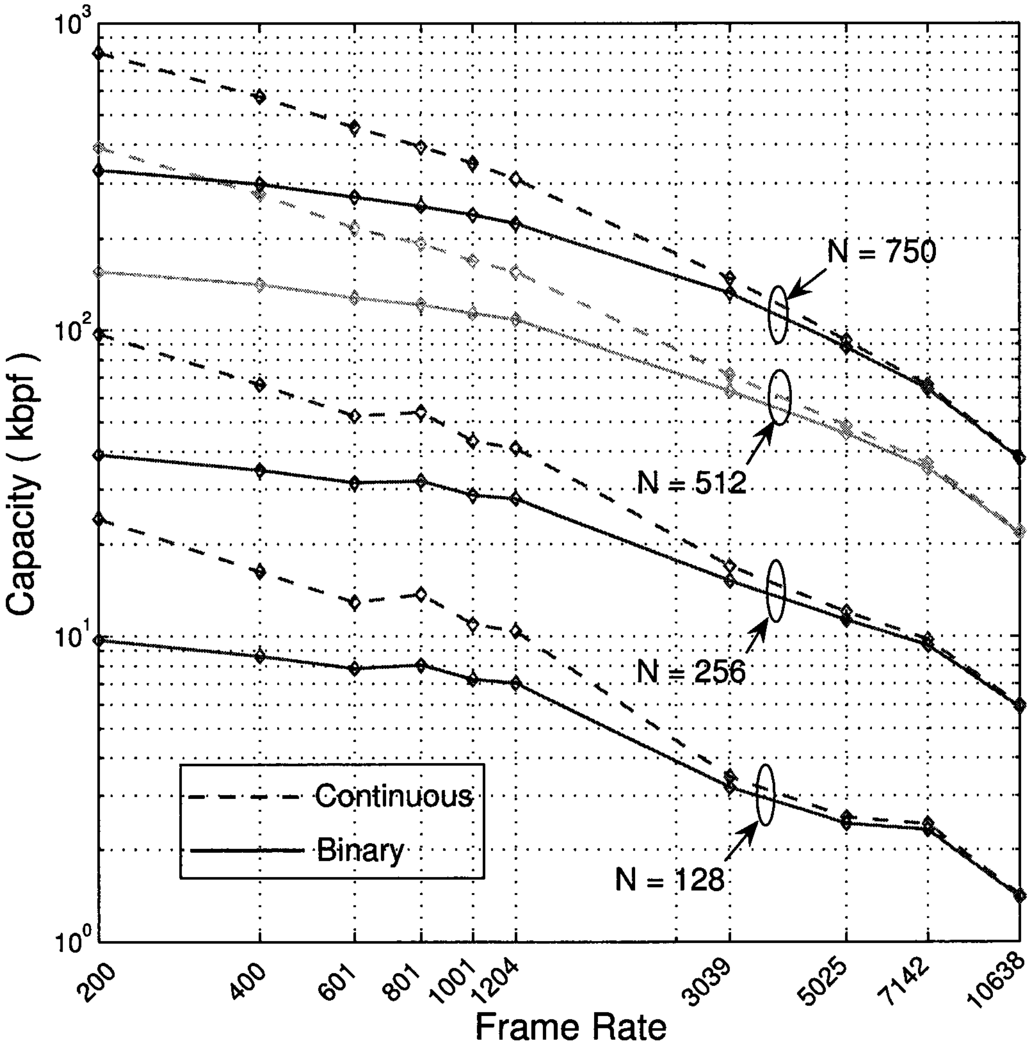

Figure 4.21: Capacity of the pixelated channel, in kbpf, versus frame rate with $\sigma_x^2 = 0.2$. The linearized analytical model in Sec. 4.3.4 is compared to a continuous SDMT transmitter without non-negativity constraint. The presented results are based on the measured channel parameters.

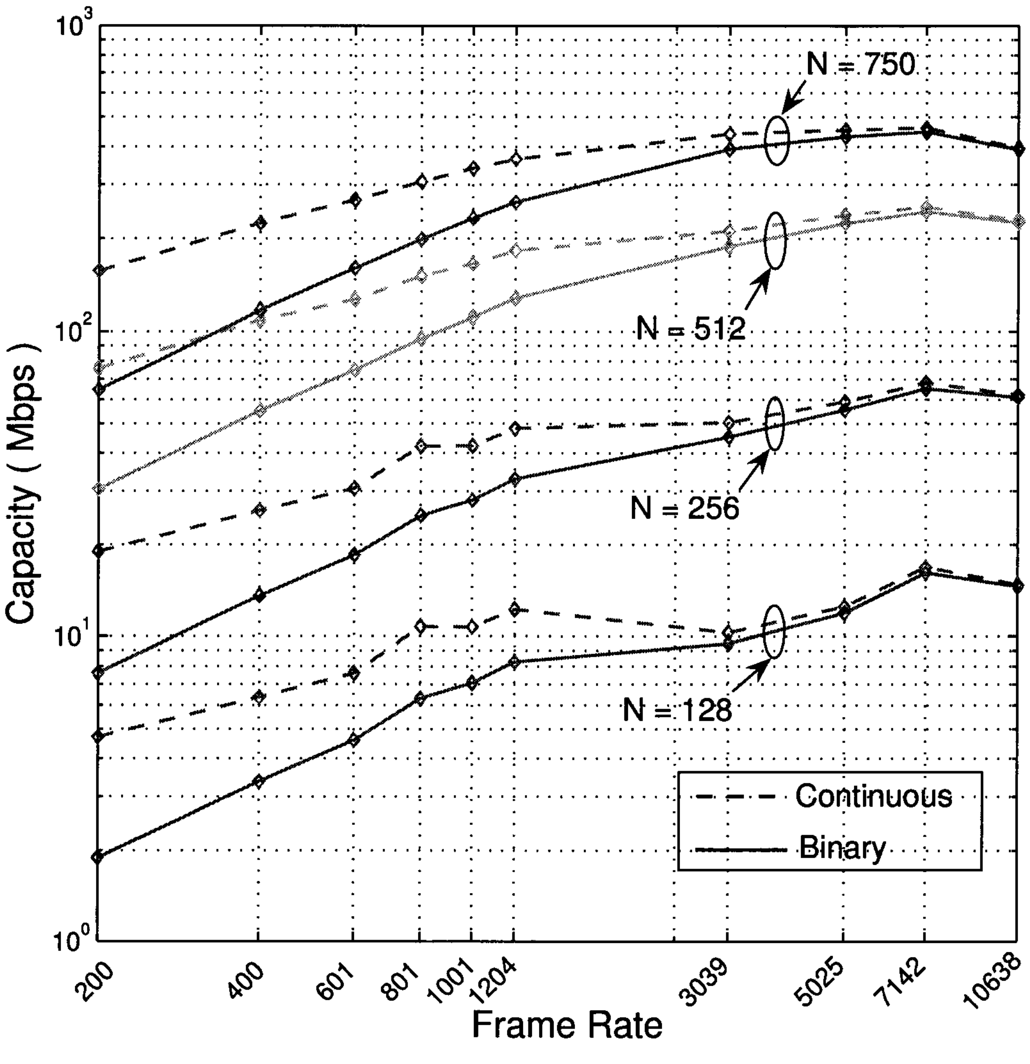

Figure 4.22: Capacity of the pixelated channel, in Mbps, versus frame rate with $\sigma_x^2 = 0.2$. The linearized analytical model in Sec. 4.3.4 is compared to a continuous SDMT transmitter without non-negativity constraint. The presented results are based on the measured channel parameters.

rate as shown in Fig. 4.18. Hence the system tends to be optical power-limited as the frame rate increases, and the capacity of the binary-level transmitter approaches the upper bound as shown in Figs. 4.21 and 4.22.

On the other hand, the capacity in Mbps increases with frame rate, as in Fig. 4.22, at low and moderate frame rates. If the channel noise were uncorrelated in time, then σ_z^2 would increase linearly with the frame rate, and therefore, from (4.14), ρ would vary inversely as the square root of the frame rate. In this case, the capacity would saturate to a limiting value as the frame rate increases due to the fact that the number of channel uses per second increases as the frame rate, and the electrical SNR (proportional to ρ^2) decreases at the same rate. In Fig. 4.22, the capacity does not saturate as the frame rate increases. In fact it decreases beyond a frame rate of 7.142 kfps, where maximum capacity is achieved. This is attributed to the fact that the noise is not white for this experimental link.

4.6 Conclusions

The capacity and data rates of indoor point-to-point wireless optical channels can be significantly improved by using spatial degrees of freedom. In this chapter, the design of these channels has been considered in which only binary-level optical intensity transmitters are used. The approach proposed combines SDMT modulation with halftoning ideas from image processing. Using a simple error diffusion filter, the channel capacity using a binary-level transmitter has been shown to approach that when using an idealized continuous transmitter that is capable of transmitting positive and negative amplitudes. In practice, the capacities reported in this chapter could be approached using spatio-temporal coding of the data bins, as was done in [58] for a pixelated wireless optical channel. However, the goal of this chapter is to demonstrate that the fundamental limits of pixelated channels with binary-level transmission are significant and merit continued study.

In the next chapter, spatial degrees of freedom are used to improve detection in FSO links.

Chapter 5

Diversity Reception for FSO Communications using Linear Projections

5.1 Introduction

This chapter treats the detection problem for point-to-point outdoor FSO channels. Unlike indoor wireless optical links, treated in Chapters 3 and 4, outdoor FSO links suffer from atmospheric turbulence effects. While the transmitter temporal and spatial degrees of freedom have been used in Chapters 3 and 4 for modulation design, the receiver spatial degrees of freedom are used in this chapter to improve symbol detection.

For atmospheric FSO links, the PSF is subject to random spatial fluctuations, as shown in Fig. 1.6, and is subject to random excursions in the focal-plane. Spatial diversity reception can be achieved through the use of a multiple-detector array receiver to mitigate the PSF degradation due to atmospheric turbulence. However, as mentioned in Sec. 1.3.4, it is quite expensive to build multiple-detector array imagers which are (i) high-speed, (ii) operating in the photon-counting mode, and (iii) operating in the infrared spectral region.

This chapter proposes a novel spatial diversity receiver that eliminates the need for such expensive multiple-detector imaging arrays. The proposed receiver provides spatial diversity in the detection process by using at most four photodetectors and three DMD arrays. It estimates the turbulence-degraded PSF and simultaneously employs this estimate to improve the detection accuracy [160–163].

As described in Sec. 5.4, only two of the four photodetectors are used for detecting the transmitted pulse. These two detectors need to operate at the high pulse transmission rate. The other two detectors are used solely for PSF estimation, and are operated at the same rate as the DMD arrays, which is much slower than the pulse transmission rate. For example, while the transmitted pulse duration is on the order of nanoseconds and the turbulence varies on time-scales of milliseconds, the DMD switching period is on the order of microseconds [206].

Since it is less expensive to build two high-speed single detectors than a high-speed multiple-detector array, the proposed DMD receiver is less expensive than the multiple-detector array receiver of Fig. 1.7. The DMDs are also less expensive when compared to high-speed multiple-detector array imagers [188, 206]. Although fixed-pattern and circuit noise are not considered in this chapter, the DMD receiver does not suffer from these types of noise that are associated with high-speed multiple-detector arrays. DMDs are passive optical components that do not add noise to the signal and have small insertion loss. Notice also that the DMD arrays operate over a wide range of wavelengths. This makes it much easier to modify the DMD receiver to allow operation at different wavelengths. Only the four detectors need to be replaced to operate at a different wavelength. On the other hand, modifying the multiple-detector array receiver requires the replacement of all the array elements.

5.2 Array Receiver

5.2.1 Receiver Model

For an array receiver, a lens collects the incident radiation on the receiver aperture and projects it onto a two-dimensional array of photodetectors that is placed in the focal-plane of the receiver lens, as shown in Fig. 1.7. Therefore, the PSF is given by the intensity distribution over the array surface. According to the channel model (2.14), the received optical power, incident on the n^{th} array element at time t, is given by

$$r_n(t) = \lambda_n(t) + \lambda_b(t), \tag{5.1}$$

where

$$\lambda_n(t) = \iint_{n^{\text{th}}\text{ element}} x(t)\, h_0\, h_t(u,v)\, dudv \tag{5.2}$$

is the signal power, in photons per second, incident over the n^{th} array element,

$$\lambda_b(t) = \iint_{n^{\text{th}}\text{ element}} z(t,u,v)\, dudv$$

is the background noise power, in photons per second, incident over the array element, $x(t) \in \{0,1\}$ is a binary-level transmit signal, $h_t(u,v)$ is the PSF defined in (2.2),

$z(t, u, v)$ is the background noise, and h_0 is a scaling factor that accounts for the transmit power and optical path loss. Notice that $\lambda_b(t)$ is independent of n. If $x(t) = 1$, then the collection of signal components $\{\lambda_n(t) : n = 1, 2, \cdots, N\}$ is termed the *pixelated* PSF, and the photodetector array is said to *pixelate* the PSF, where N is the number of array elements.*

For links employing PPM, $x(t)$ consists of a sequence of symbols, and each symbol consists of L successive chips such that one of the L chips is on, and $L - 1$ chips are off as mentioned in Sec. 3.2. Notice that $x(t) = 1$ during the interval of an on chip, and $x(t) = 0$ during the interval of an off chip. At the receiver, a photon-counting detector can be well modeled as a Poisson random point process as mentioned in Sec. 2.1.3. The process mean is equal to the integral of the optical power incident on the detector surface over the PPM chip duration [22]. Therefore, the output current samples of the n^{th} photodetector are proportional to a Poisson counting process

$$I_n^{(j)} \sim \text{Poisson}[\mu_n^{(j)}], \tag{5.3}$$

where $I_n^{(j)}$ is the photon count of the n^{th} detector at the end of the j^{th} PPM chip, and $\mu_n^{(j)}$ is the mean of $I_n^{(j)}$, given by

$$\mu_n^{(j)} = \int_{j\,T_c}^{(j+1)T_c} r_n(t)\, dt = K_n^{(j)} + K_b, \tag{5.4}$$

*Notice that the total number of array elements is represented by N in this chapter, whereas in Chapter 4, the total number of array elements has been represented by N^2.

where T_c is the PPM chip duration, and

$$K_n^{(j)} = \int_{j\,T_c}^{(j+1)T_c} \lambda_n(t)\,dt, \tag{5.5}$$

$$K_b = \int_{j\,T_c}^{(j+1)T_c} \lambda_b(t)\,dt, \tag{5.6}$$

are the signal energy, in photons, incident over the n^{th} array element during the j^{th} PPM chip duration, and the background noise energy in photons per array element per chip duration, respectively. Notice that K_b is assumed independent of j [147]. The total signal energy, in photons, incident over the entire array during the j^{th} PPM chip duration is given by

$$K^{(j)} = \sum_{n=1}^{N} K_n^{(j)} = \begin{cases} K^{\text{ON}} & : \; j^{\text{th}} \text{ PPM chip is on} \\ 0 & : \; j^{\text{th}} \text{ PPM chip is off,} \end{cases} \tag{5.7}$$

where K^{ON} is the total signal energy in photons per chip duration, when the chip is on. While the shape of $h_t(u, v)$ defines the redistribution of energy in space, the value of K^{ON} is dependent on the PPM chip duration, T_c, and the scaling factor, h_0, in (5.2). As in [147], it is assumed that the fluctuations in the total received signal energy, K^{ON}, can be ignored due to aperture averaging, i.e. K^{ON} is independent of j.

5.2.2 PSF Estimation

For simplicity of notation, define the vector $\mathbf{x}^{(j)}$ as the collection of signal energies,

$$\mathbf{x}^{(j)} = \left[K_1^{(j)}, K_2^{(j)}, \cdots, K_N^{(j)}\right]^{\text{T}},$$

where the transpose of a matrix is designated by the superscript 'T'. Notice that, if the j^{th} PPM chip is on, then $\mathbf{x}^{(j)}$ is the time integral of the pixelated PSF over the j^{th} PPM chip interval.

Practically, the FSO receiver attempts to estimate $\mathbf{x}^{(j)}$ for an on chip, rather than the PSF, $h_t(u, v)$, itself. This is the approach used in [134, 147] which is considered a benchmark for performance comparison in the numerical results of Sec. 5.6. In [134], the components of $\mathbf{x}^{(j)}$, for an on chip, are estimated as

$$K_n^{(j)} \approx \frac{1}{J}\left(\sum_{k=j-JL+1}^{j} I_n^{(k)} - JLK_b\right),$$

where J is the number of past PPM symbols involved in the estimation process. This implies that all the past JL images captured by the array imager need to be stored at the receiver.

5.2.3 Selection Combining

A simple and efficient detection technique is *selection combining* detection, where the elements with high SNR are summed and used for detection, while the other elements are ignored. Let the array elements be indexed by the set of indices $\mathsf{S} = \{1, 2, \cdots, N\}$, and let S be partitioned to two mutually exclusive sets $\mathsf{S}_{\mathcal{G}}$ and $\mathsf{S}_{\mathcal{B}}$ such that $\mathsf{S}_{\mathcal{G}}$ carries the indices of the good elements, i.e. the elements with high SNR, and $\mathsf{S}_{\mathcal{B}}$ carries the indices of the bad elements, i.e. the elements with low SNR. Since only the detector elements with high SNR contribute to the detection process, the decision statistic is given by

$$I_{\mathcal{G}}^{(j)} = \sum_{n \in \mathsf{S}_{\mathcal{G}}} I_n^{(j)}. \tag{5.8}$$

At the receiver, the decoded symbol is the symbol corresponding to the chip that produces the highest value for the decision statistic.

Another detection technique is *equal-gain combining* detection, where the outputs of all the N array elements are combined to produce the decision statistic. This is equivalent to the conventional single-detector receiver, and can be represented by the special case $\mathsf{S}_{\mathcal{G}} = \mathsf{S}$ and $\mathsf{S}_{\mathcal{B}} = \phi$.

In both cases of equal-gain and selection combining, the decision statistic in (5.8) is a sum of independent Poisson processes, and hence, is also a Poisson process. From (5.4) and (5.8), the mean of $I_{\mathcal{G}}^{(j)}$ is given by

$$\mu_{\mathcal{G}}^{(j)} = \sum_{n \in \mathsf{S}_{\mathcal{G}}} K_n^{(j)} + |\mathsf{S}_{\mathcal{G}}| K_b, \tag{5.9}$$

where $|\mathsf{S}_{\mathcal{G}}|$ is the cardinality of $\mathsf{S}_{\mathcal{G}}$. Since the decision statistic is Poisson distributed, an upper bound on the SER of L-PPM can be calculated as

$$\mathrm{SER}^{(j)} < \sum_{n=0}^{\infty} p_{sb}(n) \left[1 - \left(\sum_{k=0}^{n-1} p_b(k) \right)^{L-1} \right], \tag{5.10}$$

where p_{sb} is the Poisson probability mass function of mean $\mu_{\mathcal{G}}^{(j)}$, and p_b is the Poisson probability mass function of mean $|\mathsf{S}_{\mathcal{G}}| K_b$ [207].

The partitioning of S to $\mathsf{S} = \mathsf{S}_{\mathcal{G}} \cup \mathsf{S}_{\mathcal{B}}$ at every time interval can be performed by sorting the estimated signal distribution such that $K_{n_1}^{(j)} \geq K_{n_2}^{(j)} \cdots \geq K_{n_N}^{(j)}$, and setting $\mathsf{S}_{\mathcal{G}} = \{n_1, n_2, \cdots, n_{|\mathsf{S}_{\mathcal{G}}|}\}$ and $\mathsf{S}_{\mathcal{B}} = \{n_{|\mathsf{S}_{\mathcal{G}}|+1}, \cdots, n_N\}$ [134, 147]. The optimal value of the number of good elements, i.e. $|\mathsf{S}_{\mathcal{G}}|$, can be determined by exhaustive optimization. That is, by simulating the system for all values $|\mathsf{S}_{\mathcal{G}}| \in \{1, 2, \cdots, N\}$ and choosing the value that corresponds to the lowest SER. This exhaustive optimization is not easy to implement in practice, however, it is performed in Sec. 5.6, as in [134, 147], in order to demonstrate the performance improvement limits of selection over equal-gain combining. Some practical methods to determine a sub-optimal value for $|\mathsf{S}_{\mathcal{G}}|$ are given in [134].

5.3 DMD Receiver

In Sec. 5.2, it was shown that the array receiver is capable of performing the PSF estimation and the selection combining detection simultaneously. In Sections 5.3.2 and 5.3.3, it is shown that each of the two tasks can be performed by using a DMD, which is a simple and inexpensive passive optical element. In Sections 5.4 and 5.5, it will be shown that PSF estimation and selection combining can be performed simultaneously by using DMD arrays.

5.3.1 Digital Micromirror Devices

A DMD is a micro-electro-mechanical component that consists of an array of deflectable micromirrors [188, 206]. Each micromirror can be independently switched into one of two positions, and hence reflects the light incident on its surface to one of two predefined directions. In each of the two directions, a lens concentrates the reflected field onto a photodetector which outputs a current proportional to the integral of the incident fields over the detector surface. As is the case with the array imager, the DMD pixelates the spatial intensity distribution falling over its surface, which allows the optical computation of linear projections of the signal distribution onto an arbitrary binary basis. This concept has been employed in [208] to build a single-pixel camera that estimates the falling intensity image by computing its linear projections onto a random binary basis.

The DMD switching period, T_D, is the period of time during which the micromirrors are fixed in a given position. The DMD switching rate is the reciprocal of its switching period. Commercial DMD arrays of 1024×768 micromirrors are available at switching rates of 32.55 kHz [188, DLP® Discovery™ 4000] and 40 kHz [188, DLP® Discovery™ 1100], while faster DMDs whose switching period is about 8-16 µsec are used to eliminate motion blur in high-definition television [188, DLP® HDTV].

5.3.2 Selection Combining using a DMD

As shown in Fig. 5.1, the DMD array, M1, is placed in the focal-plane of the receiver lens such that the PSF is given by the intensity distribution over its surface. The micromirror array, which constitutes the surface of M1, pixelates the PSF. That is, if the number of micromirrors is N, then the PSF can be represented by an array of N optical powers that corresponds to the micromirror array of M1. Therefore, equation (5.1) can be used to describe the system, where the n^{th} element of the photodetector array, used in Sec. 5.2, is replaced by the corresponding n^{th} micromirror of M1.

As in Sec. 5.2, let the N micromirrors be indexed by $\mathsf{S} = \{1, 2, \cdots, N\}$, and let S be partitioned into two mutually exclusive sets $\mathsf{S}_{\mathcal{G}}$ and $\mathsf{S}_{\mathcal{B}}$ which carry the indices of the high and low SNR micromirrors respectively. This partitioning is performed as in Sec. 5.2.3, where a PSF estimate is assumed to be available. In Fig. 5.1, the micromirrors of M1, whose indices are in $\mathsf{S}_{\mathcal{G}}$, reflect their optical powers toward the

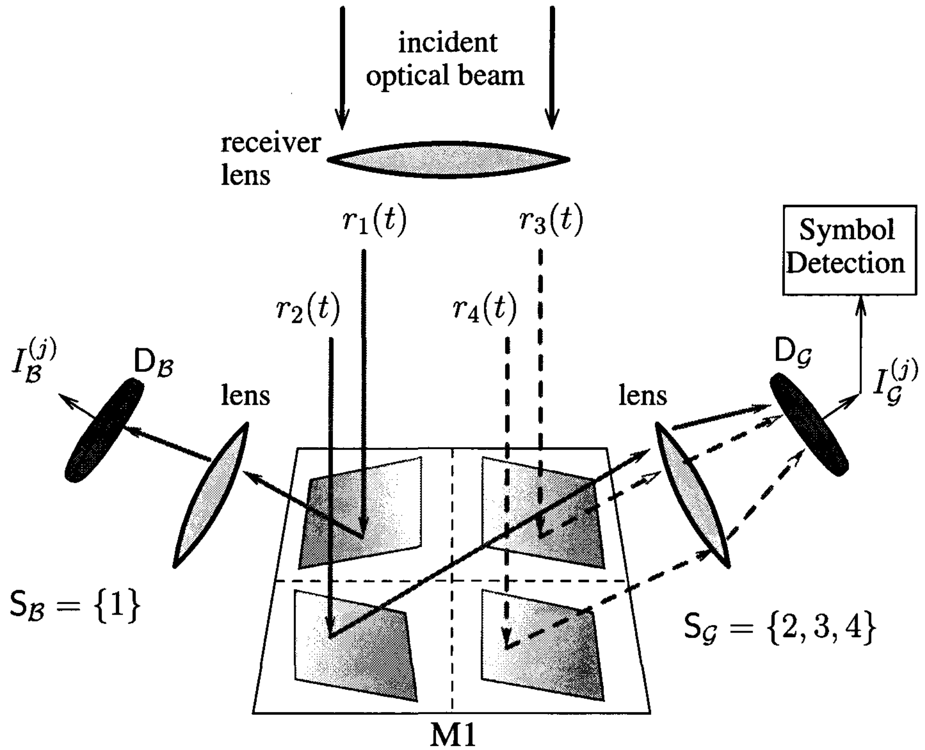

Figure 5.1: An illustration of how the DMD array is used to pixelate the PSF, and to perform the selection combining detection. For drawing simplicity, the number of micromirrors is taken as $N = 4$. In this diagram, $\mathsf{S} = \{1, 2, 3, 4\}$, $\mathsf{S}_{\mathcal{B}} = \{1\}$, and $\mathsf{S}_{\mathcal{G}} = \{2, 3, 4\}$.

photodetector $\mathsf{D}_{\mathcal{G}}$, and the complement set, whose indices are in $\mathsf{S}_{\mathcal{B}}$, reflect their powers toward $\mathsf{D}_{\mathcal{B}}$. Therefore the output current samples of $\mathsf{D}_{\mathcal{G}}$ follow the same Poisson counts defined by (5.8) and (5.9). Notice that, in contrast to the multiple-detector array receiver, the individual counts, $I_n^{(j)}$, in (5.8) are not accessible. Consequently, the SER is given by (5.10), with the same definitions of $K_n^{(j)}$ and K_b as in (5.5) and (5.6), where each array element is replaced by the corresponding micromirror as mentioned before. Notice that, although $I_{\mathcal{B}}^{(j)}$ is not used in the detection process, the detector $\mathsf{D}_{\mathcal{B}}$ is placed in Fig. 5.1 as it serves the presentation of the full receiver architecture in Sec. 5.4.

5.3.3 PSF Estimation using a DMD

In this section, it is shown that PSF estimation can be performed by the use of a DMD array, instead of an imager array. This is done by computing linear projections of the PSF onto a binary orthogonal basis, then estimating the PSF by using these measurements.

As mentioned in Sec. 5.2.2, if the j^{th} PPM chip is on, then the PSF can be represented by the components, $K_n^{(j)}$, which are the time averages of $\lambda_n(t)$ over the j^{th} chip duration. While the array receiver of Sec. 5.2 estimates the time averages over the chip duration, the DMD array can be used to estimate the time averages of $\lambda_n(t)$ over the DMD switching period, T_D, which is much larger than the PPM chip duration T_c. Define $\tilde{K}_n^{(i)}$ and $\tilde{K}_b$ as the averages of $\lambda_n(t)$ and $\lambda_b(t)$ over the i^{th} DMD switching period

$$\tilde{K}_n^{(i)} = \int_{iT_D}^{(i+1)T_D} \lambda_n(t)\, dt, \tag{5.11}$$

$$\tilde{K}_b = \int_{iT_D}^{(i+1)T_D} \lambda_b(t)\, dt. \tag{5.12}$$

In other words, $\tilde{K}_n^{(i)}$ and $\tilde{K}_b$ are the average signal and background noise energies, in photons, received by the n^{th} micromirror during each T_D interval. The total energy received by the entire array is given by

$$\tilde{K} = \sum_{n=1}^{N} \tilde{K}_n^{(i)} = \frac{T_D}{LT_c} K^{\text{ON}}, \tag{5.13}$$

which is independent of i by assuming that $\frac{T_D}{LT_c}$ is an integer, where LT_c is the PPM symbol duration. For simplicity of notation, define the vector $\tilde{\mathbf{x}}^{(i)}$ as the collection of signal energies of all the N micromirrors in a DMD switching interval,

$$\tilde{\mathbf{x}}^{(i)} = \left[\tilde{K}_1^{(i)}, \tilde{K}_2^{(i)}, \cdots, \tilde{K}_N^{(i)}\right]^{\mathrm{T}}, \tag{5.14}$$

where $i \in \{0, 1, 2, \cdots\}$. Therefore, the time-varying PSF is represented by the time-varying vector, $\tilde{\mathbf{x}}^{(i)}$, which is required to be estimated by using the DMD array.

To estimate $\tilde{\mathbf{x}}^{(i)}$, its linear projections onto a binary orthogonal basis are computed successively in time. Consider an $M \times N$ binary measurement matrix, A, of ± 1's, and let $\mathbf{a}_{m(i)}^{\mathrm{T}}$ be the m^{th} row of A, where the row index m is defined as a function of the time index i,

$$m(i) = 1 + (i \bmod M),$$

such that m varies from 1 to M as i varies as $i = 0, 1, 2, \cdots$. This is intuitive since at most M binary orthogonal measurement vectors $\mathbf{a}_{m(i)}$ exist. In case $M = N$, the measurement matrix is referred to as a *full measurement matrix*, whereas it is referred to as a *partial measurement matrix* in case $M < N$.

The index set, S, is partitioned into two mutually exclusive sets S_+ and S_- such that S_+ contains the indices of the positive entries of $\mathbf{a}_{m(i)}$, and S_- contains the indices of the negative entries. The micromirrors, whose indices are in S_+, reflect their optical powers toward the photodetector D_+, and those whose indices are in S_-, reflect toward D_- as shown in the illustrative diagram of Fig. 5.2. Therefore, the output Poisson counts of D_+ and D_- are $\tilde{I}_+^{(i)}$ and $\tilde{I}_-^{(i)}$ with means

$$\begin{aligned} \mu_+^{(i)} &= \sum_{n \in \mathsf{S}_+} \tilde{K}_n^{(i)} + |\mathsf{S}_+|\tilde{K}_b, \\ \mu_-^{(i)} &= \sum_{n \in \mathsf{S}_-} \tilde{K}_n^{(i)} + |\mathsf{S}_-|\tilde{K}_b, \end{aligned}$$

respectively. If y_i is the difference measurement between the detectors output counts,

$$y_i = \tilde{I}_+^{(i)} - \tilde{I}_-^{(i)}, \tag{5.15}$$

then, for a given $\tilde{\mathbf{x}}^{(i)}$, the mean, variance and distribution of y_i are given by

$$\begin{aligned} \mathbb{E}[y_i] &= \mu_+^{(i)} - \mu_-^{(i)} = \mathbf{a}_{m(i)}^{\mathrm{T}} \tilde{\mathbf{x}}^{(i)} + (|\mathsf{S}_+| - |\mathsf{S}_-|)\tilde{K}_b, && (5.16a) \\ \mathrm{Var}[y_i] &= \mu_+^{(i)} + \mu_-^{(i)} = \tilde{K} + N\tilde{K}_b, && (5.16b) \\ f_{y_i}(k) &= e^{-\mu_+^{(i)} - \mu_-^{(i)}} \left(\frac{\mu_+^{(i)}}{\mu_-^{(i)}} \right)^{\frac{k}{2}} \mathsf{I}_k \left(2\sqrt{\mu_+^{(i)} \mu_-^{(i)}} \right), && (5.16c) \end{aligned}$$

where k is an integer and I_k is the modified Bessel function of the first kind of order k [209].

The measurement, y_i, can alternatively be written as

$$y_i = \mathbf{a}_{m(i)}^{\mathrm{T}} \tilde{\mathbf{x}}^{(i)} + n_i, \tag{5.17}$$

where $\mathbb{E}[n_i] = (|\mathsf{S}_+| - |\mathsf{S}_-|)\tilde{K}_b$, which is known since $\tilde{K}_b$ is assumed known at the receiver, $\mathrm{Var}[n_i]$ is the same as in (5.16b), and $f_{n_i}(k)$ is the same as in (5.16c) but shifted about the mean $\mathbb{E}[n_i]$. That is, the measurement y_i can be regarded as the projection, $\mathbf{a}_{m(i)}^{\mathrm{T}} \tilde{\mathbf{x}}^{(i)}$, of $\tilde{\mathbf{x}}^{(i)}$ onto the subspace spanned by $\mathbf{a}_{m(i)}$, plus a noise term,

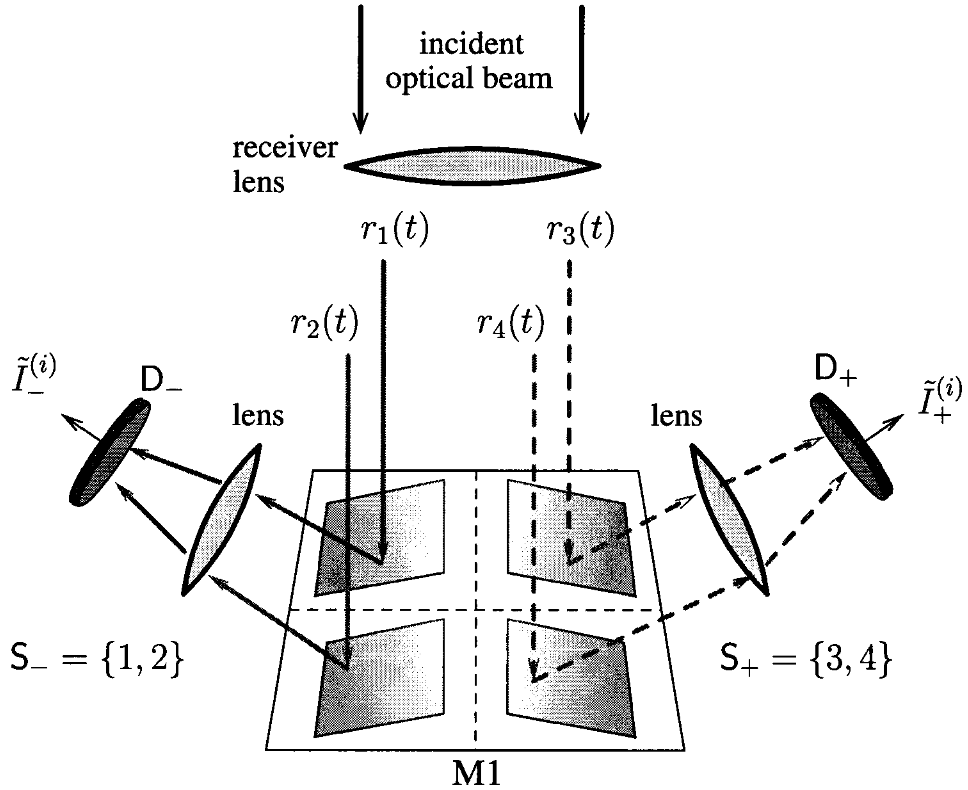

Figure 5.2: An illustration of how the DMD array is used to estimate the PSF through linear measurements. For drawing simplicity, the number of micromirrors is taken as $N = 4$. In this diagram, $\mathsf{S} = \{1, 2, 3, 4\}$, $\mathsf{S}_- = \{1, 2\}$, and $\mathsf{S}_+ = \{3, 4\}$. That is, $\mathbf{a}_{m(i)} = [-1, -1, +1, +1]^{\mathrm{T}}$.

n_i. Therefore, by repeating the above procedure for all vectors $\mathbf{a}_{m(i)}$, the projection of $\tilde{\mathbf{x}}^{(i)}$ onto the basis defined by A can be approximately calculated.

Every T_D seconds, a new measurement y_i is taken while the states of the micromirrors are defined by the corresponding vector $\mathbf{a}_{m(i)}$. Therefore, at the end of the i^{th} DMD period, the sliding window of measurements

$$[y_i, y_{i-1}, \cdots, y_{i-M+1}]^{\mathrm{T}} \tag{5.18}$$

approximates the linear projection of $\tilde{\mathbf{x}}^{(i)}$ onto the space spanned by the rows of A. This approximation is adequate since typically $T_D \ll T_{coh}$, implying $\tilde{\mathbf{x}}^{(i)}$ does not change significantly during the period of M successive measurements.

An estimate of $\tilde{\mathbf{x}}^{(i)}$ can be calculated in terms of the measurements (5.18) as

$$\hat{\mathbf{x}}^{(i)} = \frac{1}{\|\mathbf{a}\|^2} \sum_{k=i-M+1}^{i} y_k \, \mathbf{a}_{m(k)}, \tag{5.19}$$

since the rows of A are orthogonal and have the same ℓ_2-norm of $\|\mathbf{a}\|$. Moreover, the PSF estimate can be updated adaptively every T_D seconds as follows,

$$\hat{\mathbf{x}}^{(i+1)} = \hat{\mathbf{x}}^{(i)} + \frac{1}{\|\mathbf{a}\|^2}(y_{i+1} - y_{i-M+1})\mathbf{a}_{m(i+1)}, \tag{5.20}$$

which requires N addition/subtraction operations, since $\mathbf{a}_{m(i)}$ is a vector of ± 1's. That is, turbulence-degraded PSF is estimated from the measurements taken by the receiver during a sliding time window of NT_D seconds. The estimate is updated every T_D seconds, and is used to improve the accuracy of symbol detection. The computational requirement is N/T_D floating-point addition/subtraction operations per second. Moreover, these N operations can be performed in parallel every T_D seconds, which simplifies the computational requirements even further.

5.4 3-chip DMD Optical Receiver Architecture

A single DMD is shown to be capable of performing the selection combining detection in Sec. 5.3.2, and is shown to be capable of estimating the PSF in Sec. 5.3.3. However, a single DMD is incapable of performing both tasks at the same time. This is because the partitioning of S to $\mathsf{S}_{\mathcal{G}} \cup \mathsf{S}_{\mathcal{B}}$ may contradict its partitioning to $\mathsf{S}_{+} \cup \mathsf{S}_{-}$. For example, consider the two cases illustrated in Figs. 5.1 and 5.2. The mirrors orientations in Fig. 5.1, required to have the shown values of $\mathsf{S}_{\mathcal{G}}$ and $\mathsf{S}_{\mathcal{B}}$, are different than their orientations in Fig. 5.2, required to have the shown values of S_{+} and S_{-}.

To achieve both combining and PSF estimation simultaneously, two additional DMD arrays are added to the proposed receiver as depicted in Fig. 5.3. These extra micromirror arrays introduce the necessary degrees of freedom that enable both tasks simultaneously. The DMD array, M1, is placed in the focal-plane of the receiver lens. Its function is to define the partitioning of S to $\mathsf{S}_{+} \cup \mathsf{S}_{-}$, which is similar to its function in Fig. 5.2. The DMD arrays M2 and M3 are identical to M1, and are assumed to be well aligned to M1 such that, by the help of lenses, each component $r_n(t)$ can be projected precisely onto the corresponding micromirror of M2 or M3 as shown in the illustrative example of Fig. 5.4. The strict alignment of the three DMDs is feasible in practice. For example, in the commercially available 3-chip DLP projection system [188, 206], three DMD chips are used for red, green and blue color components. The three DMDs are strictly aligned such that the light projected by them coincides to form the projected image.

The DMD array M2 partitions S_{-} to two mutually exclusive sets $\mathsf{S}_{\mathcal{G}-}$ and $\mathsf{S}_{\mathcal{B}-}$, such that the components whose indices are in $\mathsf{S}_{\mathcal{G}-}$ are reflected toward the photodetector $\mathsf{D}_{\mathcal{G}-}$, and those whose indices are in $\mathsf{S}_{\mathcal{B}-}$ are reflected toward $\mathsf{D}_{\mathcal{B}-}$. Similarly, M3 partitions S_{+} to $\mathsf{S}_{\mathcal{G}+}$ and $\mathsf{S}_{\mathcal{B}+}$ whose signals are collected by $\mathsf{D}_{\mathcal{G}+}$ and $\mathsf{D}_{\mathcal{B}+}$ as shown in Figs. 5.3 and 5.4. That is, M1 is responsible for PSF measurements, while M2 and M3 perform the selection combining. In fact, the three DMD arrays partition the set

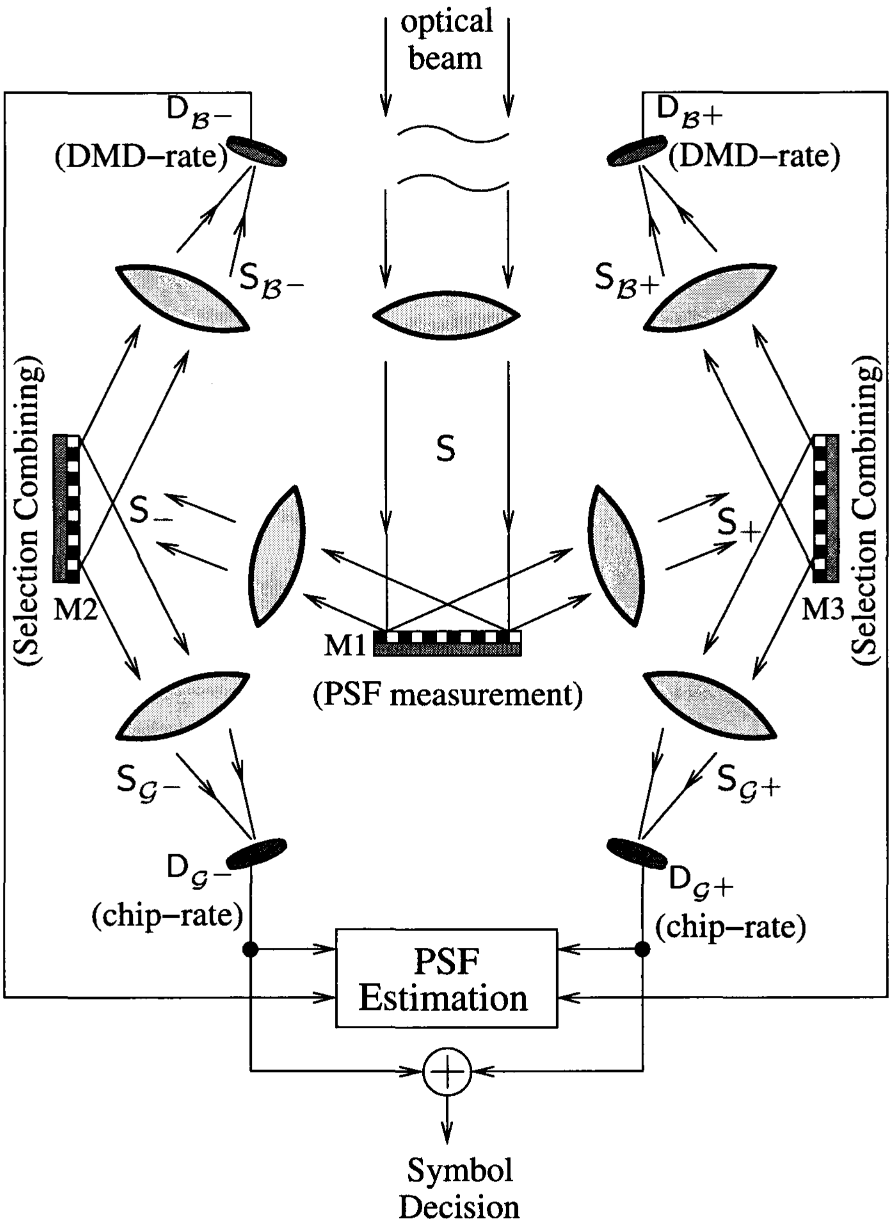

Figure 5.3: 3-chip DMD optical receiver [162].

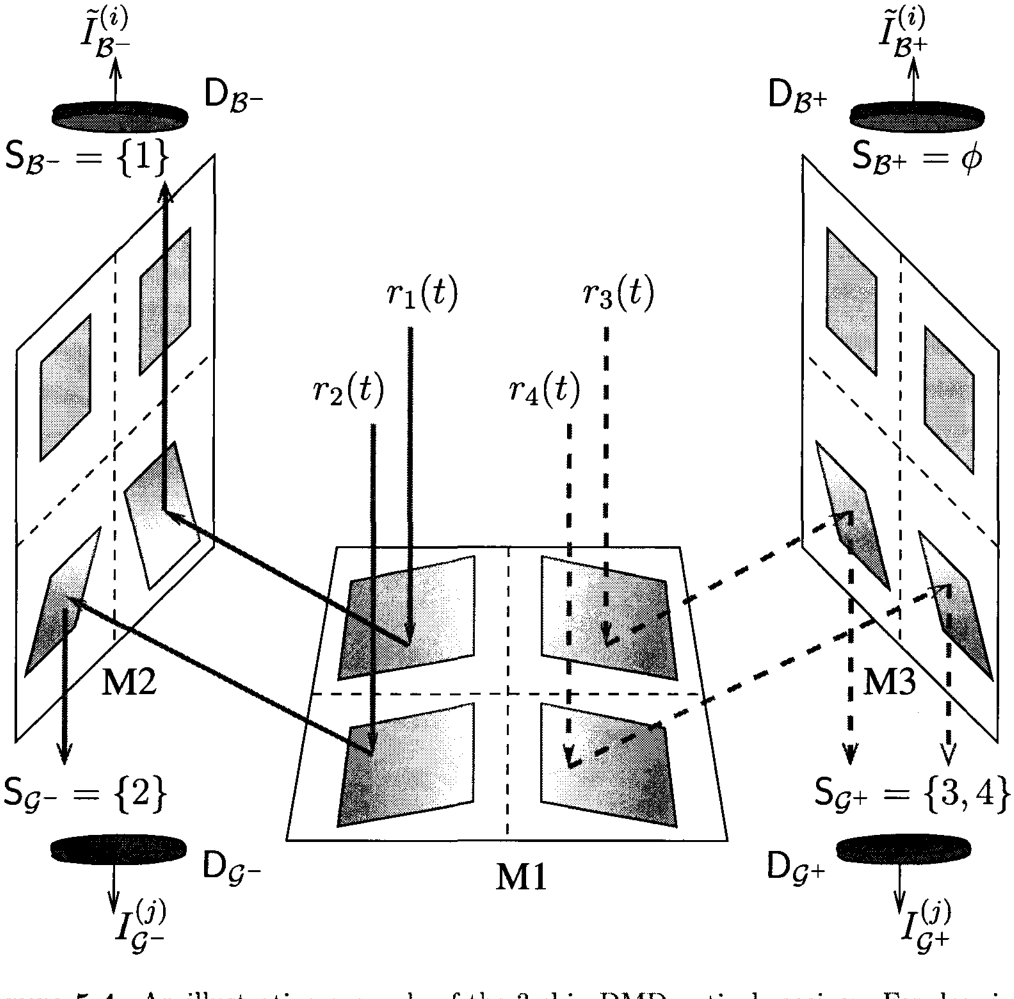

Figure 5.4: An illustrative example of the 3-chip DMD optical receiver. For drawing simplicity, the number of micromirrors is taken as $N = 4$. In this example, $\mathsf{S} = \{1, 2, 3, 4\}$, $\mathsf{S}_{\mathcal{B}} = \mathsf{S}_{\mathcal{B}+} \cup \mathsf{S}_{\mathcal{B}-} = \{1\}$, $\mathsf{S}_{\mathcal{G}} = \mathsf{S}_{\mathcal{G}+} \cup \mathsf{S}_{\mathcal{G}-} = \{2, 3, 4\}$, $\mathsf{S}_{+} = \mathsf{S}_{\mathcal{B}+} \cup \mathsf{S}_{\mathcal{G}+} = \{3, 4\}$, and $\mathsf{S}_{-} = \mathsf{S}_{\mathcal{B}-} \cup \mathsf{S}_{\mathcal{G}-} = \{1, 2\}$. Notice that this configuration gives the same values of $\mathsf{S}_{\mathcal{B}}$ and $\mathsf{S}_{\mathcal{G}}$ as in Fig. 5.1, and the same values of S_{-} and S_{+} as in Fig. 5.2. Imaging lenses are omitted for diagram clarity.

of indices, S, to four mutually exclusive sets $\mathsf{S}_{\mathcal{B}+}$, $\mathsf{S}_{\mathcal{B}-}$, $\mathsf{S}_{\mathcal{G}+}$ and $\mathsf{S}_{\mathcal{G}-}$, such that

$$\mathsf{S}_{\mathcal{G}} = \mathsf{S}_{\mathcal{G}+} \cup \mathsf{S}_{\mathcal{G}-}, \quad \mathsf{S}_{-} = \mathsf{S}_{\mathcal{B}-} \cup \mathsf{S}_{\mathcal{G}-},$$
$$\mathsf{S}_{\mathcal{B}} = \mathsf{S}_{\mathcal{B}+} \cup \mathsf{S}_{\mathcal{B}-}, \quad \mathsf{S}_{+} = \mathsf{S}_{\mathcal{B}+} \cup \mathsf{S}_{\mathcal{G}+},$$

and the incident radiation components $r_n(t)$, indexed by each of these four sets, are collected by the corresponding photodetector as shown in Figs. 5.3 and 5.4.

The detector $\mathsf{D}_{\mathcal{G}}$ of Fig. 5.1 is operated at the PPM chip rate, $1/T_c$, while D_{+} and D_{-} of Fig. 5.2 are operated at the DMD switching rate, $1/T_D$. That is $\mathsf{D}_{\mathcal{G}}$ is a high-speed detector, while D_{+} and D_{-} are much slower since typically $T_c \ll T_D$. Similarly, with the full receiver architecture of Fig. 5.3, the two detectors $\mathsf{D}_{\mathcal{G}+}$ and $\mathsf{D}_{\mathcal{G}-}$ are high-speed detectors since they are operated at the PPM chip rate, while $\mathsf{D}_{\mathcal{B}+}$ and $\mathsf{D}_{\mathcal{B}-}$ are operated at the much lower DMD switching rate. In fact, the receiver performance relies on the ratios between the three different rates: (i) PPM chip rate, $1/T_c$, which is the fastest, (ii) DMD switching rate, $1/T_D$, and (iii) rate of change of the PSF, $1/T_{coh}$, which is the slowest. Define the ratios as

$$\zeta = \frac{T_D}{T_c} \quad \text{and} \quad \eta = \frac{T_{coh}}{T_D}, \tag{5.21}$$

which are assumed to be integers. Although this assumption is not required in practice, it is made to simplify the analysis. That is, within every turbulence state, we have η DMD switching periods, and within each of these periods, ζ PPM chip pulses are detected by the receiver. If the atmospheric turbulence coherence time is 10−100 msec [134], the DMD switching period is 25−100 μsec [188], and the PPM chip duration is on the order of nanoseconds for a high-speed link, then typical values of ζ and η are 1000 and 100−4000, respectively.

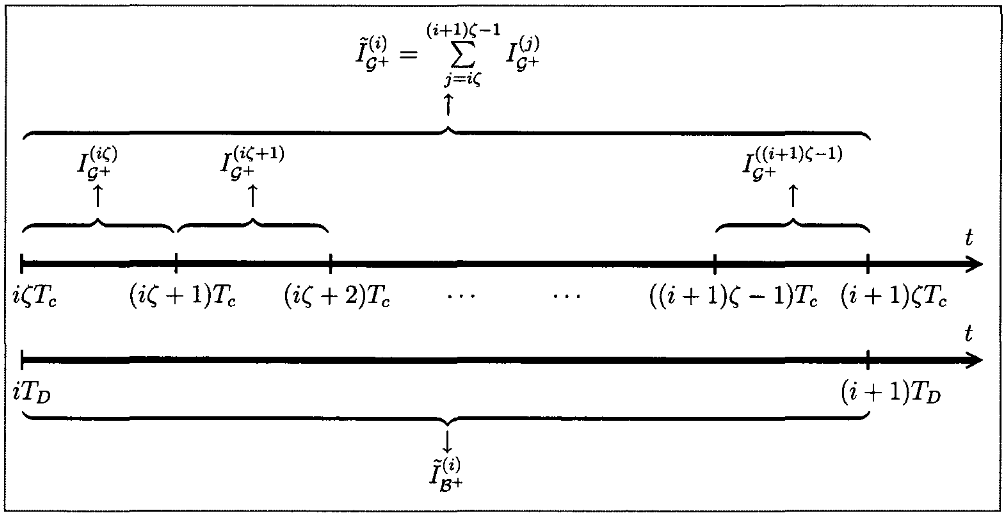

Figure 5.5: A timing diagram showing that each DMD period, $[iT_D, (i+1)T_D)$, is divided to ζ PPM chips such that $[iT_D, (i+1)T_D) = \bigcup_{j=i\zeta}^{(i+1)\zeta-1} [jT_c, (j+1)T_c)$. The counts $\tilde{I}_{\mathcal{B}+}^{(i)}$ and $\tilde{I}_{\mathcal{G}+}^{(i)}$ are shown, while $\tilde{I}_{\mathcal{B}-}^{(i)}$ and $\tilde{I}_{\mathcal{G}-}^{(i)}$ are eliminated for diagram clarity. The counts $I_{\mathcal{G}+}^{(j)}$, where $i\zeta \leq j < (i+1)\zeta$, are used for detecting the ζ chips, while their sum $\tilde{I}_{\mathcal{G}+}^{(i)}$ is used to compute the i^{th} PSF measurement, y_i.

Notice that the averages over the i^{th} DMD switching period given by (5.12) and (5.13) are related to the averages over the j^{th} PPM chip given by (5.6) and (5.7) as follows,

$$\begin{aligned} \tilde{K}_b &= \sum_{j=i\zeta}^{(i+1)\zeta-1} K_b &&= \zeta K_b, \\ \tilde{K} &= \sum_{j=i\zeta}^{(i+1)\zeta-1} K^{(j)} &&= \frac{\zeta}{L} K^{\text{ON}}, \end{aligned}$$

where each DMD period consists of ζ PPM chips as shown in the timing diagram of Fig. 5.5. The scale factors differ by L since only one of the L PPM chips contains a signal pulse, while all the chips contain background noise.

The decision statistic $I_{\mathcal{G}}^{(j)}$, defined in (5.8), that is used for symbol detection in

Sections 5.2.3 and 5.3.2, is calculated as

$$I_{\mathcal{G}}^{(j)} = I_{\mathcal{G}+}^{(j)} + I_{\mathcal{G}-}^{(j)},$$

where $I_{\mathcal{G}+}^{(j)}$ and $I_{\mathcal{G}-}^{(j)}$ are the Poisson counts of the detectors $\mathsf{D}_{\mathcal{G}+}$ and $\mathsf{D}_{\mathcal{G}-}$ respectively. This statistic is available every T_c seconds for symbol detection, has the same mean defined by (5.9), and yields the same SER upper bound given by (5.10). On the other hand, to calculate the measurements, y_i, as in (5.15), the following two counts are computed

$$\begin{aligned} \tilde{I}_{+}^{(i)} &= \tilde{I}_{\mathcal{B}+}^{(i)} + \tilde{I}_{\mathcal{G}+}^{(i)}, \\ \tilde{I}_{-}^{(i)} &= \tilde{I}_{\mathcal{B}-}^{(i)} + \tilde{I}_{\mathcal{G}-}^{(i)}, \end{aligned}$$

where $\tilde{I}_{\mathcal{B}+}^{(i)}$ and $\tilde{I}_{\mathcal{B}-}^{(i)}$ are the Poisson counts of the detectors $\mathsf{D}_{\mathcal{B}+}$ and $\mathsf{D}_{\mathcal{B}-}$ respectively, and

$$\begin{aligned} \tilde{I}_{\mathcal{G}+}^{(i)} &= \sum_{j=i\varsigma}^{(i+1)\varsigma-1} I_{\mathcal{G}+}^{(j)}, \\ \tilde{I}_{\mathcal{G}-}^{(i)} &= \sum_{j=i\varsigma}^{(i+1)\varsigma-1} I_{\mathcal{G}-}^{(j)}, \end{aligned}$$

as shown in Fig. 5.5.

That is, in every T_D interval, two events occur simultaneously: (i) the outputs of the two detectors $\mathsf{D}_{\mathcal{G}+}$ and $\mathsf{D}_{\mathcal{G}-}$ are used to detect ς PPM chip pulses, and (ii) the outputs of the four photodetectors are used to take the measurement y_i. As mentioned in Sec. 5.3.3 and described in Sec. 5.6.3, an estimate of $\tilde{\mathbf{x}}^{(i)}$ can be calculated in terms of the measurements (5.18), and is used to select the subset of the micromirrors with high SNR to be used in the detection process by the photodetectors $\mathsf{D}_{\mathcal{G}+}$ and $\mathsf{D}_{\mathcal{G}-}$. This is done by defining the states of the micromirrors of the DMD arrays M2 and M3 such that $\mathsf{S}_{\mathcal{G}+}$ and $\mathsf{S}_{\mathcal{G}-}$ constitute the indices of the high SNR mirrors, and $\mathsf{S}_{\mathcal{B}+}$

and $\mathsf{S}_{\mathcal{B}}$- constitute the indices of the low SNR mirrors. Independently, the states of M1 are defined every T_D seconds according to the rows of the measurement matrix A. That is, the proposed receiver in Fig. 5.3 is simultaneously capable of estimating the PSF and detecting the transmitted pulses, where the detection is based on the high SNR elements only.

5.5 2-chip DMD Optical Receiver Architecture

An optical receiver that uses only two DMD arrays is shown in Fig. 5.6, where the DMD array M1, of Fig. 5.3, and a high-speed photodetector are replaced by a beam splitter. The two arrays M2 and M3 have to be identical and strictly aligned with the splitter. The beam splitter splits the incident energy $K^{(j)}$, defined in (5.7), to two components $K^{(j)}_{est}$ and $K^{(j)}_{det}$ for PSF estimation and PPM chip detection respectively, where $K^{(j)}_{est} + K^{(j)}_{det} = K^{(j)}$. The component $K^{(j)}_{est}$ is pixelated by the DMD array M2, and the index set, S, is partitioned to S_+ and S_- whose radiations are collected by D_+ and D_- respectively. Similarly, the component $K^{(j)}_{det}$ is pixelated by the DMD array M3, and S is partitioned to $\mathsf{S}_{\mathcal{G}}$ and $\mathsf{S}_{\mathcal{B}}$. The radiations of the mirrors indexed by $\mathsf{S}_{\mathcal{G}}$ are collected by $\mathsf{D}_{\mathcal{G}}$, while the radiations of the mirrors indexed by $\mathsf{S}_{\mathcal{B}}$ are ignored. The outputs of D_+ and D_- are used for calculating the PSF linear projections as in Fig. 5.2, and the output of $\mathsf{D}_{\mathcal{G}}$ is used for PPM symbol detection as in Fig. 5.1.

The 2-chip DMD receiver of Fig. 5.6 is simpler than the 3-chip DMD receiver of Fig. 5.3 since it uses one high-speed detector instead of two and uses a beam splitter instead of a DMD array. On the other hand, it is shown in Sec. 5.6.4 that the performance of the 3-chip receiver is better than the 2-chip receiver. This can be attributed to the fact that all the received energy is available for both estimation and

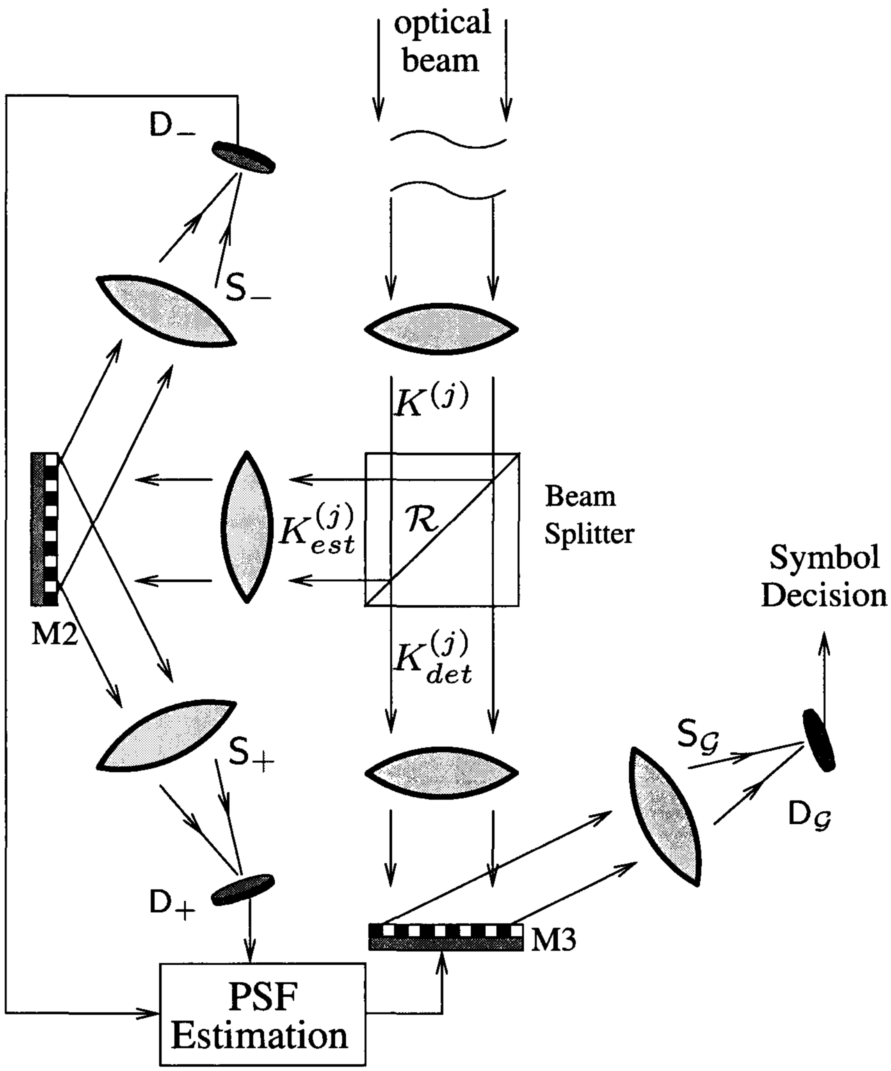

Figure 5.6: 2-chip DMD optical receiver. A beam splitter is used to split the incident energy $K^{(j)}$ to two components $K_{est}^{(j)}$ and $K_{det}^{(j)}$ for PSF estimation and PPM chip detection respectively.

detection in case of the 3-chip receiver, while the 2-chip receiver splits the energy to two components, one for estimation and the other for detection.

Define the reflection coefficient of the beam splitter as the ratio,

$$\mathcal{R} = K_{est}^{(j)}/K^{(j)},$$

which is a parameter of the 2-chip receiver that affects its performance as shown in the numerical results of Sec. 5.6. In [210], two prisms have been used to design a continuously adjustable beam splitter such that $\mathcal{R}$ can be varied continuously by sliding one prism on the other.

5.6 Simulation results

5.6.1 Simulating a Time-Evolved PSF

As mentioned in Sec. 2.4, a realization of the turbulence degraded PSF can be obtained by generating a Kolmogorov phase screen, $\Theta_t(u, v)$, then substituting by (2.15) in (2.2). In order to simulate the PSF on a digital computer, Equation (2.2) is sampled in both the spatial and frequency domains to obtain an expression for the samples of the PSF in terms of the samples of the pupil function,

$$h_t\left(\lambda f_\ell \frac{n_1}{D}, \lambda f_\ell \frac{n_2}{D}\right) = \frac{D^4}{|\lambda f_\ell|^2 \mathcal{E}_P} \left| \mathcal{F}^{-1}\left\{ P\left(-D\frac{k_1}{N_1}, -D\frac{k_2}{N_2}\right)\right\}\right|^2, \tag{5.22}$$

where $n_1, k_1 \in \{0, 1, 2, \cdots, N_1 - 1\}$, $n_2, k_2 \in \{0, 1, 2, \cdots, N_2 - 1\}$. Equation (5.22) is developed in Appendix C, where the pupil function $P(u, v)$ is assumed to have support on $|u|, |v| < D/2$.

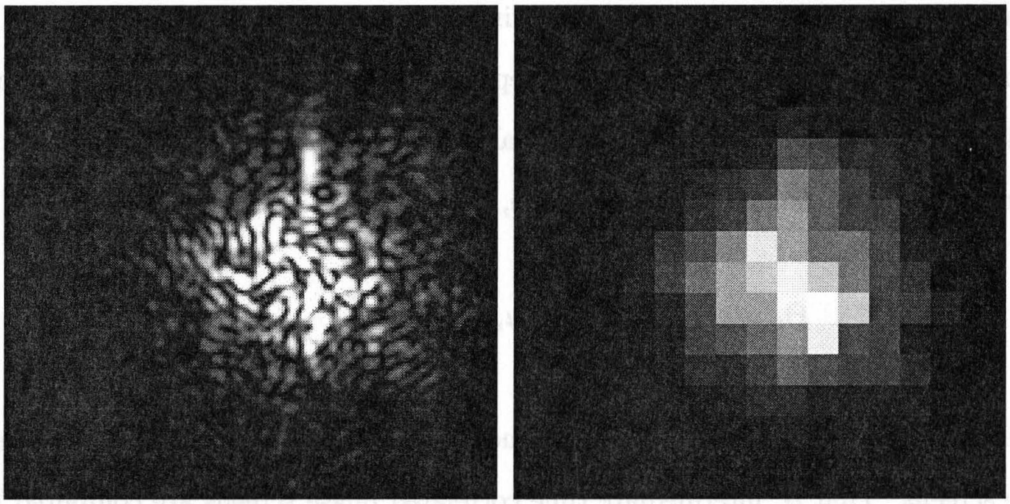

(a) (b)

Figure 5.7: The instantaneous turbulence-degraded PSF for $D/r_0 = 11.92$. (a) An energy plot of the PSF. (b) The integration of the PSF over the surface of a 16×16 array receiver.

A fast algorithm that generates Kolmogorov phase screens for a given turbulence strength is presented in [28], where the turbulence strength is measured by the ratio D/r_0. This algorithm is used to simulate Kolmogorov phase screens for simulations in this section.† The generated screens and (2.15) are used in (5.22) to generate samples of the turbulence-degraded PSF. An example snapshot of a realization of the turbulence-degraded PSF is shown in Fig. 5.7 for $D/r_0 = 11.92$. This value of D/r_0 is a typical value that is used to simplify the comparison to the results reported in [134, 147], where the same value of D/r_0 has been used with a 16×16 array which is the same array size used in our simulations, i.e. $N = 256$.

For the proposed DMD receiver, the PSF estimation is done through successive time measurements. Therefore, it is necessary to evolve the PSF with time to reflect

†The author would like to thank Dr. Richard Lane for providing a Matlab implementation of the algorithm described in [28] for the generation of Kolmogorov phase screens.

its time-varying nature. A simple approximate model of the time-varying PSF is obtained by generating a sequence of independent phase screens at different times and lowpass filter the sequence by an ideal lowpass filter whose bandwidth is the reciprocal of the turbulence coherence time,

$$\Theta_t(u,v) = \sum_{i=-(\ell-1)}^{\ell} \Theta_i(u,v)\,\mathrm{sinc}\left(\frac{t}{T_{coh}} - i\right),$$

where Θ_t is the phase screen at time t, and $\{\Theta_i\}$ is a sequence of 2ℓ independent phase screens. That is, intermediate time correlated phase screens are computed by the bandlimited interpolation of the independently generated screens [163]. Samples of the time-varying PSF are then computed by substituting by Θ_t and (2.15) in (5.22).

5.6.2 Measurement Matrices

The measurement matrix, A, can be taken as an $N \times N$ Hadamard basis matrix, which is a square binary orthogonal matrix of ± 1's. It can also be formed by $M < N$ rows of an $N \times N$ Hadamard basis matrix. In this case, the M Hadamard rows must be selected carefully, as in Sec. 5.6.3, such that the PSF, $\tilde{\mathbf{x}}^{(i)}$, approximately lies in the subspace spanned by the selected rows. The PSF estimate, $\hat{\mathbf{x}}^{(i)}$, is given by (5.20) for $M \leq N$, where $\|\mathbf{a}\| = \sqrt{N}$. The case of $M < N$ is particularly useful when the PSF is fast varying process, since it updates each projection of $\hat{\mathbf{x}}^{(i)}$ every MT_D rather than NT_D seconds.

Another possibility for the measurement matrix is an $N \times N$ identity matrix. The PSF estimate is also given by (5.20), where $\|\mathbf{a}\| = 1$. In this case, S_+ contains the indices of the positive entries of $\mathbf{a}_{m(i)}$, and S_- contains the indices of the zero entries.

Since any row, $\mathbf{a}_{m(i)}$, of the identity matrix contains only one non-zero entry, then $|\mathsf{S}_+| = 1$, and therefore the DMD receiver of Fig. 5.3 can be simplified by replacing the DMD array M3 by the detector $\mathsf{D}_{\mathcal{G}+}$, and removing the detector $\mathsf{D}_{\mathcal{B}+}$. The simplified DMD receiver is shown in Fig. 5.8. If $\mathsf{S}_+ \subset \mathsf{S}_\mathcal{G}$, i.e. the single micromirror of M1 that reflects its light towards $\mathsf{D}_{\mathcal{G}+}$ is also a good mirror, then the output of $\mathsf{D}_{\mathcal{G}+}$ is combined with that of $\mathsf{D}_{\mathcal{G}-}$ for detection, otherwise, detection is based solely on $\mathsf{D}_{\mathcal{G}-}$. Additionally, the detector $\mathsf{D}_{\mathcal{B}-}$ can be removed since the PSF estimate is given directly by the measurements (5.18), where each measurement, y_i, is given by (5.15) with $\tilde{I}_-^{(i)} = 0$. The statistics of measurements for PSF estimation are given by (5.16) with $\mu_-^{(i)} \to 0$.

5.6.3 Symbol Error Rates

To numerically compute the infinite summation in (5.10), the summation set, $\{0, 1, \cdots\}$, is partitioned into non-overlapping subsets. The first subset is given by the integers in the interval $\left[0,\, \mu_\mathcal{G}^{(j)} + \sqrt{\mu_\mathcal{G}^{(j)}}\right]$, where $\mu_\mathcal{G}^{(j)}$ and $\sqrt{\mu_\mathcal{G}^{(j)}}$ are the mean and standard deviation of the probability mass function p_{sb}, as mentioned in Sec. 5.2.3. The summation is first evaluated on this subset where most of the probability mass is concentrated. Next, the summation is evaluated over neighboring subsets in the intervals, $\left(\mu_\mathcal{G}^{(j)} + k\sqrt{\mu_\mathcal{G}^{(j)}},\, \mu_\mathcal{G}^{(j)} + (k+1)\sqrt{\mu_\mathcal{G}^{(j)}}\right]$, where $k = 1, 2, 3, \cdots$. The obtained values are accumulated until the increment corresponding to the k^{th} subset is less than 10^{-6} of the accumulated value.

The SER upper bound, given in (5.10), is simulated for a 2-PPM system using the 3-chip DMD receiver, and plotted in Figs. 5.9 and 5.10 versus the total array signal energy, K^{ON}, in photons per chip duration. High background noise level of $K_b = 1.0$

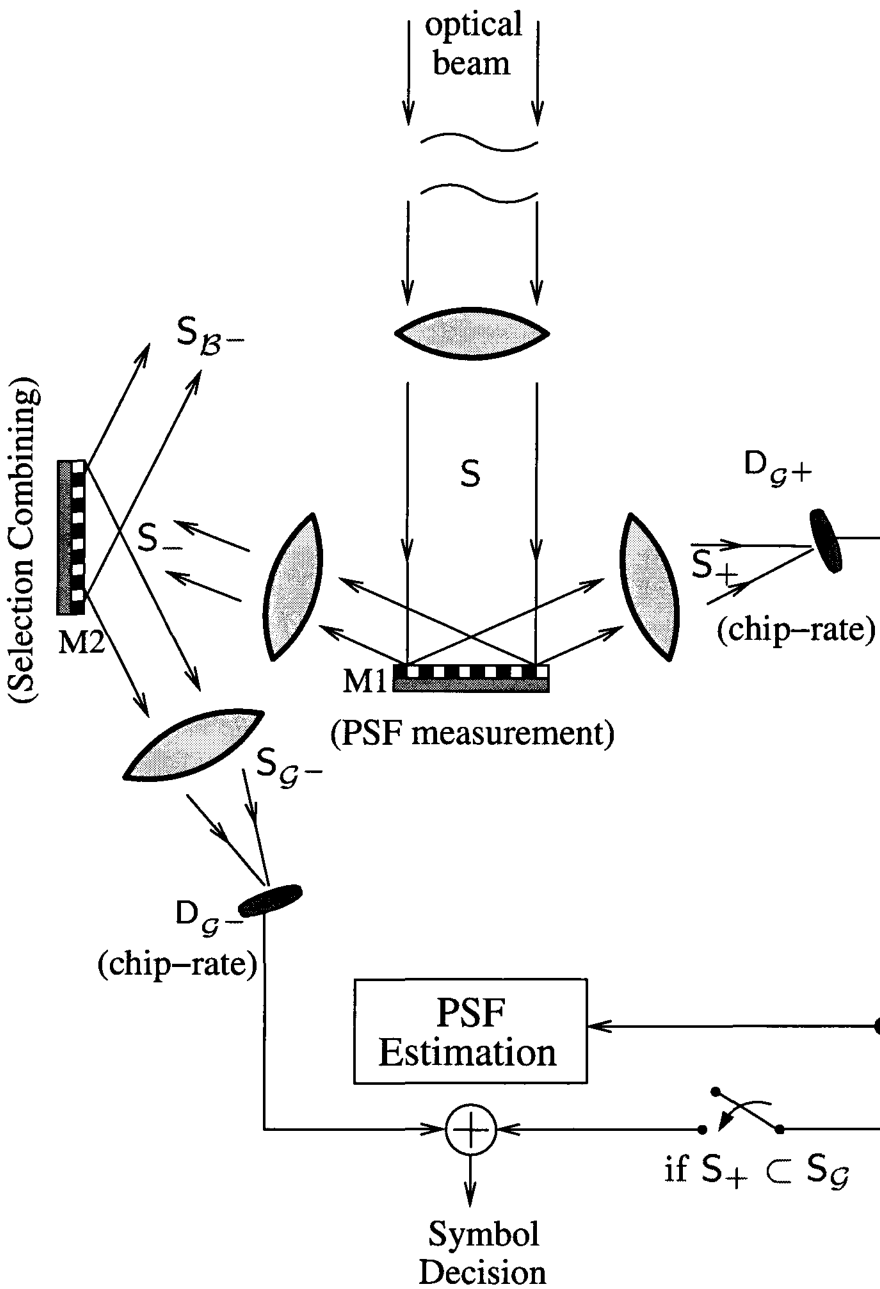

Figure 5.8: A simplified version of the 3-chip DMD optical receiver of Fig. 5.3 when employing a full identity measurement matrix. The simplified DMD receiver uses two DMDs and two high-speed detectors.

and low background noise level of $K_b = 0.1$ photons per micromirror per chip duration are considered in the two figures respectively, as in [134, 147]. The results presented are the average over 10^3 random initial turbulence states. The performance of equal-gain combining, which is equivalent to a conventional single-detector receiver that receives the entire focal-plane signal distribution, is compared to that of optimal selection combining, which assumes that the PSF is known exactly at the receiver in order to define the detection set $\mathsf{S}_{\mathcal{G}}$. It is clear that the optimal selection combining is idealistic since it assumes that the PSF can be estimated perfectly. The SER of selection combining by using a multiple-detector array receiver is lower bounded by that of the optimal selection combining.

It is evident from the figures that the gain, in total energy K^{ON}, of optimal selection over equal-gain combining is considerable. This motivates the use of spatial diversity receivers for enhancing the performance of atmospheric turbulence links. As mentioned in Sec. 5.2.3, the number of detection elements, $|\mathsf{S}_{\mathcal{G}}|$, has been determined by exhaustive optimization in order to demonstrate the performance limits of different optical receivers [134, 147]. The values of $|\mathsf{S}_{\mathcal{G}}|$ has been determined for the case of optimal selection combining, and are shown in Figs. 5.9 and 5.10. These values are used with all spatial diversity receivers simulated in this section so that all the considered receivers are compared at the same number of detection elements.

Consider Figs. 5.9 and 5.10 where a 256×256 full identity matrix, a 256×256 full Hadamard matrix and a 27×256 partial Hadamard matrix have been used for PSF measurement. In the case of the partial Hadamard measurements, the 27 measurement vectors are selected by generating 1000 independent PSFs and projecting them on a complete Hadamard basis, then selecting the basis vectors that span 99% of the

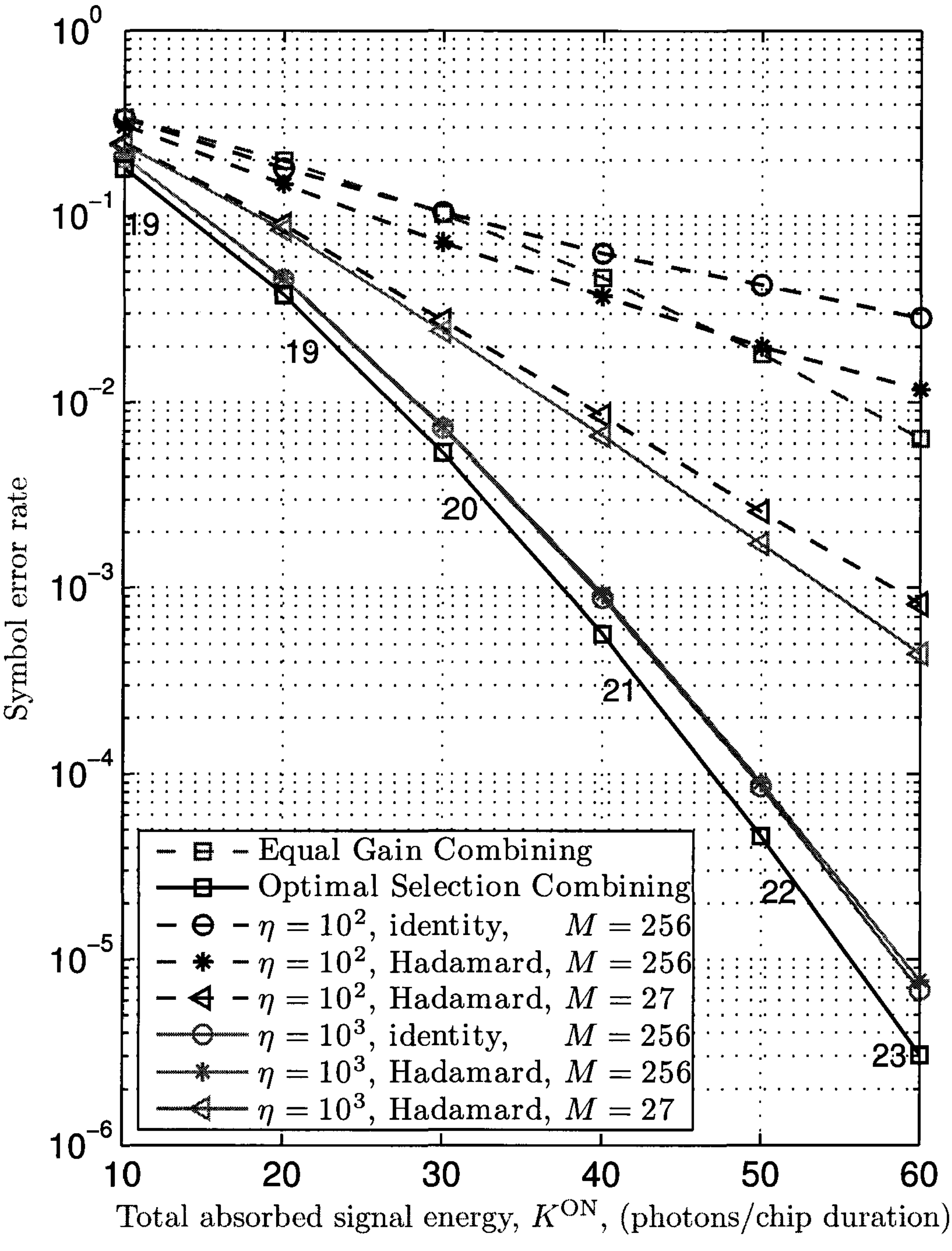

Figure 5.9: SER upper bound for 2-PPM system using the 3-chip DMD receiver at $K_b = 1.0$, $D/r_0 = 11.92$ and $\zeta = 1000$. The optimal number of detection elements used is shown for each K^{ON}.

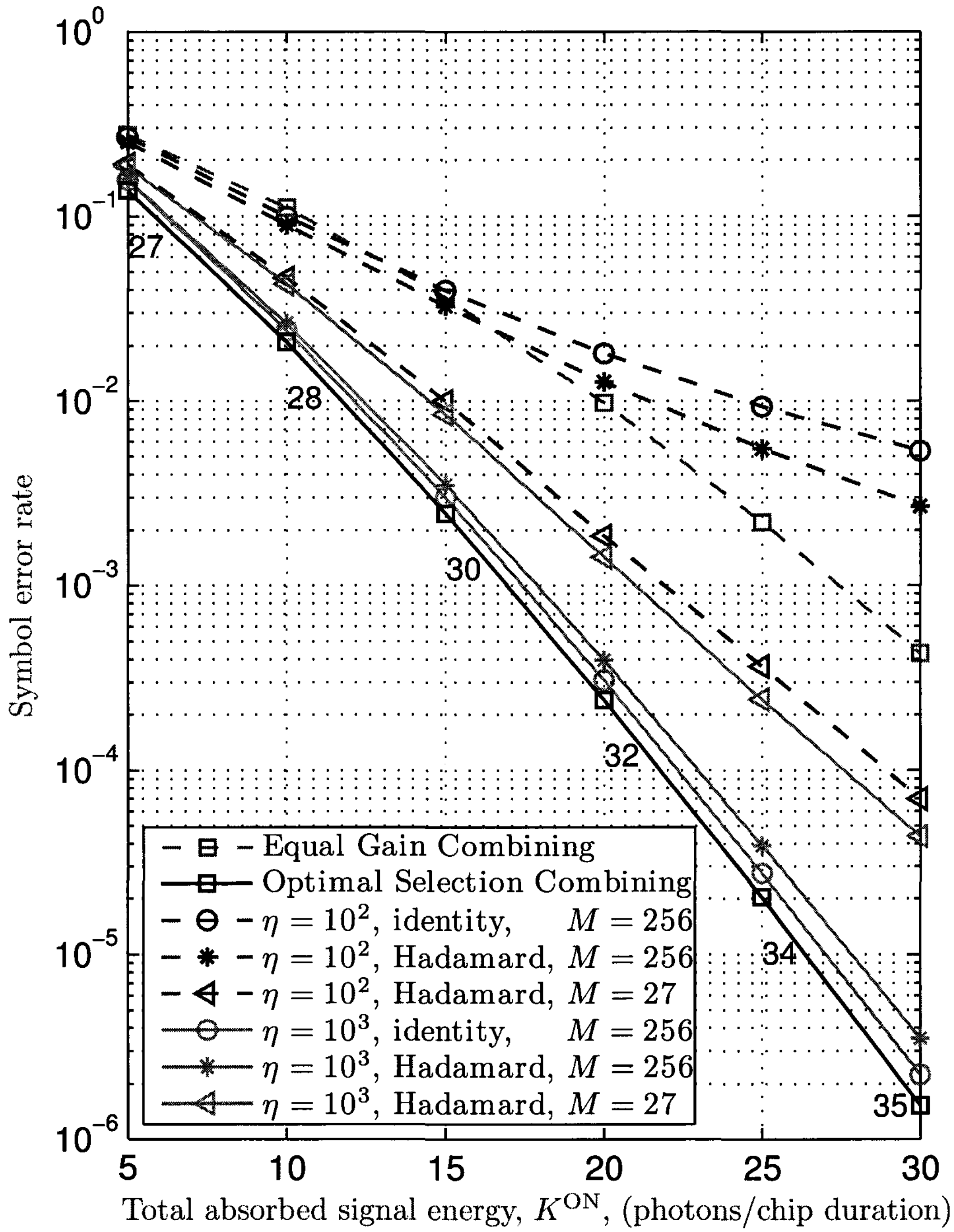

Figure 5.10: SER upper bound for 2-PPM system using the 3-chip DMD receiver at $K_b = 0.1$, $D/r_0 = 11.92$ and $\zeta = 1000$. The optimal number of detection elements used is shown for each K^{ON}.

PSF energy. The selected vectors are fixed and used for all subsequent simulations. Notice that the selected set of vectors will change for different values of D/r_0.

As shown in the figures, for $\eta = 1000$, i.e. a slow turbulence process, the performance of the DMD receiver is very close to that of the optimal selection combining receiver in case of full identity and Hadamard measurements. For example, at SER $= 10^{-2}$, $\eta = 1000$ and $K_b = 1.0$, the gain in total absorbed signal energy, K^{ON}, over the single-detector is about 3.2 dBo for the optimal selection combining array receiver and 2.9 dBo for the DMD receiver with identity or Hadamard measurement matrix. While at $K_b = 0.1$ and the same SER $= 10^{-2}$ and $\eta = 1000$, the gain is about 2.3 dBo for the optimal selection combining array receiver, 2.1 dBo for the DMD receiver with identity measurement matrix, and 2.0 dBo for the DMD receiver with Hadamard measurement matrix. That is, the 3-chip DMD receiver is capable of achieving the majority of the gain in K^{ON} when η is high. This is because, at high η, the atmosphere seems frozen to the successive DMD measurements, and hence the PSF estimate is a better approximation to the time-varying vector $\tilde{\mathbf{x}}^{(i)}$ in (5.14).

Full measurement receivers outperform the partial Hadamard receiver at $\eta =$ 1000. However, at $\eta = 100$, i.e. a fast turbulence process, the partial Hadamard receiver outperforms the full measurement receivers. This can be attributed to the fact that the PSF estimate is fully updated every $27T_D$ seconds in case of the partial Hadamard receiver, while it is fully updated every $256T_D$ seconds in case of the full measurement receivers. In fact, the performance of the full measurement DMD receivers can be outperformed by the equal-gain combining receiver at $\eta = 100$, as shown in Figs. 5.9 and 5.10, due to the fast varying PSF. Notice also that the performance of the full identity measurements is slightly better than that of the full

Hadamard measurements at $\eta = 1000$. Whereas, at $\eta = 100$, the performance of the full Hadamard measurements is better than that of the full identity measurements.

Thus, full measurement DMD receivers are recommended for slowly varying channels, i.e. high values of η, while the partial Hadamard DMD receiver is recommended for fast varying channels, i.e. low values of η. With the availability of high-speed DMD arrays, as mentioned in Sec. 5.3.1, it is expected that the DMD receiver can always operate at high values of η, and hence the performance of optimal selection combining can be approached by a DMD receiver with a full measurement matrix. Although a full identity or Hadamard measurement matrices can be used in this case, an identity matrix has the advantage of fewer hardware components as mentioned in Sec. 5.6.2.

5.6.4 Beam Splitter Reflection Coefficient

The reflection coefficient $\mathcal{R}$ affects the performance of the 2-chip receiver, and should be optimized for each value of K^{ON}. To demonstrate the effect of this ratio on the receiver performance, the performances of the 3-chip and 2-chip receivers are compared in Figs. 5.11 and 5.12 for different values of $\mathcal{R}$ and full Hadamard measurements. It is clear from the figures that a smaller value of $\mathcal{R}$ is required as K^{ON} increases in order to minimize the SER. This is because when the total number of received photons increases, the fraction that is sacrificed for PSF estimation can be decreased without degrading the estimation accuracy. Nevertheless, the 3-chip full Hadamard receiver is still outperforming the 2-chip full Hadamard receiver due to the fact that the 2-chip receiver devotes a percentage of the received energy for PSF estimation rather than symbol detection.

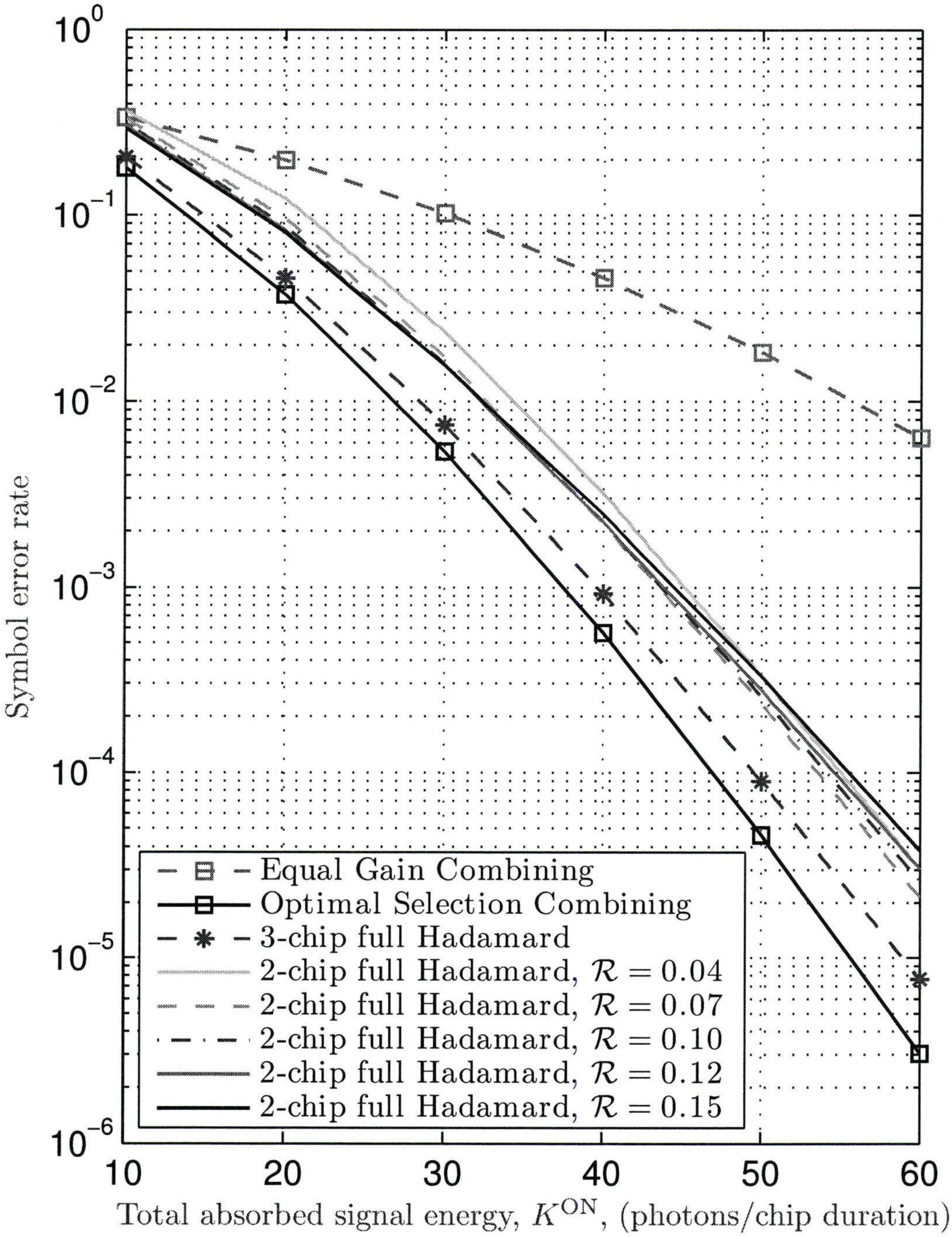

Figure 5.11: SER upper bound for 2-PPM at $K_b = 1.0$, $D/r_0 = 11.92$ and $\zeta = \eta = 1000$. A 3-chip full Hadamard DMD receiver is compared to a 2-chip full Hadamard DMD receiver at different values of $\mathcal{R}$.

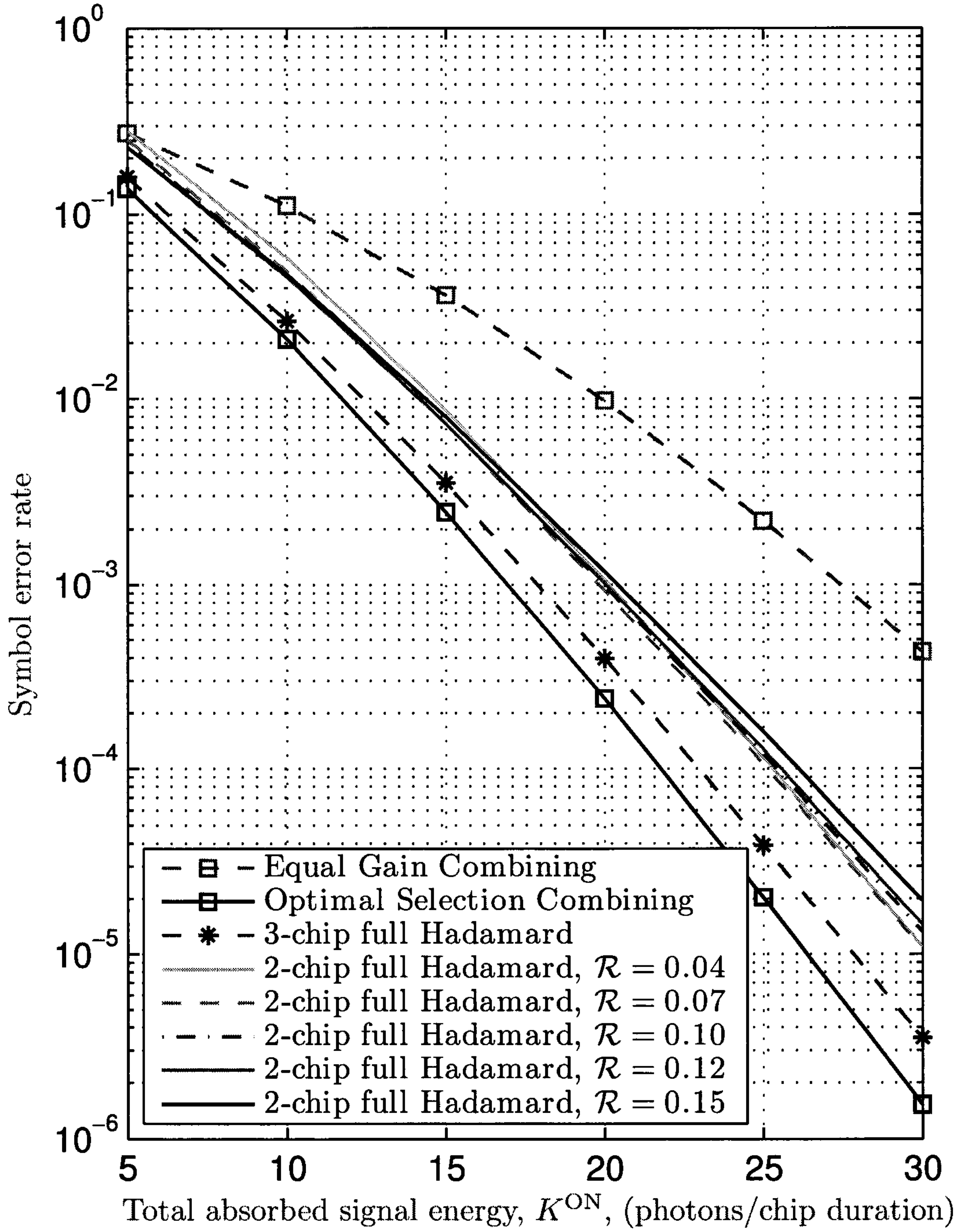

Figure 5.12: SER upper bound for 2-PPM at $K_b = 0.1$, $D/r_0 = 11.92$ and $\zeta = \eta = 1000$. A 3-chip full Hadamard DMD receiver is compared to a 2-chip full Hadamard DMD receiver at different values of $\mathcal{R}$.

5.7 Conclusions

A new receiver, based on DMD arrays, is presented for FSO channels with atmospheric turbulence. While the single-detector receiver integrates all the signal and noise over its surface, the DMD receiver only chooses those portions of the intensity distribution that contain signal and suppresses those that are dominated by noise. For the same PPM chip rate, the frame rate of the multiple-detector array receiver is equal to the PPM chip rate, while the frame rate of the DMD arrays used in the DMD receiver is much slower and defined by the turbulence rate. For the DMD receiver, only two single detectors have to operate at the PPM chip rate. Therefore, the DMD receiver is much simpler and can operate at much higher speeds than a comparable multiple-detector array receiver. High-speed multiple-detector arrays are expensive and often produce noisy output. This is particularly important since deep-space communication links are operating in the photon-counting detection mode and employing the near-infrared spectral region. The DMD receiver does not suffer from fixed-pattern noise and circuit noise associated with multiple-detector arrays. Although preamplifier noise is not considered in this chapter, the DMD receiver uses only two high-speed preamplifiers after the photodetectors $\mathsf{D}_{\mathcal{G}^+}$ and $\mathsf{D}_{\mathcal{G}^-}$, and hence the noise at the output is lower than the multiple-detector array receiver. The DMDs used are passive components that do not add noise to the signal, and have a small insertion loss.

It should also be noted that the DMD receiver is practical as it performs selection combining based on the noisy measurements taken by the photodiodes. Its performance approaches that of the optimal selection combining receiver, which is idealistic in the sense that the signal distribution $\tilde{K}_n^{(i)}$ for all $n = \{1, 2, \cdots, N\}$ is assumed known in order to be able to do the optimal selection.

Chapter 6

Conclusions and Future Work

6.1 Conclusions

This thesis has proposed new modulation and detection schemes for use over optical wireless communication links. Conventional schemes, originally designed for RF links, are seldom efficient when used over optical wireless channels because they do not take into consideration the specific optical channel characteristics and constraints. Unlike these conventional schemes, the proposed schemes take into consideration such characteristics and constraints in order to improve communication performance over indoor and outdoor optical wireless channels. These improvements have been achieved by utilizing temporal and spatial degrees of freedom that are available at the transmitter/receiver.

A new modulation scheme, OIM, has been proposed in Chapter 3 for indoor diffuse wireless optical links. OIM employs the transmitter extra degrees of freedom in the temporal frequency domain to improve both the link power efficiency and immunity to multipath dispersion, while decreasing the receiver complexity. Such degrees of freedom exist due to the fact that current transmitters, e.g. LDs and LEDs, have higher pulse rates than can be supported by the lowpass indoor diffuse channel. Although such high frequency emissions are attenuated by the channel and are not detected by the receiver, OIM employs them to satisfy the optical channel amplitude constraints, while data are confined to the lowpass region.

OIM enables the use of arbitrary pulse shapes over optical intensity channels, and thus approaches the ISI immunity of bandlimited pulse shapes. In fact, OIM exploits the wide unregulated bandwidth available in indoor wireless optical channels to satisfy amplitude constraints while transmitting bandwidth efficient pulses. Thus, OIM is able to simultaneously achieve high bandwidth and power efficiencies.

A key advantage of OIM is that the receiver design is independent of the transmitter. Actually, the OIM receiver can change from one Nyquist filter to another independent of the transmitter and without the need to feedback any information. For example, the receiver filter can be selected to be a double-jump filter with excess bandwidth which need not be known at the transmitter. In simulations, the information rate of OIM-OOK is higher than that of Rect-OOK with a complex WMF for all delay spreads and over all SNRs. Similarly, the average optical power requirement for OIM-OOK is lower than that required by Rect-OOK employing a WMF for all delay spreads, and lower than that required by Rect-OOK employing a WMF followed by a DFE for normalized delay spreads up to 0.2. A key point to emphasize is that the front end of the OIM filter is a simple lowpass filter that is fixed for all channels, while WMF and DFE equalizers require channel knowledge at the receiver.

Another modulation scheme, HSDMT modulation, is proposed in Chapter 4 for point-to-point indoor MIMO wireless optical links. HSDMT modulation employs the transmitter extra degrees of freedom in the spatial frequency domain to improve the link spectral efficiency and to decrease the transmitter complexity by considering binary-level SLMs. Such degrees of freedom exist due to the fact that current SLMs have higher spatial bandwidth than can be supported by the spatially lowpass MIMO channel. Although such high spatial frequency emissions are attenuated by the channel and are not detected by the receiver, HSDMT modulation employs them to decrease the transmitter complexity, while data are confined to the spatial lowpass region.

Neither strict spatial alignment between transmitter and receiver nor independence among the spatial channels is required for HSDMT modulation. It has been shown that with a simple feedback filter, the capacity of the channel using a binary-level transmitter approaches that when using an idealized continuous transmitter that is capable of transmitting positive and negative amplitudes. Potential applications of HSDMT modulation include holographic storage, page-oriented memories, optical interconnects, 2D barcodes, and MIMO wireless optical links.

A new spatial diversity receiver has been proposed in Chapter 5 for outdoor long-range FSO links. The receiver extra degrees of freedom in the spatial intensity domain are used to mitigate the atmospheric turbulence effects and to decrease the receiver complexity. Using DMDs, the receiver optically computes linear projections of the turbulence-degraded PSF onto an orthogonal binary basis. An estimate of the PSF is computed in terms of these projections and updated adaptively to follow the time variations of the PSF. The estimate is used to perform selection combining, i.e., to select the portions of the focal-plane which contain significant energy for symbol detection. The proposed receiver is less complex, requires fewer high-speed components, has lower preamplifier noise and can operate at higher rates than a comparable multiple-detector array receiver. While the multiple-detector receiver requires more high-speed analogue hardware, the DMD receiver requires more digital hardware for the signal processing and the control of the DMD arrays, which is simpler and more reliable.

The DMD receiver tracks those portions of the PSF that contain the majority of signal energy, and is capable of achieving a majority of the energy gain achieved by an optimal selection combining receiver. SER is simulated on a photon-counting channel and performance improvements near 3.0 dBo over a conventional single-detector receiver are obtained at SER $= 10^{-2}$. The proposed receiver is best suited to long range terrestrial, or space-to-earth FSO links, where atmospheric turbulence effects are considerable.

6.2 Future Work

OIM has been shown to be a general scheme to transmit non-negative discrete sequences over a dispersive optical intensity channel. It can be used with all PAM-based modulation techniques. It would be interesting to quantify its performance when used with differential PPM [211] and multiple PPM [212] techniques. Moreover, error-correcting codes can be applied to approach the information rates of OIM promised in Chapter 3. Since RF and optical wireless communication technologies are complementary technologies, hybrid RF/infrared indoor wireless modems are possible. For such modems, an RF channel and a diffuse infrared channel employing OIM can be established in parallel to maximize the net throughput. OIM may also find application in other non-negative dispersive channels. For example, it may find application in wireless ultraviolet communication links, which are gaining popularity for outdoor non-line-of-sight communications [213–216]. This popularity is mainly due to recent progress in ultraviolet solid-state devices and successful experimental test-beds. Such wireless ultraviolet links depend on the strong scattering of ultraviolet waves while traversing the atmosphere, which creates diverse non-line-of-sight communication paths from source to destination. As a result, ultraviolet FSO links share many properties with indoor diffuse wireless infrared links. In particular, they share the same general dispersive channel model, and therefore, OIM is expected to perform well over ultraviolet channels.

For indoor point-to-point wireless optical MIMO channels, the development of the binary-level pixelated channel prototype needs to be continued. Additionally, reduced complexity spatio-temporal coding and decoding techniques for these channels should be explored to permit real-time operation and to approach the capacities reported in Chapter 4. The signalling techniques considered in Chapter 4 assume that the receive image is an orthographic projection of the transmit intensity image with unity magnification. While magnification errors have been considered in [165], techniques to mitigate errors due to rotational and projective distortions of the receive image need further investigation.

It would be interesting to examine MIMO techniques for outdoor FSO channels. The main challenge is to mitigate the effect of the time-varying atmospheric turbulence. An accurate channel model is required to know how the PSF varies under spatial shift. This is important in order to simulate the received focal-plane signal distribution when transmitting an array of planar spatial impulses. An experimental

FSO prototype link needs to be developed to demonstrate the performance of the different DMD receivers designed in Chapter 5. It would be interesting to demonstrate such receivers under different atmospheric turbulence conditions.

Appendix A

Bit Error-Rate of L-PAM over Dispersive ISI Channels

Consider an L-PAM system over the discrete system model (3.8), where the individual symbols, a_k, are independent and uniformly distributed over the set,

$$a_k \in \left\{0, \frac{2\,\mu_a}{L-1}, \frac{4\,\mu_a}{L-1}, \frac{6\,\mu_a}{L-1}, \cdots, \frac{(2L-2)\,\mu_a}{L-1}\right\}.$$

The discrete-time system model (3.8) can be written as

$$\begin{aligned} \hat{a}_k &= \sum_i a_i q_{k-i} + z_k \\ &= a_k q_0 + (X_k + z_k), \end{aligned}$$

where

$$X_k = \sum_{i \neq k} a_i\, q_{k-i}$$

represents the ISI from the neighbouring symbols. Notice that $X_k \geq 0$ since both a_k and q_k are non-negative. That is, the received symbol, $\hat{a}_k$, is given by a scaled version of the transmitted symbol, $q_0\, a_k$, contaminated by non-zero-mean Gaussian noise, $X_k + z_k$. The *signal constellation* is defined as the set,

$$\left\{0, \frac{2\,\mu_a\, q_0}{L-1}, \frac{4\,\mu_a\, q_0}{L-1}, \frac{6\,\mu_a\, q_0}{L-1}, \dots, \frac{(2L-2)\,\mu_a\, q_0}{L-1}\right\},$$

and each element of this set is referred to as a *constellation point*. At the receiver, the detector thresholds are assumed fixed at the midpoints,

$$\left\{\frac{\mu_a\, q_0}{L-1}, \frac{3\,\mu_a\, q_0}{L-1}, \frac{5\,\mu_a\, q_0}{L-1}, \frac{7\,\mu_a\, q_0}{L-1}, \dots, \frac{(2L-3)\,\mu_a\, q_0}{L-1}\right\},$$

which depend on the channel cursor q_0.

The SER can be calculated by considering a given sequence of symbols $\mathbf{a} = (\cdots, a_{k-1}, a_k, a_{k+1}, \cdots)$. The conditional probability densities associated with two neighbouring constellation points are illustrated in Fig. A.1. The conditional probability of error associated with these two points, conditioned on the transmit sequence $\mathbf{a}$, is given by the following integrals of the Gaussian tails,

$$\int_{\frac{(2k+1)\mu_a q_0}{L-1}}^{\infty} f_1(x)\, dx + \int_{-\infty}^{\frac{(2k+1)\mu_a q_0}{L-1}} f_2(x)\, dx$$
$$= Q\left(\frac{1}{\sigma_z}\left[\frac{\mu_a q_0}{L-1} - X_k\right]\right) + Q\left(\frac{1}{\sigma_z}\left[\frac{\mu_a q_0}{L-1} + X_k\right]\right), \quad \text{(A.1)}$$

where $Q(x) = \int_x^\infty \exp(-u^2/2)/\sqrt{2\pi}\, du$, and $f_1(x)$ and $f_2(x)$ are Gaussian densities with variance σ_z^2 and means $\frac{2k\mu_a q_0}{L-1} + X_k$ and $\frac{(2k+2)\mu_a q_0}{L-1} + X_k$, respectively, as shown in Fig. A.1. Therefore, the conditional probability that the estimate $\hat{a}_k$ is in error is

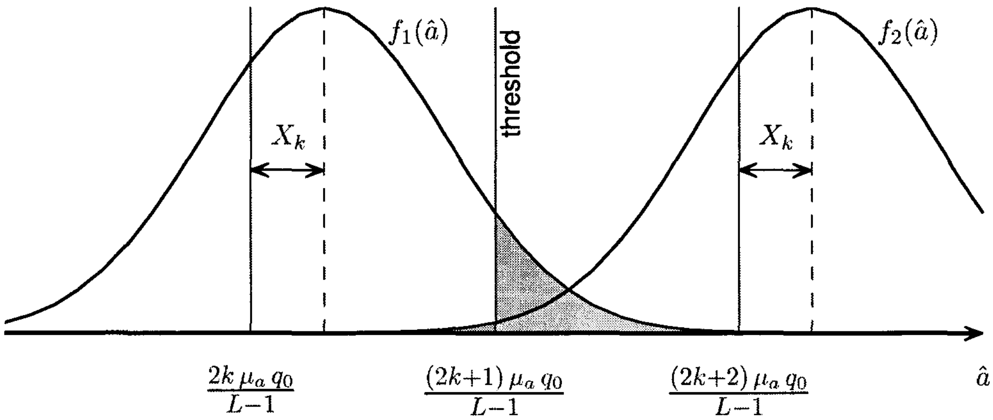

Figure A.1: Conditional probability densities associated with two neighbouring constellation points.

given by

$$\mathbb{P}[\hat{a}_k \neq a_k|\mathbf{a}] = \frac{L-1}{L}\left[Q\left(\frac{1}{\sigma_z}\left[\frac{\mu_a\,q_0}{L-1} - X_k\right]\right) + Q\left(\frac{1}{\sigma_z}\left[\frac{\mu_a\,q_0}{L-1} + X_k\right]\right)\right], \quad \text{(A.2)}$$

where the scaling factor, $\frac{L-1}{L}$, is due to the fact that the probability of error is given by the first term of (A.1) in case of the first constellation point, 0, and by the second term of (A.1) in case of the last constellation point, $\dfrac{(2L-2)\,\mu_a\,q_0}{L-1}$.

The SER can be found by averaging over all possible symbol sequences, $\mathbf{a}$,

$$\text{SER} = \frac{1}{L^M}\sum_{\mathbf{a}}\mathbb{P}[\hat{a}_k \neq a_k|\mathbf{a}] \quad \text{(A.3)}$$

where the summation is done over all L^M sequences $\mathbf{a}$, where M is the length of the impulse response tails, assumed to be finite [61]. That is, q_k is assumed non-zero for $M+1$ values, which are the cursor sample, q_0, in addition to M samples that represent the tails of q_k.

For the results presented in this thesis, it is assumed that *Gray encoding* is used to map each group of $\log_2(L)$ bits to an L-PAM symbol. According to this encoding, the adjacent PAM levels differ by only one bit, and therefore, the BER is approximately equal to the SER since errors are more likely to occur between adjacent levels [170, Sec. 4.3]. In this case, the BER expression can be found by substituting from (A.2) in (A.3) to get

$$\mathrm{BER} = \frac{L-1}{L^{M+1}} \sum_{\mathbf{a}} \left[Q\left(\frac{1}{\sigma_z}\left[\frac{\mathcal{P}_t T q_0}{L-1} - X_k\right]\right) + Q\left(\frac{1}{\sigma_z}\left[\frac{\mathcal{P}_t T q_0}{L-1} + X_k\right]\right)\right], \tag{A.4}$$

where $\mu_a = \mathcal{P}_t T$ from (3.5). At $L = 2$, the expression in (A.4) reduces to the BER of OOK given in [61].

A.1 Performance at Zero Delay Spread

Over a flat channel, i.e., at zero delay spread, (A.4) reduces to

$$\mathrm{BER} = 2\frac{L-1}{L} Q\left(\frac{1}{\sigma_z}\left[\frac{\mathcal{P}_t T q_0}{L-1}\right]\right),$$

since X_k vanishes in this case. For Rect-PAM, $q_0 = H_0/\sqrt{T}$ at zero delay spread as shown by (3.22), and therefore,

$$\mathrm{BER} = 2\frac{L-1}{L} Q\left(\frac{H_0 \mathcal{P}_t \sqrt{T}}{(L-1)\sigma_z}\right).$$

Moreover, the symbol duration is $T = \log_2(L)T_b$, and hence, the transmit power required to achieve a given BER over a flat channel can be expressed as

$$\mathcal{P}_t = \frac{\sigma_z}{H_0\sqrt{T_b}} \cdot \frac{L-1}{\sqrt{\log_2(L)}} \cdot Q^{-1}\left(\frac{L \cdot \mathrm{BER}}{2(L-1)}\right),$$

where $Q^{-1}(x)$ is the inverse of $Q(x)$. For Rect-OOK, this last expression reduces to

$$\mathcal{P}_t^{\mathrm{OOK}} = \frac{\sigma_z}{H_0\sqrt{T_b}} \cdot Q^{-1}(\mathrm{BER}). \tag{A.5}$$

The power required to achieve a given BER at zero delay spread is conventionally normalized to $\mathcal{P}_t^{\mathrm{OOK}}$ as follows,

$$\frac{\mathcal{P}_t}{\mathcal{P}_t^{\mathrm{OOK}}} = \frac{L-1}{\sqrt{\log_2(L)}} \cdot Q^{-1}\left(\frac{L \cdot \mathrm{BER}}{2(L-1)}\right) \Big/ Q^{-1}(\mathrm{BER}). \tag{A.6}$$

Appendix B

Bit Error-Rate of L-PPM over Dispersive ISI Channels

For an L-PPM system, a transmitted symbol consists of L pulses called *chips*, each of duration T_c. Therefore the symbol duration is given by $T = L\,T_c$. The PPM system is similar to that shown in Fig. 3.1, however, the pulse rate is $1/T_c$ rather than $1/T$. For example, the transmit and receive filters of Rect-PPM are given by

$$\text{Rect-PPM} \quad : \quad p(t) = \frac{1}{T_c}\,\mathrm{rect}\left(\frac{t}{T_c}\right), \tag{B.1a}$$

$$r(t) = \frac{1}{\sqrt{T_c}}\,\mathrm{rect}\left(\frac{t}{T_c}\right). \tag{B.1b}$$

The system model is similar to the discrete system model (3.8). However the PAM symbol, a_k, in (3.8) is replaced by the PPM chip, b_k, as follows

$$\hat{b}_k = q_k \otimes b_k + z_k, \tag{B.2}$$

where $\hat{b}_k$ is the received chip value. The k^{th} PPM symbol utilizes L chips,

$$\{b_{k-L+1}, b_{k-L+2}, \cdots, b_k\},$$

to transmit one of L distinct messages,

$$\left\{\boxed{1}, \boxed{2}, \cdots, \boxed{\text{L}}\right\},$$

to the receiver. If the k^{th} PPM symbol transmits message $\boxed{\text{m}}$, then $b_{k-L+m} = L\mathcal{P}_t T_c$, and all other $L-1$ chips are zeros. At the receiver, the symbol detection is based on the maximum received chip value. That is, if $\{\hat{b}_{k-L+1}, \hat{b}_{k-L+2}, \cdots, \hat{b}_k\}$ are the received chips, then message $\boxed{\text{m}}$ is detected if $\hat{b}_{k-L+m} > \hat{b}_{k-L+j}$ for all $j \in \{1, 2, \cdots, L\}$.

The BER can be calculated by considering a given sequence of PPM chips $\mathbf{b} = (\cdots, b_{k-1}, b_k, b_{k+1}, \cdots)$, where the individual chip values obey the rule that each group of L consecutive chips has only one non-zero chip. Given a sequence $\mathbf{b}$ and a transmit message $\boxed{\text{m}}$, the conditional probability of error in detecting the transmitted symbol is bounded above by the union bound

$$\sum_{\substack{j=1 \\ j \neq m}}^{L} \mathbb{P}\left[\hat{b}_{k-L+m} < \hat{b}_{k-L+j}\right],$$

and the conditional probability of bit error is given by

$$\mathbb{P}\left[\text{error} \,|\, \boxed{\text{m}}, \mathbf{b}\right] \leq \frac{L/2}{L-1} \sum_{\substack{j=1 \\ j \neq m}}^{L} \mathbb{P}\left[\hat{b}_{k-L+m} < \hat{b}_{k-L+j}\right], \tag{B.3}$$

where $\frac{L/2}{L-1}$ is the average number of bit errors per symbol error [73].

The discrete-time system model (B.2) can be written as

$$\hat{b}_k = s_k + z_k$$

where

$$s_k = q_k \otimes b_k,$$

and hence,

$$\begin{aligned}\mathbb{P}\left[\hat{b}_{k-L+m} < \hat{b}_{k-L+j}\right] &= \mathbb{P}\left[s_{k-L+m} + z_{k-L+m} < s_{k-L+j} + z_{k-L+j}\right] \\ &= \mathbb{P}\left[z_{k-L+j} - z_{k-L+m} > s_{k-L+m} - s_{k-L+j}\right].\end{aligned}$$

Since z_k is zero-mean Gaussian noise with variance σ_z^2, then $(z_{k-L+j} - z_{k-L+m})$ is zero-mean Gaussian noise with variance $2\sigma_z^2$, and therefore

$$\mathbb{P}\left[\hat{b}_{k-L+m} < \hat{b}_{k-L+j}\right] = Q\left(\frac{s_{k-L+m} - s_{k-L+j}}{\sigma_z\sqrt{2}}\right),$$

and (B.3) can be written as

$$\mathbb{P}\left[\text{error} \mid \boxed{\text{m}}, \mathbf{b}\right] \leq \frac{L/2}{L-1} \sum_{\substack{j=1 \\ j \neq m}}^{L} Q\left(\frac{s_{k-L+m} - s_{k-L+j}}{\sigma_z\sqrt{2}}\right). \tag{B.4}$$

The BER can be found by averaging over all L messages and all possible chip sequences, $\mathbf{b}$. That is

$$\text{BER} = \frac{1}{L\tilde{M}} \sum_{\boxed{\text{m}}=\boxed{1}}^{\boxed{\text{L}}} \sum_{\mathbf{b}} \mathbb{P}\left[\text{error} \mid \boxed{\text{m}}, \mathbf{b}\right], \tag{B.5}$$

where the summation is done over $\tilde{M}$ sequences, $\mathbf{b}$. Each sequence consists of $M+1$ chips, where $M+1$ is the length of the impulse response, assumed to be finite [73]. For a given transmit message, $\boxed{\mathrm{m}}$, each sequence has L chips that are fixed according to $\boxed{\mathrm{m}}$ and $M-L+1$ chips that are varying according to the neighbouring symbols. Since the number of neighbouring symbols is on the order of $(M-L+1)/L$, then $\tilde{M}$ is on the order of $L^{(M-L+1)/L}$ sequences.* Therefore the total number of terms, $L\tilde{M}$, in the double summation of (B.5) is on the order of $L^{(M+1)/L}$.

B.1 Performance at Zero Delay Spread

Over a flat channel, i.e., at zero delay spread, then $s_{k-L+m} = q_0 L\mathcal{P}_t T_c$ and $s_{k-L+j} = 0$ in (B.4). Therefore, the BER in (B.5) reduces to

$$\mathrm{BER} \le \frac{L}{2} Q\left(\frac{q_0 L\mathcal{P}_t T_c}{\sigma_z\sqrt{2}}\right).$$

For Rect-PPM, $q_0 = H_0/\sqrt{T_c}$ at zero delay spread, which is obtained by substituting $h(t) = H_0\delta(t)$ and (B.1) in (3.6). Moreover, the chip duration is $T_c = \log_2(L)T_b/L$, and hence, the transmit power required to achieve a given BER over a flat channel is bounded by

$$\mathcal{P}_t \le \frac{\sigma_z}{H_0\sqrt{T_b}}\sqrt{\frac{2}{L\log_2(L)}} \cdot Q^{-1}\left(\frac{2}{L}\mathrm{BER}\right),$$

which is conventionally normalized to $\mathcal{P}_t^{\mathrm{OOK}}$, defined in (A.5), to get

$$\frac{\mathcal{P}_t}{\mathcal{P}_t^{\mathrm{OOK}}} \le \sqrt{\frac{2}{L\log_2(L)}} \cdot Q^{-1}\left(\frac{2}{L}\mathrm{BER}\right) \Big/ Q^{-1}(\mathrm{BER}). \tag{B.6}$$

*Since $(M-L+1)/L$ may not be an integer, then we may have fractions of a symbol

Appendix C

Development of (5.22)

As mentioned in Sec. 2.1.2, $P_f(f_u, f_v)$ is the continuous Fourier transform of the pupil function, $P(u,v)$. Therefore the following sequence constitutes a sequence of continuous Fourier transform pairs.

$$\begin{aligned} P(u,v) &\longleftrightarrow P_f(f_u, f_v) \\ P_f(u,v) &\longleftrightarrow P(-f_u, -f_v) \\ P_f\left(\frac{u}{\lambda f_\ell}, \frac{v}{\lambda f_\ell}\right) &\longleftrightarrow |\lambda f_\ell|^2 P(-\lambda f_\ell f_u, -\lambda f_\ell f_v) \end{aligned} \tag{C.1}$$

Sampling (C.1) in space by $u = n_1\Delta$ and $v = n_2\Delta$, the following constitutes a discrete-time Fourier transform (DTFT) pair,

$$P_f\left(\frac{n_1\Delta}{\lambda f_\ell}, \frac{n_2\Delta}{\lambda f_\ell}\right) \longleftrightarrow \frac{|\lambda f_\ell|^2}{\Delta^2} \sum_{k_1,k_2} P\left(-\lambda f_\ell \frac{\nu_1 - k_1}{\Delta}, -\lambda f_\ell \frac{\nu_2 - k_2}{\Delta}\right),$$

where ν_1 and ν_2 are normalized frequencies such that $0 \le \nu_1 < 1$ and $0 \le \nu_2 < 1$.

Since $P(u,v)$ is supported on $|u| < D/2, |v| < D/2$, there will be no frequency domain aliasing when $\Delta \leq \lambda f_\ell/D$. Setting $\Delta = \lambda f_\ell/D$ and considering only one period $0 \leq \nu_1 < 1$ and $0 \leq \nu_2 < 1$, therefore

$$P_f\left(\frac{n_1}{D}, \frac{n_2}{D}\right) \longleftrightarrow D^2 P(-D\nu_1, -D\nu_2). \tag{C.2}$$

Sampling (C.2) in frequency domain, $\nu_1 = \dfrac{k_1}{N_1}$ and $\nu_2 = \dfrac{k_2}{N_2}$, where N_1 and N_2 are large enough so that aliasing in spatial domain is negligible, the following constitutes a DFT pair

$$P_f\left(\frac{n_1}{D}, \frac{n_2}{D}\right) \longleftrightarrow D^2 P\left(-D\frac{k_1}{N_1}, -D\frac{k_2}{N_2}\right),$$

where $n_1, k_1 \in \{0, 1, 2, \cdots N_1 - 1\}$, and $n_2, k_2 \in \{0, 1, 2, \cdots N_2 - 1\}$.

Therefore,

$$P_f\left(\frac{n_1}{D}, \frac{n_2}{D}\right) = D^2 \mathcal{F}^{-1}\left\{P\left(-D\frac{k_1}{N}, -D\frac{k_2}{N}\right)\right\}. \tag{C.3}$$

Equation (2.2) can be sampled by setting $u = n_1\lambda f_\ell/D$ and $v = n_2\lambda f_\ell/D$ to get

$$h_t\left(n_1\frac{\lambda f_\ell}{D}, n_2\frac{\lambda f_\ell}{D}\right) = \frac{1}{|\lambda f_\ell|^2 \mathcal{E}_P}\left|P_f\left(\frac{n_1}{D}, \frac{n_2}{D}\right)\right|^2.$$

Substituting from (C.3),

$$h_t\left(n_1\frac{\lambda f_\ell}{D}, n_2\frac{\lambda f_\ell}{D}\right) = \frac{D^4}{|\lambda f_\ell|^2 \mathcal{E}_P}\left|\mathcal{F}^{-1}\left\{P\left(-D\frac{k_1}{N}, -D\frac{k_2}{N}\right)\right\}\right|^2,$$

which is equation (5.22).

Bibliography

[1] J. E. Brittain, "Electrical engineering Hall of Fame: Guglielmo Marconi," *Proceedings of the IEEE*, vol. 92, no. 9, pp. 1501–1504, Aug. 2004.

[2] A. Jeffries, M. Repeta, W. Tong, D. Wessel, and P. Zhu, "New enabling technologies: Building blocks for next-generation wireless solutions," *Nortel Technical Journal*, no. 2, pp. 24–30, July 2005. [Online]. Available: http://www.nortel.com/corporate/news/collateral/ntj2_enabling.pdf (last accessed Oct. 2009)

[3] F. Gfeller and U. Bapst, "Wireless in-house data communication via diffuse infrared radiation," *Proceedings of the IEEE*, vol. 67, no. 11, pp. 1474–1486, Nov. 1979.

[4] T.-S. Chu and M. Gans, "High speed infrared local wireless communication," *IEEE Communications Magazine*, vol. 25, no. 8, pp. 4–10, Aug. 1987.

[5] G. Yun and M. Kavehrad, "Spot-diffusing and fly-eye receivers for indoor infrared wireless communications," in *Proceedings of the IEEE International Conference on Selected Topics in Wireless Communications*, June 1992, pp. 262–265.

[6] J. M. Kahn and J. R. Barry, "Wireless infrared communications," *Proceedings of the IEEE*, vol. 85, no. 2, pp. 263–298, Feb. 1997.

[7] D. J. T. Heatley, D. R. Wisely, I. Neild, and P. Cochrane, "Optical wireless: the story so far," *IEEE Communications Magazine*, vol. 36, no. 12, pp. 72–74, 79–82, Dec. 1998.

[8] G. Pang, T. Kwan, H. Liu, and C.-H. Chan, "LED wireless," *IEEE Industry Applications Magazine*, vol. 8, no. 1, pp. 21–28, Jan./Feb. 2002.

[9] S. Hranilovic, *Wireless Optical Communication Systems.* Springer, 2004.

[10] M. O. Bouchet, M. Y. Dutertre, and M. Monerie, "Infrared wireless indoor: a new multimedia communication concept," in *Proceedings of the SPIE*, vol. 5465, Strasbourg, France, Apr. 2004, pp. 188–199.

[11] Zenith Radio Corporation. URL: http://www.zenith.com.

[12] H. Willebrand and B. Ghuman, "Fiber optics without fiber," *IEEE Spectrum*, vol. 38, no. 8, pp. 40–45, Aug. 2001.

[13] R. Dettmer, "A ray of light [free space optical transmission]," *IEE Review*, vol. 47, no. 2, pp. 32–33, Mar. 2001.

[14] M. Jeganathan and P. Ionov, "Multi-gigabits-per-second optical wireless communications," White paper, Optical Crossing Incorporated. [Online]. Available: http://www.freespaceoptic.com/whitepapers.htm

[15] V. W. S. Chan, "Optical space communications," *IEEE Journal of Selected Topics in Quantum Electronics*, vol. 6, no. 6, pp. 959–975, Nov./Dec. 2000.

[16] ——, "Free-space optical communications," *IEEE/OSA Journal of Lightwave Technology*, vol. 24, no. 12, pp. 4750–4762, Dec. 2006.

[17] K. Wilson and M. Enoch, "Optical communications for deep space missions," *IEEE Communications Magazine*, vol. 38, no. 8, pp. 134–139, Aug. 2000.

[18] K. Birnbaum, W. H. Farr, J. Gin, B. Moision, K. J. Quirk, and M. W. Wright, "Tests of optical communications for deep space show promise," SPIE Newsroom, 18 June 2009. [Online]. Available: http://spie.org/x35376.xml?highlight=x2414&ArticleID=x35376

[19] H. Hemmati, Ed., *Deep Space Optical Communications*, ser. JPL Deep Space Communications and Navigation. Wiley-Interscience, 2006.

[20] "Alexander Graham Bell, inventor of the photophone," America's Library. [Online]. Available: http://www.americaslibrary.gov/cgi-bin/page.cgi/jb/gilded/bell_1

[21] J. Goodman, *Introduction to Fourier Optics*, 2nd ed. McGraw-Hill, 1996.

[22] R. M. Gagliardi and S. Karp, *Optical Communications.* John Wiley & Sons, 1976.

[23] J. H. Churnside and C. M. McIntyre, "Heterodyne receivers for atmospheric optical communications," *Applied Optics*, vol. 19, no. 4, pp. 582–590, Feb. 1980.

[24] A. Belmonte and J. M. Kahn, "Capacity of coherent free-space optical links using atmospheric compensation techniques," *Optics Express*, vol. 17, no. 4, pp. 2763–2773, Feb. 2009.

[25] E. J. Lee and V. W. S. Chan, "Diversity coherent and incoherent receivers for free-space optical communication in the presence and absence of interference," *IEEE/OSA Journal of Optical Communications and Networking*, vol. 1, no. 5, Oct. 2009.

[26] E. A. Lee and D. G. Messerschmitt, *Digital Communication*, 2nd ed. Kluwer Academic Publishers, 1994.

[27] R. G. Lane, A. Glindemann, and J. C. Dainty, "Simulation of a Kolmogorov phase screen," *Waves in Random Media*, vol. 2, no. 3, pp. 209–224, July 1992.

[28] C. M. Harding, R. A. Johnston, and R. G. Lane, "Fast simulation of a Kolmogorov phase screen," *Applied Optics*, vol. 38, no. 11, pp. 2161–2170, 1999.

[29] P. Negrete-Regagnon, "Practical aspects of image recovery by means of the bispectrum," *Journal of the Optical Society of America A: Optics, Image Science, and Vision*, vol. 13, no. 7, pp. 1557–1576, July 1996.

[30] V. Jungnickel, A. Forck, T. Haustein, U. Kruger, V. Pohl, and C. von Helmolt, "Electronic tracking for wireless infrared communications," *IEEE Transactions on Wireless Communications*, vol. 2, no. 5, pp. 989–999, Sept. 2003.

[31] Infrared Data Association (IrDA). URL: http://www.irda.org.

[32] KDDI Corporation. URL: http://www.kddi.com.

[33] P. Huang and A. Boucouvalas, "Future personal e-payment: IrFM," *IEEE Wireless Communications Magazine*, vol. 13, no. 1, pp. 60–66, Feb. 2006.

[34] Talking Signs Incorporated. URL: http://www.talkingsigns.com.

[35] R. M. Shelby, J. A. Hoffnagle, G. W. Burr, C. M. Jefferson, M.-P. Bernal, H. Coufal, R. K. Grygier, H. Gunther, R. M. Macfarlane, and G. T. Sincerbox, "Pixel-matched holographic data storage with megabit pages," *Optics Letters*, vol. 22, no. 19, pp. 1509 – 1511, Oct. 1997.

[36] G. W. Burr, J. Ashley, H. Coufal, R. K. Grygier, J. A. Hoffnagle, C. M. Jefferson, and B. Marcus, "Modulation coding for pixel-matched holographic data storage," *Optics Letters*, vol. 22, no. 9, pp. 639 – 641, May 1997.

[37] S. Nabavi and B. V. K. V. Kumar, "Detection methods for holographic data storage," in *Proceedings of the IEEE Optical Data Storage Topical Meeting*, Montreal, QC, Canada, 23-26 Apr. 2006, pp. 156 – 158.

[38] P. H. Siegel, "Information-theoretic limits of two-dimensional optical recording channels," in *Proceedings of the IEEE Optical Data Storage Topical Meeting*, Montreal, QC, Canada, 23-26 Apr. 2006, pp. 165– 167.

[39] L. Huang, G. Mathew, and T. C. Chong, "Channel modeling and target design for two-dimensional optical storage systems," *IEEE Transactions on Magnetics*, vol. 41, no. 8, pp. 2414 – 2424, Aug. 2005.

[40] R. Villán, S. Voloshynovskiy, O. Koval, and T. Pun, "Multilevel 2-D bar codes: Toward high-capacity storage modules for multimedia security and management," *IEEE Transactions on Information Forensics and Security*, vol. 1, no. 4, pp. 405–420, Dec. 2006.

[41] W. Claycomb and D. Shin, "Using a two dimensional colorized barcode solution for authentication in pervasive computing," in *Proceedings of the ACS/IEEE*

International Conference on Pervasive Services, Lyon, France, 26-29 June 2006, pp. 173 – 180.

[42] D. C. O'Brien, S. Quasem, S. Zikic, and G. E. Faulkner, "Multiple input multiple output systems for optical wireless: Challenges and possibilities," in *Proceedings of the SPIE*, vol. 6304, San Diego, CA, USA, Aug. 2006, p. 630416.

[43] J. Faucher, M. B. Venditti, and D. V. Plant, "Application of parallel forward-error correction in two-dimensional optical-data links," *IEEE/OSA Journal of Lightwave Technology*, vol. 21, no. 2, pp. 466 – 475, Feb. 2003.

[44] D. V. Plant and A. G. Kirk, "Optical interconnects at the chip and board level: challenges and solutions," *Proceedings of the IEEE*, vol. 88, no. 6, pp. 806 – 818, 2000.

[45] B. S. Leibowitz, B. E. Boser, and K. S. J. Pister, "CMOS smart pixel for free-space optical communication," in *Proceedings of the SPIE*, vol. 4306, Jan. 2001, pp. 308–318.

[46] D. C. O'Brien, G. E. Gaulkner, K. Jim, E. B. Zyamba, D. J. Edwards, M. Whitehead, P. Stavrinou, G. Parry, J. Bellon, M. J. Sibley, V. A. Lalithambika, V. M. Joyner, R. J. Samsudin, D. M. Holburn, and R. J. Mears, "High-speed integrated transceivers for optical wireless," *IEEE Communications Magazine*, vol. 41, no. 3, pp. 58 – 62, 2003.

[47] S. Kleinfelder, S. Lim, X. Liu, and A. El Gamal, "A 10000 frames/s CMOS digital pixel sensor," *IEEE Journal of Solid-State Circuits*, vol. 36, no. 12, pp. 2049–2059, Dec. 2001.

[48] S. Kleinfelder, S. Lim, X. Liu, and A. E. Gamal, "A 10 kframe/s 0.18 μm CMOS digital pixel sensor with pixel-level memory," in *Proceedings of the IEEE International Solid-State Circuits Conference*, San Francisco, CA, USA, 4-8 Feb. 2001, pp. 88 – 89.

[49] M. El-Desouki, M. Jamal Deen, Q. Fang, L. Liu, F. Tse, and D. Armstrong, "CMOS image sensors for high speed applications," *Sensors*, vol. 9, no. 1, pp. 430–444, 2009. [Online]. Available: http://www.mdpi.com/1424-8220/9/1/430

[50] T. Etoh, D. Poggemann, G. Kreider, H. Mutoh, A. Theuwissen, A. Ruckelshausen, Y. Kondo, H. Maruno, K. Takubo, H. Soya, K. Takehara, T. Okinaka, and Y. Takano, "An image sensor which captures 100 consecutive frames at 1000000 frames/s," *IEEE Transactions on Electron Devices*, vol. 50, no. 1, pp. 144–151, Jan. 2003.

[51] S. Kleinfelder, Y. Chen, K. Kwiatkowski, and A. Shah, "High-speed CMOS image sensor circuits with in situ frame storage," *IEEE Transactions on Nuclear Science*, vol. 51, no. 4, pp. 1648–1656, Aug. 2004.

[52] Metro Newspaper. URL: http://www.metronews.ca.

[53] Y.-H. Chang, C.-H. Chu, and M.-S. Chen, "A general scheme for extracting QR code from a non-uniform background in camera phones and applications," in *In Proceedings of the 9th IEEE International Symposium on Multimedia*, Taichung, Taiwan, Dec. 2007, pp. 123–130.

[54] G. Kim, X. Han, and R. Chen, "An 8-Gb/s optical backplane bus based on microchannel interconnects: design, fabrication, and performance measurements,"

IEEE/OSA Journal of Lightwave Technology, vol. 18, no. 11, pp. 1477–1486, Nov. 2000.

[55] M. G. Bevan, M. A. G. Darrin, S. C. Walts, W. Schneider, C. S. Mills, and R. F. Conde, "Free-space optical data bus for spacecraft," in *Proceedings of the 3rd annual Earth Science Technology Conference*, Maryland, USA, June 2003.

[56] E. Bisaillon, D. F. Brosseau, T. Yamamoto, M. Mony, E. Bernier, D. Goodwill, D. V. Plant, and A. G. Kirk, "Free-space optical link with spatial redundancy for misalignment tolerance," *IEEE Photonics Technology Letters*, vol. 14, no. 2, pp. 242 – 244, 2002.

[57] S. Hranilovic and F. R. Kschischang, "Short-range wireless optical communication using pixelated transmitters and imaging receivers," in *Proceedings of the IEEE International Conference on Communications*, vol. 2, Paris, France, 20-24 June 2004, pp. 891–895.

[58] ——, "A pixelated MIMO wireless optical communication system," *IEEE Journal of Selected Topics in Quantum Electronics*, vol. 12, no. 4, pp. 859–874, Jul/Aug 2006.

[59] J. M. Kahn, J. R. Barry, M. D. Audeh, J. B. Carruthers, W. J. Krause, and G. W. Marsh, "Non-directed infrared links for high-capacity wireless LANs," *IEEE Personal Communications*, vol. 1, no. 2, pp. 12–25, 1994.

[60] M. Kotzin and A. van den Heuvel, "A duplex infra-red system for in-building communications," in *Proceedings of the 36th IEEE Vehicular Technology Conference*, vol. 36, May 1986, pp. 179–185.

[61] J. R. Barry, J. M. Kahn, W. J. Krause, E. A. Lee, and D. G. Messerschmitt, "Simulation of multipath impulse response for indoor wireless optical channels," *IEEE Journal on Selected Areas in Communications*, vol. 11, no. 3, pp. 367–379, Apr. 1993.

[62] H. Hashemi, G. Yun, M. Kavehrad, F. Behbahani, and P. A. Galko, "Indoor propagation measurements at infrared frequencies for wireless local area networks applications," *IEEE Transactions on Vehicular Technology*, vol. 43, no. 3, pp. 562–576, Aug. 1994.

[63] H. Hashemi, G. Yun, M. Kavehrad, and F. Behbahani, "Frequency response measurements of the wireless indoor channel at infrared frequencies," in *Proceedings of the IEEE International Conference on Communications*, vol. 3, May 1994, pp. 1511–1515.

[64] J. M. Kahn, W. J. Krause, and J. B. Carruthers, "Experimental characterization of non-directed indoor infrared channels," *IEEE Transactions on Communications*, vol. 43, no. 234, pp. 1613–1623, Feb./Mar./Apr. 1995.

[65] M. R. Pakravan and M. Kavehrad, "Indoor wireless infrared channel characterization by measurements," *IEEE Transactions on Vehicular Technology*, vol. 50, no. 4, pp. 1053 – 1073, July 2001.

[66] Y. A. Alqudah and M. Kavehrad, "MIMO characterization of indoor wireless optical link using a diffuse-transmission configuration," *IEEE Transactions on Communications*, vol. 51, no. 9, pp. 1554 – 1560, Sept. 2003.

[67] F. J. López-Hernández, R. Pérez-Jiménez, and A. Santamaría, "Ray-tracing algorithms for fast calculation of the channel impulse response on diffuse IR wireless indoor channels," *Optical Engineering*, vol. 39, no. 10, pp. 2775–2780, 2000.

[68] O. González, S. Rodriguez, R. Pérez-Jiménez, B. R. Mendoza, and A. Ayala, "Error analysis of the simulated impulse response on indoor wireless optical channels using a Monte Carlo-based ray-tracing algorithm," *IEEE Transactions on Communications*, vol. 53, no. 1, pp. 124–130, Jan. 2005.

[69] Y. Cocheril and R. Vauzelle, "A new ray-tracing based wave propagation model including rough surfaces scattering," *Progress In Electromagnetics Research, PIER 75*, pp. 357–381, 2007.

[70] H.-S. Lee, "A photon modeling method for the characterization of indoor optical wireless communication," *Progress In Electromagnetics Research, PIER 92*, pp. 121–136, 2009.

[71] J. B. Carruthers and J. M. Kahn, "Modeling of nondirected wireless infrared channels," *IEEE Transactions on Communications*, vol. 45, no. 10, pp. 1260–1268, Oct. 1997.

[72] V. Jungnickel, V. Pohl, S. Nönnig, and C. von Helmolt, "A physical model of the wireless infrared communication channel," *IEEE Journal on Selected Areas in Communications*, vol. 20, no. 3, pp. 631 – 640, Apr. 2002.

[73] M. D. Audeh, J. M. Kahn, and J. R. Barry, "Performance of pulse-position modulation on measured non-directed indoor infrared channels," *IEEE Transactions on Communications*, vol. 44, no. 6, pp. 654 – 659, June 1996.

[74] ——, "Decision-feedback equalization of pulse-position modulation on measured nondirected indoor infrared channels," *IEEE Transactions on Communications*, vol. 47, no. 4, pp. 500 – 503, Apr. 1999.

[75] D. C. Lee, J. M. Kahn, and M. D. Audeh, "Trellis-coded pulse-position modulation for indoor wireless infrared communications," *IEEE Transactions on Communications*, vol. 45, no. 9, pp. 1080–1087, Sept. 1997.

[76] D. C. Lee and J. M. Kahn, "Coding and equalization for PPM on wireless infrared channels," *IEEE Transactions on Communications*, vol. 47, no. 2, pp. 255–260, Feb. 1999.

[77] F. Gfeller and W. Hirt, "Advanced infrared (AIr): physical layer for reliable transmission and medium access," in *Proceedings of the International Zurich Seminar on Broadband Communications*, Zurich, Switzerland, 15-17 Feb. 2000, pp. 77–84.

[78] P. Barker, V. Vitsas, and A. C. Boucouvalas, "Simulation analysis of advanced infrared (Alr) MAC wireless communications protocol," *IEE Proceedings Circuits, Devices and Systems*, vol. 149, no. 3, pp. 193–197, June 2002.

[79] R. T. Valadas, A. R. Tavares, A. M. deO. Duarte, A. C. Moreira, and C. T. Lomba, "The infrared physical layer of the IEEE 802.11 standard for wireless

local area networks," *IEEE Communications Magazine*, vol. 36, no. 12, pp. 107–112, Dec. 1998.

[80] D. Lee and J. Kahn, "Experimental 25-Mb/s wireless infrared link using 4-PPM with scalar decision-feedback equalization," in *Proceedings of the IEEE International Conference on Communications*, vol. 1, Atlanta, GA, USA, June 1998, pp. 26–30.

[81] G. W. Marsh and J. M. Kahn, "50-Mb/s diffuse infrared free-space link using on-off keying with decision-feedback equalization," *IEEE Photonics Technology Letters*, vol. 6, no. 10, pp. 1268–1270, Oct. 1994.

[82] ——, "Performance evaluation of experimental 50-Mb/s diffuse infrared wireless link using on-off keying with decision-feedback equalization," *IEEE Transactions on Communications*, vol. 44, no. 11, pp. 1496 – 1504, Nov. 1996.

[83] D. O'Brien and M. Katz, "Optical wireless communications within fourth-generation wireless systems [invited]," *Journal of Optical Networking*, vol. 4, no. 6, pp. 312–322, June 2005.

[84] Visible Light Communications Consortium. URL: http://www.vlcc.net.

[85] Japan Electronics and Information Technology Industries Association. URL: http://www.jeita.or.jp.

[86] OMEGA, the Home Gigabit Access Project. URL: http://www.ict-omega.eu.

[87] The European Commission. URL: http://ec.europa.eu.

[88] The OMEGA Project Flyer. [Online]. Available: http://www.ict-omega.eu/fileadmin/documents/flyers/OMEGA_Project_Flyer.pdf

[89] "Future networks," Projects Portfolio, Seventh EU Framework Programme for Research and Technological Development, Information Society and Media, European Commission, Mar. 2008. [Online]. Available: ftp://ftp.cordis.europa.eu/pub/fp7/ict/docs/future-networks/fp7-project-future-networks-portfolio_en.pdf

[90] National Science Foundation. URL: http://www.nsf.gov.

[91] Boston University. URL: http://www.bu.edu.

[92] Rensselaer Polytechnic Institute. URL: http://www.rpi.edu.

[93] University of New Mexico. URL: http://www.unm.edu.

[94] Smart Lighting Engineering Research Center. URL: http://smartlighting.rpi.edu.

[95] *IEC 60825-1, Safety of Laser Products - Part 1: Equipment classification, requirements, and user's guide*, International Electrotechnical Commission (IEC), 2001, edition 1.2.

[96] A. C. Boucouvalas, "IEC 825-1 eye safety classification of some consumer electronic products," in *Proceedings of the IEE Colloquium on Optical Free Space Communication Links*, IEE Savoy Place, London, 19 Feb. 1996, pp. 13/1 – 13/6.

[97] D. O'Brien, G. Parry, and P. Stavrinou, "Optical hotspots speed up wireless communication," *Nature Photonics*, vol. 1, no. 5, pp. 245–247, May 2007.

[98] D. O'Brien, M. Katz, P. Wang, K. Kalliojarvi, S. Arnon, M. Matsumoto, R. Green, and S. Jivkova, "Short-range optical wireless communications," White paper, Wireless World Research Forum, 2005. [Online]. Available: http://www.wireless-world-research.org/index.php?id=106

[99] G. Nykolak, P. Szajowski, G. Tourgee, and H. Presby, "2.5 Gbit/s free space optical link over 4.4 km," *Electronics Letters*, vol. 35, no. 7, pp. 578–579, Apr. 1999.

[100] M.-C. Jeong, J.-S. Lee, S.-Y. Kim, S.-W. Namgung, J.-H. Lee, M.-Y. Cho, S.-W. Huh, and J.-S. Lee, "8×10 Gb/s terrestrial optical free space transmission over 3.4 km using an optical repeater," in *Proceedings of the Optical Fiber Communication Conference and Exhibit*, Mar. 2002, pp. 405–407.

[101] E. Ciaramella, Y. Arimoto, G. Contestabile, M. Presi, A. D'Errico, V. Guarino, and M. Matsumoto, "1.28 Terabit/s (3240 Gbit/s) WDM transmission over a double-pass free space optical link," in *Proceedings of the Conference on Optical Fiber Communication - incudes post deadline papers*, San Diego, CA, USA, Mar. 2009, pp. 1–3.

[102] T. Manzur, "Free space optical communications (FSO)," in *Proceedings of the IEEE Avionics, Fiber-Optics and Photonics Technology Conference*, Victoria, BC, Canada, Oct. 2007, pp. 21–21.

[103] C. Moore, H. Burris, W. Rabinovich, M. Suite, L. Wasiczko, J. Jaremko, J. Ibanez, E. Georges, S. Uecke, J. Mock, J. Sender, J. Muth, and T. Wood,

"Lasercomm demonstration during US navy trident warrior 06 forcenet exercise," in *Proceedings of the IEEE Antennas and Propagation Society International Symposium*, June 2007, pp. 17–20.

[104] H. R. Burris, C. I. Moore, L. A. Swingen, M. J. Vilcheck, D. A. Tulchinsky, R. Mahon, L. M. Wasiczko, M. F. Stell, M. R. Suite, M. A. Davis, S. W. Moore, W. S. Rabinovich, J. L. Murphy, G. C. Gilbreath, and W. J. Scharpf, "Latest results from the 32 km maritime lasercom link at the Naval Research Laboratory, Chesapeake Bay Lasercom Test Facility," in *Proceedings of the SPIE*, vol. 5793, Orlando, FL, USA, Mar. 2005, pp. 209–219.

[105] J. Juarez, A. Dwivedi, A. Mammons, S. Jones, V. Weerackody, and R. Nichols, "Free-space optical communications for next-generation military networks," *IEEE Communications Magazine*, vol. 44, no. 11, pp. 46–51, Nov. 2006.

[106] B. Wu, B. Marchant, and M. Kavehrad, "Channel modeling of light signals propagating through a battlefield environment: analysis of channel spatial, angular, and temporal dispersion," *Applied Optics*, vol. 46, no. 25, pp. 6442–6448, 2007.

[107] M. Aljada, K. Alameh, and K. Al-Begain, "Distributed wireless optical communications for humanitarian assistance in disasters," in *Proceedings of the Third IEEE International Workshop on Electronic Design, Test and Applications*, Jan. 2006.

[108] J. Barthold, "Free space optics finds focus," TelephonyOnline, Penton Media Incorporated, 14 Jan. 2002. [Online]. Available: http://telephonyonline.com/mag/telecom_free_space_optics/

[109] SONAbeam, fSONA Systems Corporation. [Online]. Available: http://www.fsona.com/prod/SONAbeam-Datasheets.pdf

[110] Canobeam DT-100 Series, AIRLINX Communications Incorporated. [Online]. Available: http://www.airlinx.com/files/AIRLINX Canobeam DT-100Series Data Sheet 0606.pdf

[111] SuperGiga, Geodesy Incorporated. [Online]. Available: http://www.geodesy-fso.com/user_files/download/geodesy_fso_giga_super.pdf

[112] Solectek FSO-100E, Solectek Corporation. [Online]. Available: http://www.solectek.com/files/pdf/datasheets/FSO-100E.pdf

[113] G. Pang, T. Kwan, C.-H. Chan, and H. Liu, "LED traffic light as a communications device," in *In Proceedings of the IEEE/IEEJ/JSAI International Conference on Intelligent Transportation Systems*, Tokyo, Japan, Oct. 1999, pp. 788–793.

[114] G. Pang, C.-H. Chan, and T. Kwan, "Tricolor light-emitting diode dot matrix display system with audio output," *IEEE Transactions on Industry Applications*, vol. 37, no. 2, pp. 534–540, Mar./Apr. 2001.

[115] K. E. Wilson, "An overview of the GOLD experiment between the ETS-VI satellite and the Table Mountain Facility," Jet Propulsion Laboratory, California Institute of Technology, TDA Progress Report 42-124, 15 Feb. 1996.

[116] K. E. Wilson, J. R. Lesh, K. Araki, and Y. Arimoto, "Preliminary results of the ground/orbiter lasercom demonstration experiment between Table Mountain

and the ETS-VI satellite," in *Proceedings of the SPIE*, vol. 2699, San Jose, CA, USA, Jan. 1996, pp. 121–132.

[117] T. Tolker-Nielsen and J.-C. Guillen, "SILEX: The first European optical communication terminal in orbit," *ESA Bulletin*, no. 96, Nov. 1998. [Online]. Available: http://www.esa.int/esapub/bulletin/bullet96/NIELSEN.pdf

[118] B. Laurent, "SILEX: Overview on the european optical communications programme," *Acta Astronautica*, vol. 37, pp. 417–423, Oct. 1995.

[119] A. Alonso, M. Reyes, and Z. Sodnik, "Performance of satellite-to-ground communications link between artemis and the optical ground station," in *Proceedings of the SPIE*, vol. 5572, Maspalomas, Gran Canaria, Spain, Sept. 2004, pp. 372–383.

[120] Jet Propulsion Laboratory (JPL), California Institute of Technology. URL: http://www.jpl.nasa.gov/.

[121] K. Wilson, J. Kovalik, A. Biswas, and W. T. Roberts, "Recent experiments at the JPL optical communications telescope laboratory," Jet Propulsion Laboratory, California Institute of Technology, IPN Progress Report 42-173, 15 May 2008.

[122] A. Biswas and S. Lee, "Ground-to-ground optical communications demonstration," Jet Propulsion Laboratory, California Institute of Technology, TMO Progress Report 42-141, 15 May 2000.

[123] A. Biswas and M. W. Wright, "Mountain-top-to-mountain-top optical link demonstration: Part I," Jet Propulsion Laboratory, California Institute of Technology, IPN Progress Report 42-149, 15 May 2002.

[124] ——, "Mountain-top-to-mountain-top optical link demonstration: Part II," Jet Propulsion Laboratory, California Institute of Technology, IPN Progress Report 42-151, 15 Nov. 2002.

[125] CAPANINA Consortium. URL: http://www.capanina.org.

[126] D. Grace, M. Capstick, M. Mohorcic, J. Horwath, M. Pallavicini, and M. Fitch, "Integrating users into the wider broadband network via high altitude platforms," *IEEE Wireless Communications Magazine*, vol. 12, no. 5, pp. 98–105, Oct. 2005.

[127] National Aeronautics and Space Administration (NASA). URL: http://www.nasa.gov/.

[128] D. M. Boroson, A. Biswas, and B. L. Edwards, "MLCD: Overview of NASA's Mars laser communications demonstration system," in *Proceedings of the SPIE*, vol. 5338, San Jose, CA, USA, Jan. 2004, pp. 16–28.

[129] D. M. Boroson, R. S. Bondurant, and J. J. Scozzafava, "Overview of high-rate deep-space laser communications options," in *Proceedings of the SPIE*, vol. 5338, San Jose, CA, USA, Jan. 2004, pp. 37–49.

[130] W. D. Williams, M. Collins, D. M. Boroson, J. Lesh, A. Biswas, R. Orr, L. Schuchman, and O. S. Sands, "RF and optical communications: A comparison of high data rate returns from deep space in the 2020 timeframe," National

Aeronautics and Space Administration, Technical Memorandum NASA/TM-2007-214459, 12 Mar. 2007.

[131] K. E. Wilson and J. R. Lesh, "An overview of the Galileo optical experiment (GOPEX)," Jet Propulsion Laboratory, California Institute of Technology, TDA Progress Report 42-114, 15 Aug. 1993.

[132] J. Mendenhall, L. Candell, P. Hopman, G. Zogbi, D. Boroson, D. Caplan, C. Digenis, D. Hearn, and R. Shoup, "Design of an optical photon counting array receiver system for deep-space communications," *Proceedings of the IEEE*, vol. 95, no. 10, pp. 2059–2069, Oct. 2007.

[133] C.-C. Chen and C. Gardner, "Impact of random pointing and tracking errors on the design of coherent and incoherent optical intersatellite communication links," *IEEE Transactions on Communications*, vol. 37, no. 3, pp. 252–260, Mar. 1989.

[134] V. Vilnrotter and M. Srinivasan, "Adaptive detector arrays for optical communication receivers," Jet Propulsion Laboratory, California Institute of Technology, TMO Progress Report 42-141, 15 May 2000.

[135] L. C. Andrews, R. L. Phillips, C. Y. Hopen, and M. A. Al-Habash, "Theory of optical scintillation," *Journal of the Optical Society of America A: Optics, Image Science, and Vision*, vol. 16, no. 6, pp. 1417–1429, June 1999.

[136] X. Zhu and J. M. Kahn, "Free-space optical communication through atmospheric turbulence channels," *IEEE Transactions on Communications*, vol. 50, no. 8, pp. 1293–1300, Aug. 2002.

[137] J. C. Ricklin and F. M. Davidson, "Atmospheric turbulence effects on a partially coherent Gaussian beam: implications for free-space laser communication," *Journal of the Optical Society of America A: Optics, Image Science, and Vision*, vol. 19, no. 9, pp. 1794–1802, Sept. 2002.

[138] J. Wu and Y. Li, "Atmospheric effects on wireless optical communications," in *Proceedings of the SPIE*, vol. 6041, Dec. 2005.

[139] L. C. Andrews and R. L. Phillips, *Laser Beam Propagation through Random Media*, 2nd ed. SPIE Publications, 2005.

[140] ——, "Free-space optical communication link and atmospheric effects: single aperture and arrays," in *Proceedings of the SPIE*, vol. 5338, San Jose, CA, USA, Jan. 2004, pp. 265–275.

[141] E. J. Lee and V. W. S. Chan, "Part 1: Optical communication over the clear turbulent atmospheric channel using diversity," *IEEE Journal on Selected Areas in Communications*, vol. 22, no. 9, pp. 1896–1906, Nov. 2004.

[142] S. C. Wilks, J. R. Morris, J. M. Brase, S. S. Olivier, J. R. Henderson, C. Thyompson, M. Kartz, and A. J. Ruggiero, "Modeling of adaptive optics-based free-space communications systems," in *Proceedings of the SPIE*, vol. 4821, Seattle, WA, USA, July 2002, pp. 121–128.

[143] C. A. Thompson, M. W. Kartz, L. M. Flath, S. C. Wilks, R. A. Young, G. W. Johnson, and A. J. Ruggiero, "Free space optical communications utilizing MEMS adaptive optics correction," in *Proceedings of the SPIE*, vol. 4821, Seattle, WA, USA, July 2002, pp. 129–138.

[144] R. Mukai, K. Wilson, and V. Vilnrotter, "Application of genetic and gradient descent algorithms to wavefront compensation for the deep-space optical communications receiver," Jet Propulsion Laboratory, California Institute of Technology, IPN Progress Report 42-161, 15 May 2005.

[145] M. Troy, J. Roberts, S. Guiwits, S. Azevedo, S. Bikkannavar, G. Brack, V. Garkanian, D. Palmer, B. Platt, T. Truong, K. Wallace, and K. Wilson, "Performance of the optical communication adaptive optics testbed," Jet Propulsion Laboratory, California Institute of Technology, IPN Progress Report 42-161, 15 May 2005.

[146] R. Mukai, V. A. Vilnrotter, and C.-W. Lau, "Adaptive wavefront-correction algorithms using focal-plane array intensity measurements," Jet Propulsion Laboratory, California Institute of Technology, IPN Progress Report 42-166, 15 Aug. 2006.

[147] V. Vilnrotter and M. Srinivasan, "Adaptive detector arrays for optical communications receivers," *IEEE Transactions on Communications*, vol. 50, no. 7, pp. 1091–1097, July 2002.

[148] ——, "Adaptive optical array receiver: Communicating through atmospheric turbulence," *IPN-ISD Technology & Science News*, no. 14, pp. 14–20, Sept. 2001. [Online]. Available: http://tmot.jpl.nasa.gov/Program_Overview_Information/IND_Program_News/Issue14.pdf

[149] V. Vilnrotter, C. Lau, K. Andrews, and M. Srinivasan, "Two-element optical array receiver concept demonstration," Jet Propulsion Laboratory, California Institute of Technology, IPN Progress Report 42-161, 15 May 2005.

[150] V. Vilnrotter, C. Lau, K. Andrews, P. Vo, M. Srinivasan, and D. Lee, "Two-element optical array receiver field demonstration," Jet Propulsion Laboratory, California Institute of Technology, IPN Progress Report 42-165, 15 May 2006.

[151] Z. Hajjarian, J. Fadlullah, and M. Kavehrad, "MIMO free space optical communications in turbid and turbulent atmosphere," *Journal of Communications*, vol. 4, no. 8, pp. 524–532, Sept. 2009.

[152] S. Navidpour, M. Uysal, and M. Kavehrad, "BER performance of free-space optical transmission with spatial diversity," *IEEE Transactions on Wireless Communications*, vol. 6, no. 8, pp. 2813–2819, Aug. 2007.

[153] M. K. Emsley, O. Dosunmu, and M. S. Unlu, "High-speed resonant-cavity-enhanced silicon photodetectors on reflecting silicon-on-insulator substrates," *IEEE Photonics Technology Letters*, vol. 14, no. 4, pp. 519–521, Apr 2002.

[154] K. A. McIntosh, J. P. Donnelly, D. C. Oakley, A. Napoleone, S. D. Calawa, L. J. Mahoney, K. M. Molvar, E. K. Duerr, S. H. Groves, and D. C. Shaver, "InGaAsP/InP avalanche photodiodes for photon counting at 1.06 μm," *Applied Physics Letters*, vol. 81, no. 14, pp. 2505–2507, Sept. 2002.

[155] M. D. A. Mohamed and S. Hranilovic, "Optical impulse modulation for indoor diffuse wireless communications," *IEEE Transactions on Communications*, vol. 57, no. 2, pp. 499–508, Feb. 2009.

[156] ——, "Optical impulse modulation for diffuse indoor wireless optical channels," in *Proceedings of the IEEE International Conference on Communications*, Glasgow, Scotland, 24-28 June 2007, pp. 2140–2145.

[157] ——, "Information rates of optical impulse modulation over indoor diffuse wireless channels," in *Proceedings of the 24th Biennial Symposium on Communications*, Kingston, ON, Canada, 24-26 June 2008, pp. 196–199.

[158] ——, "Two-dimensional binary halftoned optical intensity channels," *IET Communications* (formerly, *IEE Proceedings Communications*), Special Issue on Optical Wireless Communication Systems, vol. 2, no. 1, pp. 11–17, Jan. 2008.

[159] M. D. A. Mohamed, A. Dabbo, and S. Hranilovic, "MIMO optical wireless channels using halftoning," in *Proceedings of the IEEE International Conference on Communications*, Beijing, China, 19-23 May 2008, pp. 1360–1364.

[160] M. D. A. Mohamed and S. Hranilovic, "Spatial multiplexing and diversity techniques for multiple element optical wireless links," in *Conference Record of the 43rd Asilomar Conference on Signals, Systems & Computers*, Pacific Grove, CA, USA, 1-4 Nov. 2009.

[161] ——, "Diversity reception for deep-space optical communication using linear projections," *IEEE Journal of Selected Topics in Quantum Electronics*, Special Issue on Enabling Technologies for Digital Optical Communication Systems, accepted for publication.

[162] ——, "Compressive sensing receiver for free-space optical communication through the atmosphere," in *Proceedings of the IEEE Global Telecommunications Conference*, New Orleans, LA, USA, 30 Nov. - 4 Dec. 2008.

[163] ——, "Optical communication through time-varying turbulent atmosphere using compressive sensing," in *Proceedings of the 11th Canadian Workshop on Information Theory*, Ottawa, ON, Canada, 13-15 May 2009, pp. 140–143.

[164] W. Hubbard, "The approximation of a Poisson distribution by a Gaussian distribution," *Proceedings of the IEEE*, vol. 58, no. 9, pp. 1374–1375, Sept. 1970.

[165] A. Dabbo and S. Hranilovic, "Receiver design for wireless optical MIMO channels with magnification," in *Proceedings of the 10th International Conference on Telecommunications, ConTEL 2009*, Zagreb, Croatia, 8-10 June 2009, pp. 51–58.

[166] A. Dabbo, "Design of wireless optical MIMO links," Master's thesis, Department of Electrical and Computer Engineering, McMaster University, 2009.

[167] T. Chen, P. Catrysse, A. E. Gamal, and B. Wandell, "How small should pixel size be?" in *Proceedings of the SPIE Electronic Imaging Conference*, vol. 3965, San Jose, CA, USA, Jan. 2000.

[168] G. C. Holst, *CCD Arrays, Cameras, and Displays*, 2nd ed. Bellingham, WA, USA: SPIE Optical Engineering Press, 1998.

[169] G. Held, *Introduction to Light Emitting Diode Technology and Applications.* Auerbach, 2008.

[170] J. G. Proakis, *Digital Communications*, 4th ed. McGraw-Hill, 2001.

[171] W. Kang and S. Hranilovic, "Optical power reduction for multiple-subcarrier modulated indoor wireless optical channels," in *Proceedings of the IEEE International Conference on Communications*, vol. 6, Istanbul, Turkey, June 2006, pp. 2743–2748.

[172] ——, "Power reduction techniques for multiple-subcarrier modulated diffuse wireless optical channels," *IEEE Transactions on Communications*, vol. 56, no. 2, pp. 279–288, Feb. 2008.

[173] L. Yang and G. B. Giannakis, "Ultra-wideband communications: an idea whose time has come," *IEEE Signal Processing Magazine*, vol. 21, no. 6, pp. 26–54, Nov. 2004.

[174] H. Nyquist, "Certain topics in telegraph transmission theory," *Transactions of the AIEE*, vol. 47, pp. 617–644, Feb. 1928.

[175] N. C. Beaulieu and M. O. Damen, "Parametric construction of Nyquist-I pulses," *IEEE Transactions on Communications*, vol. 52, no. 12, pp. 2134–2142, Dec. 2004.

[176] G. A. Bliss, *Lectures on the Calculus of Variations.* The University of Chicago Press, 1946.

[177] L. E. Franks, "Further results on Nyquist's problem in pulse transmission," *IEEE Transactions on Communication Technology*, vol. 16, no. 2, pp. 337–340, Apr. 1968.

[178] D. M. Arnold and H.-A. Loeliger, "On the information rate of binary-input channels with memory," in *Proceedings of the IEEE International Conference on Communications*, vol. 9, Helsinki, Finland, 11-14 June 2001, pp. 2692–2695.

[179] H. D. Pfister, J. B. Soriaga, and P. H. Siegel, "On the achievable information rates of finite state ISI channels," in *Proceedings of the IEEE Global Telecommunications Conference*, vol. 5, San Antonio, TX, USA, 2001, pp. 2992–2996.

[180] D. M. Arnold, H.-A. Loeliger, P. O. Vontobel, A. Kavcic, and W. Zeng, "Simulation-based computation of information rates for channels with memory," *IEEE Transactions on Information Theory*, vol. 52, no. 8, pp. 3498–3508, Aug. 2006.

[181] U. Sethakaset and T. A. Gulliver, "On the capacity of indoor optical wireless communications," *IEEE Communications Letters*, vol. 10, no. 7, pp. 552 – 554, July 2006.

[182] H. Park and J. R. Barry, "Performance analysis and channel capacity for multiple-pulse position modulation on multipath channels," in *Proceedings of the IEEE International Symposium on Personal, Indoor and Mobile Radio Communications*, vol. 1, Taipei, Taiwan, 15-18 Oct. 1996, pp. 247 – 251.

[183] T. M. Cover and J. A. Thomas, *Elements of Information Theory*. NY, USA: John Wiley & Sons, 1991.

[184] P. H. Algoet and T. M. Cover, "A sandwich proof of the Shannon-McMillan-Breiman theorem," *The Annals of Probability*, vol. 16, no. 2, pp. 899–909, 1988.

[185] L. R. Bahl, J. Cocke, F. Jelinek, and J. Raviv, "Optimal decoding of linear codes for minimizing symbol error rate," *IEEE Transactions on Information Theory*, vol. 20, no. 2, pp. 284–287, Mar. 1974.

[186] A. Dabbo and S. Hranilovic, "Multilevel error diffusion for wireless optical MIMO channels," in *Proceedings of the 24th Biennial Symposium on Communications*, Kingston, ON, Canada, 24-26 June 2008, pp. 208–211.

[187] A. Peled and A. Ruiz, "Frequency domain data transmission using reduced computational complexity algorithms," in *Proceedings of the IEEE International Conference on Acoustics, Speech, and Signal Processing*, vol. 5, Denver, CO, USA, 9-11 Apr. 1980, pp. 964 – 967.

[188] Texas Instruments Incorporated, Digital Light Processing. URL: http://www.dlp.com.

[189] M. B. Venditti, E. Laprise, J. Faucher, P.-O. Laprise, J. E. A. Lugo, and D. V. Plant, "Design and test of an optoelectronic-VLSI chip with 540-element receiver-transmitter arrays using differential optical signaling," *IEEE Journal of Selected Topics in Quantum Electronics*, vol. 9, no. 2, pp. 361 – 379, Mar./Apr. 2003.

[190] D. C. OBrien, G. E. Faulkner, E. B. Zyambo, K. Jim, D. J. Edwards, P. Stavrinou, G. Parry, J. Bellon, M. J. Sibley, V. A. Lalithambika, V. M. Joyner, R. J. Samsudin, D. M. Holburn, and R. J. Mears, "Integrated transceivers for optical wireless communications," *IEEE Journal of Selected Topics in Quantum Electronics*, vol. 11, no. 1, pp. 173 – 183, Jan./Feb. 2005.

[191] R. Ulichney, *Digital Halftoning.* Cambridge, MA, USA: MIT Press, 1987.

[192] B. L. Shoop, *Photonic Analog-to-Digital Conversion.* Berlin, Germany: Springer-Verlag, 2001.

[193] R. W. Floyd and L. Steinberg, "An adaptive algorithm for spatial gray scale," in *SID Symposium Digest, Society for Information Display*, 1975, pp. 36–37.

[194] D. Anastassiou, "Error diffusion coding for A/D conversion," *IEEE Transactions on Circuits and Systems*, vol. 36, no. 9, pp. 1175–1186, Sept. 1989.

[195] B. L. Shoop and E. K. Ressler, "An error diffusion neural network for digital image halftoning," in *Proceedings of the IEEE Workshop on Neural Networks for Signal Processing*, 31 Aug.-2 Sept. 1995, pp. 427–436.

[196] ——, "Optimal error diffusion for digital halftoning using an optical neural network," in *Proceedings of the IEEE International Conference on Image Processing*, vol. 2, Austin, TX, USA, 13-16 Nov. 1994, pp. 1036–1040.

[197] S. R. Norsworthy, R. Schreier, and G. C. Temes, Eds., *Delta-Sigma Data Converters: Theory, Design, and Simulation.* NY, USA: Wiley-IEEE Press, 1996.

[198] D. A. Johns and K. W. Martin, *Analog Integrated Circuit Design.* John Wiley & Sons, 1996.

[199] S. Diggavi and T. Cover, "The worst additive noise under a covariance constraint," *IEEE Transactions on Information Theory*, vol. 47, no. 7, pp. 3072–3081, Nov. 2001.

[200] J. Tellado, *Multicarrier modulation with low PAR: applications to DSL and wireless.* Norwell, MA, USA: Kluwer Academic Publishers, 2000.

[201] NEC Corporation. URL: http://www.nec.com.

[202] Mikrotron GmbH. URL: http://www.mikrotron.de.

[203] Matrox Imaging. URL: http://www.matrox.com.

[204] NorPix Incorporated. URL: http://www.norpix.com.

[205] National Instruments Corporation. URL: http://www.ni.com.

[206] L. J. Hornbeck, "Current status and future applications for DMD-based projection displays," in *Proceedings of the 5th International Display Workshop, IDW '98*, Kobe, Japan, 1998, pp. 713–716.

[207] M. Charbit and C. Bendjaballah, "Probability of error and capacity of PPM photon counting channel," *IEEE Transactions on Communications*, vol. 34, no. 6, pp. 600–605, June 1986.

[208] D. Takhar, J. N. Laska, M. B. Wakin, M. F. Duarte, D. Baron, S. Sarvotham, K. F. Kelly, and R. G. Baraniuk, "A new compressive imaging camera architecture using optical-domain compression," in *Proceedings of SPIE Electronic Imaging*, San Jose, CA, Jan. 2006, pp. 43–52.

[209] J. Strackee and J. J. Denier van der Gon, "The frequency distribution of the difference between two Poisson variates," *Statistica Neerlandica*, vol. 16, no. 1, pp. 17 – 23, 1962.

[210] N. J. Harrick, "A continuously variable optical beam splitter and intensity controller," *Applied Optics*, vol. 2, no. 11, pp. 1203–1204, Nov. 1963.

[211] D. Shiu and J. M. Kahn, "Differential pulse-position modulation for power-efficient optical communication," *IEEE Transactions on Communications*, vol. 47, no. 8, pp. 1201–1210, Aug. 1999.

[212] H. Sugiyama and K. Nosu, "MPPM: a method for improving the band-utilization efficiency in optical PPM," *IEEE/OSA Journal of Lightwave Technology*, vol. 7, no. 3, pp. 465 – 472, Mar. 1989.

[213] H. Ding, G. Chen, A. Majumdar, B. Sadler, and Z. Xu, "Modeling of non-line-of-sight ultraviolet scattering channels for communication," *IEEE Journal on Selected Areas in Communications*, vol. 27, no. 9, pp. 1535–1544, Dec. 2009.

[214] G. Chen, Z. Xu, H. Ding, and B. M. Sadler, "Path loss modeling and performance trade-off study for short-range non-line-of-sight ultraviolet communications," *Optics Express*, vol. 17, no. 5, pp. 3929–3940, Mar. 2009.

[215] Z. Xu and B. Sadler, "Ultraviolet communications: Potential and state-of-the-art," *IEEE Communications Magazine*, vol. 46, no. 5, pp. 67–73, May 2008.

[216] G. A. Shaw, A. M. Siegel, J. Model, and D. Greisokh, "Recent progress in short-range ultraviolet communication," in *Proceedings of the SPIE*, E. M. Carapezza, Ed., vol. 5796, no. 1, Orlando, FL, USA, 2005, pp. 214–225.